Quantitative Characterization of Biological Tissues by NMR Relaxation in the Rotating Frame

By

John Thomas Spear

Dissertation

Submitted to the Faculty of the

Graduate School of Vanderbilt University

in partial fulfillment of the requirements

for the degree of

DOCTOR OF PHILOSOPHY

in

Physics

May, 2016

Nashville, Tennessee

Approved:

John C. Gore, Ph.D.

Daniel F. Gochberg, Ph.D.

Michael S. Hutson, Ph.D.

Erin C. Rericha, Ph.D.

Thomas E. Yankeelov, Ph.D.

Acknowledgements

I would like to thank my wonderful advisor John Gore for all the guidance, support, and insight he provided over the past few years. My contributions would not have been possible without his counsel, encouragement, and willingness to fund my project. I also thank my committee members Dr. Gochberg, Dr. Yankeelov, Dr. Rericha, and Dr. Hutson for all their guidance and instruction over the years that helped me become the researcher and person I am today. Finally I thank all my family and friends, especially my wife and daughter Ashley and Ariana, for the unconditional support they offered on a daily basis.

List of Figures

Figure 1: The current loop (red) in a magnetic field (grey) results in a torque that creates the force vectors in blue that cause the loop to orient itself with respect to the static field. 6

Figure 2: Spherical coordinate system used to convey an arbitrary magnetization vector. 9

Figure 3: Energy levels of a heteronuclear AX system with the corresponding transition rates.. 16

Figure 4: a.) A hard pulse initially tips the magnetization into the transverse plane. b.) The locking pulse creates an effective field in the y-z plane that the magnetization precesses about. c.) The magnetization is tipped back to the longitudinal z-axis. 20

Figure 5: Variations of spin-locking pulse sequences, each with features meant to mitigate image artifacts. 21

Figure 6: An example of chemical exchange between the bulk water pool and the glucose solute pool. The coupled exchange rates describe the rate of this process and are determined by the relative pool fractions of each pool. 23

Figure 7: Schematic of an exchanging two-pool system. Each pool has independent initial magnetizations, relaxation rates, chemical shifts, and coupled exchange rates. 32

Figure 8: Simulated $R_{1\rho}$ dispersion curves compared to the Chopra and Trott models. a,b.) Simulations with different sets of intrinsic pool relaxation rates. c,d.) Simulated data fit to each model to compare the calculated exchange rates to the true rate that was simulated... 47

Figure 9: Simulated $R_{1\rho}$ dispersions for the intermediate exchange regime. a,b.) Comparison of each simulated dispersion to the theoretical Trott and Chopra models. c,d.) Examining the estimated exchange rates from fitting the simulated data to each model. 49

Figure 10: Simulated $R_{1\rho}$ dispersions for the fast exchange regime. a,b.) Comparison of each simulated dispersion to the theoretical Chopra and Trott models. c,d.) Examining the estimated exchange rates from fitting the simulated data to each model. 51

Figure 11: a.) Simulated $R_{1\rho}$ dispersions for pool fractions from 0.5% - 4% were fit to both the Chopra and Trott Models. b.) The estimated exchange rates from each fit were compared to the simulated exchange rate of 3,000 Hz (dotted black line)..... 53

Figure 12: 7T $R_{1\rho}$ dispersions of 200 mM glucose at 20°C (a) and 37°C (b). The data are fit to both the Chopra and Trott models to estimate the exchange rates at each temperature. 54

Figure 13: 7T $R_{1\rho}$ dispersions of 200 mM myo-inositol at 20C (a) and 37C (b). The data are fit to both the Chopra and Trott models to estimate the exchange rates at each temperature. 55

Figure 14: 7T $R_{1\rho}$ dispersions of 1M ethanol solutions at 20°C (a) and 37°C (b). These data were fit to both models at each temperature to estimate the exchange rates. 56

Figure 15: a,b.) $R_{1\rho}$ dispersions of 200 mM glucose solutions with different amounts of D_2O present at 4.7T and 7T. c.) Measured R_1 values for each sample at 4.7T and 7T. 57

Figure 16: The low locking field limit of $R_{1\rho}$ plotted as a function of D_2O for both 4.7T and 7T. Extrapolating the linear fit for each field strength allows the estimation of the dipolar contributions when the sample is fully deuterated at 0% ^1H. 58

Figure 17: a.) $R_{1\rho}$ dispersions of 200 mM glucose solution at verious temperatures at 7T. b.) Exchange rates calculated from fitting for each temperature. c.) $R_{1\rho}$ dispersions for 200 mM glucose solutions at 7T for various pH values. d.) Exchange rates calculated from fitting for each pH value..... 59

Figure 18: a.) R1rho dispersions of 200 mM glucose over a smaller range of pH values. b.) The estimated exchange rates calculated from the dispersion fits. 60

Figure 19: a.) $R_{1\rho}$ dispersions of 200 mM glucose at 4.7T for pH = 6.0 - 7.4. b.) Theoretical $R_{1\rho}$ dispersion magnitudes are shown as a function of exchange rate for various B_0 field strengths. 61

Figure 20: $R_{1\rho}$ dispersion inflection point frequencies plotted as functions of chemical exchange rates at multiple field strengths for two chemical shifts of $\Delta\omega_b$ = 1 ppm (a) and $\Delta\omega_b$ = 3.5 ppm (b). 62

Figure 21: The $R_{1\rho}$ ratio plotted for multiple field strengths decreases with exchange rate but provides a fast method for estimating exchange rates in practice. 63

Figure 22: a.) Two-pool $R_{1\rho}$ dispersions with exchange rates ranging from 100 - 10,000 Hz. b.) ERC curves calculated from the fitted $R_{1\rho}$ dispersions with vertical dotted lines indicating the peak positions. 64

Figure 23: The colored theoretical EWIC curves are shown to shift to higher locking amplitudes compared to the black ERC curve as the locking time increases. 65

Figure 24: EWIC peak frequency as a function of locking time 5 different dispersion magnitudes. 67

Figure 25: $R_{1\rho}$ dispersion (a) and ERC curve (b) for 200 mM glucose solution in PBS with pH = 6.7 68

Figure 26: Comparison of an $R_{1\rho}$ image at 562 Hz with a locking time of 50 ms, a $R_{1\rho}$ map at 562 Hz, and an ERC image at 562 Hz. 69

Figure 27: Average intensities for the $R_{1\rho}$ image, the $R_{1\rho}$ map, and the ERC image with error bars representing ± 1 standard deviation. The normal and tumor regions displayed significant contrasts in all images ($p < 0.05$). 70

Figure 28: Schematic of an arbitrary 3-pool system with unique initial magnetizations, relaxation rates, and chemical shifts. Arrows and rate constants represent exchange between each pool with minor exchange between solute pools in gray since this is typically ignored. 74

Figure 29: Maximum theoretical ERC contrast is shown to be 99% when the peaks are separated by 20 kHz and only 50% when they are separated by 5 kHz. 79

Figure 30: Chemical structures for the creatine, glucose, and uracil metabolites used in the mixture solution experiments. 82

Figure 31: a,c.) Simulated $R_{1\rho}$ dispersions for individual exchange pools (red and blue), with both pools simulated simultaneously (black), which is compared to the addition of the individual curves (orange). b,d.) Simulated $R_{1\rho}$ double dispersions with the addition of minor exchange described by rates of 0 – 5,000 Hz. 85

Figure 32: a,c.) Measured R1rho dispersions in solutions of creatine, glucose, and uracil along with double dispersions of corresponding mixtures in black. b,d.) The double dispersion fit for each pool contribution is compared to the individually measured contributions. 88

Figure 33: a.) Simulated R1rho dispersions with increasing pool fraction of pc = 0 - 1%. b.) The corresponding ERC curves calculated from the simulated R1rho dispersion curves with the position of the pool c peak shown by the thick black line. c.) The ERC values of all concentrations along the thick black line at the locking field of 160 Hz. 90

Figure 34: a.) Theoretical ERC curves with peak separations from 200 - 2,000 Hz. b.) The pool fraction dependent ERC values for each pair of ERC peaks. 91

Figure 35: a.) $R_{1\rho}$ map of glucose and uracil solutions at a locking strength of 545 Hz. b.) The corresponding $R_{1\rho}$ dispersion curves of each sample in the $R_{1\rho}$ map calculated from ROI analysis. 92

Figure 36: a.) ERC map at a locking strength of 545 Hz emphasizes solutions with glucose due to its exchange rate. b.) The mean ERC values are plotted as a function of glucose concentration. 93

Figure 37: Simulated $R_{1\rho}$ dispersions and $R_{1\rho}$ contrasts plotted as functions of various exchange parameters (a-f). Z-spectra and CEST contrasts plotted as a function of the same exchange parameters for comparison (g-l). 103

Figure 38: $R_{1\rho}$ dispersions for 2DG phantoms and homogenates at various concentrations (a,c). The corresponding $R_{1\rho}$ contrasts plotted as a function of 2DG concentration (b,d). 105

Figure 39: CEST Z-spectra with pulse powers of 1, 2, and 3 T for 2DG phantoms with concentrations of 50, 100, and 150 mM (a,b,c). The corresponding CEST contrasts are plotted as a function of 2DG concentration (d). 106

Figure 40: The $R_{1\rho}$ dispersions and Z-spectra are plotted for 4 time points for rat #1 (a,c). The corresponding $R_{1\rho}$ and CEST contrasts are plotted for all 4 healthy rats as a function of time (b.d). 108

Figure 41: a.) $R_{1\rho}$ contrast time course in normal and tumor regions of the brain. b.) Anatomical image of the brain to illustrate the tumor region acquired prior to the infusion. c,d.) $R_{1\rho}$ contrast image depicting greater tumor differentiation reflecting elevated 2DG levels compared to the CEST contrast image. Both images represent the time point 70 minutes after the start of infusion. 109

Figure 42: An example of four nuclei diffusing though a simulated gradient field induced by packed microspheres. Following the paths shows how the local field experienced by these nuclei fluctuates with time. 113

Figure 43: The 3 unit cells used for simulating diffusion through susceptibility variations. Each structure was assigned radii and spaced out to achieve specific volume fractions..... 123

Figure 44: a-c.) $R_{1\rho}$ dispersions for various radii with 60% volume fractions packed in BCC, FCC, and Cylinder structures respectively. d-f.) $R_{1\rho}$ dispersions for various volume fractions of BCC, FCC, and Cylinder structures with 5 μm radii..... 127

Figure 45: a.) $R_{1\rho}$ dispersions for R = 5 μm, 60% volume fraction BCC structures with susceptibilities 1 - 6 times that of polystyrene. b.) $R_{1\rho}$ dispersions of the same structure with varying matrix sizes to change the voxel resolutions. 128

Figure 46: a.) Correlation times plotted against radius for each packing structure at 60 % volume fraction. b.) Correlation times plotted against volume fraction for each packing structure with 5 μm radii. 130

Figure 47: Theoretical spatial frequency plotted versus the fitted spatial frequency assuming D = 2.5 $\mu m^2/ms$ for varying radii in each of the packing structures. 131

Figure 48: $R_{1\rho}$ dispersions of polystyrene microspheres ranging from 1 - 90 μm in diameter... 133

Figure 49: a.) g^2D plotted versus radius shows a gradient strength dependence of $r^{-0.915}$. b.) Experimental correlation times (red) are shown to match well with the simulated correlation times (blue) from the BCC structures. 134

Figure 50: a.) Correlation time map (seconds) for microsphere samples ranging from 1 - 20 μm in diameter. b.) Correlation times for each sample with different sphere spacings achieved by diluting. 135

Figure 51: Illustration of chemical exchange occurring in the presence of susceptibility gradients. 140

Figure 52: a.) Simulated $R_{1\rho}$ dispersions for the case of chemical exchange and diffusion for the BCC structures. b.) The R = 10 μm double dispersion compared to individual effects shows the effects are independent of one another. 147

Figure 53: Estimated exchange parameters compared to the theoretical values (a,b). The estimated diffusion parameters were compared to the individual diffusion parameters from chapter 5 (c,d). 148

Figure 54: Simulated spin-locked signal decay in the presence of only diffusion (a) and in the presence of both diffusion and exchange (b) may be accounted for with different decay models. 149

Figure 55: a.) $R_{1\rho}$ map calculated in whole bovine blood at the locking field of 50 Hz for all oxygenation levels. b.) The corresponding $R_{1\rho}$ double dispersions. 150

Figure 56: a.) The exchange and diffusion portions of Eq. 6.1 are plotted individually to show the manner in which the diffusion dispersion decreases with oxygen saturation. b.) The gradient strength parameter decreases as expected with sO_2. c.) The spatial frequency parameter decreases with sO_2 indicating a smaller concentration of cells containing deoxyhemoglobin. 151

Figure 57: The simulated correlation times from the BCC structures were related to radius by fitting to an exponential model. 152

Figure 58: $R_{1\rho}$ dispersions in 8 separate rat livers at 7T, 4 after a tail vein injection of Gd-DTPA and 4 controls without Gd-DTPA. 154

Figure 59: Average values of rat liver T_1 (a) and the correlation times, τ_c (b), before and after a tail vein injection of Gd-DTPA. Both parameters revealed statistically significant changes. 155

Figure 60: Red blood cells containing paramagnetic deoxyhemoglobin (blue) generate relatively large local field gradients that can induce transverse dephasing. 160

Figure 61: Activation maps for one volunteer using each sequence. The number of significant pixels decreases from left to right due to the sequences becoming more selective. 165

Figure 62: Time course of the frontal cortex and the visual cortex shows only significant changes due to the stimulus occurred in the visual cortex. 166

Figure 63: a.) Percent signal change plotted for all sequences, with statistical significance indicated by *. b.) The change in $T_{1\rho}$ compared at both locking fields was shown to be statistically significant. 167

Figure 64: Percent signal change in the visual cortex resulting from the spin-lock sequence at each amplitude. Statistical significance with $p < 0.05$ represented by ** while * represented $p < 0.01$. 168

Figure 65: Signal change time course for all 4 pulse sequences collapsed across all subjects and acquisitions. The solid horizontal bar indicates the application of the visual stimulus. 169

Table of Contents

Acknowledgements ..... **ii**

List of Figures ..... **iii**

Chapter

1. Introduction to Magnetic Resonance Imaging Contrast and Relaxation in the Rotating Frame **1**

Objective **1**

Background and Literature Review **2**

A Brief History of NMR 2

Classical Precession 5

Quantum Mechanical Basis for MRI 9

Adding Relaxation Terms to the Bloch Equations 12

Introduction to Relaxation Theory 14

Factors Influencing $R_{1\rho}$ 18

Motivation for $R_{1\rho}$ Based Imaging 27

Conclusion **28**

2. Exchange Rate Contrast in MRI **30**

Introduction **30**

Motivation 30

Two-Pool Models of Exchange 31

Exchange Rate Contrast 37

Specific Aims **39**

Aim 1 39

Aim 2 40

Aim 3 40

Aim 4 41

Aim 5 41

Methods **41**

Comparing $R_{1\rho}$ Models 41

Effects of Deuteration 43

Effects of Temperature and pH 44

Exchange Rate Contrast vs. Exchange Weighted Image Contrast 45

Exchange Rate Contrast in vivo 46

Results and Discussion **46**

Comparing $R_{1\rho}$ Models 46

Effects of Deuteration 56

Effects of Temperature and pH 59

Exchange Rate Contrast vs. Exchange Weighted Image Contrast 64

Exchange Rate Contrast in vivo 68

Conclusions **71**

3. Rotating Frame Relaxation in Systems of *n*-Exchanging Pools **73**

Introduction and Theory **73**

Extended Chopra Model 73

Extended Exchange Rate Contrast 77

Specific Aims **80**

Aim 1 80

Aim 2 80

Aim 3 80
Aim 4 81
Methods 81
3-Pool Bloch McConnell Simulations and Experiments 81
3-Pool ERC Simulations and Experiments 83
Results and Discussion 84
3-Pool $R_{1\rho}$ Simulations and Experiments 84
3-Pool ERC Simulations and Experiments 89
Conclusions 93

4. Detection of Exogenous Contrast Agents Using Spin-Locking Pulse Sequences in Model Systems and in vivo 96
Introduction and Theory 96
Specific Aims 98
Aim 1 98
Aim 2 98
Aim 3 99
Methods 99
Numerical $R_{1\rho}$ and CEST Simulations 99
$R_{1\rho}$ and CEST Measurements in Model Systems of 2DG 101
$R_{1\rho}$ and CEST Measurements in Rat Brains in vivo 102
Results and Discussion 103
Numerical $R_{1\rho}$ and CEST Simulations 103
$R_{1\rho}$ and CEST Measurements in Model Systems of 2DG 105
$R_{1\rho}$ and CEST Measurements in Rat Brains in vivo 107
Conclusions 110

5. Characterizing Heterogeneous Media by Analyzing the Spatial Scales of Susceptibility Variations With $R_{1\rho}$ Dispersion 112
Introduction 112
Theory 115
Deriving the Influence of Diffusion on $R_{1\rho}$ 115
Interpreting Diffusion Parameters 119
Specific Aims 122
Aim 1 122
Aim 2 122
Methods 122
$R_{1\rho}$ Diffusion Simulations 122
$R_{1\rho}$ Diffusion Experiments 125
Results and Discussion 127
$R_{1\rho}$ Diffusion Simulations 127
$R_{1\rho}$ Diffusion Experiments 132
Conclusions 136

6. Analyzing Systems With Both Chemical Exchange and Diffusion in the Presence of Susceptibility Gradients With $R_{1\rho}$ Dispersion 139
Introduction and Theory 139
Specific Aims 142
Aim 1 142
Aim 2 142
Aim 3 143
Methods 143

Simulations with Exchange and Diffusion 143
Measuring $R_{1\rho}$ Dispersions in Blood 145
Measuring $R_{1\rho}$ Dispersions in Rat Liver 146
Results and Discussion 147
Simulations with Exchange and Diffusion 147
Measuring $R_{1\rho}$ Dispersions in Blood 150
Measuring $R_{1\rho}$ Dispersions in Rat Liver 153
Conclusions 157

7. Spin-Locking Preparation Pulses in Functional MRI 159
Introduction 159
Specific Aims 162
Aim 1 162
Methods 162
Results and Discussion 164
Conclusions 170

8. Conclusions and Future Directions 171
Chemical Exchange $R_{1\rho}$ Dispersion Methods 171
$R_{1\rho}$ Dispersion vs. CEST 173
$R_{1\rho}$ Diffusion Methods 174
Combined Effects and Applications 175
Overall Evaluations of $R_{1\rho}$ Methods 176

References 179

CHAPTER 1

Introduction to Magnetic Resonance Imaging Contrast and Relaxation in the Rotating Frame

Objective

The theories and experiments described in this thesis aim to advance the utilization of quantitative measures in magnetic resonance imaging (MRI) to characterize heterogeneous biological tissues at high static field strengths. More specifically, to advance the manner in which spin-locking techniques are utilized in both spectroscopic and imaging contexts to estimate intrinsic characteristics of the medium of interest. Spin-locking pulse sequences have the ability to probe relaxation mechanisms at a range of time scales by measuring the spin-lattice relaxation time in the rotating frame, $T_{1\rho}$, and have been previously exploited to characterize tissues and assess pathological changes in various research and clinical applications. Similar experiments have been used in the past to investigate molecular interactions in various physiological or pathologic changes such as in animal stroke and tumor models (*1–5*), with activation in human brain in fMRI (*6–9*), in amyloid plaques in Alzheimer's disease (*10–14*), knee cartilage degradation (*15–18*), and examining healthy tissues such as muscle, liver, spleen, kidney, and heart (*19*).

The rate $R_{1\rho}$ is usually measured by applying an on-resonance spin-locking field along the direction of the bulk transverse magnetization in the rotating reference frame for a series of locking times. The decay of locked transverse magnetization with increasing locking time may usually be well fit to a mono-exponential with a characteristic time constant $T_{1\rho}$ ($=1/R_{1\rho}$) (*20*, *21*). In conventional MRI, $T_{1\rho}$-weighted imaging has been interpreted mainly as reflecting the

relatively slow motional characteristics of macromolecules, especially when implemented at low static field strengths (*22*, *23*). While previous work has emphasized the contributions of slow macromolecular motions, at high field chemical exchange may become the primary mechanism affecting $T_{1\rho}$. Although a few studies have measured exchange effects on $T_{1\rho}$, most studies have failed to examine $T_{1\rho}$ at various locking fields. Chemical exchange begins to dominate relaxation at fields $\geq$ 3T, so spin-locking may provide novel information under these circumstances. Diffusion of water through microscopic susceptibility gradients may also cause transverse losses and so may also be a contributing mechanism at high fields that has been largely overlooked by the MR community. Advancing the methods of characterizing tissues using spin-locking methods will be valuable for the understanding of fundamental mechanisms influencing rotating frame relaxation and improving the detection and distinguishing between various pathologies. In this chapter a brief summary of the history of MRI is provided along with fundamental background that explains the manner in which MR experiments work and the critical processes that affect relaxation.

Background and Literature Review

A Brief History of NMR

Magnetic resonance imaging has the unique versatility, compared to other imaging modalities, to generate unparalleled soft tissue contrast while maintaining sensitivity to a variety of fundamental physiologic processes. Though the first MR image was not acquired until 1973 by Paul Lauterbur (*24*), the fundamentals of NMR had been previously under investigation for decades. The theory of intrinsic spin angular momentum was established in the early 1920's when the Stern-Gerlach experiment was performed by shooting a collimated beam of silver atoms through an inhomogeneous magnetic field, splitting their trajectory (*25*, *26*). The first

experiment that detected the NMR phenomenon years later was not in stationary bulk material, but rather with a beam of hydrogen molecules. In 1939 Kellogg, Rabi, and Ramsey found that when the beam of hydrogen molecules ran through a magnetic field and were subjected to RF radiation, absorption occurred at a well defined frequency (*27*, *28*). While some experiments failed to detect the NMR phenomenon in solids (*29*), Purcell, Torrey, and Pound at MIT and Bloch, Hansen, and Packard at Stanford were successful in performing NMR experiments in bulk materials in 1946 (*30*–*32*) which paved the way for rapid discovery over subsequent years. In the same year Bloch also formulated the famous Bloch equations describing how an ensemble of nuclear magnetic moments form a classical magnetization vector that precesses in the transverse plane with respect to a static magnetic field. He did this by realizing the temporal change in the resultant angular momentum vector of an ensemble of nuclei would simply equal the total torque, which can be explained classically. Though this was a simplified theory, all experiments done were on a macroscopic scale, which made the theory very accurate and applicable. Bloch and Purcell eventually received the Nobel prize in 1952 for their work in experimental NMR.

Bloembergen, Purcell, and Pound at Harvard laid out a detailed theory for NMR relaxation of nuclear spins in a strong magnetic field in 1948, two years after the first NMR experiments, which is sometimes referred to as BPP theory (*33*). They performed a multitude of experiments such as measuring the resonance peaks, line-widths, and relaxation times in multiple liquids with various viscosities, measured relaxation times in ice and hydrogen gas, examined the effects of paramagnetic ions, and derived theoretical expressions for the relaxation times. Hahn realized certain transverse relaxation could be refocused when he used Bloch's theory to describe spin-echoes that he experimentally confirmed with experiments on glycerine in 1950 (*34*). The

Hahn spin-echo theory was later extended by Carr and Purcell in 1954 which would become useful for imaging later (*35*). Electronic shielding was also shown to have an effect on the resonance frequency in metals by W. Knight in 1949 (*36*), and by Proctor and Yu at Stanford and Dickinson at MIT in other chemical compounds in 1950 (*37*, *38*). This was the first real evidence of chemical shifts influencing proton resonance frequencies, and the following year Arnold, Dharmatti, and Packard at Stanford discovered these chemical shifts in liquid organic compounds at 0.76 T (*39*). The discovery of chemical shifts in metals and organic compounds was vital in extending the applications of NMR to various types of spectroscopy and laid the foundation for assessing relevant physiologic processes like chemical exchange.

The effects of exchange on NMR spectra were laid out by Gutowsky and McCall in 1953 (*40*), and Albert Overhauser discovered the Overhauser effect by examining how electron spin populations affect spin polarization in the same year (*41*). This effect would prove to be vital to chemical exchange related techniques, especially chemical exchange saturation transfer (CEST) in the future. Two years later, Soloman analyzed the dipolar nature of the case of an interacting two-spin system further by calculating the transition probabilities per unit time between states in 1955 at Harvard (*42*), which further advanced relaxation theory. Later the same year at Harvard, the first theory and experiments on relaxation in the rotating frame were performed by Alfred Redfield who called the experiment "rotary saturation" (*20*). Redfield laid out the theory for transforming the Hamiltonian into the rotating frame specifically for the case of solids, and expanded upon the theory making it more general using the density matrix formalism in 1957 (*43*). The famous two pool model was applied to the Bloch equations by McConnell in 1958 (*44*), but the first $R_{1\rho}$ investigation of chemical exchange did not occur until Deverell laid out a theory for exchange based $R_{1\rho}$ relaxation using the density matrix formalism and examined the

rate of isomerization in cyclohexane in 1970 (*45*). This was a very important result for the work of this thesis for reasons that will be apparent in subsequent chapters. Three years later, Paul Lauterbur coined the term "zeugmatography", or "that which is used for joining" in Greek, when he constructed the first MR images of water in capillaries from a back projection reconstruction method in 1973 (*24*). It is noteworthy that Peter Mansfield also proposed using the Fourier transform method to acquire projections and images in 1973 (*46*), and Raymond Damadian arguably prompted both of these discoveries by demonstrating NMR relaxation times are measurably different in tumors compared to healthy tissues in 1971 (*47*). Even though Damadian's contributions were significant, only Lauterbur and Mansfield were awarded a Nobel prize for their efforts in 2003. Since the first images were acquired, the fields of NMR and MRI have significantly progressed over the years to arguably become the most versatile imaging modality today.

Classical Precession

The Nuclear Magnetic Resonance phenomenon arises from nuclear spins interacting with a static external magnetic field. Nuclear magnetic interactions are quantum mechanical in nature, but explaining the interactions in a classical manner proves to be accurate and convenient since the vast majority of all NMR and MRI experiments are done on macroscopic ensembles of nuclei. Hydrogen nuclei are the most widely used, especially in MRI experiments, due to the abundance of water present in biological tissues. Nuclei with spin-1/2 such as ^{1}H have microscopic dipole moments due to their total angular momentum. These magnetic dipoles will tend to align with an applied external field to create a bulk magnetization. For a spin-1/2 system, the ratio of spin-up to spin-down states can be calculated from the Boltzmann factor ratio

$\frac{N_{\uparrow}}{N_{\downarrow}} = e^{-\gamma\hbar B_0 / kT}$, which assumes spin-up is the higher energy state (*48*). This ratio corresponds to a spin excess of only ~3/million spins at physiologic temperature in a 1T magnetic field, but there is still a large detectable bulk magnetization since there are very large numbers of spins present in practical experiments. For this reason the following example will be shown in the context of classical physics, and a more accurate quantum mechanical treatment will be examined later to compare the classical equations to the quantum expectation values. The classical situation can be approached by treating each nucleus as a tiny current loop immersed in an external magnetic field as shown in Figure 1.

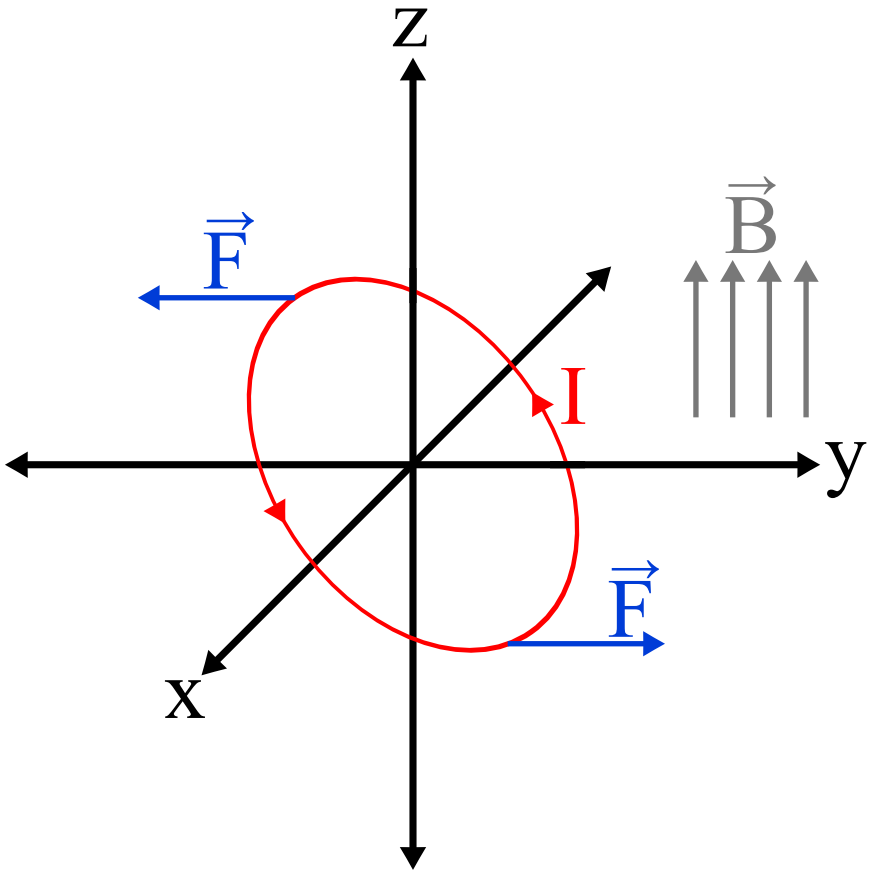

Figure 1: The current loop (red) in a magnetic field (grey) results in a torque that creates the force vectors in blue that cause the loop to orient itself with respect to the static field.

Simple electrodynamics says this current loop will experience a torque ($\vec{N}$) due to the interaction of its magnetic dipole moment ($\vec{\mu}$) with the magnetic field ($\vec{B}$) (*49*).

$$\vec{N} = \vec{\mu} \times \vec{B} \qquad 0.1$$

For this simple case, the dipole moment can be written as the product of the current with the area of the loop. The torque equation provides the basis for the precession in the classical derivation since the cross product hints that rotation is involved. In order to take the next step in deriving the equations of motion for the bulk magnetization, two important insights are needed. First, the fundamental definition of torque states that it describes the rate of change of the angular momentum $\vec{J}$.

$$\vec{N} = \frac{d\vec{J}}{dt} \qquad 0.2$$

The total angular momentum of a nucleus is also related to the magnetic dipole moment through the gyromagnetic ratio in a very simple expression.

$$\vec{\mu} = \gamma \vec{J} \qquad 0.3$$

For a proton, as in the case of a hydrogen nucleus, $\gamma = 2\pi(42.58$ MHz/T). Combining equations 0.1 - 0.3 with the simple notion that the bulk magnetization is related to an ensemble of dipole moments by $\vec{M} = n\vec{\mu}$ (where n is the number of dipoles per unit volume), the equations of motion for the vector form of the Bloch equations may be derived.

$$\frac{d\vec{M}}{dt} = \gamma \vec{M} \times \vec{B} \qquad 0.4$$

These were the simple equations Bloch derived in 1946 without considering relaxation (which Bloch did include in his derivation), which will be described in further detail later. These are the fundamental classical phenomenological equations that describe the precession of magnetization in a static magnetic field. Equation 0.4 can be quantitatively shown to describe a precession of the bulk magnetization in the transverse plane with respect to the static field at the Larmor frequency ($\omega_0 = \gamma B_0$) by calculating the cross product with the assumption that $\overrightarrow{M} = M_x\hat{x} + M_y\hat{y} + M_z\hat{z}$ and $\vec{B} = B_0\hat{z}$. Performing this cross product and then integrating to solve for each component results in the following equations.

$$\begin{aligned} M_x(t) &= M_{x0}\cos(\omega_0 t) + M_{y0}\sin(\omega_0 t) \\ M_y(t) &= -M_{x0}\sin(\omega_0 t) + M_{y0}\cos(\omega_0 t) \\ M_z(t) &= M_{z0} \end{aligned} \qquad 0.5$$

Here M_{x0}, M_{y0}, and M_{z0} are the initial components of the magnetization vector at time = 0 immediately following a tip into the transverse plane. This may be simplified further by relating all the initial magnetization components to the overall vector $M_0 = \sqrt{M_{x0}^2 + M_{y0}^2 + M_{z0}^2}$ with spherical coordinates.

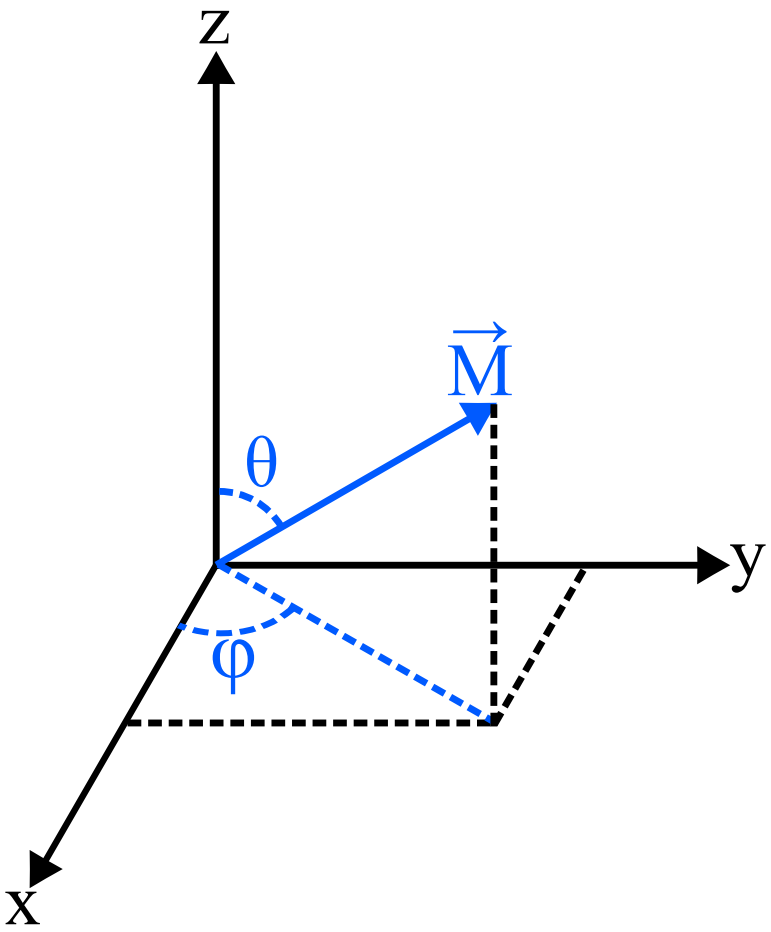

Figure 2: Spherical coordinate system used to convey an arbitrary magnetization vector.

Figure 2 describes the coordinates used to re-write Eq. 0.5 as follows.

$$\begin{aligned} M_x(t) &= M_0 \sin(\theta)\cos(\phi_0 - \omega_0 t) \\ M_y(t) &= M_0 \sin(\theta)\sin(\phi_0 - \omega_0 t) \\ M_z(t) &= M_0 \cos(\theta) \end{aligned} \qquad 0.6$$

The form of Eq. 0.6 makes the precession phenomenon abundantly evident and will act as an easy reference to compare the results of the quantum derivation of precession in the next section.

Quantum Mechanical Basis for MRI

The classical case of nuclear precession in a magnetic field describes large ensembles of nuclei very well experimentally, but the nuclear interactions are truly quantum in nature and

important aspects of the appropriate theory should be noted. In order for a nucleus to be detectable in an NMR experiment, it must have intrinsic angular momentum, known as spin, that will result in a dipole moment analogous to what was described for the classical precession example. In the rare case when a nucleus has a spin of $I = 0$ such as in ^{12}C, ^{16}O, or ^{32}S, no spin transitions may occur and the nucleus is thought to be "NMR silent" since it cannot produce a measureable signal with this technique. While NMR may be performed on any nucleus with spin $I > 0$, MRI is almost exclusively performed on the ^{1}H nuclei of water molecules that possess $I = 1/2$. There are naturally $(2I + 1)$ degenerate spin states for a nucleus of spin I, but placing the nucleus in a magnetic field breaks the degeneracy by splitting the energy levels by a difference of $\Delta E = \hbar\omega_0$ through a phenomenon called "Zeeman Splitting" (*50*). The explicit dependence of the energy difference between states on the Larmor frequency (ω_0) should be noted since this is the origin of the resonance phenomenon. Transitions can occur only at that specific energy, so only on resonance RF radiation will excite the nuclei in any NMR experiment. The number of accessible spin states is $(2I + 1)$, so spin-1/2 particles are the simplest case for NMR experiments because only 2 spin states exist and there are no quadrupolar effects that are present in particles with $I \geq 1$.

Deriving the time dependence of the magnetic moment will provide insight into the behavior of this quantum system and allow the comparison of the results with those from the classical derivation. Solving for the equations of motion in a quantum system means finding the expectation value of the time dependent magnetic moment following the derivation of Haacke (*48*, *51*).

$$\langle \Psi | \vec{\mu} | \Psi \rangle = \int \Psi^{\dagger} \vec{\mu} \Psi \, dV \qquad 0.7$$

The state $\sum_{m=\pm 1/2} C_m \psi_m e^{-\frac{i}{\hbar}E_m t}$ may be inserted into Eq. 0.7 to write the following form.

$$\langle \Psi | \vec{\mu} | \Psi \rangle = \gamma V \sum_m \sum_{m'} C^*_{m'} C_m \psi^\dagger_{m'} \vec{S} \psi_m e^{\frac{i}{\hbar}\Delta E t} \tag{0.8}$$

In Eq. 0.8 $\vec{S} = \frac{\hbar}{2}\vec{\sigma}$, where $\vec{\sigma}$ is the vector of Pauli spin matrices, and V is the volume of the proton that came from the integration. In order to solve this expectation value, the term $\psi^\dagger_{m'} \vec{S} \psi_m$ needs to be examined in more detail. Substituting for $\vec{S}$, it can be written as

$$\frac{\hbar}{2}\psi^\dagger_{m'} \vec{\sigma} \psi_m = \frac{\hbar}{2}\left(\hat{x}\delta_{m',-m} + 2mi\hat{y}\delta_{m',-m} + 2m\hat{z}\delta_{m',m}\right) \tag{0.9}$$

since m can only be ±1/2. The coordinates may be transformed to spherical coordinates and keeping in mind $\Delta E = \hbar\omega_0$ and that the states are normalized so $\langle \Psi | \Psi \rangle = 1$, the three components of Eq. 0.8 may be written as Eq. 0.10.

$$\begin{aligned}
\langle \Psi | \mu_x | \Psi \rangle &= \frac{\gamma\hbar}{2}\sin(\theta)\cos(\phi_0 - \omega_0 t) \\
\langle \Psi | \mu_y | \Psi \rangle &= \frac{\gamma\hbar}{2}\sin(\theta)\sin(\phi_0 - \omega_0 t) \\
\langle \Psi | \mu_z | \Psi \rangle &= \frac{\gamma\hbar}{2}\cos(\theta)
\end{aligned} \tag{0.10}$$

Examining these equations shows these equations are identical to Eq. 0.6 when $M_0 = \frac{\gamma\hbar}{2}$. This shows the quantum expectation value behaves as the classical case for a large ensemble of nuclei, as expected.

Adding Relaxation Terms to the Bloch Equations

The first set of Bloch equations derived earlier described the manner in which magnetization precesses about a static magnetic field, but failed to take into account the extremely important phenomena of nuclear spin relaxation. It is important to note that an ensemble of spins is weakly coupled thermally to its surroundings and the relaxation occurs between surrounding molecules, sometimes referred to as the "lattice." In order to derive an expression that describes longitudinal relaxation, the change in the number of spins in the spin-up state needs to be written as Eq. 0.11 (*48*, *52*).

$$\frac{dN_+}{dt} = N_- n_l W_{-+} - N_+ n_h W_{+-} \qquad 0.11$$

Here, $N_\pm$ are the number of spins in the ±1/2 state, $n_{l,h}$ are the number of lattice states with low or high energy, and W_{+-} and W_{-+} are the probability of transitions from the +1/2 to the -1/2 spin state or the -1/2 to the +1/2 state respectively. The system may be assumed to be in equilibrium and the approximation that $W_{+-} = W_{-+} = W$ may be used. The number of spins in each state may be re-written as $N_\pm = \frac{1}{2}(N \pm \Delta N)$ by defining the difference in spins $\Delta N = N_+ - N_-$ and the total number of spins $N = N_+ + N_-$. Using this notion, Eq. 0.11 can then be re-written as shown in Eq. 0.12.

$$\frac{d\Delta N}{dt} = WN(n_l - n_h) - W\Delta N(n_l + n_h) \qquad 0.12$$

In order to put this expression in a more useful form, the difference in spin states at equilibrium may be found, which follows simply by setting the derivative of ΔN with respect to time equal to

zero to find $\Delta N_{eq} = \frac{(n_l - n_h)}{(n_l + n_h)} N$. Plugging this back into the time derivative in Eq. 0.12 gives the following result.

$$\frac{d\Delta N}{dt} = W(n_l + n_h)\left[\Delta N_{eq} - \Delta N\right] \tag{0.13}$$

This expression is useful since n_l and n_h are assumed to be large and do not change, so $W(n_l + n_h)$ is a constant with inverse time units. This can be interpreted as the rate of longitudinal relaxation, R_1 which can be defined as $1/T_1$.

$$R_1 = \frac{1}{T_1} = W(n_l + n_h) \tag{0.14}$$

Eq. 0.14 is really a statement of how fast spin-states may relax due to the number of states in the lattice the spins can interact with. ΔN_{eq} and ΔN are directly related to the z-components of the magnetization and may be substituted for M_0 and M_z respectively to quantify the evolution of the longitudinal magnetization in differential form.

$$\frac{dM_z}{dt} = \frac{M_0 - M_z}{T_1} \tag{0.15}$$

The spin-spin relaxation may be derived in a simpler manner since the transverse magnetization has been observed to decay exponentially due to the "fanning out" or dephasing of local contributions to magnetization within the plane, described by Eq. 0.16.

$$\vec{M}_\perp(t) = \vec{M}_\perp(0) e^{-\frac{t}{T_2}} \tag{0.16}$$

Here, $\overrightarrow{M}_{\perp} = M_x \hat{x} + M_y \hat{y}$ simply quantifies the entire transverse magnetization, t is the time, and T_2 is the spin-spin relaxation time. In order to put this in a form that can be added to the Bloch equations, the derivative of both sides can be taken and simplified to Eq. 0.17.

$$\frac{d\overrightarrow{M}_{\perp}}{dt} = -\frac{\overrightarrow{M}_{\perp}}{T_2} = -R_2 \overrightarrow{M}_{\perp} \tag{0.17}$$

This now describes the time evolution of the transverse magnetization in differential form that can be added to the Bloch equations shown below.

$$\begin{aligned} \frac{dM_x}{dt} &= \Delta\omega_0 M_y - R_2 M_x \\ \frac{dM_y}{dt} &= -\Delta\omega_0 M_x - R_2 M_y \\ \frac{dM_z}{dt} &= R_1\left(M_0 - M_z\right) \end{aligned} \tag{0.18}$$

These are the full Bloch equations that describe the precession of magnetization about the static B_0 field with longitudinal and transverse relaxation.

Introduction to Relaxation Theory

When a strong magnetic field interacts with a proton, the simplest atomic nucleus, the spin-1/2 particle to experiences a field dependent splitting in the energy levels of the two spin states, making one spin state more probable than the other. The important characteristic with respect to relaxation is how two neighboring nuclei acting as dipoles can interact. The following derivation is known as BPP theory (*33*). Classically, when two magnetic dipoles interact, the potential energy may be described by Eq. 0.19 (*49*, *53*).

$$U = \frac{\mu_0}{4\pi}\left[\frac{\vec{\mu}_1 \bullet \vec{\mu}_2}{r^3} - 3\frac{\left(\vec{\mu}_1 \bullet \vec{r}\right)\left(\vec{\mu}_2 \bullet \vec{r}\right)}{r^5}\right] \tag{0.19}$$

Here μ_0 is the permeability of free space, $\vec{\mu}_1$ and $\vec{\mu}_2$ are the dipole vectors, and r is the relative distance between nuclei. Quantum mechanically, the dipoles can be expressed as $\hat{\mu} = \gamma\hbar\hat{I}$ so the Hamiltonian may be written as Eq. 0.20.

$$\hat{H}_{dd} = \frac{\mu_0\gamma_1\gamma_2\hbar^2}{4\pi}\left[\frac{\hat{I}_1 \bullet \hat{I}_2}{r^3} - 3\frac{\left(\hat{I}_1 \bullet \vec{r}\right)\left(\hat{I}_2 \bullet \vec{r}\right)}{r^5}\right] \tag{0.20}$$

Expanding this Hamiltonian is a lengthy endeavor, but the results when transformed into polar coordinates are well documented and can be expressed as shown below (*33*, *54*).

$$\hat{H}_{dd} = \frac{\mu_0\gamma_1\gamma_2\hbar^2}{4\pi r^3}\left[A + B + C + D + E + F\right] \tag{0.21}$$

The factor $\frac{\mu_0\gamma_1\gamma_2\hbar}{4\pi r^3}$ is commonly referred to as the dipolar coupling constant, while terms A – F are known as the dipolar alphabet, which are explicitly written in Eq. 0.22.

$$\begin{aligned}
A &= -I_{1z}I_{2z}\left(3\cos^2(\theta) - 1\right) \\
B &= \frac{1}{4}\left[I_{1+}I_{2-} + I_{1-}I_{2+}\right]\left(3\cos^2(\theta) - 1\right) \\
C &= -\frac{3}{2}\left[I_{1z}I_{2+} + I_{1+}I_{2z}\right]\sin(\theta)\cos(\theta)e^{-i\phi} \\
D &= -\frac{3}{2}\left[I_{1z}I_{2-} + I_{1-}I_{2z}\right]\sin(\theta)\cos(\theta)e^{i\phi} \\
E &= -\frac{3}{4}I_{1+}I_{2+}\sin^2(\theta)e^{-2i\phi} \\
F &= -\frac{3}{4}I_{1-}I_{2-}\sin^2(\theta)e^{2i\phi}
\end{aligned} \tag{0.22}$$

The I_+ and I_- terms are the quantum raising and lowering operators, which can be written as $I_\pm = I_x \pm iI_y$. Terms A and B give rise to secular perturbations while terms C – F describe periodic perturbations of a much smaller amplitude (*33*).

Since in general the two nuclei need not be the same, this system is often referred to as an AX, or heteronuclear, system with energy levels and transition rates described in Figure 3.

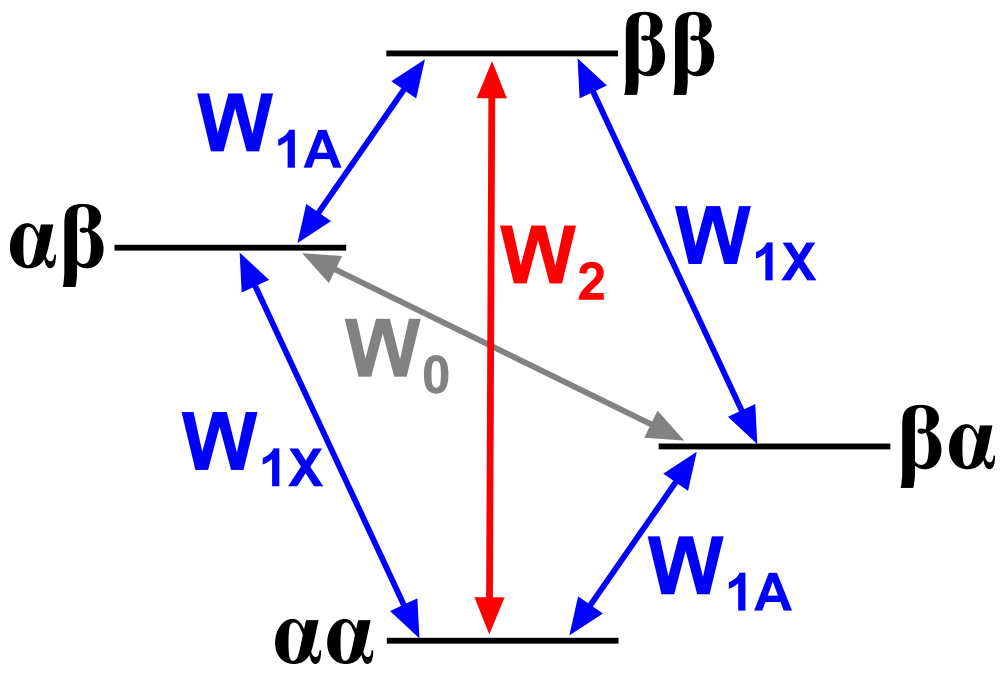

Figure 3: Energy levels of a heteronuclear AX system with the corresponding transition rates.

For simplicity, only the homonuclear system where the αβ and βα states are degenerate will be analyzed since this describes free water well. This degeneracy will cause $W_{1A} = W_{1X}$ and the W_0 transition may be ignored since there is no change in energy due to the states being identical. There are only two transitions in this case, W_1 and W_2, which correspond to blue and red transitions respectively in Figure 3. Thus defining the spin-lattice relaxation similar to the

method in the previous section for the Bloch equations, the relaxation rate R_1 may be found to be a function of the transition probabilities (*54*).

$$R_1^{dd} = 2W_1 + W_2 \tag{0.23}$$

These transition probabilities may be written out explicitly below.

$$W_n = R^2 \sum_{m=-n}^{n} \overline{\langle A_m \rangle^2} \int_{-\infty}^{\infty} G(\tau) e^{-i\omega_0 \tau} \, d\tau \tag{0.24}$$

Here n = 1 or 2 since these are the possible transitions, R is the dipolar coupling constant, A is the angular part of the dipolar alphabet terms, G is a correlation function of the time-dependent molecular motions, and τ is the correlation time of the molecular motions. The integral in the right had side of Eq. 0.24 is called the spectral density, which may be written according to Eq. 0.25.

$$J(n\omega_0) = \frac{\tau_c}{1 + n^2 \omega_0^2 \tau_c^2} \tag{0.25}$$

Plugging Eq.'s 0.24 and 0.25 into Eq. 0.23 leads to the following expression for the spin-lattice relaxation rate.

$$R_1^{dd} = \frac{3R^2}{10}\left[J(\omega_0) + 4J(2\omega_0)\right] = \frac{3\gamma^4 \mu_0^2 \hbar^2}{10(4\pi)^2 r^6}\left[\frac{\tau_c}{1+\omega_0^2\tau_c^2} + \frac{4\tau_c}{1+4\omega_0^2\tau_c^2}\right] \tag{0.26}$$

The terms $C - F$ in Eq. 0.22 thus affect R_1 and in a similar manner, terms A and B contribute to R_2. The spin-spin relaxation rate can be found by calculating these terms, of which A now contributes the term $3J(0)$, and written as Eq. 0.27.

$$R_2^{dd} = \frac{3R^2}{20}\left[3J(0) + 5J(\omega_0) + 2J(2\omega_0)\right] = \frac{3\gamma^4\mu_0^2\hbar^2}{20(4\pi)^2 r^6}\left[3\tau_c + \frac{5\tau_c}{1+\omega_0^2\tau_c^2} + \frac{2\tau_c}{1+4\omega_0^2\tau_c^2}\right] \quad 0.27$$

Finally, the spin-lattice relaxation rate in the rotating frame may be derived in a similar manner to Eq. 0.26, except in this case there will be a spectral density according to the Larmor frequency about the effective field that arises from the application of the spin-lock pulse (*54–57*).

$$R_{1\rho}^{dd} = \frac{3R^2}{20}\left[3J(2\omega_1) + 5J(\omega_0) + 2J(2\omega_0)\right] = \frac{3\gamma^4\mu_0^2\hbar^2}{20(4\pi)^2 r^6}\left[\frac{3\tau_c}{1+4\omega_1^2\tau_c^2} + \frac{5\tau_c}{1+\omega_0^2\tau_c^2} + \frac{2\tau_c}{1+4\omega_0^2\tau_c^2}\right] \quad 0.28$$

Eq. 0.28 looks almost identical to R_2^{dd}, but it depends on the term $3J(2\omega_1)$ rather than $3J(0)$. It is also worthy to point out in the extreme narrowing case when $\omega_0^2\tau_c^2 \ll 1$,

$$R_1^{dd} = R_2^{dd} = R_{1\rho}^{dd} = \frac{3\gamma^4\mu_0^2\hbar^2\tau_c}{2(4\pi)^2 r^6}. \quad 0.29$$

This corresponds to very rapid motion with very short correlation times that will cause a long T_1, which may occur in non-viscous fluids at relatively high temperatures.

Factors Influencing $R_{1\rho}$

Though many important discoveries have been made in the field of MRI over the years with countless applications, this work primarily focuses on the applications of examining chemical exchange and diffusion through the spin-lattice relaxation rate in the rotating frame ($R_{1\rho} = 1/T_{1\rho}$). While many factors may contribute to spin-lattice relaxation in the rotating frame, the work reported in this dissertation provides evidence that at high static fields (≥3T) the contributions of chemical exchange and diffusion begin to dominate other effects like traditional dipolar effects. Both the chemical exchange and diffusion phenomena have been studied

significantly in various contexts within both NMR and MRI over the years, but relatively little work has been focused on their study by spin-lock MRI. Most of these previous studies of $T_{1\rho}$-based contrast have been performed at relatively low B_0 fields, and these have emphasized the sensitivity of $T_{1\rho}$ measurements to slow molecular motions around the Larmor frequency corresponding to the locking field, typically from ~100 Hz to a few kHz (*7*, *11*, *19*, *58*). The low frequency motions of macromolecules may affect water via dipolar interactions, and $T_{1\rho}$ may often provide a more specific probe of such effects than other relaxation measurements. Variations of $R_{1\rho}$ with locking field ($R_{1\rho}$ dispersion) then reflect changes in the spectral density of the local dipolar fields experienced by protons due to relatively slow molecular motions. However, at higher fields, there may be additional significant contributions to $R_{1\rho}$ (as well as R_2) from chemical exchange between sites of different chemical shifts, and these increase rapidly with field strength and may dominate the dispersion curves measured experimentally (*59*). It is noteworthy that recent reports have shown that measured relaxation rates have a more complex dependence when spin-locking is achieved with a train of adiabatic pulses since the modulation in the pulse as a function of time changes the exchange conditions through the time dependent effective field (*60*, *61*). Mäkelä et. al. investigated the B_0 dependence of $R_{1\rho}$ dispersion in protein phantoms and rat brains in vivo and while they claim classical dipolar interactions are the most important mechanism, they also state that other effects such as diffusion and exchange are likely influencing the relaxation (*56*).

Spin-locking pulse sequences are needed to measure $R_{1\rho}$, and multiple forms of these sequences exist. All the experiments throughout this work use an advanced pulse sequence described by Witschey et. al. (*62*), but the simplest spin-lock preparation pulse is described below for illustrative purposes. Figure 4 illustrates a standard spin-locking pulse sequence and

the effects of each of the pulses on the precessing magnetization.

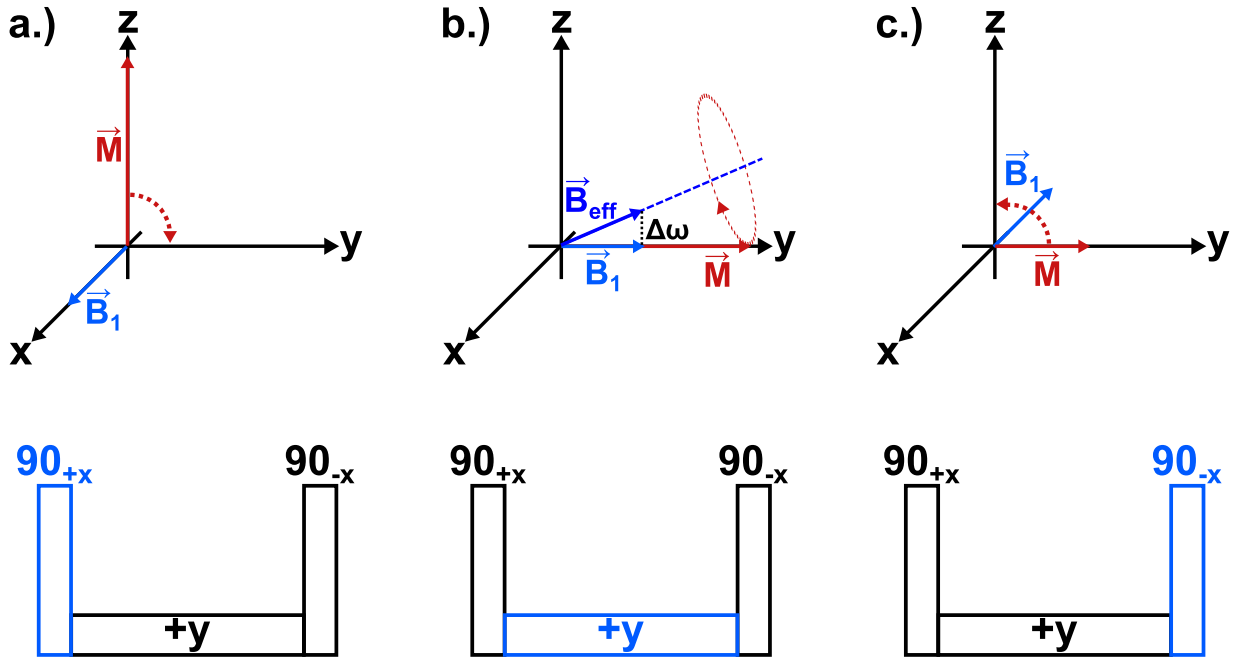

Figure 4: a.) A hard pulse initially tips the magnetization into the transverse plane. b.) The locking pulse creates an effective field in the y-z plane that the magnetization precesses about. c.) The magnetization is tipped back to the longitudinal z-axis.

The magnetization is initially tipped down 90° in to the transverse plane with a hard pulse along the x-direction in the rotating frame, placing the magnetization along the y-axis as shown in Figure 4a. The long duration, low amplitude locking pulse is applied along the magnetization in the y-direction in the rotating frame, but the field inhomogeneity represented by Δω causes the effective field to gain a z-component in the rotating frame as shown in Figure 4b. The magnetization relaxes while precessing around this effective field at a rate that depends on the locking amplitude and the spectral density function since interactions occurring at a frequency that is on the order of the effective field will induce relaxation. The remaining magnetization then returns to the longitudinal z-axis with the application of another hard pulse, this time along

the –x-direction as shown in Figure 4c. This simple locking pulse diagram is known as a preparatory pulse cluster and can be followed by another spectroscopic or imaging pulse sequence, making this a very flexible method for creating $T_{1\rho}$ weighted images. Changing the amplitude of the applied spin-locking pulse will increase the magnitude of the effective field, which will change the rate the magnetization relaxes. The range of frequencies accessible in a spin-locking experiment typically range from 10^1-10^4 Hz on small bore animal scanners, and up to 10^3 Hz on larger bore human scanners. This range of frequencies excludes many fast molecular tumbling that induces dipolar relaxation, which corresponds to correlation times on the order of 10^{-12} seconds for free water (*63*).

Various sequences may be used to measure $R_{1\rho}$ but the most important sequence used in this work is that described by Witschey et. al. (*62*). The advantage of the Witschey sequence over other similar sequences is its ability to minimize artifacts arising from B_0 and B_1 inhomogeneities. Pulse variations of locking sequences are shown below in Figure 5.

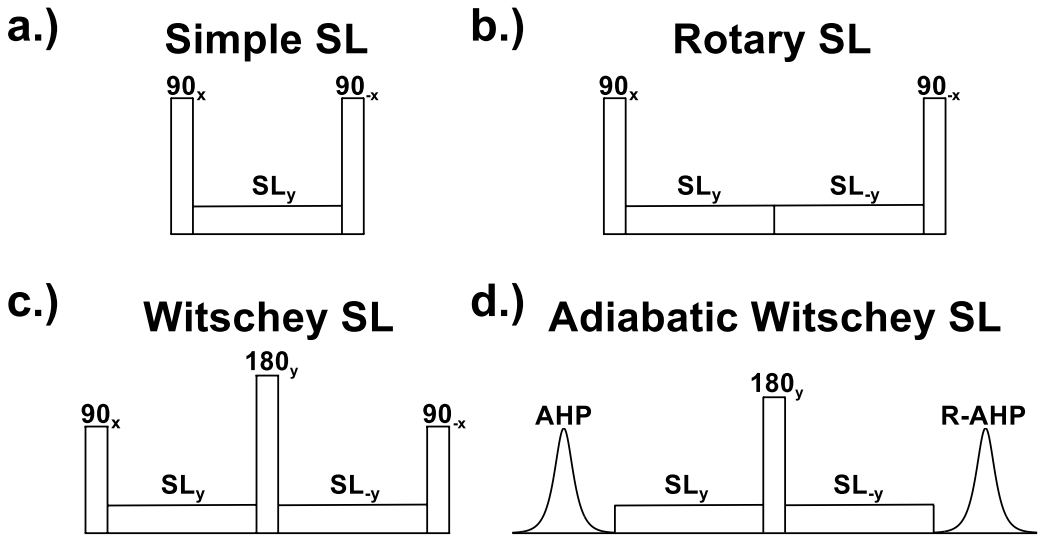

Figure 5: Variations of spin-locking pulse sequences, each with features meant to mitigate image artifacts.

The spin-lock sequence shown in Figure 5a is the simplest possible sequence, but can suffer from significant B_0, B_1, and imperfect tip angle artifacts in practice. The rotary sequence was proposed to alleviate B_1 artifacts from imperfect tip angles and low locking field oscillations (*64*), but these effects still linger in practice using this pulse. In 2007, Witschey proposed the sequence with the 180° pulse inserted in the center of the locking pulse shown in Figure 5c. This sequence performs very well in mitigating B_0 and B_1 inhomogeneities in practice, but continues to suffer from imperfect excitation flip angle effects. The first solution they proposed to this was to change the phase of the last 90° pulse to +x so the magnetization would end in the –z direction after the prep. This works well, but their second solution depicted in Figure 5d using adiabatic half passage pulses to excite performs the best in terms of minimizing artifacts mentioned. It is important to note the locking pulses are not adiabatic pulses, which may also be used to achieve spin-locking under the correct conditions (*65–67*), but are not of interest for this thesis. The adiabatic pulses do increase the overall Specific Absorption Rate (SAR) of the sequence, which may be a problem for many in vivo studies, but most of the work presented in this thesis are on phantoms that do not have require strict SAR limitations. Thus, the adiabatic Witschey sequence described in Figure 5d will be used in all experiments throughout this thesis.

Chemical exchange in the context of MRI describes the physical swapping of hydrogen nuclei between bulk water sites and amides, amines, or hydroxyls. The exchange rate and chemical shift of the smaller solute pool determine the magnitude of such exchange contributions to transverse dephasing, but the application of appropriately strong locking fields can reduce these effects. This ability to reduce exchange contributions by varying the locking field gives rise to a dispersion in $R_{1\rho}$ values with locking field that then provides information about exchange processes in the intermediate to fast time-scale regimes (*68*). This is of particular importance for

imaging compounds with fast exchanging protons such as in hydroxyl groups (¯OH) found in compounds such as glucose or glutamic acid, key energy sources and neurotransmitters in the human brain respectively. Figure 6 depicts an example of chemical exchange between the bulk water pool labeled pool a, and a single glucose molecule labeled pool b.

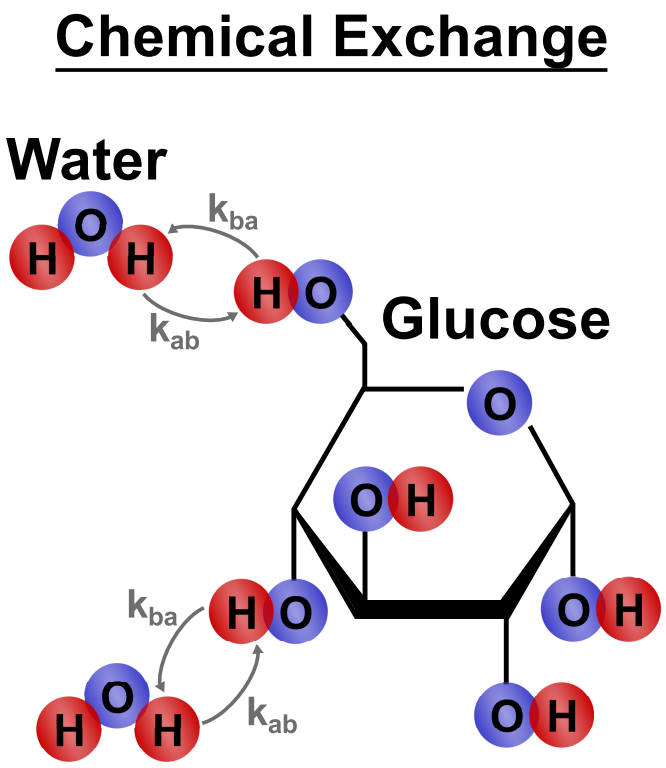

Figure 6: An example of chemical exchange between the bulk water pool and the glucose solute pool. The coupled exchange rates describe the rate of this process and are determined by the relative pool fractions of each pool.

The protons in pools *a* (bulk water) and *b* (solute) exchange at different rates that depend on the relative pool fractions as $p_a k_{ab} = p_b k_{ba}$, where p_a and p_b are the respective pool fractions. The $R_{1\rho}$ dispersion curve provides valuable information by exhibiting an inflection point at a frequency that is a function of the exchange rate and chemical shift. A corresponding dispersion of R_2

values with pulse rate in CPMG sequences can in principle provide similar exchange information by comparing the different apparent T_2 values obtained at long pulse spacings, where exchange will significantly influence the linewidth, and short pulse spacings, where exchange will have very little impact. However, the practicality of using multi-echo sequences in imaging is limited by technical constraints on achievable pulse rates to probing relatively slower exchange (*59*).

Contrast in traditional MR images is the direct result of distinct intrinsic nuclear magnetic resonance (NMR) relaxation times between tissues. The spin-lattice relaxation time, T_1, quantifies the time required to regrow 63% of the magnetization back to the z-axis equilibrium position. Similarly the aforementioned spin-spin relaxation time, T_2, reports on the intrinsic transverse dephasing of magnetization during free precession (*48*). Furthermore, T_2^* quantifies the transverse dephasing from field inhomogeneity that, unlike intrinsic T_2 effects, can be reversed by applying the proper pulse sequence techniques. Different mechanisms contribute to each relaxation time, so estimating relaxation times can shed light on molecular processes present in the medium. Molecular tumbling, for example, contributes to R_2 through the rapidly changing dipolar interactions between molecules arising from their magnetic moments and T_1 is related to the spectral density of the medium since it quantifies the time scale of which the energy is distributed to the surrounding "lattice" (*48*). Other T_1 effects do exist such as the coupling of nuclear spins to the radiation field to induce emission or absorption of radiation to change the spin-energy states. The transition probability for this coupling has been calculated in detail to be on the order of $\sim 10^{-10}$ Hz under reasonable conditions though, making this effect hopelessly weak and essentially negligible experimentally (*21*).

Studies have demonstrated dipolar interactions and cross-relaxation, or the relaxation due to the coupling of two different proton pools in the cross terms of the Solomon equations (*42*,

50), tend to decrease their contributions to relaxation as the static field increases (*68*). Subsequent studies reveal that some other mechanism increases transverse relaxation rates (R_2) in protein solutions with increasing B_0 field, contradictory to expectation (*69*). Since chemical exchange constitutes the breaking and forming of labile hydrogen molecular bonds, it contributes to R_2 since the exchange sites typically have distinct local magnetic environments that cause dephasing when protons exchange back and forth. This change in local magnetic environment at exchange sites that stems from a shielding effect, due to the chemical shift caused by the electron cloud configuration, becomes more pronounced at higher static fields. Thus the exchange mechanism is thought to dominate traditional dipolar and cross-relaxation effects at very high fields. In addition to chemical exchange, the influences of diffusion through susceptibility-induced gradients on transverse relaxation rates R_2 and R_2^* have been extensively analyzed by theory and computer simulations and studied experimentally (*70–81*). These effects are significant at high fields and will contribute in conjunction with exchange to dominate dipolar and cross relaxation effects.

Effects other than chemical exchange have also been reported to affect the dispersions of R_2 and $R_{1\rho}$ including water diffusion through internal field gradients caused by interfaces of unequal susceptibility. For example, Hills et al. reported a double dispersion behavior of R_2 as a function of reciprocal CPMG 90°-180° pulse spacing at 7T in suspensions of packed sephadex beads carrying hydroxyl protons in water (*82*). The dispersion curve was compared to theoretical simulations that took only chemical exchange into account and accurately matched the short pulse spacing data, but failed to coincide with the long pulse spacing portion of the curve. This disparity for long pulse spacings was postulated to be due to water diffusion into and out of the sephadex beads as well as through the intrinsic gradients produced immediately outside the

beads. This diffusion produced a separate dispersion because the local field experienced by spins evolved on a much slower time scale (around 4 Hz) compared to the chemical exchange effects occurring at 2,500 Hz. The low frequency dispersion of $R_{1\rho}$ reflects the time scale over which magnetization is dephased, which directly depends on the magnetic microstructure of the medium. Similar findings were experimentally confirmed in plant tissues (*83*). We have more recently shown how diffusion through susceptibility gradients, in the absence of chemical exchange, can produce significant $R_{1\rho}$ dispersion and reveal details of the inhomogeneities causing the gradients, and that such effects are measureable in biological tissues. The experimental results described in subsequent chapters have verified the new theoretical predictions of such effects (*84*, *85*). Diffusion of water through susceptibility gradients could be very relevant to studies of tissue microvasculature, which may induce intrinsic gradients within tissues. However, some previous studies have claimed $T_{1\rho}$ is not sensitive to changes in intravascular susceptibility. For example, Kettunen et. al. has shown $T_{1\rho}$ is only marginally sensitive to intravascular effects after injection of the susceptibility agent AMI-227 using a locking field of 1.6 G (≈ 6,800 Hz) whereas T_2 was much more sensitive to these effects (*86*). We show below that significant effects are not expected using such a strong locking field, but that $T_{1\rho}$ is very sensitive to the presence of susceptibility agents when the locking field is much weaker. Simulations and theory described in this thesis indicate that diffusion-related $R_{1\rho}$ dispersion effects depend on the relationship between the locking field frequency and the time needed for water molecules to diffuse distances of the order of the size of the vessels, which is typically on the order of many milliseconds. Rane et. al. have recently provided strong evidence that $T_{1\rho}$ is sensitive to intravascular susceptibility changes at low locking fields by detecting BOLD signals in the brain at different locking strengths (*9*). Thus in addition to chemical

exchange, $R_{1\rho}$ dispersion measurements can report on diffusion processes in inhomogeneous tissues.

Motivation for $R_{1\rho}$ Based Imaging

The spin-lattice relaxation time in the rotating frame ($T_{1\rho}=1/R_{1\rho}$) was first investigated decades ago (*20*, *45*, *87*) and is a sort of hybrid of T_1 and T_2 that has considerable potential for characterizing tissues and assessing pathological or other changes in various research and clinical applications (*88*). The rate $R_{1\rho}$ is usually measured by applying an on-resonance spin-locking field along the direction of the bulk transverse magnetization in the rotating reference frame for an array of locking times. Subsequent measurements can be acquired at various locking amplitudes to obtain the dispersion of $R_{1\rho}$. If the locked magnetization decays mono-exponentially, which is the case in most experiments, then the time constant of the decay is $T_{1\rho}$. Measurements of $T_{1\rho}$ have been used to characterize various media for many years (*7*, *10*, *15*, *86*, *89*), but have not found widespread use in conventional MRI for different reasons. Moreover, few prior uses of spin-locking in imaging have emphasized the ability to quantify dynamic processes such as chemical exchange or diffusion at high fields. Chemical exchange is the most commonly investigated process with chemical exchange saturation transfer (CEST) experiments (*90*), with spin-locking gaining popularity. Spin-locking methods provide a promising means to quantify exchange rates in tissues that are dependent on important physiological parameters such as temperature, pH, and metabolite concentrations.

$R_{1\rho}$ is well known to report on slow molecular motions and chemical exchange processes (*45*), and the dispersion of $R_{1\rho}$ with locking field can provide quantitative information about these processes occurring in the intermediate to fast time-scale regimes at high field where exchange is thought to dominate relaxation (*91*). There has been considerable recent interest of

measuring chemical exchange effects using CEST, but these methods rely on distinguishing chemical shifts while spin-locking measurements can provide complimentary information since they are sensitive to chemical exchange rates and are more robust for rates in the fast exchange regime ($k_{ex}/\Delta\omega_b >> 1$) where CEST spectra begin to coalesce. This is of particular importance for imaging compounds with hydroxyl groups (^{-}OH) such as glucose or glutamic acid, key energy sources and neurotransmitters in the human brain respectively. Other experimental issues like direct water pool saturation and the Nuclear Overhauser Effect (NOE) that confound CEST calculations are avoided using $R_{1\rho}$ dispersion methods. Spin-locking experiments are sensitive to metabolite concentrations and pH, which are very important parameters for imaging cancer tissues since they often change significantly with respect to healthy tissues. The exchange mechanism can also be exploited to infer glucose metabolism using exogenous glucose analogues in tumors, which has been demonstrated with CEST and will be attempted using $R_{1\rho}$ dispersion imaging in this project. The dispersion of $R_{1\rho}$ will be shown to be sensitive to multiple exchange processes occurring simultaneously and can be used to quantify multiple rates or calculate parametric images depicting metabolite concentration in specific cases. Finally, $R_{1\rho}$ experiments are very easy to implement since a non-slice-selective spin-locking pulse cluster followed by a spoiler gradient simply needs to be added to the beginning of an imaging sequence to generate $T_{1\rho}$ weighted images.

Conclusion

Spin-locking methods have been in use since the beginnings of NMR, but have never found widespread utility among the MRI community. A significant amount of previous $R_{1\rho}$ experiments did not take full advantage of the method by only taking measurements at a single locking field or were performed at low static fields. Rotating frame relaxation may provide novel

or in some cases, less ambiguous, information that is not available through traditional T_1 or T_2 weighted acquisitions. New insights into rotating frame relaxation are presented in the subsequent chapters that highlight the ability of $R_{1\rho}$ dispersion methods to simultaneously quantify chemical exchange rates in multiple solute pools, calculate image contrast that reflects exchange rates, estimate solute concentrations in mixtures, and even infer sub-voxel geometric structural information through proper analysis of $R_{1\rho}$ data. All the experiments presented in this thesis are based on examining chemical exchange mechanisms or water diffusion in the presence of susceptibility gradients. In each of these methods, one key recurring concept is the entire dispersion curve is needed to properly derive robust quantitative data. Acquiring dispersion curves can be very time consuming, which may be unacceptable in certain clinical procedures, but these methods should still find plenty of use in other research realms like materials or food sciences, and below some simplified approaches are described that may be more practical. Hopefully the following results will encourage the use of $R_{1\rho}$ dispersion methods in a wider array of scientific studies moving forward.

CHAPTER 2

Exchange Rate Contrast in MRI

Introduction

Motivation

The aim in this thesis is to further develop and evaluate magnetic resonance imaging (MRI) methods that exploit novel contrast mechanisms based on chemical exchange and diffusion, which can be used to characterize tissues and assess tissue microstructure and composition in new ways. MRI continues to move to increasingly high field strengths, especially in important pre-clinical studies of small animal models of disease, and with increasing field different relaxation mechanisms evolve, providing new opportunities for characterizing tissues. In particular, water transverse relaxation in tissues at high fields is dominated by chemical exchange rather than dipole-dipole interactions, with additional contributions from diffusion through susceptibility gradients that mimic exchange. These processes are affected by very different factors than dipolar interactions, and they can be exploited to provide new types of image contrast. To date, Chemical Exchange Saturation Transfer (CEST) has been used to exploit exchange and provide information on amide and hydroxyl composition as well as pH, but relies on identifying components within tissues distinguished by their chemical shifts and is not well suited for detecting hydroxyl protons because their chemical shifts are small. Spin-locking sequences provide an alternative approach to exploiting exchange effects based on measurements of $R_{1\rho}$. The following work shows the variation of $R_{1\rho}$ with the locking field amplitude ($R_{1\rho}$ dispersion) provides a way not only to quantify the parameters of the exchange, but also to emphasize contributions to image contrast from sub-populations of protons that exchange at

specific rates rather than possess specific chemical shifts. Rotating frame relaxometry therefore provides a method for detecting and measuring exchanging species and modifying image contrast with exchange-based effects. Before developing new contrast metrics, the theory is reviewed for how exchange affects $R_{1\rho}$ and some of the factors that affect $R_{1\rho}$ are evaluated.

Two-Pool Models of Exchange

Labile hydrogen protons such as hydroxyls (^{-}OH), amides (NH^{+}), or amines (NH_2) may undergo physical exchange with solvent water protons at a rate dependent on several factors such as temperature, pH, and chemical environment. These exchange sites in general have different chemical shifts and intrinsic relaxation rates compared to water protons. The chemical shift differences correspond to different intrinsic precession rates so exchange leads to a mix of different phases resulting in transverse signal losses. Spin-locking methods typically first nutate the bulk magnetization into the transverse plane with either an adiabatic or hard RF pulse, and subsequently "lock" the magnetization by applying a relatively long duration, low amplitude RF pulse of strength $B_1 = \omega_1/\gamma$ along the direction of the magnetization as described in the previous chapter. Transverse magnetization under the influence of this continuous, in phase, and on-resonance RF locking field decays along the same axis at the rate $R_{1\rho} = 1/T_{1\rho}$. Chemical shift differences introduce a small longitudinal field component, but increasing the locking amplitude tends to ensure the effective field remains in the transverse plane so that dephasing effects are reduced. This tends to decrease the relaxation rate $R_{1\rho}$ in a manner that depends on the time scale of the relevant molecular interactions corresponding to the locking field period. This differs from CEST experiments where saturation pulses are applied at a range of frequency offsets to partially saturate longitudinal magnetization to decrease the solvent signal after the exchange of saturated spins. Though the experiments are different, simulations have shown off-resonance spin-locking

and CEST are derived from the same eigenvalue of the Bloch-McConnell equations and the measurements are sensitive to the same exchange effects (*92*).

Chemical exchange between water and surrounding labile protons in solute pools induces relaxation in the rotating frame, but only with a theoretical model can practical data about the medium be inferred. Multiple models have been proposed that explicitly quantify $R_{1\rho}$ relaxation, but most of these are related to deriving an equation that states the relaxation will be a function of the spectral density function at different frequencies. This notion, while true, lacks the ability to afford much insight into relevant parameters like chemical shifts or exchange rates. In order to theoretically evaluate the effects on $R_{1\rho}$ dispersion of exchange between water and one functional group with a distinct chemical shift, a two-pool exchange model may be adopted. A schematic of an arbitrary two-pool system is shown in Figure 7, each pool with intrinsic constant values of initial magnetization (related to concentration), R_1, R_2, and a chemical shift offset.

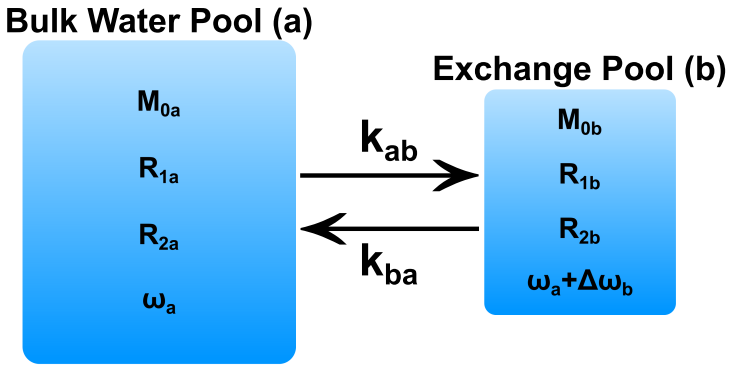

Figure 7: Schematic of an exchanging two-pool system. Each pool has independent initial magnetizations, relaxation rates, chemical shifts, and coupled exchange rates.

The bulk water pool can physically exchange protons back and forth with amide (-NH), amine (-NH_2), and hydroxyl (-OH) functional groups at a rate (k_{ab} , k_{ba}) dependent on factors including

temperature, concentration, and pH. McConnell analyzed this model in 1958 by assuming the exchange reactions were first order equilibrium reactions that occurred almost instantly, so protons spent a negligible amount of time in any intermediate radical stage (*44*). Also, the two pools have innate relaxation characteristics that are both independent of each other and independent of the exchange rates between pools. With these simple assumptions, the standard Bloch equations described in chapter 1 may be modified by adding linear terms that account for the exchange process and to account for the locking field ω_1. The two-pool Bloch-McConnell equations in matrix form are shown below (*44*).

$$\frac{d}{dt}\begin{bmatrix} M_x^a \\ M_x^b \\ M_y^a \\ M_y^b \\ M_z^a \\ M_z^b \end{bmatrix} = \begin{bmatrix} -\left(R_2^a + k_{ab}\right) & k_{ba} & \Delta\omega_a & 0 & 0 & 0 \\ k_{ab} & -\left(R_2^b + k_{ba}\right) & 0 & \Delta\omega_b & 0 & 0 \\ -\Delta\omega_a & 0 & -\left(R_2^a + k_{ab}\right) & k_{ba} & \omega_1 & 0 \\ 0 & -\Delta\omega_b & k_{ab} & -\left(R_2^b + k_{ba}\right) & 0 & \omega_1 \\ 0 & 0 & -\omega_1 & 0 & -\left(R_1^a + k_{ab}\right) & k_{ba} \\ 0 & 0 & 0 & -\omega_1 & k_{ab} & -\left(R_1^b + k_{ba}\right) \end{bmatrix} \begin{bmatrix} M_x^a \\ M_x^b \\ M_y^a \\ M_y^b \\ M_z^a \\ M_z^b \end{bmatrix} + \begin{bmatrix} 0 \\ 0 \\ 0 \\ 0 \\ R_1^a M_0^a \\ R_1^b M_0^b \end{bmatrix} \quad 1.1$$

In Eq. 1.1, M_i^a is the ith magnetization component of pool a, $R_{1,2}^a$ are the longitudinal and transverse relaxation rates of pool a (bulk water pool), $\Delta\omega_a$ is the chemical shift of pool a, $k_{ab}=\frac{p_b}{p_a}k_{ba}$ is the exchange rate from pool a to pool b (exchange pool), p_a is the pool fraction of pool a, ω_1 is the magnitude of the applied RF field along the x-direction in the rotating frame, and M_0^a is the equilibrium magnetization component of pool a. Pool b has identical expressions as pool a with switched indices. These first order coupled differential equations predict the evolution of magnetization with striking accuracy, but a closed form expression cannot be found without invoking certain simplifying assumptions.

Two model solutions of $R_{1\rho}$ from the Bloch-McConnell equations found using different

simplifying assumptions will be of interest for this work, the first was derived by Chopra et al. in 1984 (*93*), and the second was derived by Trott and Palmer in 2002 (*94*). Both models derive closed form expressions by finding the largest real eigenvalue of the determinant in the 6x6 matrix of Eq. 1.1, since this eigenvalue dominates the time evolution of the magnetization (*94*). Trott and Palmer solved these equations for $R_{1\rho}$ using the assumptions that $R_1^a = R_1^b = R_1$, $R_2^a = R_2^b = R_2$, and the solution is diluted ($p_a \gg p_b$) to derive the following expression.

$$R_{1\rho} = R_1 \sin^2(\theta) + R_2 \cos^2(\theta) + \frac{\sin^2(\theta) p_a p_b \delta^2 k}{\omega_{aeff}^2 \omega_{beff}^2 / \omega_{eff}^2 + k^2} \qquad 1.2$$

In Eq. 1.2, $\theta = \tan^{-1}(\omega_1/\Delta\omega)$, $\delta = \Delta\omega_b - \Delta\omega_a$, $k = k_{ab} + k_{ba}$, $\omega_{aeff}^2 = \Delta\omega_a^2 + \omega_1^2$, $\omega_{beff}^2 = \Delta\omega_b^2 + \omega_1^2$, and $\omega_{eff}^2 = \Delta\omega^2 + \omega_1^2$ where $\Delta\omega$ is a population averaged frequency offset. The first two terms on the left of Eq. 1.2 are the effective relaxation rates governed by spin-lattice contributions at high locking field and the transverse relaxation at low locking field, and the third term is the chemical exchange contribution R_{ex}. This model may be used to fit for R_1, R_2, $p_a p_b$, and k to estimate the exchange rate. The Trott and Palmer model has proven useful in various experiments, a more realistic analysis was provided in the Chopra model that assumes on resonance RF ($\Delta\omega_a = 0$), asymmetric pool fractions ($p_a \gg p_b$), and that exchange is not slow compared to relaxation ($R_1^b + k_{ba} \gg R_{1\rho}$, $R_2^b + k_{ba} \gg R_{1\rho}$). Under these conditions, finding the largest real eigenvalue leads to a different expression.

$$R_{1\rho} = \left\{ \frac{R_2 + \frac{R_{1\rho}^{\infty} \omega_1^2}{S_\rho^2}}{1 + \frac{\omega_1^2}{S_\rho^2}} \right\} \qquad 1.3$$

In Eq. 1.3, the parameters $R_{1\rho}^{\infty} = R_2^a + p_b k_{ba}\left(\frac{R_2^b}{R_2^b + k_{ba}}\right)$, $R_2 = R_2^a + p_b k_{ba}\left(\frac{R_2^b\left(R_2^b + k_{ba}\right) + \Delta\omega_b^2}{\left(R_2^b + k_{ba}\right)^2 + \Delta\omega_b^2}\right)$, and $S_\rho^2 = \frac{\left(R_1^b + k_{ba}\right)}{\left(R_2^b + k_{ba}\right)}\left[\left(R_2^b + k_{ba}\right)^2 + \Delta\omega_b^2\right]$. This accords well with the situation in biological tissues and does in fact reduce to Eq. 1.3 for practical on-resonance conditions when $R_1^a = R_1^b$ and $R_2^a = R_2^b$. If $R_{1\rho}$ is measured over a range of locking fields, this model may be used to fit the dispersion curve for the three parameters R_2, $R_{1\rho}^{\infty}$, and S_ρ^2. In the biologically relevant case when $k_{ba} \gg R_2^b \geq R_1^b$, then $S_\rho^2 \approx k_{ba}^2 + \Delta\omega_b^2$ and the exchange rate k_{ba} can be explicitly found when the chemical shift is known.

Where the second derivative of Eq. 1.3 with respect to ω_1 is equal to zero, the dispersion curve undergoes an inflection, and the corresponding locking field is then $\omega_1^{\text{infl}} = \sqrt{S_\rho^2/3}$. The two models use slightly different assumptions in their respective derivations and give different functional forms, but produce almost identical results when simulated numerically with biologically relevant parameter values. They have been shown to model dynamical effects well for small exchanging proton pool fractions ($p_b \ll 1$) in Bloch simulations as well as model systems of various metabolites (*68*, *91*, *95*). The Chopra model shown in Eq. 1.3 is slightly more general for the on-resonance spin-locking condition as the individual site relaxation rates do not need to be identical, so the hypothesis is this model will be more applicable to all the systems studied throughout this project. The Trott and Palmer model may be needed in certain scenarios such as when off-resonance locking pulses are used.

Elucidating the efficiency of chemical exchange in producing NMR relaxation will be

advantageous for improving quantitative MRI in both research and diagnostic settings. Previous studies have demonstrated dipolar interactions and cross-relaxation tend to decrease their relaxation contributions with field (*96*), and subsequent studies reveal that some other mechanism increases R_2 relaxation rates in protein solutions with static field (*69*). Chemical exchange has been shown to contribute to $R_{1\rho}$ relaxation through simulations and has been claimed to be the dominant factor of relaxation in many previous spin-locking experiments (*68*, *91*, *95*, *97*, *98*), but no study to our knowledge systematically verifies that chemical exchange is the prime governing mechanism of the dispersion. The interactions thought to be responsible for the majority of the relaxation in exchanging systems are dipolar coupling, cross-relaxation, and chemical exchange between distinct pools (*91*, *99*). Previous simulations have shown exchange alone can produce dispersion in $R_{1\rho}$, but how these other effects contribute to the dispersion in conjunction with exchange has not been analyzed. Introducing deuterium to the system while keeping temperature and pH constant will alter the overall dipolar coupling and intramolecular cross-relaxation in the system without significantly modifying exchange dynamics. Thus the effects other than exchange may be reduced to quantify their contribution at many field strengths to determine if exchange really dominates in a certain regime.

The use of deuterium in NMR has a long history and has been used for many purposes. Deuterium is a stable isotope of hydrogen with spin-1 that occurs with a natural abundance of 0.015% (*100*). It is commonly used in NMR for frequency locking to avoid drift in the resonance frequency throughout experiments and is used more directly for investigating protein structures and dynamics (*101–110*). The deuteron possesses a much smaller magnetic moment than the proton and thus has a smaller gyromagnetic ratio and a smaller dipolar field (*27*, *111*). The nuclear mass of the deuteron is doubled and there is an isotope effect with respect to the

exchange dynamics (*97*, *112*), but all these effects may be used to help establish the relative influences of exchange and dipolar effects at various fields. The deuterium nuclei replaces hydrogen nuclei rapidly through chemical exchange and the vastly different precession frequency of the deuteron causes these nuclei to be invisible to proton NMR, though direct detection may be performed with the right equipment (*113*). Thus deuteration of a medium in equilibrium undergoing exchange should result in decreased $R_{1\rho}$ values at low locking fields from the reduced exchange contribution and a reduction in the dipolar effects. Temperature and pH may also significantly affect chemical exchange parameters since these are known to influence most chemical reactions rates in general (*114*). Both have been investigated previously in chemical exchange experiments (*69*, *115–120*), but few have studied the effects on $R_{1\rho}$ (*91*, *95*, *121*, *122*). Quantifying the magnitude of all these effects on $R_{1\rho}$ will further advance the understanding of how chemical exchange influences relaxation in the rotating frame.

Exchange Rate Contrast

Distinguishing tissues based on chemical exchange rates can aid in quantitatively characterizing diseased and healthy tissues non-invasively. One such method to do this may be done by deriving image intensity that depends directly on exchange rate. Cobb et. al. described a method to derive such a contrast through a method called Exchange Rate Contrast or ERC (*98*). The ERC can be used in spectroscopic and image based experiments by emphasizing exchanging species with a specific inflection point. The theory starts by assuming $k_{ba} \gg R_2^b \geq R_1^b$ to write a simplified form of the Chopra $R_{1\rho}$ equation.

$$R_{1\rho} \approx R_2^a + p_b \left[R_2^b + \frac{k_{ba}\Delta\omega_b^2}{k_{ba}^2 + \Delta\omega_b^2 + \omega_1^2} \right] \qquad 1.4$$

By measuring three relaxation rates at judiciously selected locking strengths of $\omega_1 \approx 0$, ∞, and any intermediate value, Eq. 1.4 may be used to define the Exchange Rate Contrast (ERC) by which images may be generated that exhibit novel contrast based on the dominant exchange rates within the system.

$$ERC(\omega_1) = 4\frac{\left[R_{1\rho}(\omega_1 = 0) - R_{1\rho}(\omega_1)\right]\left[R_{1\rho}(\omega_1) - R_{1\rho}(\omega_1 = \infty)\right]}{\left[R_{1\rho}(\omega_1 = 0) - R_{1\rho}(\omega_1 = \infty)\right]^2} \qquad 1.5$$

Substituting Eq. 1.4 with the proper values of ω_1 into Eq. 1.5, the ERC can be written in terms of the intrinsic tissue parameters.

$$ERC(\omega_1) = 4\frac{\left(k_{ba}^2 + \Delta\omega_b^2\right)\omega_1^2}{\left(k_{ba}^2 + \Delta\omega_b^2 + \omega_1^2\right)^2} \qquad 1.6$$

The ERC is a smooth and Lorenztian-like curve when plotted versus ω_1 that displays a peak value of 1 when $\omega_1 = \sqrt{k_{ba}^2 + \Delta\omega_b^2}$. It falls off monotonically for values of ω_1 different from this value, and the width of the ERC is described by the parameter $\alpha = \frac{\omega_1}{\sqrt{k_{ba}^2 + \Delta\omega_b^2}}$. The ERC is thus a spectral response function in which the magnitude depends on the relationship of the locking field to the exchange rate and chemical shift frequency. This provides the basis for producing images that emphasize species of particular exchange rates. Cobb et al. have shown this can be used in an imaging context for single site exchange to emphasize specific exchange rates in studies of potential exchange based contrast agents in vitro (*68*). The relaxation rates in Eq. 1.5 may be replaced with image signal intensities (*SI*) from a single locking time at the respective locking amplitudes to produce parametric images that obey a similar behavior and emphasize the

protons undergoing exchange at a rate corresponding to the selected intermediate locking field, i.e. exchange weighted image contrast (EWIC).

$$EWIC = 4\frac{\left[SI(\omega_1 = 0) - SI(\omega_1)\right]\left[SI(\omega_1) - SI(\omega_1 = \infty)\right]}{\left[SI(\omega_1 = 0) - SI(\omega_1 = \infty)\right]^2} \quad 1.7$$

If this intermediate locking amplitude is chosen to be at the ERC peak of a specific exchanging species in the presence of single species exchange, then the derived image intensity will scale with the local concentration of that species. By changing the locking field of the acquired images, individual proton pools may be emphasized over others and distinguished by their specific exchange properties. The EWIC image is much faster to derive since it requires only three images, but is sensitive to the spin-lock time used for each image and thus, complicates the accurate estimation of the exchange rate. ERC maps calculated from $R_{1\rho}$ maps at 3 locking fields are much more robust in estimating exchange rates since there is no dependence on the locking time, but these require more images and longer acquisition times. The EWIC dependence on locking time needs to be assessed to determine how feasible this method is in practice.

Specific Aims

Five specific aims are addressed in the remainder of this chapter.

Aim 1

Compare the Trott and Palmer model to the Chorpa model by comparing both to Bloch-McConnell simulations and fitting them to dispersions from phantom experiments under various conditions to ascertain which is the more accurate and appropriate model for each condition. The conditions will include slow ($\frac{k_{ba}}{\Delta\omega_b} \ll 1$), intermediate ($\frac{k_{ba}}{\Delta\omega_b} \sim 1$), and fast exchange ($\frac{k_{ba}}{\Delta\omega_b} \gg 1$)

scenarios with both similar and disparate intrinsic pool relaxation rates to test the fast exchange and pool fraction assumptions the models employ. Various pool fractions will subsequently be examined to test how each model handles larger pool fractions since both assume very small solute pools. Finally, phantom experiments will be carried out and analyzed with both models to determine exchange rates on systems with known chemical shifts that have been examined using other methods such as NMR lineshape analysis and/or CEST. Metabolites will include glucose, ethanol, and myo-inositol.

Aim 2

Though evidence theoughout the literature suggest chemical exchange may dominate other relaxation mechanisms such as dipolar effects at high field, no study has examined this fact directly. Chemical exchange will be systematically confirmed to be the dominant effect in solutions at high fields by scanning 200 mM glucose solutions with deuterium concentrations ranging from 0-80 volume % at 4.7T, 7T, and 15T with a spin-locking sequence to measure the $R_{1\rho}$ dispersions. Analyzing the dispersion magnitudes and inflection points as a function of D_2O concentration and field strength will provide insight into the exchange and dipolar contributions.

Aim 3

The fact chemical exchange dominates $R_{1\rho}$ relaxation at high field, physiologic factors that may greatly influence exchange parameters need to be examined to establish their impact. Specifically, the influence of temperature and pH on chemical exchange parameters at high fields are determined by scanning a 200 mM glucose solution with pH = 7 at temperatures ranging from bore temperature (19°C) to 40°C, and scanning multiple samples at bore temperature with pH values ranging from 2-12.

Aim 4

Compare the Exchange Rate Contrast (ERC) method with Exchange Weighted Image Contrast (EWIC). The spin-lock time used when acquiring images for the EWIC method may influence the image contrast and the extent of this effect needs to be determined. The theories will be examined to determine what conditions may cause the EWIC to deviate from the ERC and to derive a manner of estimating this deviation with hopes to minimize it.

Aim 5

Using the ERC method provides the potential for generating image contrast that emphasizes the presence of metabolites exchanging at specific rates. A glucose model system will be analyzed with the ERC method to determine what frequency that the ERC will accentuate glucose. This method will be examined in healthy and tumor tissues in vivo to assess its contrast with the contrasts available from $R_{1\rho}$-weighted images and $R_{1\rho}$ maps.

Methods

Comparing $R_{1\rho}$ Models

The $R_{1\rho}$ dispersion methods described throughout this thesis provide new methods for quantitatively characterizing biological tissues, but this requires an accurate $R_{1\rho}$ model to assess the exchange dynamics. Both the Trott and Chopra models of exchange were derived in a very similar manner, so both were expected to perform quite well under most practical conditions but no comparison has been reported in the literature. In order to determine if one model would out-perform the other, comparing both models to various simulations was the first step. Finite difference Bloch-McConnell equations (Eq. 1.1) were evaluated in 5 ns time steps, with locking times up to 250 ms for each of the 50 spin-lock amplitudes ranging from 10 – 10,000 Hz. All $R_{1\rho}$

dispersion simulations were performed assuming a static field of 7T with p_b = 1% for fast, intermediate, and slow exchange regimes. The fast exchange simulations assumed the chemical shift difference of the solute pool was $\Delta\omega_b$ = 0.4 ppm (~119 Hz) and the exchange rate was k_{ba} = 2,400 Hz, giving a ratio of $\frac{k_{ba}}{\Delta\omega_b} \approx 20$. While this is not extremely fast exchange, the ratio is still more than an order of magnitude faster than intermediate exchange. The intermediate exchange simulations used a chemical shift of $\Delta\omega_b$ = 1 ppm (298 Hz) with an exchange rate of k_{ba} = 298 Hz to give a ratio of $\frac{k_{ba}}{\Delta\omega_b} = 1$, and the slow exchange simulations used a chemical shift of $\Delta\omega_b$ = 6 ppm (1,788 Hz) with an exchange rate of k_{ba} = 100 Hz to give a ratio of $\frac{k_{ba}}{\Delta\omega_b} \approx 0.05$. Each scenario was run using two sets of intrinsic pool relaxation rates, one with equal rates of $R_1^a = R_1^b$ = 0.1 Hz and $R_2^a = R_2^b$ = 0.4 Hz and one with unequal rates of R_1^a = 0.1 Hz, R_1^b =1.0 Hz, R_2^a = 0.4 Hz, and R_2^b = 4.0 Hz. All six simulations were compared to the theoretical Chopra and Trott models and the error was quantified using the sum of squares of the differences between the model and the simulated points since this is the quantity that would be minimized while performing a non-linear least squares fitting. Each set of simulated data was also fit to both the Chopra and Trott models with linear regression to mimic the procedure of fitting to experimental data in order to asses the accuracy of the exchange rate predictions calculated from the fitting method. Finally, the effect of the solute pool fraction was assessed by performing simulations using the parameter values of R_1^a = 0.1 Hz, R_1^b =1.0 Hz, R_2^a = 0.4 Hz, R_2^b = 4.0 Hz, $\Delta\omega_b$ = 1 ppm (298 Hz), and of k_{ba} = 298 Hz with a solute pool fraction varying from p_b = 0.5 – 4%. The calculated exchange rates were compared to the true exchange rates implemented in each of the pool fraction scenarios.

$R_{1\rho}$ experiments were performed on solutions of PBS mixed with 200 mM glucose, 200 mM myo-inositol, and 1 M ethanol to evaluate the fitting of each model to experimental data. $R_{1\rho}$ dispersions were acquired by measuring the signal decay at 5 locking times ranging from 0.01 – 1 sec for each of the 10 locking amplitudes ranging from ~40 – 10,000 Hz. Each $R_{1\rho}$ value was estimated by fitting the decay curves to a mono-exponential model and the $R_{1\rho}$ points were subsequently fit to each model. The Trott model will typically be implemented with the assumptions of asymmetric pool fractions and on-resonance RF, where the terms $\omega_{aeff}^2\omega_{beff}^2/\omega_{eff}^2 = \omega_{beff}^2$ and $\delta = \Delta\omega_b$. This model can therefore be fit for the variables R_1, R_2, $p_a p_b$, and k if the chemical shift is known, or the pool fraction can be assumed to be small (~1%) and the model can fit for R_1, R_2, $\Delta\omega_b$, and k. The chemical shift is known in all subsequent experiments so the pool fraction was used as a fitting parameter. The Chopra model was implemented to fit for R_2, $R_{1\rho}^{\infty}$, and S_ρ^2 while assuming $k_{ba} \gg R_1^b - R_2^b$. This means $S_\rho^2 = k_{ba}^2 + \Delta\omega_b^2$ and since the chemical shift was known the exchange rate could be estimated, but the rate and chemical shift cannot each be determined directly from the Chopra model fitting. The models were used to estimate the exchange rates to compare how different the estimates were since the exact exchange rate could not be determined. The experiments were all performed at 20° C and 37°C to test the fitting methods for different exchange rates in the same systems.

Effects of Deuteration

Dipolar effects are known to govern transverse relaxation in water and tissue at low fields (*23*), but chemical exchange between water molecules and labile protons such as those on amide, amine, or hydroxyl groups are believed to be the dominant mechanism of $R_{1\rho}$ dispersion at high static fields where the chemical shift frequencies become larger (*68*, *91*). Although computer

simulations and theory predict this trend (*98*, *123*), there has been no systematic experimental study to our knowledge that quantifies the evolution of dominant effects from dipolar interactions at low field strengths to chemical exchange at high field strengths. To verify and illustrate when exchange begins to dominate at high fields, experiments were performed at static fields of 4.7T and 7T on solutions of constant concentrations of exchanging species with varying levels of deuteration. Substitution of protons with deuterons reduces dipolar coupling but also reduces the number of protonated sites available for exchange. Solutions of 200 mM glucose were prepared in PBS with 0, 20, 40, 60, and 80% deuterium oxide, and proton $R_{1\rho}$ dispersions were measured with 10 logarithmically spaced locking fields ranging from 50-8,000 Hz at each static field strength, each with six logarithmically spaced locking times ranging from 20 ms - 1 sec. A simple mono-exponential fit was used to determine the relaxation rate, $R_{1\rho}$, from the decay curves. The spin-locking pulse sequence used was the standard pulse sequence described in chapter 1 by Witschey et al. designed to mitigate B_0 and B_1 field inhomogeneities (*62*). Dispersions were fit using the Chopra model of Eq. 1.3 to estimate exchange parameters and analyze the effects of B_0 and deuteration. While the low frequency limit of the dispersion provides information about T_2 values, T_1 values corresponding to the asymptotic limit of the dispersion curve were more accurately measured using a standard inversion recovery sequence.

Effects of Temperature and pH

Temperature and pH may greatly affect the exchange parameters and, therefore, the corresponding $R_{1\rho}$ dispersion. In order to establish the effects of temperature, $R_{1\rho}$ dispersion curves were measured at 7T for a 200 mM glucose sample (pH = 7.4) at five temperatures ranging from 19°C to 40°C. The sample was heated by blowing hot air down the bore of the magnet and the temperature was monitored using a thermocouple attached to an animal

physiologic monitoring system (SA Instruments, Stony Brook, NY). Dispersions were measured by acquiring signals from 5 spin-locking times ranging from 0.01 – 1 sec for each of the 10 logarithmically spaced locking amplitudes ranging from 50 – 10,000 Hz. The decay curves were fit to a mono-exponential model and the resulting $R_{1\rho}$ values were fit to the Chopra model for analysis. The effects of pH were determined by measuring $R_{1\rho}$ dispersions in two sets of samples of 200 mM glucose. One set consisted of seven samples with pH ranging from 3 – 9 and the other set consisted of five samples with a smaller range of pH from 6.00 – 7.40. All measurements were made at 7T and the dispersions were acquired in the same manner as the temperature dispersions, but all at bore temperature (19°C). The Chopra model was used again in fitting the dispersion data to determine exchange rates assuming a chemical shift of $\Delta\omega_b$ = 1ppm.

Exchange Rate Contrast vs. Exchange Weighted Image Contrast

The method of Exchange Rate Contrast was first examined through simulations similar to those from Aim 1. Finite difference Bloch-McConnell simulations were performed to simulate $R_{1\rho}$ dispersion curves for five exchange rates ranging from k_{ba} = 100 – 10,000 Hz with $\Delta\omega_b$ = 1 ppm, p_b = 1%, R_1^a = 0.1 Hz, R_1^b =1.0 Hz, R_2^a = 0.4 Hz, R_2^b = 4.0 Hz, and dt = 5 ns. The simulations were performed for 50 logarithmically spaced locking amplitudes ranging from 50 – 5,000 Hz and fit to the 2-pool Chopra model described above to obtain smooth $R_{1\rho}$ dispersions that were used to calculate the ERC curves using Eq. 1.5. The peak of each ERC was compared to the theoretical peak of $\omega_1 = \sqrt{k_{ba}^2 + \Delta\omega_b^2}$ to test the accuracy of the model. Determining the accuracy and practicality of the EWIC method was done by deriving an expression for the peak of the EWIC described in Eq. 1.7 as a function of the locking time and plotting EWIC curves at various times against an ERC curve. The shift in the EWIC curves were directly compared to the ERC curve.

Exchange Rate Contrast in vivo

The feasibility of using Exchange Rate Contrast imaging was assessed in a glucose model system and *in vivo*. In order to determine the locking amplitude that would generate ERC contrast emphasizing glucose exchange in tumor tissue, the glucose dispersion at pH = 6.7 used in the earlier pH experiments was analyzed with the ERC method. This pH was chosen since, even though there is significant variation within malignant tissue, the pH range of 5.8 – 7.6 has been reported in rodent tumors (*124*, *125*). A healthy Sprague-Dawley rat was imaged at 7T using a spin-lock prepped single shot EPI sequence to acquire $R_{1\rho}$ weighted images at 10 logarithmically spaced locking fields ranging from ~50 – 10,000 Hz, each with 5 locking times ranging from 1 – 100 ms. The rat was anesthetized using a 2%/98% isoflurane/oxygen mixture and the rectal temperature and respiration were mointored with an animal physiologic system $R_{1\rho}$ maps were calculated for each locking strength on a voxel by voxel basis by assuming a simple monoexponential decay model. With the peak ERC frequency known from the model system analysis, the $R_{1\rho}$ map, an $R_{1\rho}$ weighted image, and the ERC image at the closest locking frequency were compared and evaluated.

Results and Discussion

Comparing $R_{1\rho}$ Models

Comparing the Chopra and Trott models of $R_{1\rho}$ relaxation under various conditions may help determine which model estimates exchange parameters more accurately in practice. The first comparison between the Chopra and Trott models was done by simulating the $R_{1\rho}$ dispersion of slow exchange with the ratio $\frac{k_{ba}}{\Delta\omega_b} \approx 0.05$.

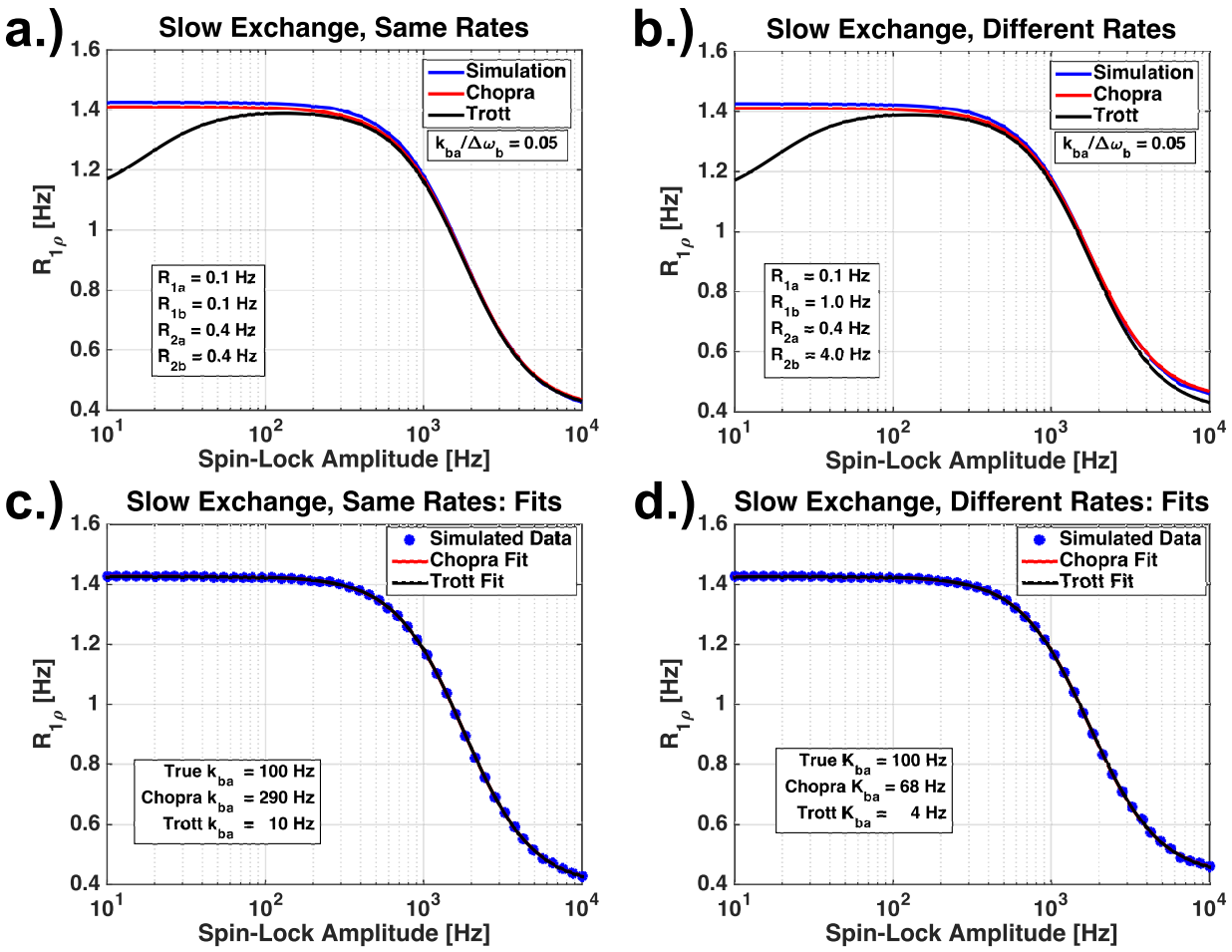

Figure 8: Simulated $R_{1\rho}$ dispersion curves compared to the Chopra and Trott models. a,b.) Simulations with different sets of intrinsic pool relaxation rates. c,d.) Simulated data fit to each model to compare the calculated exchange rates to the true rate that was simulated.

Figure 8a shows the simulated $R_{1\rho}$ dispersion in blue with the theoretical Chopra curve in red and the theoretical Trott curve in black for slow exchange with both pools relaxing at identical rates. The sum of squares for the Chopra model compared to the simulated values is 8.42×10^{-3}, which is 41 times smaller than the Trott sum of squares of 3.49×10^{-1}. Slow exchange with different pool relaxation rates is shown in Figure 8b, but since the theoretical Trott model does not allow for different pool relaxation rates, the Trott curve has identical rates and is the same as the Trott curve in Figure 8a. The Chopra sum of squares for different rates in Figure 8b is 7.55×10^{-3},

which is 47 time smaller than the Trott value of $3.55x10^{-1}$. For each scenario, the Chopra model qualitatively performs much better at low locking fields since the Trott model exhibits a strange decrease in relaxation rates at low B_1. This phenomenon can be mitigated by changing the relaxation and exchange parameters, as will be seen in the fitting, but this will cause more inaccurate estimates of the exchange parameters in practice. When the pool relaxation rates are different, the high locking field limit of the dispersion increases slightly which is predicted by the Chopra model but, not surprisingly, is not accounted for in the Trott model. Another noteworthy behavior is the fact that the inflection point occurs at such a high locking frequency since, even though the exchange is very slow, the inflection point is a function of the exchange rate and the large chemical shift in this case. Since the theoretical curves are different than the simulated data, fitting the data to these models may significantly decrease the accuracy of the estimated exchange parameters. Figure 8c,d show the fits for both the Chopra and Trott models under each scenario. When the relaxation rates are the same between pools, neither model performs well since they both assume fast exchange. While the true simulated exchange rate is k_{ba} = 100 Hz, the estimated exchange rate for the Chopra model is almost 3 times larger at 290 Hz and the Trott model is an order of magnitude off at 10 Hz. When the pool relaxation rates are different, the Chopra model performs better by estimating a rate of 68 Hz (factor of 1.5 different) while the Trott model does even worse by estimating a rate of 4 Hz. The Trott model should theoretically perform worse in the second scenario since this breaks the assumption that both pools have identical relaxation rates while the Chopra model has no such condition. Since both scenarios show the Trott model significantly underestimating the relaxation rates, this implies the chemical shift term greatly influences the estimation since the inflection point will be a function of these two parameters. The Chopra model outperforms the Trott model in the slow exchange

regime due to the low locking amplitude behaviors, but neither model necessarily excels in this regime. Both models are expected to perform much better for the intermediate and fast exchange regimes since these are the conditions for which the models were derived.

The simulations performed for intermediate exchange were similar in their behavior, and, while the Chopra model still slightly outperformed the Trott model, both models did in fact perform better than in the slow exchange regime. The exchange rate for the intermediate regime was simply set equal to the chemical shift term so the ratio $\frac{k_{ba}}{\Delta\omega_b} = 1$.

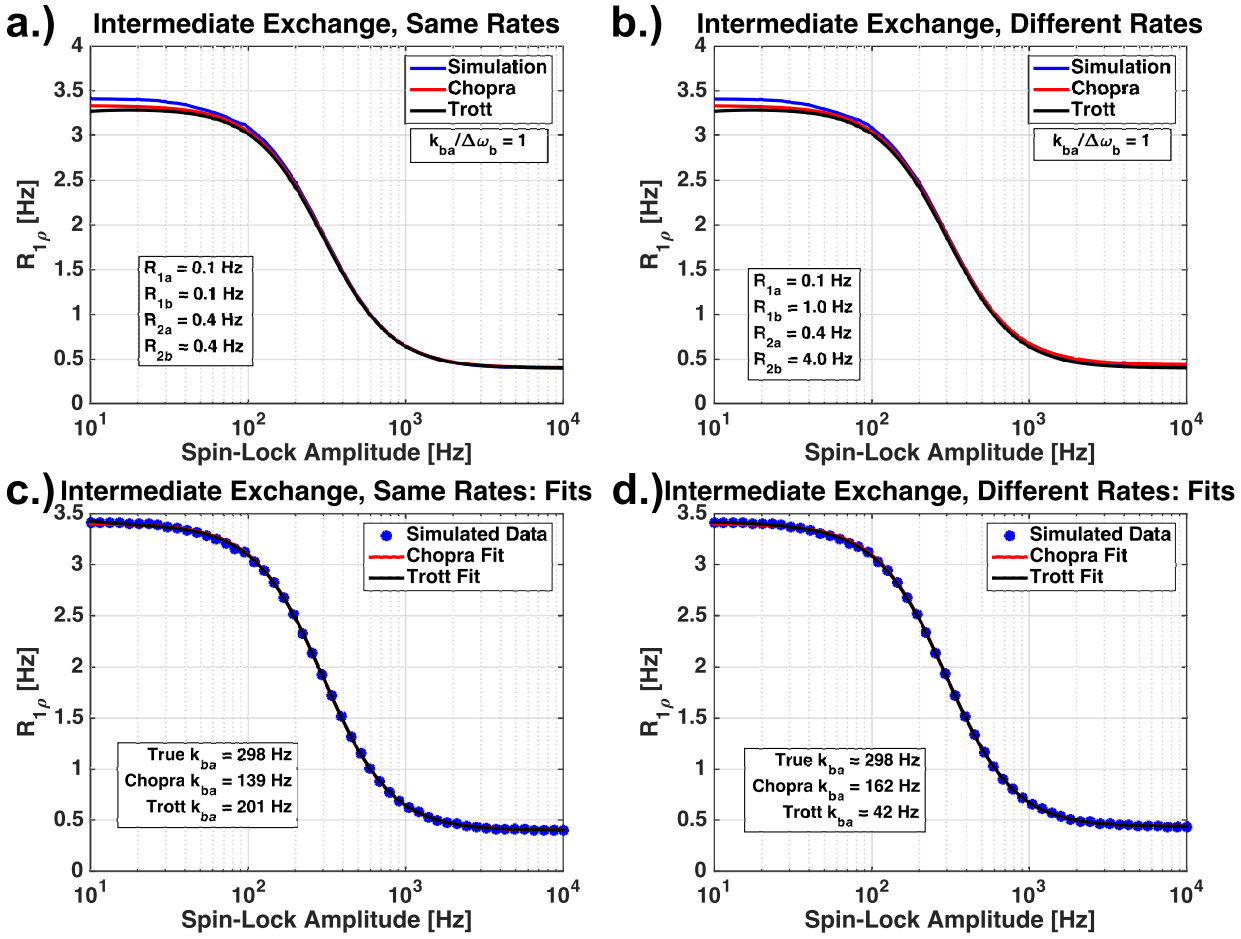

Figure 9: Simulated $R_{1\rho}$ dispersions for the intermediate exchange regime. a,b.) Comparison of each simulated dispersion to the theoretical Trott and Chopra models. c,d.) Examining the estimated exchange rates from fitting the simulated data to each model.

Figure 9a and b shows the simulated $R_{1\rho}$ dispersion plotted against the theoretical Chopra and Trott model curves for the cases of identical and different pool relaxation rates respectively. In the case of identical pool relaxation rates, the Chopra model has a sum of squares error of $7.99x10^{-2}$ while the Trott model has a 2.6 times larger sum of squares error of $2.06x10^{-1}$. The Trott model again begins to show a slight dip in relaxation rates at very low locking fields in both scenarios, but the behavior is much less pronounced than it was in the slow exchange regime. In the case if different pool relaxation rates, the Chopra sum of squares error is $7.67x10^{-2}$ which is ~3 times smaller than the Trott value of $2.27x10^{-1}$. The models slightly underestimate the low locking field limit in both scenarios and the Trott model does not account for the modest increase in the high locking field limit, similar to the behaviors in the slow exchange regime. Fitting each model to the simulated data, as shown in Figure 9c and d, estimated the exchange rate better than in the slow exchange scenario, as expected. For the case of identical exchange rates, the Chopra model predicted an exchange rate of 139 Hz, which is ~2 times smaller than the true value of k_{ba} = 298 Hz. The Trott model performed remarkably better than in the slow exchange regime by predicting an exchange rate of 201 Hz, which was also better than the Chopra model. Under the more realistic case of when the pool relaxation rates were different, the Chopa model estimated the rate to be 162 Hz while the Trott model greatly underestimated the rate to be 42 Hz. Again the Trott model did not perform well when the relaxation rates were different between pools, which has proven to limit the functionality of the model.

Both models were expected to perform quite well in the fast exchange regime since this was the true condition that both the models are based on. Examining the simulated curves in Figure 10a shows that both theoretical curves do in fact predict the simulated curve quite well qualitatively for the case of identical pool relaxation rates.

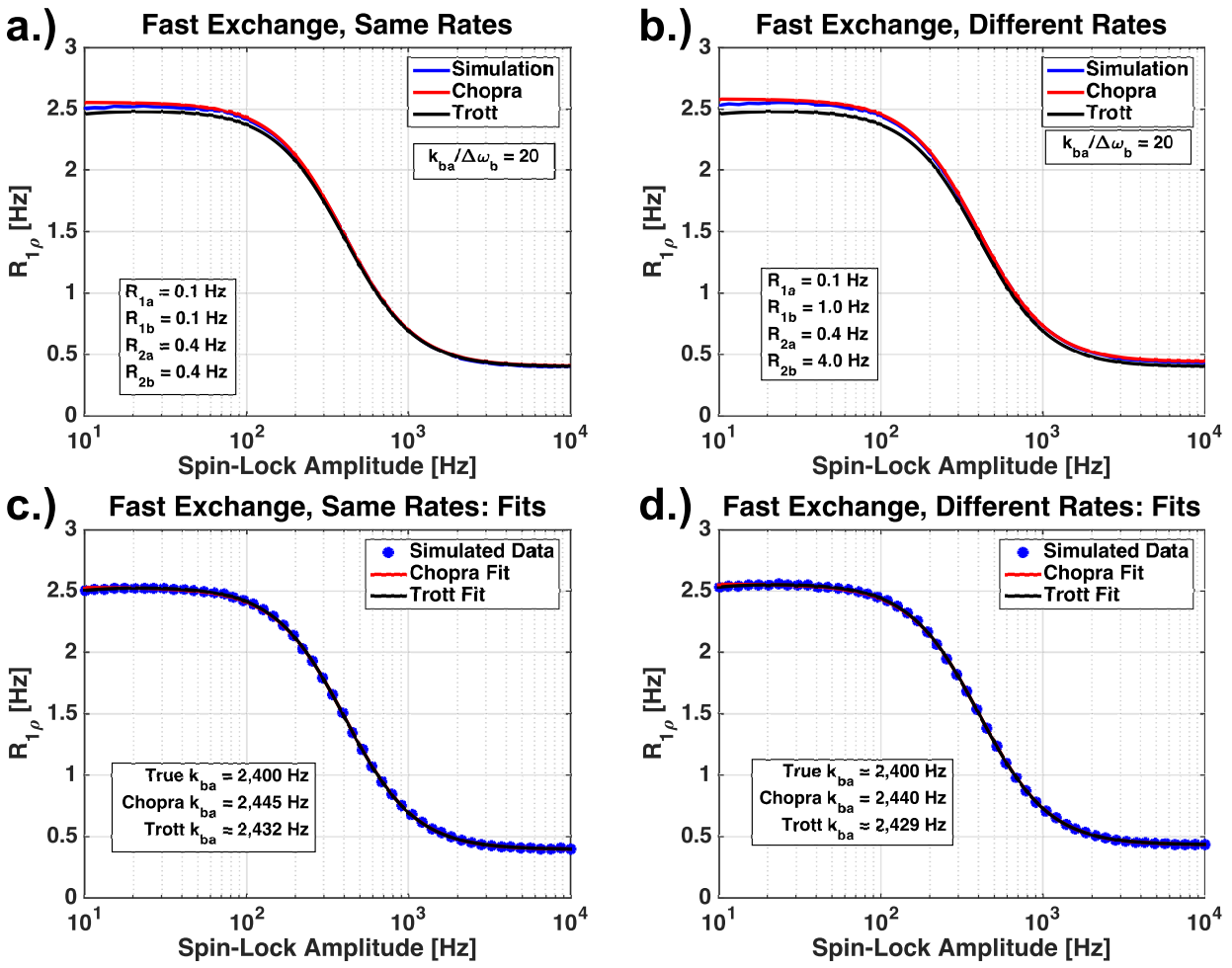

Figure 10: Simulated $R_{1\rho}$ dispersions for the fast exchange regime. a,b.) Comparison of each simulated dispersion to the theoretical Chopra and Trott models. c,d.) Examining the estimated exchange rates from fitting the simulated data to each model.

The sum of squares for the Chopra model for the case of identical relaxation rates was 1.55×10^{-2} which was ~3 times smaller than the Trott sum of squares of 4.61×10^{-2}. The Trott model still exhibits the dip at low locking fields, but the simulation surprisingly shows a similar dip that is less pronounced. This dip was not in the previous scenarios and may be a consequence of slight oscillations in the signal decay curves as a result of off-resonance effects due to the fast exchange. In the case where the pool relaxation rates are different, the Chopra sum of squares is 1.59×10^{-2}, which is 9.7 times smaller than the Trott value of 1.55×10^{-1}. The Trott model again

struggled with the case of different pool relaxation rates. Examining the estimated exchange rates from fitting each model to the data tells a different story though. For the case of identical relaxation rates, the Chopra model estimated an exchange rate of 2,445 Hz, which was roughly 1.9% different than the true value of k_{ba} = 2,400 Hz, while the Trott model estimated a rate of 2,432 Hz that was only 1.3% off the true value. When the pool exchange rates were different, the Chopra model predicted an exchange rate of 2,440 Hz (1.7% different) and the Trott model performed better by estimating a rate of 2,429 Hz (1.2% different). The fact that the Chopra model exhibited a more accurate theoretical curve for the specified exchange parameter in each scenario makes it somewhat surprising that the Trott model was more accurate in the estimation of the exchange rate. The estimations were only marginally better and the Chopra model would still be deemed acceptable under most circumstances, but the Trott model slightly out-performed the Chopra model for the fast exchange regime.

Experimentally, the concentration of an exchanging metabolite may not be known so the effect of the pool fraction on the overall $R_{1\rho}$ dispersion and on the estimation of the exchange rate may be vital. Changes in metabolite concentrations may occur naturally in diseased tissues or intentionally with the use of an exogenous contrast agent. The effect of changing the pool fraction was assessed for each model by fitting them to simulated data for various solute concentrations. The simulated data along with the corresponding fit from each model is shown below in Figure 11.

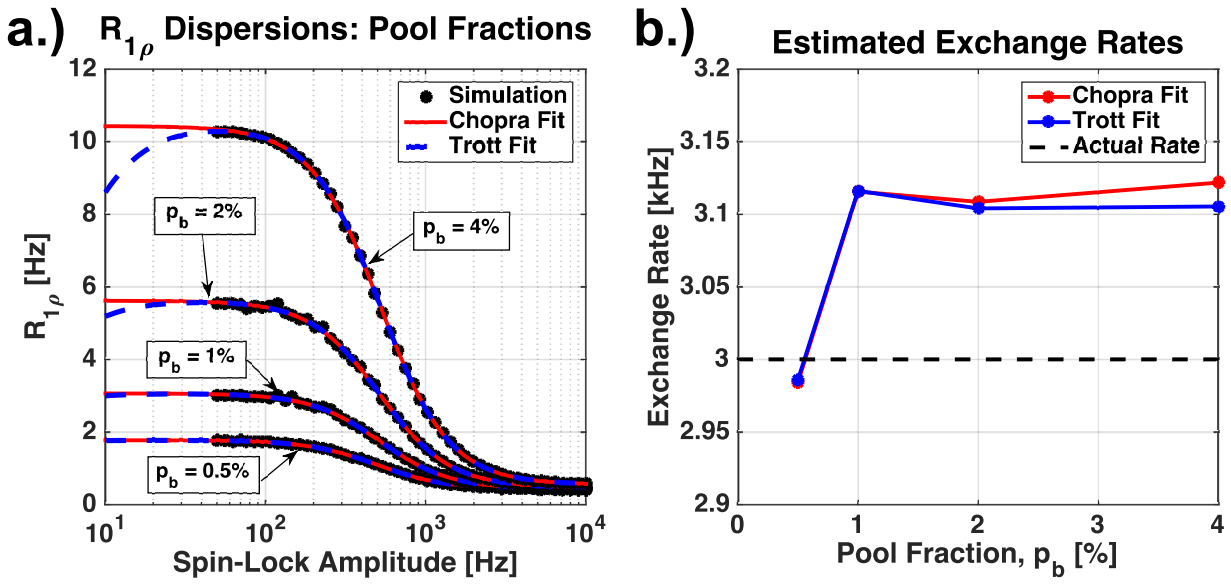

Figure 11: a.) Simulated $R_{1\rho}$ dispersions for pool fractions from 0.5% - 4% were fit to both the Chopra and Trott Models. b.) The estimated exchange rates from each fit were compared to the simulated exchange rate of 3,000 Hz (dotted black line).

The important parameters to note were the exchange rate was 3,000 Hz for each simulation, the chemical shift was $\Delta\omega_b$ = 0.5 ppm, the exchange ratio was $\frac{k_{ba}}{\Delta\omega_b} = 20$, and the pool fraction varied from 0.5 – 4%. Each model appears to fit the data well in the simulated regions just like the previous simulations, but the Trott model exhibits a strange behavior below the 50 Hz locking limit shown in Figure 11a. The relaxation rates begin to decrease rather then approach an asymptotic value like the Chopra model, which could cause problems for calculating the ERC later. Examining the estimated exchange rates in Figure 11b reveals the accuracy of each model. Both models perform very well at the lowest pool fraction of 0.5%, but then begin to overestimate the exchange rate by ~3% when $p_b \geq 1\%$. While the accuracy in both models is slightly compromised at high pool fractions, the Trott model surprisingly performs slightly better. Though realistic pool fractions in live tissues should not reach these concentrations, so the models are very comparable.

Fitting models to simulated data will provide insight into the theoretical accuracy of each model, but fitting the models to experimental data points may reveal more about the behaviors of each model since the data are affected by noise that may propogate as uncertainty in estimating exchange parameters. In the simulated examples shown above, the exact exchange rate was known since that parameter was manually input before the simulation, but experimentally this rate can be difficult to calculate exactly since it relies on so many factors. For this reason, only hydroxyls groups were tested to ensure the fast exchanging species would agree with the rapid exchange assumptions made by each model. Below in Figure 12 are two plots for 200 mM glucose at 20°C and 37°C that compare both models at each temperature.

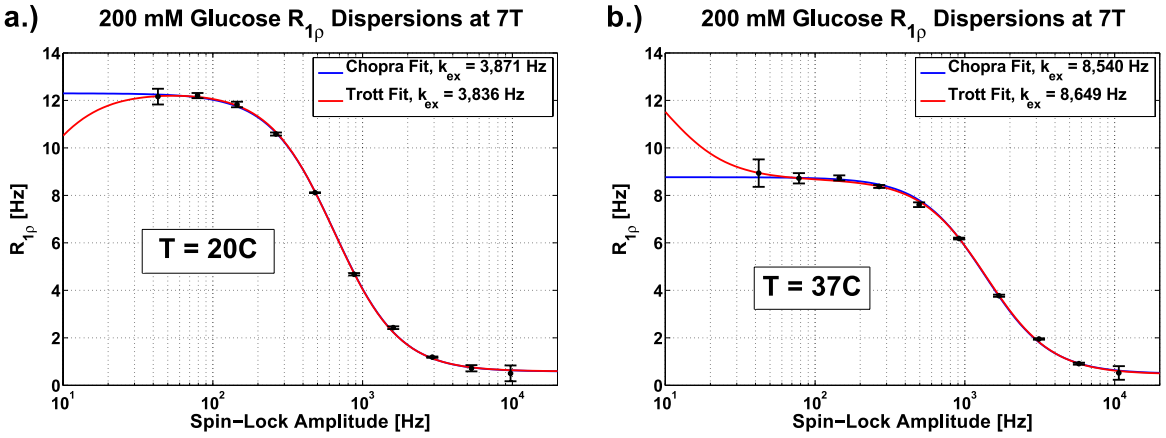

Figure 12: 7T $R_{1\rho}$ dispersions of 200 mM glucose at 20°C (a) and 37°C (b). The data are fit to both the Chopra and Trott models to estimate the exchange rates at each temperature.

Both models assumed $\Delta\omega_b$ = 0.7 ppm to compute very similar exchange rates that were well within the expected range for hydroxyl exchange for (*95*, *121*). While the Chopra model assumed a pool fraction of 1%, fitting to the Trott model estimated a pool fraction of $p_b \approx 4\%$. The estimated exchange rates of k_{chopra} = 3,871 Hz and k_{trott} = 3,836 Hz were only 0.9% different for the 20°C case and for the 37°C case the rates of k_{chopra} = 8,540 Hz and k_{trott} = 8,649 Hz were only 1.3% different, but the Trott model exhibits strange behavior in the low locking field limit that

was a result of off-resonance effects from the chemical shift, the exchange rate, and the solute pool fraction. The myo-inositol dispersions were very similar in their behaviors.

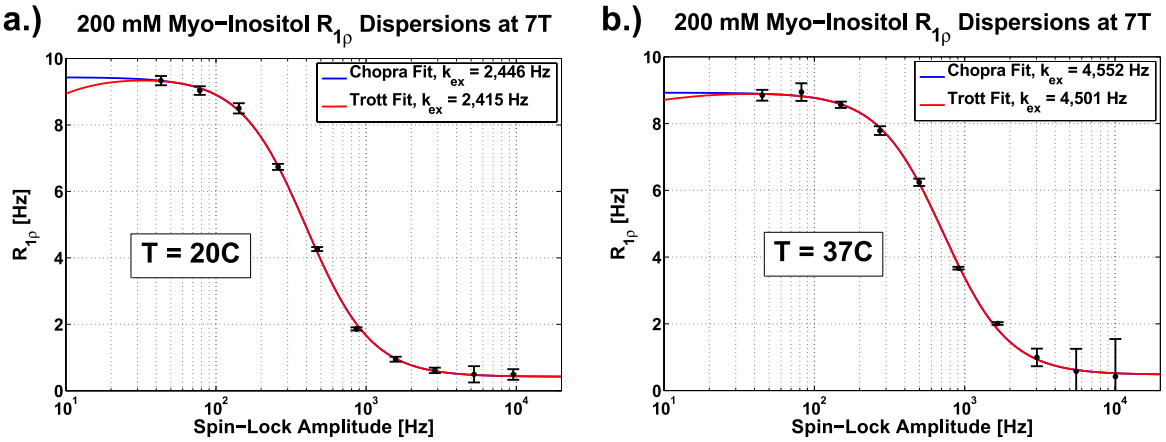

Figure 13: 7T $R_{1\rho}$ dispersions of 200 mM myo-inositol at 20C (a) and 37C (b). The data are fit to both the Chopra and Trott models to estimate the exchange rates at each temperature.

All the fitted curves in Figure 13 look very good for these data even though the Trott model continues to exhibit the dip at low locking fields. The Trott model estimated $p_b \approx 8\%$ for the myo-inositol pool while the Chopra model still assumed a 1% pool fraction. The exchange rates of k_{chopra} = 2,446 Hz and k_{trott} = 2,415 Hz were 1.3% different at 20°C while the rates of k_{chopra} = 4,552 Hz and k_{trott} = 4,501 Hz were only 1.1% different. The myo-inositol estimated exchange rates were notably slower than those in the glucose solutions which has been confirmed by other experiments in the literature (*121*). Exchange-based $R_{1\rho}$ dispersions resulting from multiple exchanging groups are common with metabolites like glucose and myo-inositol that have 5 and 6 different hydroxyl groups respectively, each with a very slightly different chemical shift. The dispersion curve will in fact be the sum of 5 or 6 separate dispersions that will all overlap to form a single indistinguishable curve since all are from hydroxyls. Other samples such as ethanol only have one hydroxyl group so only one exchange-based dispersion will contribute, so the overall dispersion magnitude should theoretically be much lower as a direct function of ethanol

concentration. The ethanol sample was prepared with higher concentration to counteract this effect, which is shown in Figure 14.

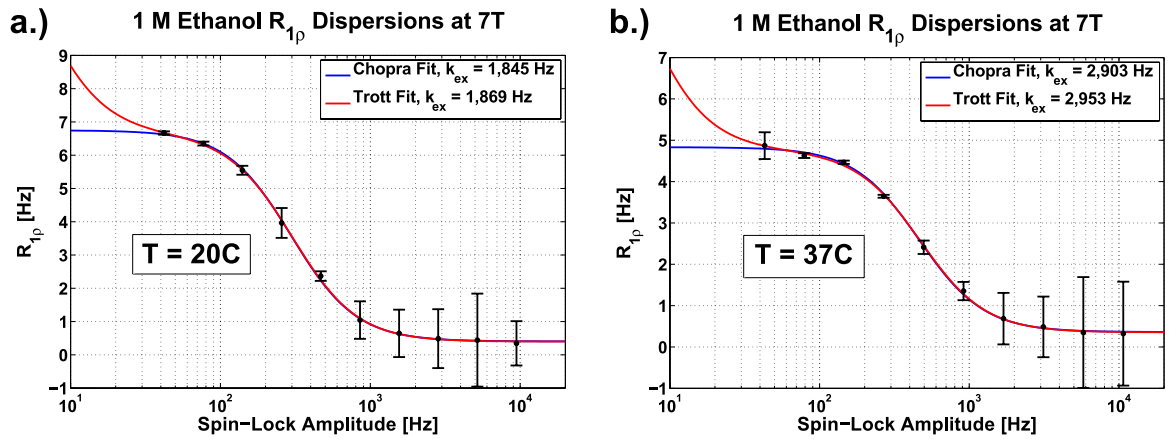

Figure 14: 7T $R_{1\rho}$ dispersions of 1M ethanol solutions at 20°C (a) and 37°C (b). These data were fit to both models at each temperature to estimate the exchange rates.

Even though the ethanol solution should have a similar pool fraction to that of the glucose solution, the Trott model estimated $p_b \approx 10\%$. The estimated exchange rates of k_{chopra} = 1,845 Hz and k_{trott} = 1,869 Hz were 1.3% different at 20°C and the rates k_{chopra} = 2,903 Hz and k_{trott} = 2,953 Hz were 1.7% different at 37°C, roughly the same as with the other solutions. The Trott model again displays the strange low locking amplitude behavior.

Effects of Deuteration

Establishing the manner in which chemical exchange dominates dipolar relaxation effects at high field is critical in more fully understanding the origin of relaxation within tissues. Adding deuterium to solutions will decrease the proton pool fractions and alter the overall exchange contribution to relaxation. $R_{1\rho}$ dispersion analysis provides a method to examine the exchange dynamics as protons are substituted with deuterons. Figure 15a and b demonstrate that increasing

the deuterium concentration reduces relaxation rates at low locking field and the magnitudes of the variations of $R_{1\rho}$ with locking field decrease in a concentration-dependent manner.

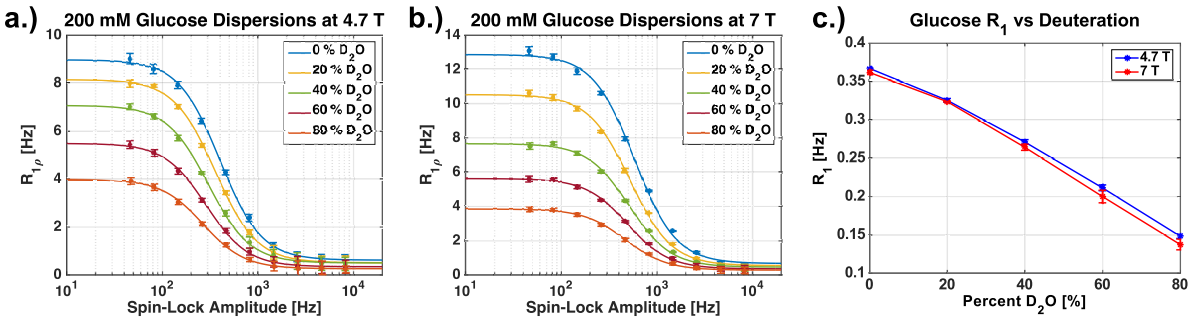

Figure 15: a,b.) $R_{1\rho}$ dispersions of 200 mM glucose solutions with different amounts of D_2O present at 4.7T and 7T. c.) Measured R_1 values for each sample at 4.7T and 7T.

These data are consistent with the loss of chemical exchange contributions to spin-lattice relaxation in the rotating frame as protons are substituted by deuterons. The dispersion magnitudes and the effects of deuteration on the dispersions also increase as the static field increases as shown in Figure 15b. This is due to the increased influence of exchange on relaxation at higher fields. Figure 15c shows the proton R_1 values decrease significantly as D_2O concentration increases, as expected, because the dipolar field of the deuteron is much less than the proton (*126*). Since both the exchange contribution and dipolar effects decrease with D_2O concentration, the dipolar effects need to be isolated in order to determine how they behave with field strength. To do this, the low locking field limits of the dispersions, $R_{1\rho}(0)$, were examined as a function of deuteration as shown in Figure 16.

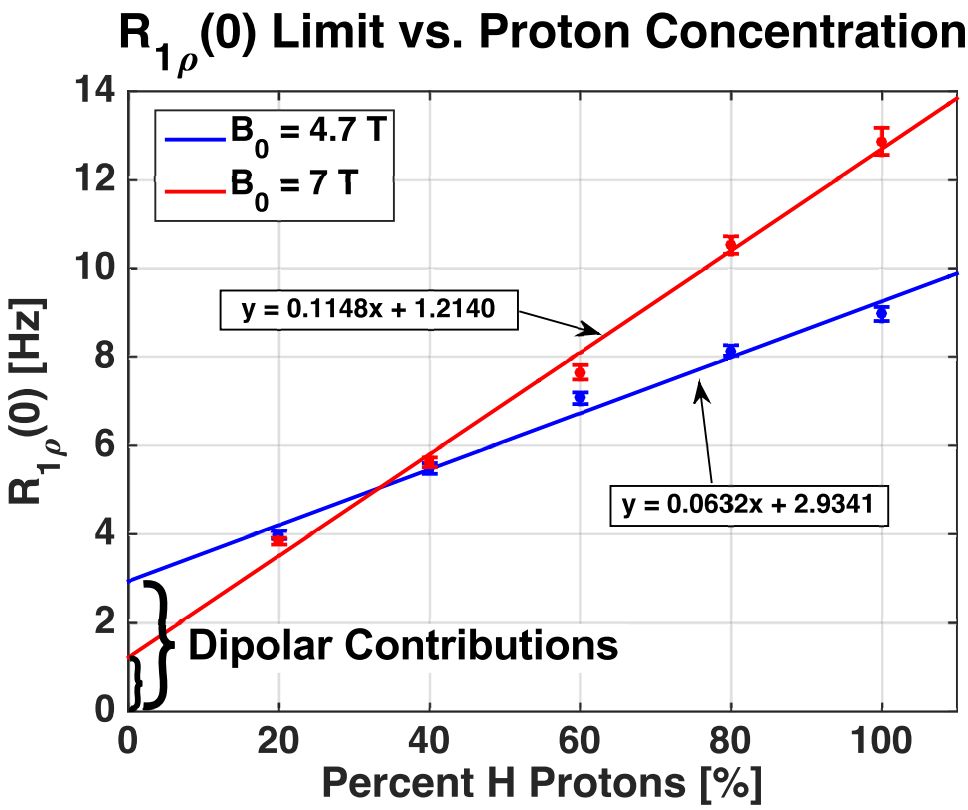

Figure 16: The low locking field limit of $R_{1\rho}$ plotted as a function of D_2O for both 4.7T and 7T. Extrapolating the linear fit for each field strength allows the estimation of the dipolar contributions when the sample is fully deuterated at 0% ^1H.

Fitting the low limit $R_{1\rho}$ values vs. proton concentration to a straight line allows one to extrapolate to estimate the amount of dipolar interactions when no exchange contribution is present. The estimated contribution of dipolar effects is roughly 59% lower at 7T than at 4.7T, as expected, confirming dipolar interactions decrease with field. The slope of the fitted line increases by a factor of 1.82 at 7T compared to 4.7T due to the effect of chemical exchange, close to the theoretical prediction (excluding all other factors) of 2.25. Moreover, the effective exchange rate is slowed by the introduction of deuterium as expected (*112*), which is evident by the shift of the inflection points of the dispersions to lower frequencies. The slowed exchange rate helps reduce the dispersion magnitude and is shown to have a larger effect at higher field.

Effects of Temperature and pH

Temperature effects were investigated by collecting $R_{1\rho}$ dispersions in a solution of 200 mM glucose dissolved in PBS for temperatures ranging from 19°C - 40°C. The effect of pH was also determined by collecting $R_{1\rho}$ dispersions in multiple solutions of 200 mM glucose dissolved in PBS at 19°C for pH = 3 – 9. Figure 17a and Figure 17b show that increasing the temperature increases exchange rates as derived from the fits to the dispersion data.

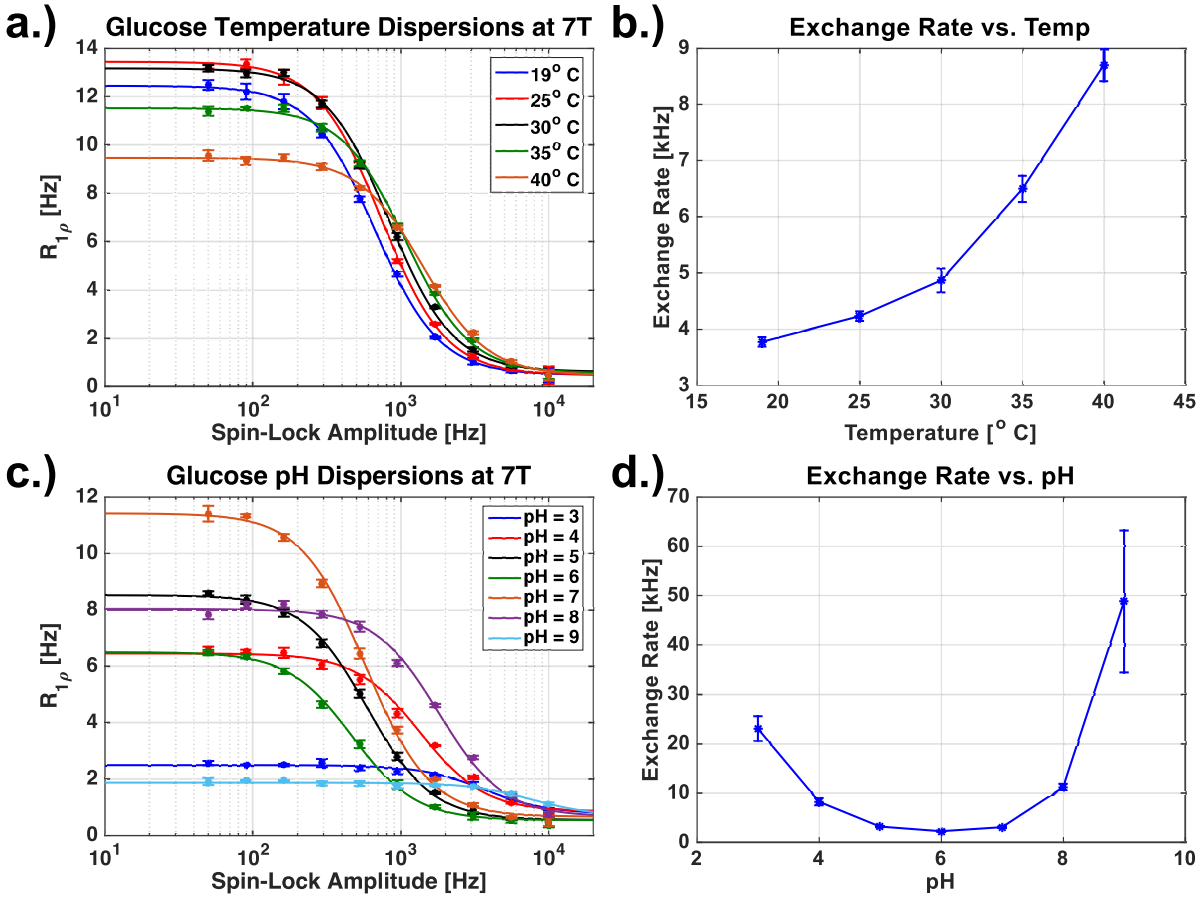

Figure 17: a.) $R_{1\rho}$ dispersions of 200 mM glucose solution at verious temperatures at 7T. b.) Exchange rates calculated from fitting for each temperature. c.) $R_{1\rho}$ dispersions for 200 mM glucose solutions at 7T for various pH values. d.) Exchange rates calculated from fitting for each pH value.

The dispersion magnitudes increase to a maximum value and then decrease beyond a certain high exchange rate, but the inflection points of the dispersions increase monotonically with

temperature. Although temperature and pH both significantly affect the rates of exchange between proton pools, changing the pH has more complex effects because the exchange rate reaches a minimum just above pH = 6, and increases with a change of pH in either direction as shown by the estimated exchange rates in Figure 17d which are derived from the dispersions shown in Figure 17c. $R_{1\rho}$ dispersions were measured over a smaller pH range to illustrate the manner in which small increases in pH around physiological levels may cause large changes in the exchange rate and a measureable shift and increase in the dispersion inflection. Figure 18 shows the dispersions and exchange rates for a 200 mM glucose solution over a pH range from 6.0 – 7.4.

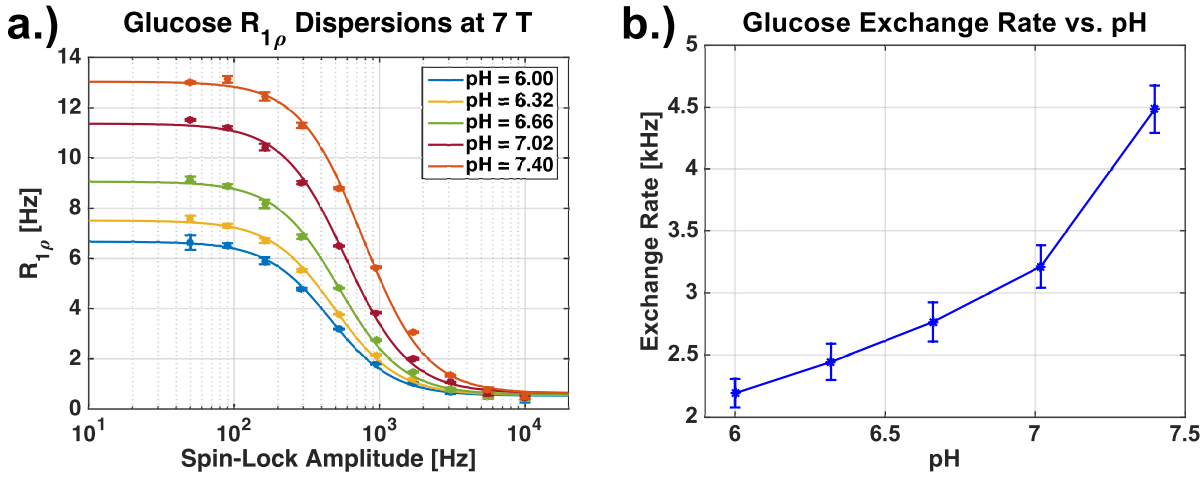

Figure 18: a.) R1rho dispersions of 200 mM glucose over a smaller range of pH values. b.) The estimated exchange rates calculated from the dispersion fits.

The exchange rates increase monotonically with pH and double in value over this range. This change in exchange rate, without changing glucose concentration, potentially provides a method to detect changes in temperature and pH in live tissues. It is important to note that the whole dispersion should be analyzed rather than one locking field since the relaxation rates will depend on a multitude of factors and the inflection point will not be known. One example of this can be

seen by examining the same samples from Figure 18 at 4.7T rather than 7T. Figure 19a shows the resulting $R_{1\rho}$ dispersions, note the dispersions do not continually increase in magnitude.

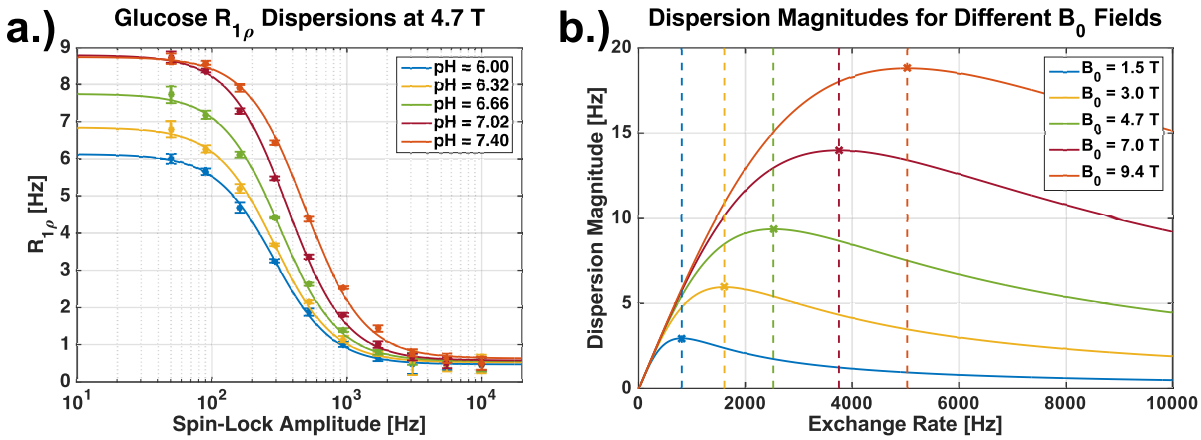

Figure 19: a.) $R_{1\rho}$ dispersions of 200 mM glucose at 4.7T for pH = 6.0 - 7.4. b.) Theoretical $R_{1\rho}$ dispersion magnitudes are shown as a function of exchange rate for various B_0 field strengths.

This occurs because the magnitude will reach a maximum value at a particular exchange rate and begin to diminish as the rate increases. This peak value will be a function of the chemical shift and field strength shown in Figure 19b. This optimal exchange rate may be calculated by finding the difference $R_2 - R_{1\rho}^{\infty}$, setting the derivative with respect to k_{ba} equal to zero, and solving for k_{ba}.

$$k_{ba} = \frac{\sqrt[3]{9\left(R_2^b\right)^3 + \sqrt{3}\sqrt{27\left(R_2^b\right)^4\Delta\omega_b^2 + 18\left(R_2^b\right)^2\Delta\omega_b^2 - \Delta\omega_b^6} + 9R_2^b\Delta\omega_b^2}}{3^{2/3}} + \frac{9\left(R_2^b\right)^2 + 3\Delta\omega_b^2}{3^{4/3}\sqrt[3]{9\left(R_2^b\right)^3 + \sqrt{3}\sqrt{27\left(R_2^b\right)^4\Delta\omega_b^2 + 18\left(R_2^b\right)^2\Delta\omega_b^4 - \Delta\omega_b^6} + 9R_2^b\Delta\omega_b^2}} \quad 1.8$$

Eq. 1.8 may be useful when the intrinsic relaxation rates and chemical shifts are known, but it reveals only the exchange rate that maximizes the dispersion magnitude and fails to provide any insight into what rate the sample will physically exhibit exchange under any conditions.

Adequate knowledge of the complete dispersion curve enables the explicit derivation of exchange parameters according to the Chopra relationship. However, location of the inflection point in the dispersion curve itself is sufficient to accurately estimate key intrinsic properties related to exchange. This inflection point varies monotonically with exchange rate as shown for two different chemical shifts at multiple static field strengths in Figure 20.

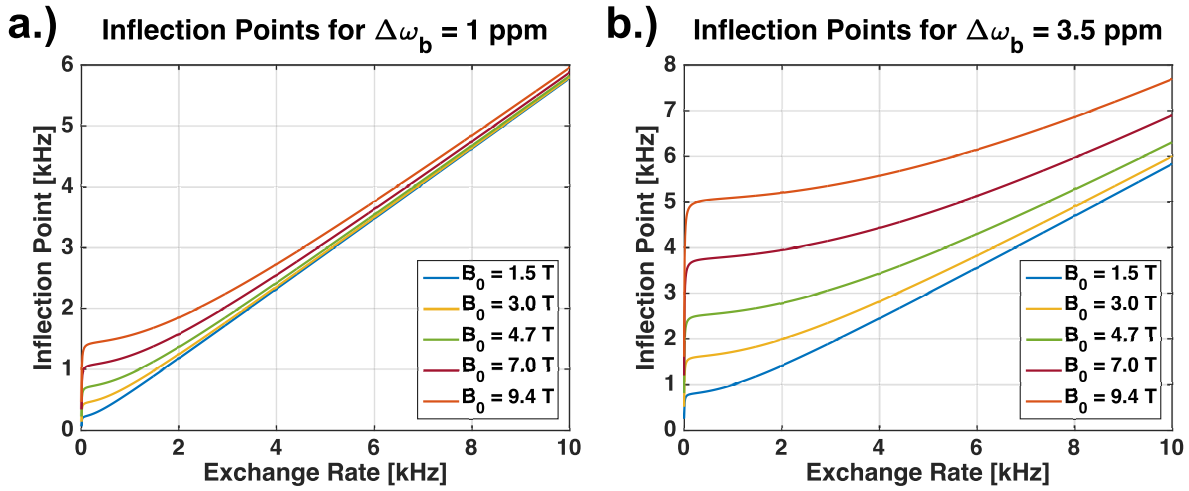

Figure 20: $R_{1\rho}$ dispersion inflection point frequencies plotted as functions of chemical exchange rates at multiple field strengths for two chemical shifts of $\Delta\omega_b$ = 1 ppm (a) and $\Delta\omega_b$ = 3.5 ppm (b).

For each chemical shift, the inflection point eventually begins to increase linearly with exchange rate at all fields and is linear at lower exchange rates for smaller chemical shifts. This relationship between the inflection point and the exchange rate is especially useful for faster exchanging metabolites possessing smaller chemical shifts such as hydroxyls. The exchange rate has an explicit relationship to both temperature and pH as shown in Figure 17b and Figure 18b. Thus, in principle, changes in the inflection point may be used to detect changes in temperature and pH. Moreover, simply measuring the dispersion change from three $R_{1\rho}$ values, which is faster but more limited, may also be used to detect changes in temperature or pH assuming the concentration of exchanging species does not change. Figure 18a shows the dispersion

magnitude increases monotonically with exchange rate for a small range of pH values. Figure 21 shows the dependence of the ratio $\left[\frac{R_{1\rho}(\omega_1=0)-R_{1\rho}(\omega_1=\infty)}{R_{1\rho}(\omega_1)-R_{1\rho}(\omega_1=\infty)}\right]$, which according to equation 3 can be simplified to $1+\frac{\omega_1^2}{S_\rho^2}=1+\frac{\omega_1^2}{k_{ba}^2+\Delta\omega_b^2}$.

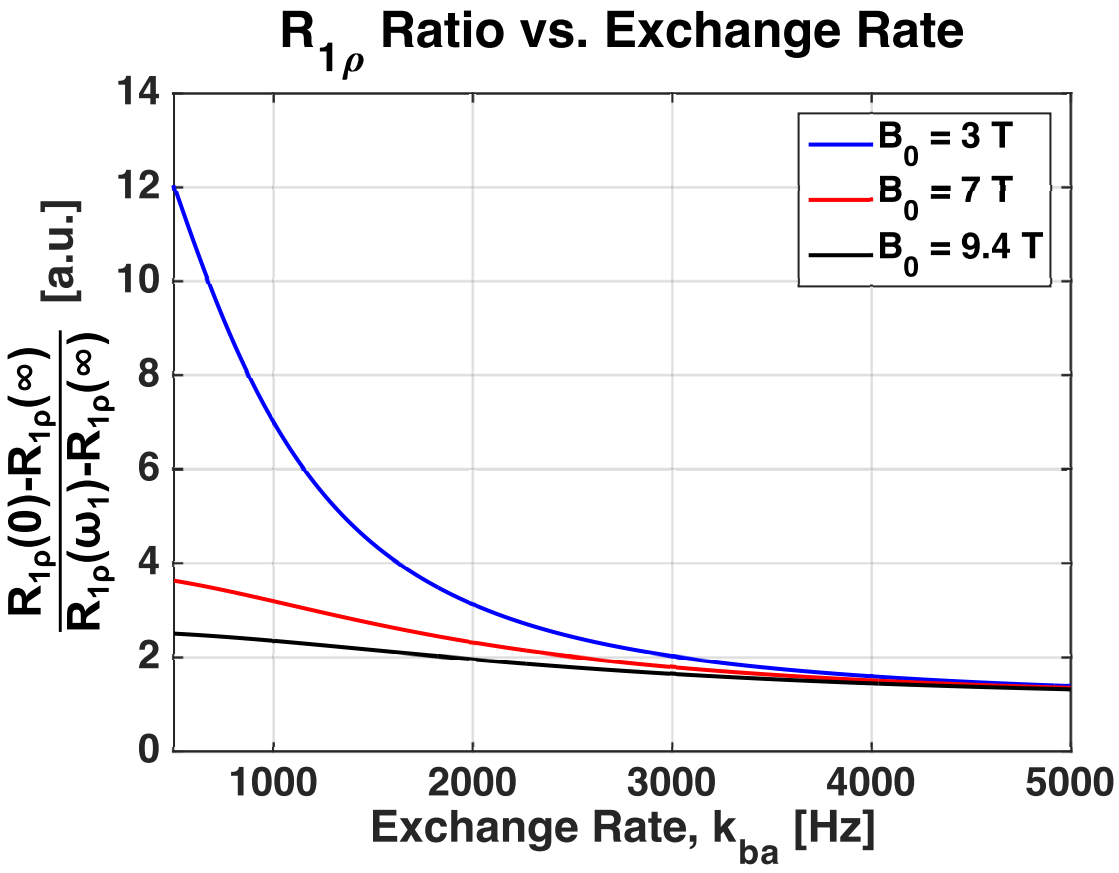

Figure 21: The $R_{1\rho}$ ratio plotted for multiple field strengths decreases with exchange rate but provides a fast method for estimating exchange rates in practice.

The curves in Figure 21 assume $\Delta\omega_b$ = 1 ppm, $R_{1\rho}^{\infty}$ = 0.8 Hz, R_2 = 5 Hz, and B_1 = 500 Hz. This ratio, which may be easily calculated from three $R_{1\rho}$ values, will have a direct relationship to the exchange rate and may be used for quick estimations without explicit fitting assuming the

chemical shift is known. The ratio shown in Figure 21 depicts greater changes at lower fields since the chemical shift dominates the equation at high fields.

Exchange Rate Contrast vs. Exchange Weighted Image Contrast

The accuracy of the ERC method was first assessed by simulating $R_{1\rho}$ dispersions for different exchange rates to calculate ERC curves and comparing the peak value of the simulated curve to the theoretical peak value. The $R_{1\rho}$ dispersions and resulting ERC curves shown in Figure 22 illustrate the manner in which the ERC peak shifts with exchange rate.

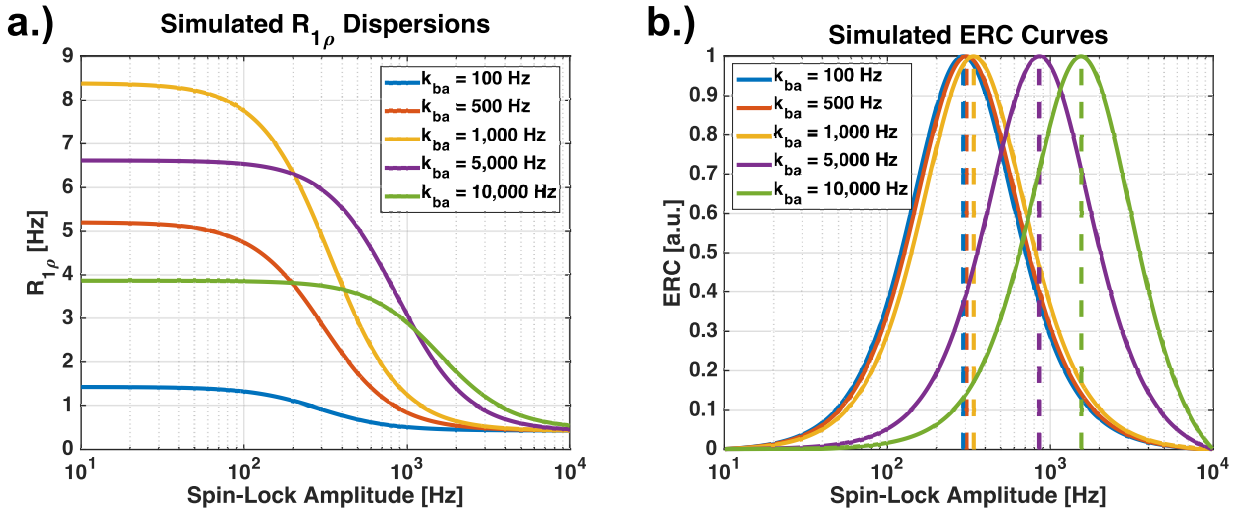

Figure 22: a.) Two-pool $R_{1\rho}$ dispersions with exchange rates ranging from 100 - 10,000 Hz. b.) ERC curves calculated from the fitted $R_{1\rho}$ dispersions with vertical dotted lines indicating the peak positions.

The shifting ERC peak positions are identified by the vertical dotted lines in Figure 22b. The fitted peak positions were compared to the theoretical peak positions, $\omega_1 = \sqrt{k_{ba}^2 + \omega_b^2}$, with a mean percent difference of 1.5%. This may have arisen from uncertainty in the $R_{1\rho}$ estimation from the low locking amplitude decay curves, which exhibited slight oscillations that will be described in chapter 6. These oscillations could not easily be remedied by smaller simulated time

steps or changing the fitting function to a more complicated function that was not mono-exponential, but regardless, the error magnitudes were very small.

The ERC method provides a novel way to emphasize metabolites by their exchange rates in an imaging context, and the EWIC method provides a less time consuming technique for acquiring similar information since only one image is needed per locking amplitude and the rate $R_{1\rho}$ is never directly calculated. A limitation arises from the fact that the acquired images are $R_{1\rho}$-weighted and possess a dependence on the locking time, *slt*. This dependence may shift the peak of the EWIC curve by an amount that depends not only on the locking time, but also on the intrinsic relaxation rates, the chemical shift of the solute pool, and the exchange rate.

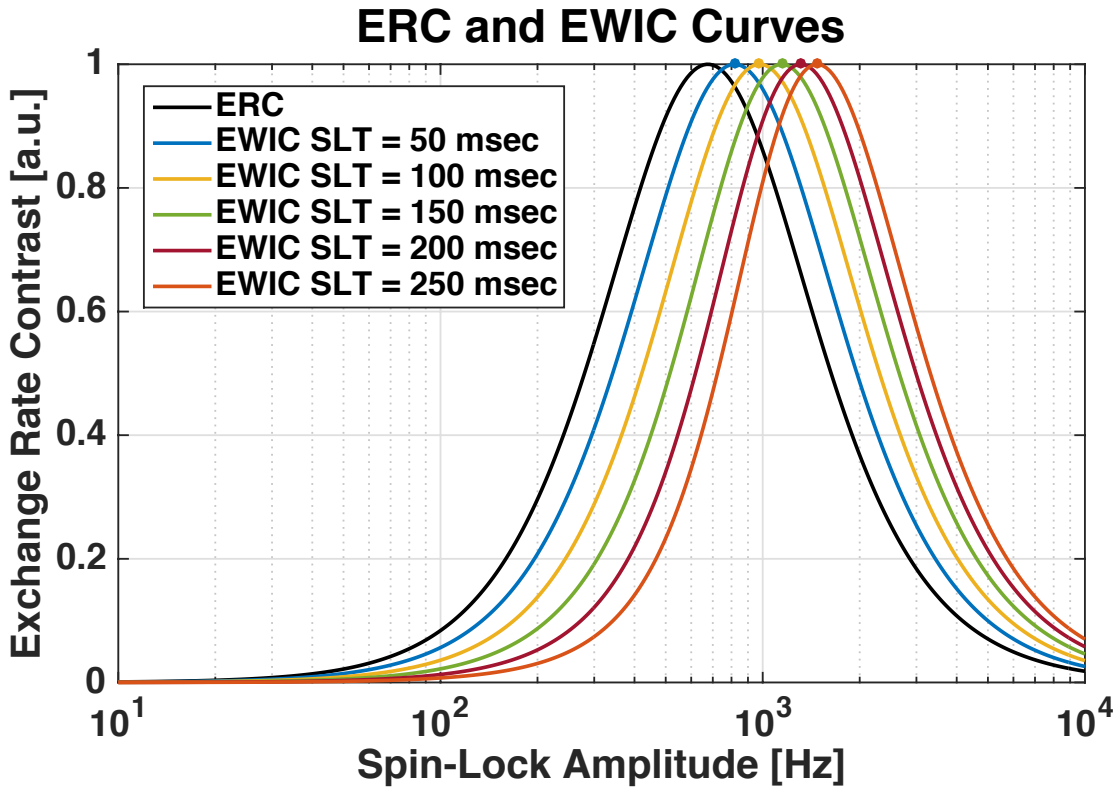

Figure 23: The colored theoretical EWIC curves are shown to shift to higher locking amplitudes compared to the black ERC curve as the locking time increases.

Figure 23 reveals and example of how the EWIC curve can shift by changing the locking times used for the images to calculate the curve. The shift in peak position can be calculated theoretically by assuming the signal will decay mono-exponentially with a rate $R_{1\rho}$ so the low, intermediate, and high amplitude images may be represented by Eq. 1.9 using the Chopra relation for $R_{1\rho}$.

$$\begin{aligned} I_1 &= M_0 e^{-R_{1\rho}(0)slt} = M_0 e^{-R_2 slt} \\ I_2 &= M_0 e^{-R_{1\rho} slt} = M_0 e^{-\left[\frac{R_2 + R_{1\rho}^{\infty}\omega_1^2 / S_\rho^2}{1+\omega_1^2/S_\rho^2}\right] slt} \\ I_3 &= M_0 e^{-R_{1\rho}(\infty)slt} = M_0 e^{-R_{1\rho}^{\infty} slt} \end{aligned} \qquad 1.9$$

By substituting these equations for the signal intensities in Eq. 1.7, taking the first derivative, and setting it equal to zero, an expression may be derived for the locking amplitude of the EWIC peak as shown in Eq. 1.10.

$$\omega_1 = S_\rho \sqrt{\frac{\left(R_{1\rho}^{\infty} - R_2\right) slt}{\ln\left(\frac{1+e^{\left(R_{1\rho}^{\infty}-R_2\right)slt}}{2}\right)} - 1} \qquad 1.10$$

Here, the $R_{1\rho}^{\infty}$, R_2, and S_ρ parameters are the same Chopra terms that are simply functions of the intrinsic pool relaxation rates, chemical shift, and exchange rate.

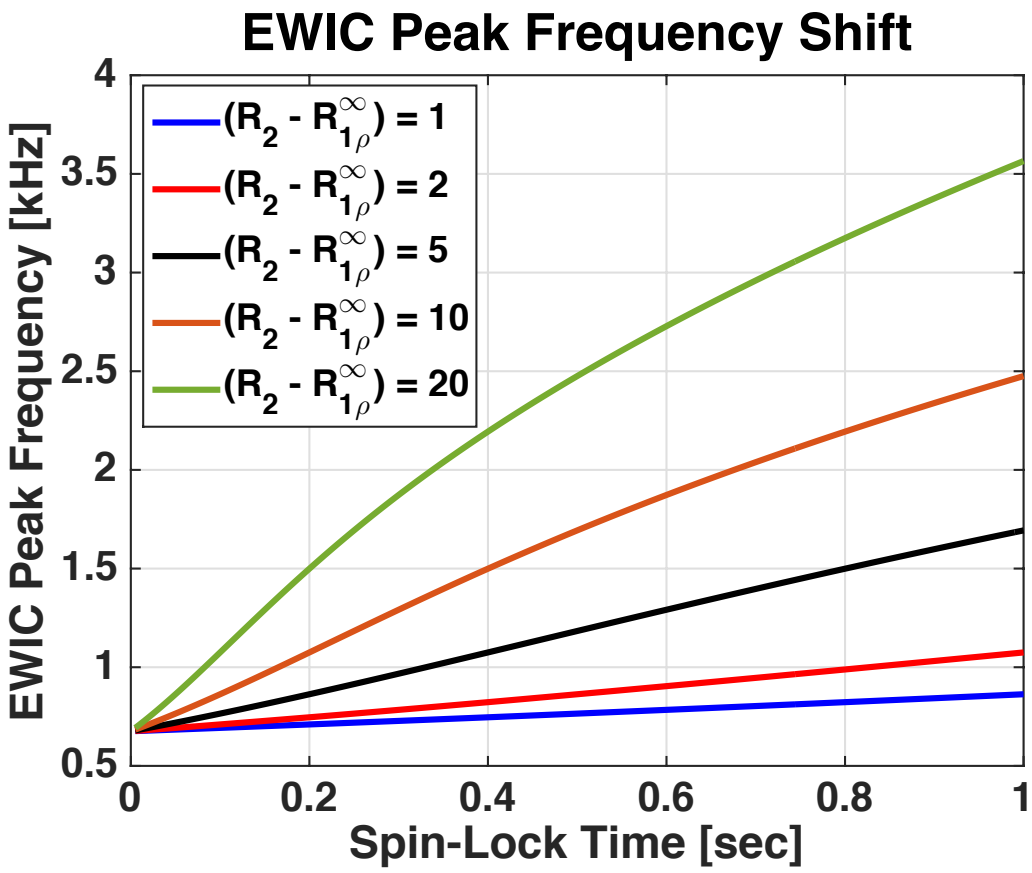

Figure 24: EWIC peak frequency as a function of locking time 5 different dispersion magnitudes.

This theoretical EWIC peak is shown to increase with spin-lock time in Figure 24 and the amount the peak can shift depends on the dispersion magnitude, or the difference of $R_2 - R_{1\rho}^{\infty}$. The EWIC approaches the ERC for very short locking times, but practically this would decrease the contrast to noise between images since it decreases the amount of time available for the signal to relax. There is no standard method to determine the optimal locking time for the EWIC method since the relaxation rates and signal to noise ratio will change between experiments. Fully accounting for the shift requires measuring the $R_{1\rho}$ dispersion parameters, but with the same information the more robust ERC method may then be used.

Exchange Rate Contrast in vivo

The glucose model system of pH = 6.7 from the pH experiments was analyzed using the ERC method to determine at what frequency glucose displays a peak value at realistic malignant tissue pH. The dispersion for the model system along with its corresponding ERC curve are shown in Figure 25.

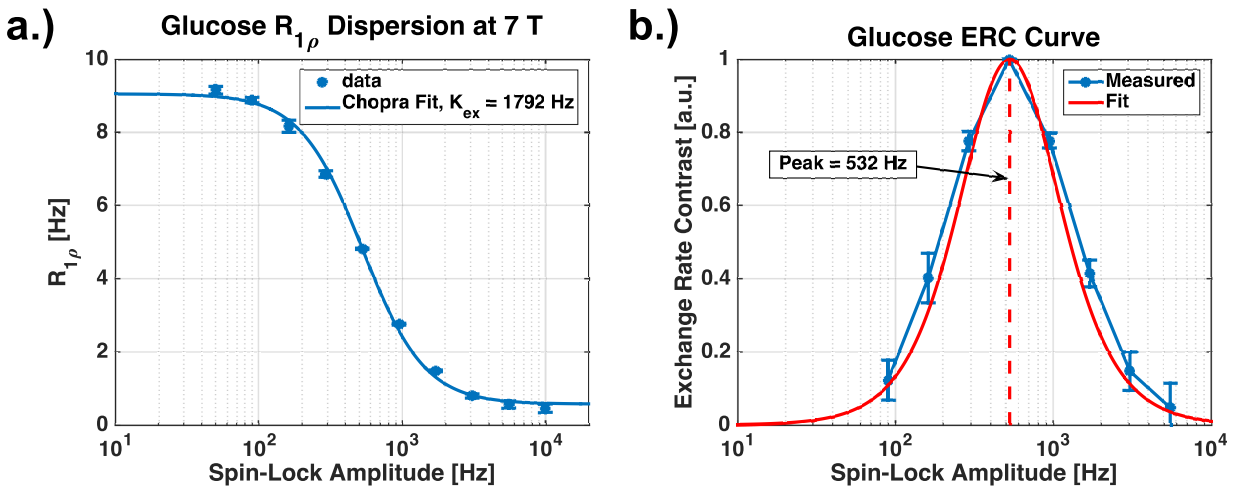

Figure 25: $R_{1\rho}$ dispersion (a) and ERC curve (b) for 200 mM glucose solution in PBS with pH = 6.7.

The error bars on the ERC points are noticeably larger than on the $R_{1\rho}$ dispersion points, which is a result of the propagation of uncertainty in the ERC equation in Eq. 1.5. The experimental ERC curve was fit to the model described in Eq. 1.6, which exhibited a calculated peak at a locking frequency of 532 Hz. ERC images at this frequency should thus emphasize regions of glucose at this pH, and suppress regions without glucose or other metabolites exchanging at this rate.

Though the tumor tissue is expected to exhibit very heterogeneous pH values, the ERC only emphasizes those corresponding to the selected locking field resulting in accentuated tumor tissue contrast compared to the surrounding healthy tissue. A live rat was imaged at 7T using a spin-lock prepped single shot EPI sequence, with the corresponding images at the locking

amplitude of 562 Hz shown in Figure 26. The $R_{1\rho}$-weighted image shown in the top right is at the locking time of 50 ms since this displayed the best combination of contrast and signal to noise ratio compared to the other locking times, and all zoomed in color images were simply masked with a hand-drawn ROI to only show the brain.

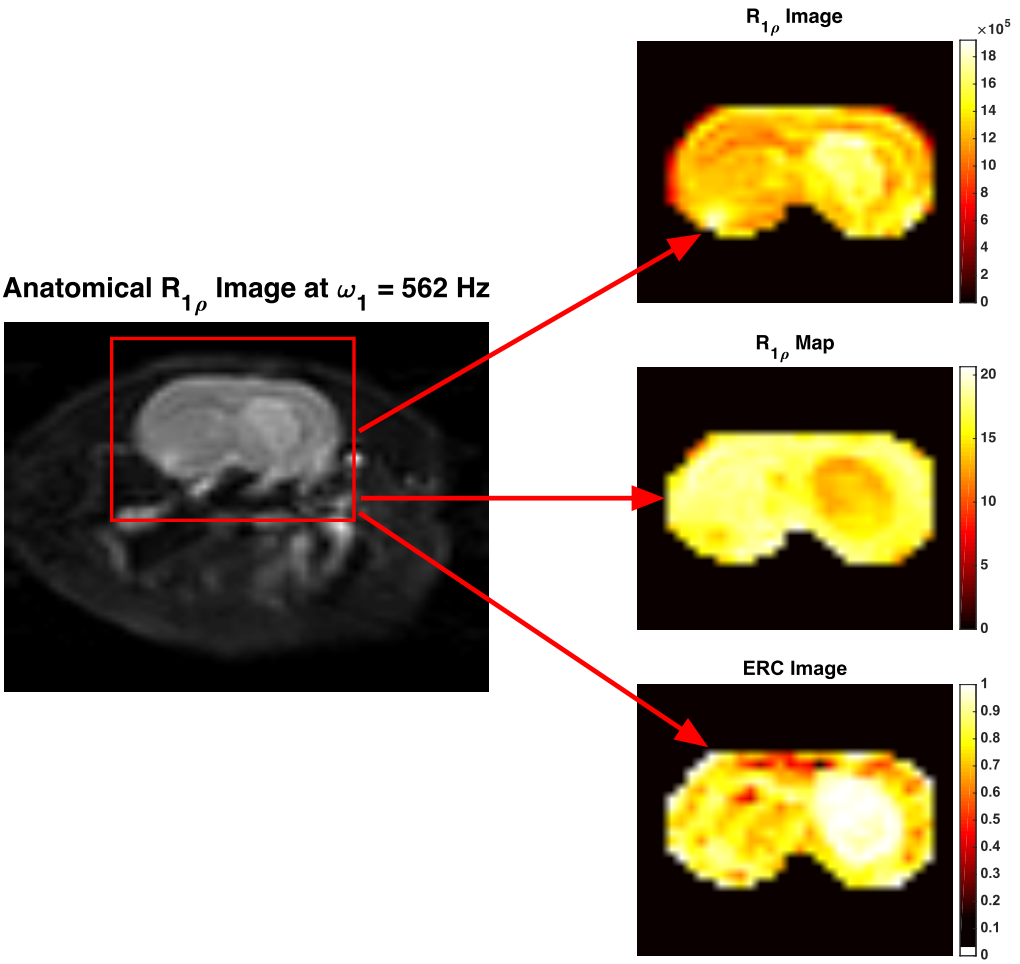

Figure 26: Comparison of an $R_{1\rho}$ image at 562 Hz with a locking time of 50 ms, a $R_{1\rho}$ map at 562 Hz, and an ERC image at 562 Hz.

Qualitatively, the $R_{1\rho}$ map and the ERC image provide very similar differences in contrast between malignant tumor tissue and healthy tissue, though the tumor is hypointense in the $R_{1\rho}$ map while it is hyperintense in the ERC image. Quantitatively, there is a 27% increase in tumor

signal intensity, a 23% drop in average tumor $R_{1\rho}$, and a 26% increase in tumor ERC, all of which are shown below in Figure 27. The important feature to note is that the ERC in the tumor region appears much higher than in the surrounding healthy tissue, implying significant glucose exchange based on the previously analyzed model system. The surrounding tissue did in fact display increased ERC values at higher locking amplitude where glucose under normal physiologic conditions would be emphasized (image not shown) which almost matched the ERC in the tumor. The fact the tumor displays hyperintense ERC values at a range of locking amplitudes, while the healthy tissue only peaks around a locking amplitude corresponding to physiological exchange conditions, implies there is much heterogeneity in pH within the tumor tissue. This heterogeneity has been well recorded in the literature but also may be partially explained through pH differences in the intracellular and extracellular space which have been previously reported (*124*). The contrasts in Figure 26 were quantitatively compared below in Figure 27 by drawing symmetric ROI's over the tumor region and the healthy tissue on the opposite side of the brain.

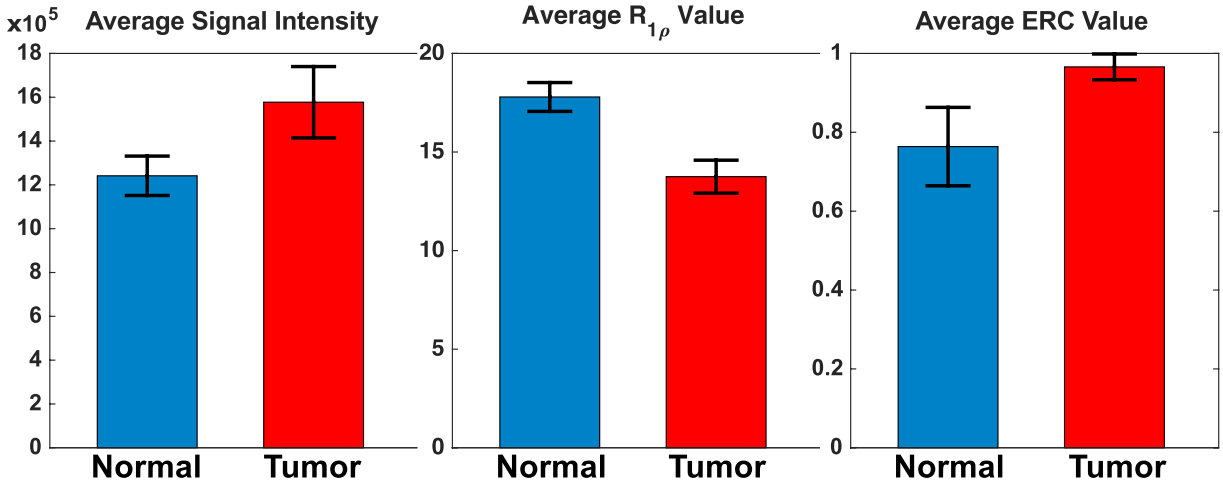

Figure 27: Average intensities for the $R_{1\rho}$ image, the $R_{1\rho}$ map, and the ERC image with error bars representing ± 1 standard deviation. The normal and tumor regions displayed significant contrasts in all images ($p < 0.05$).

All three images exhibited statistically significant contrast ($p < 0.05$) when comparing the two ROI's. The standard deviation in the normal tissue of the ERC image possessed more variability than any of the other measures, which can be qualitatively seen by the image in Figure 26 and the large error bar in Figure 27. That makes the fact the tumor region in the ERC image showed the smallest relative variability of any measure very interesting. Similar behavior can be seen when examining Figure 25b, since the ERC value at the peak displayed extremely small uncertainty and the error bars became larger as the frequency deviated further from the peak value. This may again be attributed to the propagation of error when the image is calculated. When the locking frequency is very low or very high, the relaxation rate will be very close to either R_2 or $R_{1\rho}^{\infty}$. The difference of these values with respect to the intermediate value will theoretically approach zero, and any noise fluctuation can cause large errors in the ERC calculation. On the other hand, at the peak of the ERC, the relaxation rate is as far as possible from both R_2 and $R_{1\rho}^{\infty}$, so noise fluctuations are small in comparison and do not have the same affect in this case. Even though the relative contrast is similar in each image, the ERC image provides the benefit of selectively emphasizing the exchange rate, which neither the $R_{1\rho}$ weighted image or $R_{1\rho}$ map do. Both of these images will be affected by all exchanging species that are sufficiently fast, so the ERC method provides more specificity. Exchange Rate Contrast imaging looks to have ample potential in various imaging applications, especially with chemically exchanging exogenous contrast agents, moving forward.

Conclusions

Chemical exchange has been shown to be a powerful relaxation mechanism, especially at high fields, with the potential to be used to estimate pertinent physiologic parameters such as

temperature and pH with proper calibration, which would be immensely beneficial in cancer imaging. The Chopra and Trott models of the contribution of chemical exchange to $R_{1\rho}$ relaxation are very comparable under most conditions and provide relatively accurate exchange parameter estimates, but overall the Chopra model has been shown to be slightly superior for the experiments performed throughout this thesis. The Chopra model has more general assumptions in its derivation and performed better for the slow and intermediate exchange regimes in general. The low locking field behavior of the Trott model shown in the fitting to pool fraction simulations and glucose solutions may affect exchange rate calculations and influence ERC imaging in practice. For these reasons, the Chopra model was deemed the preferred method, even though the Trott model would be needed for off-resonance spin-locking. The ERC method provided very useful information by emphasizing pools with specific exchange rates. The EWIC method provides a more practical method to calculate parametric images reflecting specific exchange rates, but the derived contrast is made more complicated by the dependence on the spin-lock time used. For relatively small dispersion magnitudes, which will occur with very low concentrations, this EWIC peak shift will be small and may possibly be ignored. Otherwise, the ERC method is much more robust. This method was successful in generating image contrast depicting exchanging glucose in the acidic malignant tissue of a rat brain tumor. The relative contrast was very similar to that available from $R_{1\rho}$ weighted images and $R_{1\rho}$ maps, but this method provided more specificity and looks to have possible potential in various research applications.

CHAPTER 3

Rotating Frame Relaxation in Systems of *n*-Exchanging Pools

Introduction and Theory

Extended Chopra Model

Exchange effects may be exploited at high B_0 field strengths using spin-locking measurements to estimate exchange rates in NMR or to generate variable exchange-based contrasts in MRI (*59*, *68*). The $R_{1\rho}$ dispersion profile exhibits an inflection point at a characteristic frequency determined by the exchange dynamics of the system. For realistic tissues of interest, more than one exchanging species may be present and contribute to the overall relaxation. Systems with multiple exchanging species, each with unique exchange rates and chemical shifts, will produce multi-dispersion $R_{1\rho}$ data that may be fit using an appropriate model to estimate the exchange rates of up to two separate species. Though this process may be expanded for any number of pools, fitting dispersion curves in practice to more than two sets of dispersion parameters becomes too imprecise to estimate the parameter values with any reasonable accuracy. Though more than two sites can theoretically contribute to the overall $R_{1\rho}$ relaxation, often times their effects will be negligible due to low concentrations or very slow exchange. The major species for exchange in tissues are hydroxyls and amides, which form two distinct groupings based on their rates of exchange. Thus, one or two exchange sites may describe $R_{1\rho}$ relaxation in tissues exhibiting exchange *in vivo* in practice, which makes the double dispersion method a relevant and useful extension of the theory.

Two distinct exchanging species (other than bulk water) with different chemical shifts

and exchange rates will produce a double dispersion phenomenon that can be approximated very well by linearly adding individual exchange contributions of the dispersions for small pool fractions, and can be generally extended to *n* exchange pools. Figure 28 schematically shows an arbitrary 3-pool system where each pool possesses unique initial magnetizations, intrinsic relaxation rates, and chemical shifts. Exchange can occur between any pool, but only exchange between the bulk water pool with a solute pool is typically considered since the solute pools are assumed to be small. This assumption implies that exchange between solute pools, referred to as minor exchange, has a negligible effect on the overall relaxation of the system, which is why these arrows and rate constants are labeled in gray.

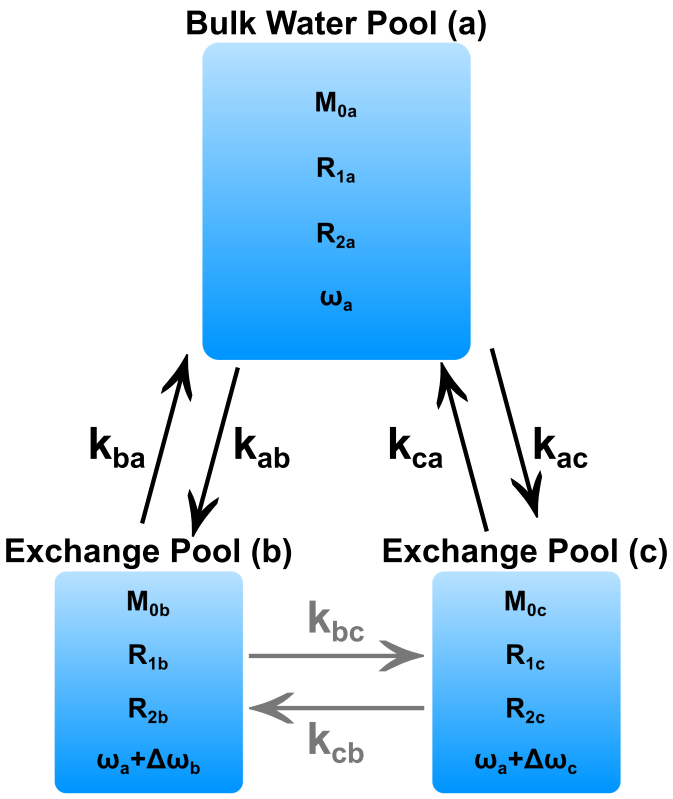

Figure 28: Schematic of an arbitrary 3-pool system with unique initial magnetizations, relaxation rates, and chemical shifts. Arrows and rate constants represent exchange between each pool with minor exchange between solute pools in gray since this is typically ignored.

The Bloch-McConnell equations may be extended to include a third pool by simply adding the corresponding rate constants to account for exchange between all pools to the same component equations (*127*). The 3-pool Bloch-McConnell equations are expressed below.

$$\begin{aligned}
\frac{dM_x^a}{dt} &= \Delta\omega_a M_y^a - R_2^a M_x^a - k_{ab} M_x^a - k_{ac} M_x^a + k_{ba} M_x^b + k_{ca} M_x^c \\
\frac{dM_x^b}{dt} &= \Delta\omega_b M_y^b - R_2^b M_x^b - k_{ba} M_x^b - k_{bc} M_x^b + k_{ab} M_x^a + k_{cb} M_x^c \\
\frac{dM_x^c}{dt} &= \Delta\omega_c M_y^c - R_2^c M_x^c - k_{ca} M_x^c - k_{cb} M_x^c + k_{ac} M_x^a + k_{bc} M_x^b \\
\\
\frac{dM_y^a}{dt} &= -\Delta\omega_a M_x^a - R_2^a M_y^a + \omega_1 M_z^a - k_{ab} M_y^a - k_{ac} M_y^a + k_{ba} M_y^b + k_{ca} M_y^c \\
\frac{dM_y^b}{dt} &= -\Delta\omega_b M_x^b - R_2^b M_y^b + \omega_1 M_z^b - k_{ba} M_y^b - k_{bc} M_y^b + k_{ab} M_y^a + k_{cb} M_y^c \\
\frac{dM_y^c}{dt} &= -\Delta\omega_c M_x^c - R_2^c M_y^c + \omega_1 M_z^c - k_{ca} M_y^c - k_{cb} M_y^c + k_{ac} M_y^a + k_{bc} M_y^b \\
\\
\frac{dM_z^a}{dt} &= -\omega_1 M_y^a - R_1^a \left(M_z^a - M_0^a \right) - k_{ab} M_z^a - k_{ac} M_z^a + k_{ba} M_z^b + k_{ca} M_z^c \\
\frac{dM_z^b}{dt} &= -\omega_1 M_y^b - R_1^b \left(M_z^b - M_0^b \right) - k_{ba} M_z^b - k_{bc} M_z^b + k_{ab} M_z^a + k_{cb} M_z^c \\
\frac{dM_z^c}{dt} &= -\omega_1 M_y^c - R_1^c \left(M_z^c - M_0^c \right) - k_{ca} M_z^c - k_{cb} M_z^c + k_{ac} M_z^a + k_{bc} M_z^b
\end{aligned} \qquad 2.1$$

In Eq. 2.1, $M_0^{a,b,c}$ are the equilibrium magnetizations of each pool. In order to properly extend the previously described Chopra theory, these 3-pool coupled differential equations would need to be solved, which would be very tedious and superfluous. A simpler procedure would be to start by re-writing the Chopra $R_{1\rho}$ equation in Eq. 1.3. Substituting the definitions of R_2, $R_{1\rho}^{\infty}$, and S_ρ^2 back into the equation, a long form expression may be derived that proves to be insightful (*93*).

$$R_{1\rho} = R_2^a + P_b k_{ba}\left(\frac{R_2^b}{R_2^b + k_{ba}}\right)\left\{\frac{\left(R_1^b + k_{ba}\right)\left(R_2^b + k_{ba} + \frac{\Delta\omega_b^2}{R_2^b}\right) + \omega_1^2}{\left(R_1^b + k_{ba}\right)\left(R_2^b + k_{ba} + \frac{\Delta\omega_b^2}{R_2^b + k_{ba}}\right) + \omega_1^2}\right\} \qquad 2.2$$

In Eq. 2.2, the first term is the offset relaxation rate when no exchange is present which is why it relies only on the relaxation rate of the dominant bulk water pool (a). The second term encompasses the entire exchange contribution to $R_{1\rho}$ from the solute pool. Note that R_2^a in the first term is not multiplied by its respective pool fraction, because P_a is assumed to be 1 since the underlying assumptions in the derivation was $P_a \gg P_b$. By keeping this assumption, adding another pool simply means adding a third term to Eq. 2.2 that is almost identical to the second term, with indices corresponding to that exchange pool. Using this strategy, the Chopra equation may be collapsed again to a more compact form that resembles the original theory.

$$R_{1\rho} = \sum_{i=1}^{n}\left\{\frac{R_{2,i} + \frac{R_{1\rho,i}^{\infty}\omega_1^2}{S_{\rho,i}^2}}{1 + \frac{\omega_1^2}{S_{\rho,i}^2}}\right\} - (n-1)R_2^a \qquad 2.3$$

In Eq. 2.3, the $(n-1)R_2^a$ term is subtracted from the sum since only the exchange contributions and not the bulk water relaxation rate need to be added. Eq. 2.3 also assumes there is negligible exchange between solute pools which can be referred to as minor exchange (e.g. $k_{cb} = 0$). This theory will be useful in situations where double dispersions occur to estimate the exchange rates of two different solute pools, but may fall apart when minor exchange is significant. It is noteworthy to point out Trott et al. also derived an $R_{1\rho}$ expression for *n*-pool exchange as an extension of their theory described in chapter 2 (*128*). This was extended further to include an

expression accounting for minor exchange but consists of too many variables to fit for, making it impractical to estimate exchange parameters experimentally. Simulations demonstrating minor exchange effects on spin-locking experiments were performed by Trott et al. but only in the context of its effects on the exchange terms of the Trott model (*128*). To our knowledge, general simulations of minor exchange effects on $R_{1\rho}$ dispersion have not been reported in the literature, and systems with exchange dependent double dispersions have only rarely been mentioned (*97*).

Extended Exchange Rate Contrast

Deriving image contrast based on chemical exchange rates can provide new ways to characterize tissues. One important method for producing such images is using the Exchange Rate Contrast (ERC) method described for 2-pool exchange in chapter 2. The ERC method combined $R_{1\rho}$ values from three locking strengths (0, ω_1, ∞) to derive contrast that exhibited a peak value of 1 when $\omega_1 = \sqrt{k_{ba}^2 + \Delta\omega_b^2}$, and falls off quickly as ω_1 deviates from that value. The ERC theory may be extended to three pools by simply extending the $R_{1\rho}$ equation used in Eq. 1.5 to account for exchange with a second solute pool, in a similar manner to how the Chopra model was extended to 3-pools.

$$R_{1\rho} \approx R_2^a + P_b\left[R_2^b + \frac{k_{ba}\Delta\omega_b^2}{k_b^2 + \Delta\omega_b^2 + \omega_1^2}\right] + P_c\left[R_2^c + \frac{k_{ca}\Delta\omega_c^2}{k_c^2 + \Delta\omega_c^2 + \omega_1^2}\right] \qquad 2.4$$

Eq. 2.4 was simplified by assuming again that $k_{ba} \gg R_2^b \geq R_1^b$, $k_{ca} \gg R_2^c \geq R_1^c$, and $p_a \gg p_b \sim p_c$. The ERC equation was described in chapter 2 and is re-written here for reference.

$$ERC(\omega_1) = 4\frac{\left[R_{1\rho}(0) - R_{1\rho}(\omega_1)\right]\left[R_{1\rho}(\omega_1) - R_{1\rho}(\infty)\right]}{\left[R_{1\rho}(0) - R_{1\rho}(\infty)\right]^2} \qquad 2.5$$

Plugging Eq. 2.4 into Eq. 2.5 and significantly simplifying terms, the 3-pool ERC equation may be written as Eq. 2.6.

$$ERC(\omega_1) = 4\omega_1^2 \beta \frac{\eta\sigma}{\xi^2} \tag{2.6}$$

The terms in this condensed ERC equation may be written out with the defined parameters as shown in Eq. 2.7.

$$\begin{aligned}
\beta &= \frac{\left(k_{ba}^2 + \Delta\omega_b^2\right)\left(k_{ca}^2 + \Delta\omega_c^2\right)}{\left(k_{ba}^2 + \Delta\omega_b^2 + \omega_1^2\right)^2 \left(k_{ca}^2 + \Delta\omega_c^2 + \omega_1^2\right)^2} \\
\eta &= P_b k_{ba} \Delta\omega_b^2 \left(k_{ca}^2 + \Delta\omega_c^2 + \omega_1^2\right) + P_c k_{ca} \Delta\omega_c^2 \left(k_{ba}^2 + \Delta\omega_b^2 + \omega_1^2\right) \\
\sigma &= P_b k_{ba} \Delta\omega_b^2 \left(k_{ca}^2 + \Delta\omega_c^2\right)\left(k_{ca}^2 + \Delta\omega_c^2 + \omega_1^2\right) + P_c k_{ca} \Delta\omega_c^2 \left(k_{ba}^2 + \Delta\omega_b^2\right)\left(k_{ba}^2 + \Delta\omega_b^2 + \omega_1^2\right) \\
\xi &= P_b k_{ba} \Delta\omega_b^2 \left(k_{ca}^2 + \Delta\omega_c^2\right) + P_c k_{ca} \Delta\omega_c^2 \left(k_{ba}^2 + \Delta\omega_b^2\right)
\end{aligned} \tag{2.7}$$

The magnitude of the 3-pool ERC curve will be governed heavily by the frequency spread between the peaks of each separate pool. The spread in ERC peak frequencies may be represented by the effective exchange parameter $\Delta K_{eff} = \sqrt{k_{ba}^2 + \Delta\omega_b^2} - \sqrt{k_{ca}^2 + \Delta\omega_c^2}$, which is simply the difference in the peak positions in Hz. When the concentration of one solute pool is non-existent or negligible, pool c for example, Eq. 2.6 collapses down to Eq. 1.6 and only a single ERC peak will be exhibited. The overall ERC curve will shift and become a function of both individual ERC curves as the concentration of pool c increases until the concentration of the other solute pool (pool b) becomes negligible with respect to pool c. The ERC curve at this point becomes an individual ERC curve and Eq. 2.6 again collapses down to Eq. 1.6 for pool c. The maximum available contrast in ERC is then simply the difference in the individual ERC curves at the locking strength $\omega_1 = \sqrt{k_{ca}^2 + \Delta\omega_c^2}$ where pool c exhibits a peak as shown by the vertical

dotted lines in Figure 29.

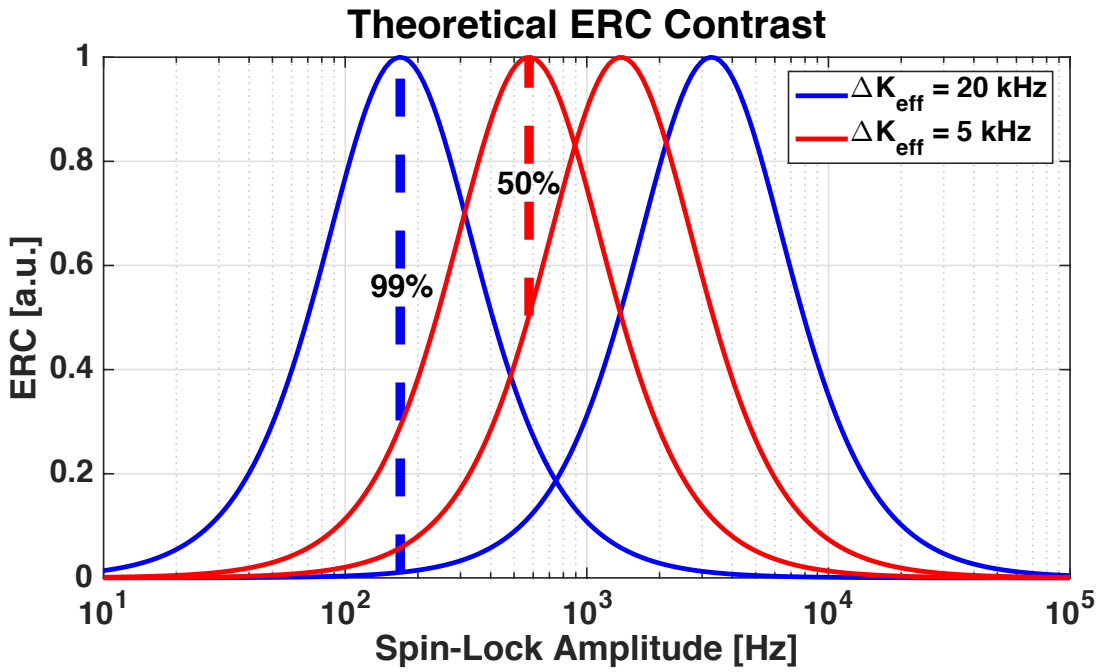

Figure 29: Maximum theoretical ERC contrast is shown to be 99% when the peaks are separated by 20 kHz and only 50% when they are separated by 5 kHz.

The maximum available contrast can then be written as Eq. 2.8.

$$\Delta ERC_{\max} = 1 - 4\frac{\left(k_{ba}^2 + \Delta\omega_b^2\right)\left(k_{ca}^2 + \Delta\omega_c^2\right)}{\left(k_{ba}^2 + \Delta\omega_b^2 + k_{ca}^2 + \Delta\omega_c^2\right)^2} \qquad 2.8$$

Eq. 2.8 equals zero when $k_{ba}^2 + \Delta\omega_b^2 = k_{ca}^2 + \Delta\omega_c^2$ and approaches 1 when the peaks are separated by a large frequency spread and these values become very different.

Specific Aims

Aim 1

To assess 3-pool exchange under various conditions through finite difference Bloch-McConnell simulations. The relative exchange rates between the bulk water pool and the solute pools are the most important parameters in these simulations and scenarios will represent very similar and very disparate exchange rates to elucidate the $R_{1\rho}$ dispersion behaviors. Performing simulations for these scenarios will help qualitatively and quantitatively demonstrate the manner in which these dispersions add and determine if certain experiments are feasible.

Aim 2

Validate the simulated behaviors from Aim 1 by performing spin-locking experiments to acquire dispersions of individual solutions of creatine, glucose, and uracil along with mixtures of creatine with glucose and creatine with uracil. These exchanging species were selected to test the double dispersion fitting method under the two distinct scenarios of mixtures with similar exchange rates (glucose and creatine) and mixtures with very different exchange rates (uracil and creatine). Comparing the dispersions of the individual solutions with the double dispersions of the mixtures should elucidate the manner in which these dispersions add experimentally.

Aim 3

Simulate Exchange Rate Contrast in 3-pool systems through analysis of similar Bloch-McConnell simulations. The ERC curves will be calculated from the corresponding simulated dispersion curves with various theoretical concentrations. The relative position of the dispersion inflection points in a double dispersion curve will have a significant effect on the available contrast in the extended ERC method. In order to quantify how the inflection frequencies impact

the available contrast and provide precedence for determining if experiments are feasible, multiple sets of simulations will be run with varying relative inflection frequencies.

Aim 4

Confirm the simulated behaviors in model systems of glucose and uracil by imaging these solutions with a spin-locking pulse sequence at 7T. ERC images will be calculated from $R_{1\rho}$ maps generated from the spin-locking experiments at the locking frequency corresponding to the ERC peak of glucose to produce image contrast directly related to glucose concentration.

Methods

3-Pool Bloch McConnell Simulations and Experiments

Multiple exchanging populations may each have an effect on both CEST spectra and $R_{1\rho}$ dispersions. Cobb et al. verified the manner in which CEST spectra add for the case of peptide and sugar exchange pools (*98*) and Trott et al. have shown how the exchange dependent contributions to $R_{1\rho}$ change as a function of the population averaged chemical shift (*128*). The effects of chemical exchange on $R_{1\rho}$ dispersion in mixtures are further quantified here using Bloch-McConnell finite difference simulations. Exchange rates of two different species mixed in water were selected to be close together for one scenario (1 kHz and 3 kHz) and far apart in another (1 kHz and 30 kHz) to visually demonstrate the nature in which the dispersion contribution from each species adds for small pool fractions. Simulations were performed using three exchange pools with $p_b = p_c = 1\%$, $\Delta\omega_b = 0.75$ ppm, $\Delta\omega_c = 0.5$ ppm, $R_{1a} = R_{1b} = R_{1c} = 0.1$ Hz, $R_{2a} = R_{2b} = R_{2c} = 0.4$ Hz, $k_{ba} = 1$ kHz, and $k_{ca} = 3$ kHz. The scenario with very different exchange rates assumed $\Delta\omega_b = 0.75$ ppm, $\Delta\omega_c = 1.75$ ppm, and $k_{ca} = 30$ kHz. Furthermore, simulations were conducted with various exchange rates from 0 Hz up to 5 kHz between pools b

and c to determine the degree in which exchange between minor pools affects $R_{1\rho}$ dispersion. The signal magnitudes calculated during the finite difference simulations, with time steps of dt = 10 nanoseconds, were fit to mono-exponential decay functions to determine $R_{1\rho}$ for each of the 30 locking strengths. All simulated $R_{1\rho}$ points were fit to Eq. 2.3 to obtain the double dispersion curve, determine the feasibility of fitting this model to data, and how the fitted parameters compared to the designated simulation parameters in each scenario.

Subsequently, solutions of PBS mixed with 100 mM creatine, 100 mM glucose, 50 mM uracil, and mixtures of 100 mM creatine with 100 mM glucose and 100 mM creatine with 50 mM uracil were prepared and studied at 7T to measure $R_{1\rho}$ dispersions and validate how the dispersions add in practice. The chemical structures of the exchanging species with their hydroxyl, amide, and amine groups are shown in Figure 30.

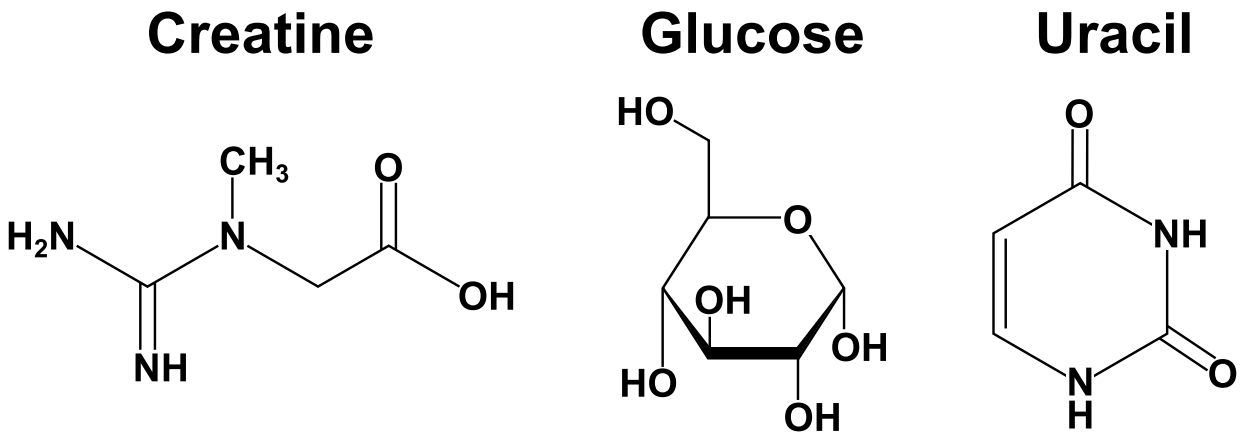

Figure 30: Chemical structures for the creatine, glucose, and uracil metabolites used in the mixture solution experiments.

Glucose shows there are 5 separate hydroxyl groups that will each undergo exchange at their own rate and chemical shift, but the dispersion will effectively represent the average of each site,

which was $\Delta\omega_b$ = 1.5 ppm for glucose (*121*, *129*). Creatine and uracil should display similar behavior, but the average chemical shifts were $\Delta\omega_b$ = 1.8 ppm and $\Delta\omega_b$ = 10.9 ppm respectively (*130–132*). The dispersion curves were acquired at a temperature of T = 37°C to elevate the exchange rates and 10 logarithmically spaced spin-lock amplitudes ranging from 50-10,000 Hz were used, each with five logarithmically spaced spin-lock times ranging from 0.01-1 sec. Each decay curve was fit to a mono-exponential decay model to determine $R_{1\rho}$ at each locking field, and the $R_{1\rho}$ points were fit to Eq. 2.3 to estimate the experimental exchange parameters. The contribution of each species was determined from the double dispersion model and compared to the dispersion curve of the corresponding individual solution since these dispersions should be linearly independent for small pool fractions. This will help to determine to feasibility of this technique for both the similar and disparate exchange rate scenarios.

3-Pool ERC Simulations and Experiments

Bloch-McConnell simulations were performed with two distinct solute pools for ERC analysis. Similarly to the 3-pool $R_{1\rho}$ simulations discussed earlier, only one of the solute pool fractions of (pool c) was varied while the other was held constant. Exchange rates of the two sites were chosen to be k_{ba} = 20,000 Hz and k_{ca} = 500 Hz which were disparate for illustrative purposes. The pool fraction for pool b remained constant at 1% while pool c varied from 0-1% to change the relative magnitudes of each dispersion in the double dispersion curve. Finite difference Bloch simulations were performed with time steps of 2 ns to generate signal decay curves that were subsequently fit to a mono-exponential model to determine $R_{1\rho}$ for 30 locking fields ranging from 40 Hz to 5 kHz. The simulated $R_{1\rho}$ points were fit to Eq. 2.3 to obtain the double dispersion curves that were then analyzed using the ERC equation described in Eq. 2.6. The ERC values were examined for each pool fraction at the spin-lock amplitude of 160 Hz,

since this was the corresponding amplitude that generated the maximum ERC value of 1 for the simulated dispersion of pool c alone. The ERC magnitude was then plotted against the concentration of pool c to obtain the curve depicting the concentration dependence. Taking this concentration dependent curve a step further, more curves were simulated in the same manner but with the ERC peaks at various relative frequency differences. The first ERC curve was simulated to have a peak at $\omega_1 = \sqrt{k_{ba}^2 + \Delta\omega_b^2} = 200$ Hz, with other ERC curves with peaks ranging from 400 – 2,200 Hz to demonstrate the manner in which the maximum available contrast depends on the frequency difference between ERC peaks.

Solutions of 40 mM uracil mixed with concentrations of glucose ranging from 0-200 mM were imaged at 7T using a $R_{1\rho}$ weighted Fast Spin Echo sequence to confirm the ERC simulation behavior experimentally. $R_{1\rho}$ dispersion curves were measured by acquiring 5 images with exponentially spaced spin-lock times ranging from 0.01 – 1 sec for each of the 12 locking amplitudes that were logarithmically spaced from 50 – 10,000 Hz. $R_{1\rho}$ maps were calculated on a voxel by voxel basis for each of the 12 locking strengths assuming a mono-exponential decay model, and the dispersions were then calculated by ROI analysis. The ERC method in Eq. 1.5 was then used to derive a concentration dependent image by using an intermediate locking amplitude of ω_1 = 545 Hz, the peak frequency of the pure glucose ERC curve. ROI analysis quantified the mean ERC intensity in each sample, which was plotted against glucose concentration to obtain the concentration dependence of the ERC.

Results and Discussion

3-Pool $R_{1\rho}$ Simulations and Experiments

Simulations of 3-pool exchanging systems were performed using the 3-pool Bloch-

McConnell equations described in Eq. 2.1. Figure 31a and Figure 31c clearly show the manner in which $R_{1\rho}$ dispersions add as if they were linearly independent of each other.

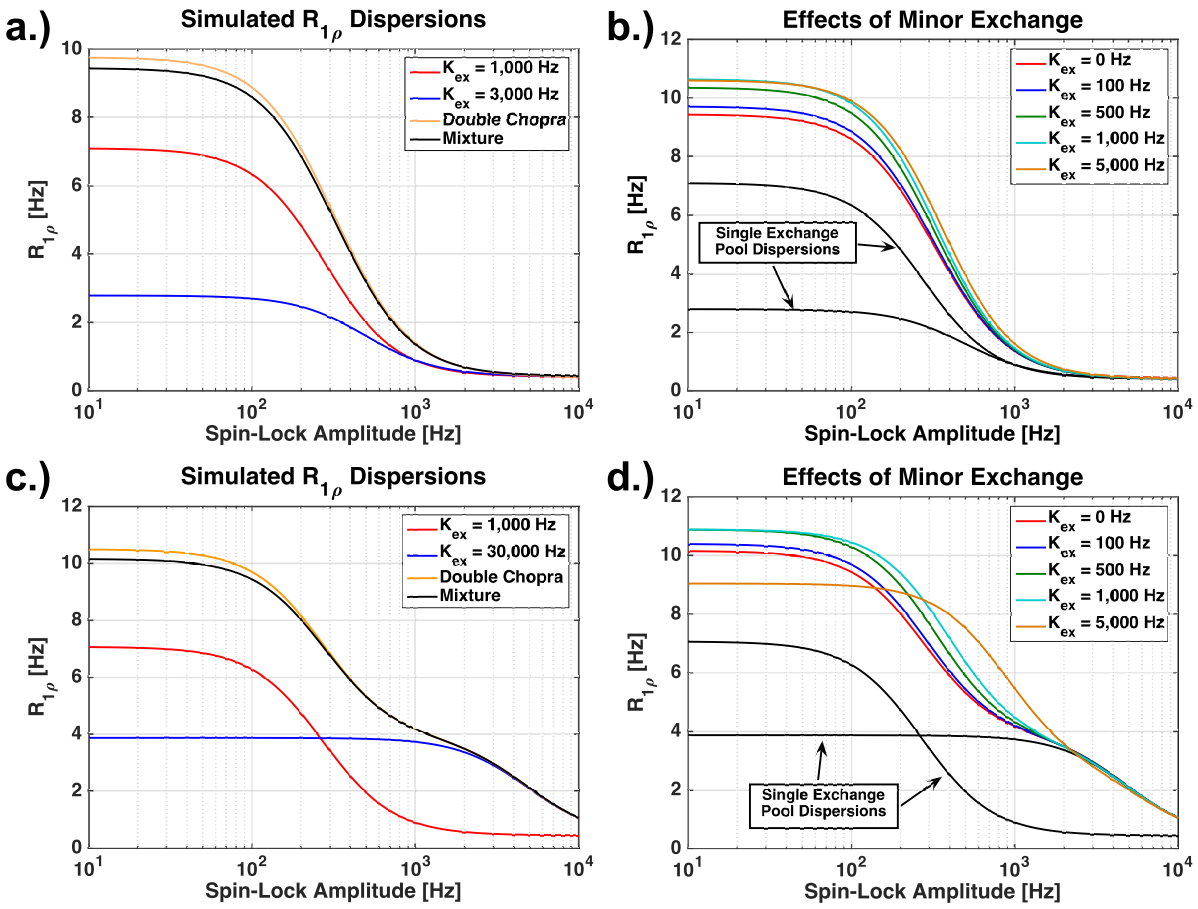

Figure 31: a,c.) Simulated $R_{1\rho}$ dispersions for individual exchange pools (red and blue), with both pools simulated simultaneously (black), which is compared to the addition of the individual curves (orange). b,d.) Simulated $R_{1\rho}$ double dispersions with the addition of minor exchange described by rates of 0 – 5,000 Hz.

The orange curves Figure 31a and Figure 31c represent the addition of the solid red and blue curves in the manner described in Eq. 2.3, which are compared to the simulated black curve. The orange and black curves are not identical as expected due to the discrepancy in the pool fractions between simulations. The individual curves in blue and red each have pool fractions of p_a = 99%

and p_b = 1%, while the black curve has pool fractions of p_a = 98% and $p_b = p_c$ = 1%. The 1% change in bulk water pool fraction accounts for the two curves being unequal at low locking fields. The scenario when solute pools possess similar exchange rates, shown in Figure 31a, may prove too difficult to fit the double dispersion to Eq. 2.3 to extract accurate exchange parameters from each pool since the dispersions overlap so closely. The resulting curve behaves too much like a single dispersion and too much uncertainty is expected in fitting for multiple exchange rates. The other scenario with very different exchange rates, shown in Figure 31c, allows each contribution to be clearly differentiated in the black double dispersion curve. These simulations did not account for the contributions to $R_{1\rho}$ that may occur from the natural abundance of H_2O^{17} (0.037 atomic %), which may slightly affect the low B_1 dispersion, though such effects should be small compared to the exchange effects due to the size of the pool fractions used in the simulation (*133–135*). Fitting this curve to Eq. 2.3 should provide much more accurate exchange rate estimates for both pools.

The simulations revealed the behavior of exchanging systems under various conditions and, even though minor exchange cannot be easily assessed experimentally, Figure 31b and Figure 31d depict the extent of influence minor exchange has on a system as a function of exchange rate. The black curves are the individual contributions and the colored curves represent specific rates of exchange between pools b and c. Figure 31b shows how increasing the minor exchange rate increases the dispersion magnitude and appears to slightly shift the overall dispersion to higher frequencies. This behavior should be expected since a third exchange contribution begins to influence the curve by effectively adding a third dispersion. The influence relies on the fact that pools b and c have different chemical shifts. If the pools had magnetically equivalent environments ($\Delta\omega_b = \Delta\omega_c$), then the change in the dispersion would be less

exaggerated even if the intrinsic pool relaxation rates were different since the chemical shift will dominate these differences at high field. This effect should also decrease with smaller solute pool fractions. The scenario in Figure 31d shows the effect of minor exchange when the individual dispersion inflection points are very easily resolved due to different exchange rates of the pools with the bulk water pool. Minor exchange again mostly affects the low locking field values, but as the minor exchange rate becomes very fast, the dispersions begin to coalesce and appear to be a single dispersion. This occurs due to the fact that the exchange between minor pools is much faster than the exchange between pools a and b (k_{ba}) so when a proton from pool a exchanges to one of the solute pools, it may then bounce back and forth between solute pools and average out their effects. This effect should diminish with pool fraction, and with smaller pool fractions in practice, the minor exchange rate should not be very high in solutions due to the statistical chance of interacting with the bulk water pool would be so much greater than the chance of solute pools interacting. Experimentally, minor exchange cannot be practically measured in a single solution with $R_{1\rho}$ dispersion methods. It may potentially be inferred by measuring the dispersion of the solute components separately, predict the double dispersion, and calculate the difference between the measured and predicted double dispersions, but this would require very significant exchange that will again be improbable for small pool fractions.

Minor exchange was ignored for the experiments performed to measure double dispersions in solutions of 100 mM creatine mixed with either 100 mM glucose or 50 mM uracil. These solutions were selected in order to depict comparable scenarios to Figure 31 with similar and very disparate exchange parameters. Figure 32a and Figure 32c show the measured $R_{1\rho}$ dispersion along with the fitted double dispersion curves from Eq. 2.3 for the individual contributions in blue and red, along with the mixture curve in black.

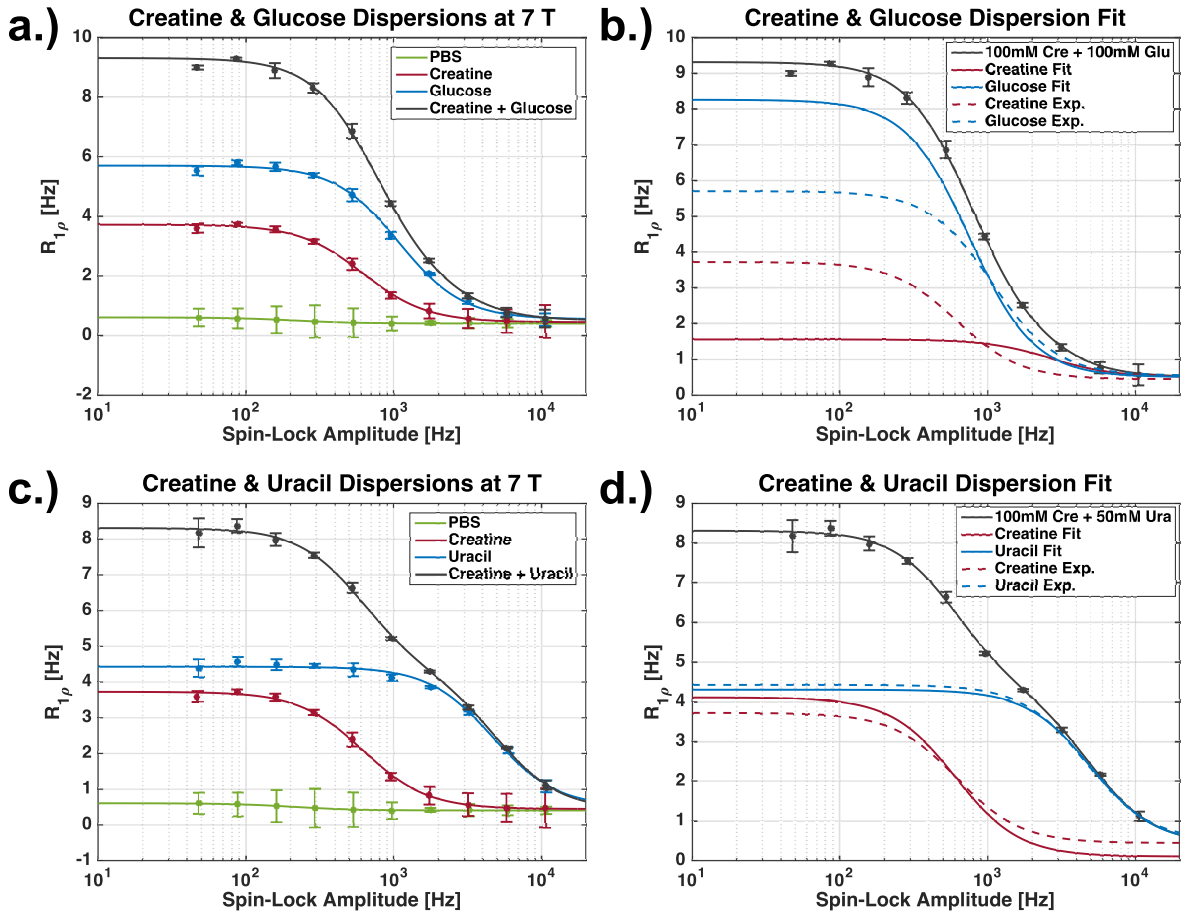

Figure 32: a,c.) Measured R1rho dispersions in solutions of creatine, glucose, and uracil along with double dispersions of corresponding mixtures in black. b,d.) The double dispersion fit for each pool contribution is compared to the individually measured contributions.

These curves were also compared to pure PBS for reference, which should not theoretically exhibit any $R_{1\rho}$ dispersion. It should be noted that the exchange of –NH in uracil is fast, but the large chemical shift of the exchanging sites is ~11 ppm which also causes the dispersion to have such a high inflection point frequency. The double dispersion for the creatine + glucose mixture appears to be a single dispersion since the individual inflections overlap so closely, only separated by 269 Hz. This makes the fitting of each solute contribution very difficult, which is apparent in Figure 32b. The solid blue and red lines representing the fitted contributions of the

two solute pools are very different in magnitude and inflection frequency than the individually measured contributions represented by the dotted red and blue lines. Examining the exchange rates accentuates the shortcomings of this method, since the single dispersion estimate of the creatine exchange rate was k_{ba} = 1,978 Hz and the estimate from the double dispersion fitting was k_{ba} = 20,204 Hz, roughly an order of magnitude different. The single glucose exchange rate was estimated to be k_{ba} = 6,270 Hz, while the double dispersion method estimated a 39% different rate of k_{ba} = 4,241 Hz. This demonstrates how dispersions overlapping too closely will result in a large discrepancy and/or uncertainty in the estimated exchange rates. The double dispersion for the creatine + uracil mixture was much more distinguishable since the inflection points were separated by 2,334 Hz. This allowed a much more accurate fitting of the contributions from each solute pool shown in Figure 32d. The creatine exchange rate estimated from the double dispersion fitting was k_{ba} = 1,945 Hz, only 1.7% different compared to the accepted value of k_{ba} = 1,978 Hz from the single dispersion fit. The estimated uracil rate was k_{ba} = 23,234 Hz which was roughly 10% different than the single dispersion fit of k_{ba} = 21,034 Hz.

3-Pool ERC Simulations and Experiments

The double dispersion method has been shown to be capable of estimating chemical exchange parameters in systems of up to 2 solute pools with reasonably distinguishable dispersion profiles. This analysis may be extended with the exchange rate contrast (ERC) method described earlier for a single solute pool to derive concentration dependent images in mixtures. Simulations were conducted to determine how double dispersion $R_{1\rho}$ curves would influence ERC curves shown in Figure 33.

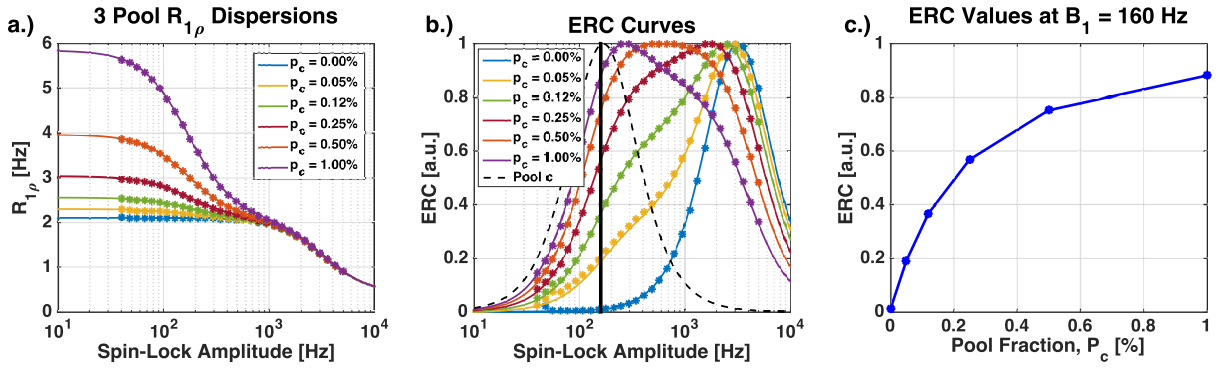

Figure 33: a.) Simulated R1rho dispersions with increasing pool fraction of pc = 0 - 1%. b.) The corresponding ERC curves calculated from the simulated R1rho dispersion curves with the position of the pool c peak shown by the thick black line. c.) The ERC values of all concentrations along the thick black line at the locking field of 160 Hz.

Pool a was assumed to be the bulk water pool, pool b was the constant pool fraction (p_b = 1%) fast exchanging species, and pool c varied in pool fraction from p_c = 0 – 1%. The double dispersions were fit to Eq. 2.3 and plotted in solid lines in Figure 33a, with the resulting ERC curves plotted in solid lines in Figure 33b. The simulated ERC points were calculated by using the fitted asymptotic values for R_2 and $R_{1\rho}^{\infty}$. Figure 33c shows the ERC value for each concentration along the thick vertical black line in Figure 33b, which is the frequency that pool c exhibits an ERC peak. The result is a concentration dependent, monotonically increasing curve quantified by Eq. 2.6 with $\omega_1 = \sqrt{k_{ca}^2 + \Delta\omega_c^2}$ shown below.

$$ERC(p_c) = \left(\frac{k_{ba}^2 + \Delta\omega_b^2}{k_{ba}^2 + \Delta\omega_b^2 + k_{ca}^2 + \Delta\omega_c^2}\right) * \frac{4p_b^2 k_{ba}^2 \Delta\omega_b^2 \left(k_{ca}^2 + \Delta\omega_c^2\right)^3 + p_c k_{ca} \Delta\omega_c^2 \left(k_{ba}^2 + \Delta\omega_b^2 + k_{ca}^2 + \Delta\omega_c^2\right)^2 \left[2p_b k_{ba} \Delta\omega_b^2 \left(k_{ca}^2 + \Delta\omega_c^2\right) + p_c k_{ca} \Delta\omega_c^2 \left(k_{ba}^2 + \Delta\omega_b^2\right)\right]}{\left[p_b k_{ba} \Delta\omega_b^2 \left(k_{ca}^2 + \Delta\omega_c^2\right) + p_c k_{ca} \Delta\omega_c^2 \left(k_{ba}^2 + \Delta\omega_b^2\right)\right]^2} \quad 2.9$$

This curve will have the maximum contrast described by Eq. 2.8, and this contrast will change as

the peaks of the individual ERC curves change. Figure 34b shows the manner in which the concentration dependent ERC function described in Eq. 2.9 changes with peak separation, $\Delta K_{eff} = \sqrt{k_{ba}^2 + \Delta\omega_b^2} - \sqrt{k_{ca}^2 + \Delta\omega_c^2}$.

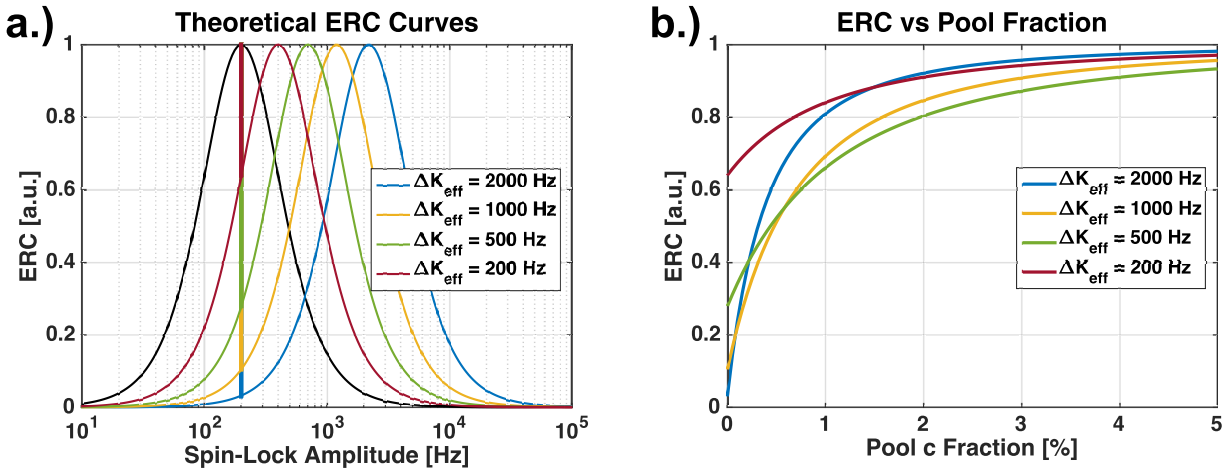

Figure 34: a.) Theoretical ERC curves with peak separations from 200 - 2,000 Hz. b.) The pool fraction dependent ERC values for each pair of ERC peaks.

Less separation between peaks causes the double dispersion to become less discernable which results in less available contrast. The change in contrast is greatest for small pool fractions, and at low pool fractions it is greater for larger peak separations. For example, a change in ERC of 0.25 corresponds to adding Δp_c = 0.15% when ΔK_{eff} = 2,000 Hz, compared to adding a pool fraction of Δp_c = 1.62% for ΔK_{eff} = 200 Hz. This method could potentially be used *in vivo* by injecting a specific concentration of an exchanging species with known exchange parameters to quantify the concentration of an existing metabolite. Since realistic concentrations used in live tissues are typically very low, choosing an exogenous agent with a large chemical shift that exchanges extremely fast would maximize the utility.

Calculating $R_{1\rho}$ maps in solutions of uracil mixed with various concentrations of glucose allows the ERC equations in Eq. 2.5 and Eq. 2.6 to be used to calculated images where the intensity specifically scales with the pool fractions of the solute pools.

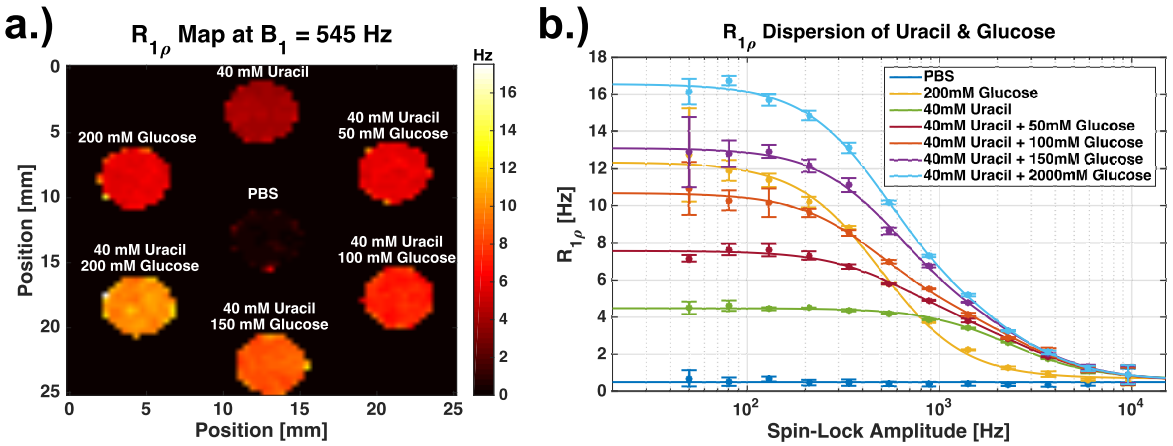

Figure 35: a.) $R_{1\rho}$ map of glucose and uracil solutions at a locking strength of 545 Hz. b.) The corresponding $R_{1\rho}$ dispersion curves of each sample in the $R_{1\rho}$ map calculated from ROI analysis.

Figure 35a shows the $R_{1\rho}$ map of these solutions at the locking amplitude of 545 Hz, since this is the frequency that glucose expresses a peak ERC value, and the dispersions of each mixture solution are plotted in Figure 35b. Note the increase in $R_{1\rho}$ at low locking fields as the concentration of either solute pool changes. Pure PBS (pH = 7.4) was scanned in the middle of the $R_{1\rho}$ map for reference to show there is no dispersion in the relaxation in the absence of exchange. The inflection points of the pure glucose and pure uracil curves occurred at ω_1 = 288 Hz and ω_1 = 1,337 Hz respectively, giving a separation of 1,049 Hz between curves. This means the corresponding ERC curve vs. pool fraction should look very close to the yellow theoretical curve in Figure 34b. ERC images were derived on a voxel by voxel basis and ROI analysis was performed on each sample to calculate the average ERC as a function of glucose concentration

shown below in Figure 36.

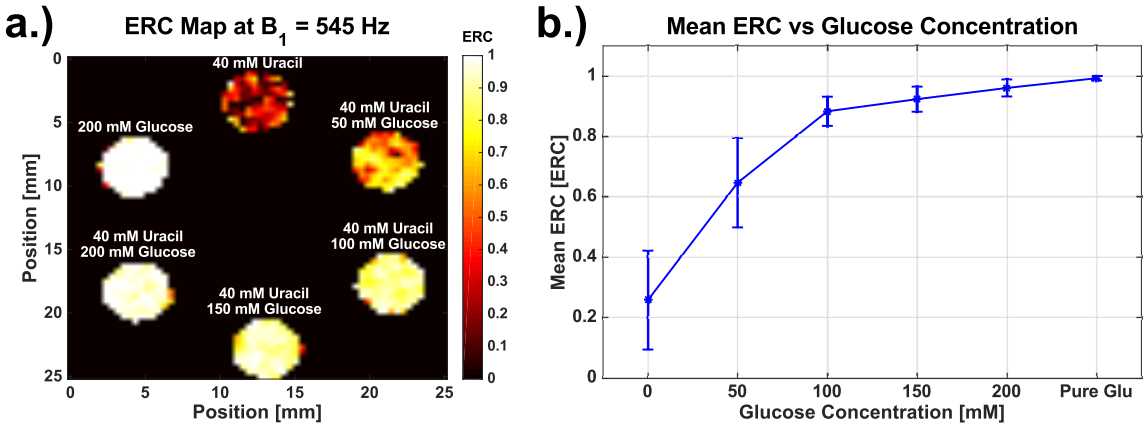

Figure 36: a.) ERC map at a locking strength of 545 Hz emphasizes solutions with glucose due to its exchange rate. b.) The mean ERC values are plotted as a function of glucose concentration.

The utility of this method may be illustrated by observing how the ERC image contrast in Figure 36a is notably different than that in the $R_{1\rho}$ map in Figure 35a. Specifically, the 200 mM glucose sample exhibits a decrease in $R_{1\rho}$ compared to the mixture of 200 mM glucose with 40 mM uracil since this contrast is sensitive to the relaxation caused by both solute pools. The 200 mM glucose sample expresses a higher intensity than the corresponding mixture in the ERC map because this contrast effectively relies on the exchange rate since the intermediate locking field was chosen to be at the glucose ERC peak. The curve in Figure 36b shows the same monotonically increasing concentration dependent behavior simulated in Figure 33c.

Conclusions

Here we conclude 3-pool analysis using $R_{1\rho}$ double dispersion analysis or ERC analysis can be useful in assessing or characterizing tissues in a more realistic manner than a simple 2-pool model. In order to accurately assess a 3-pool system using the techniques described above,

the dispersion curves due to the two solute pools must be sufficiently separated so they are distinguishable. If the curves are indistinguishable, then the system may be analyzed with a 2-pool model to derive average exchange parameters of the solute pools, or another technique may be used like CEST that is more sensitive to the chemical shift differences. Either way, it should be emphasized the entire dispersion is needed for these techniques, not the relaxation rate at only one locking field like a number of studies have done. Exchange between solute pools, or minor exchange, may potentially affect the overall $R_{1\rho}$ dispersion curve significantly when the exchange is fast compared to the exchange between the solute pools and the bulk water pool. This is thought to be very unlikely in most practical tissues since the concentrations of the solute pools will be very small compared to the water pool, so any effects will be small or negligible in these systems. The ERC method was shown to be powerful in chapter 2 by providing the ability to emphasize metabolites based on their exchange rates, but an even greater advantage exists for this method in a 3-pool system. The ability to derive concentration dependent image contrast was shown to be feasible in model systems of glucose and uracil, meaning this method may be potentially useful by injecting a contrast agent such as uracil with a very high $R_{1\rho}$ inflection point. It should be noted that the ERC method cannot be used to derive concentration dependent images in a system with only 1 solute pool, since there will be no shift in the ERC peak with an increase in concentration. It should also be pointed out that these results were obtained by increasing the glucose concentration to 200 mM, which is very high considering normal blood glucose levels are roughly 5-6 mM in the blood (*136*, *137*) and roughly 1 mM in the brain (*138*–*140*). Future studies should look into quantifying the minimum dispersion separation needed to make this method viable and testing the feasibility of these techniques *in vivo* in healthy and diseased tissues.

This approach was successful in distinguishing solute pools based on exchange rates, but does not possess the same spectral selectivity of other techniques like CEST. $R_{1\rho}$ dispersion may present notable advantages when compounds exist that have the same side groups, e.g. amides, but different exchange rates. Moreover, for fast exchanging hydroxyls, the problem of separating the resonance from water does not arise. The derived ERC image contrast surpasses the available contrast available from standard CEST MTR asymmetry techniques for many scenarios, and has potential for in vivo studies with an injectable contrast agent of an exchanging species. This technique eliminates common experimental problems encountered with CEST such as the possibility of direct water saturation while attempting to saturate protons with small chemical shifts and asymmetric CEST spectra that confound accurate MTR asymmetry calculations due to NOE effects (*119*, *141*, *142*). CEST experiments have been used to examine glucose metabolism in a similar manner to FDG-PET by injecting natural D-glucose or an analogue such as 2-deoxy-D-glucose (2DG) as an exogenous contrast agent to analyze the increase in hydroxyl exchange after cellular glucose uptake (*143–148*). In the following chapter, the advantages of spin-locking experiments over CEST are demonstrated to provide more robust measurements of either glucose analogue since they are more adept in quantifying fast hydroxyl exchange.

CHAPTER 4

Detection of Exogenous Contrast Agents Using Spin-Locking Pulse Sequences in Model Systems and in vivo

Introduction and Theory

Monitoring glucose metabolism in tissues with MRI would significantly aid in the detection, characterization, and evaluation of treatment efficacy in solid tumors. New cancer treatments often target glucose metabolism since one of the key features of cancer cells is how they increase metabolism through aerobic glycolysis in order to proliferate more efficiently (*149*, *150*). Glucose metabolism unfortunately cannot be directly measured or even inferred from simple relaxometry measurements, but utilizing 2-Deoxy-D-Glucose (2DG) as an exogenous contrast agent offers a potential work around to indirectly imply levels of glycolysis (*151*). 2DG is typically taken up by cells in a similar manner as glucose and subsequently phosphorylated by hexokinase but not metabolized further due to the missing hydroxyl group compared to glucose (*148*). Unlike glucose, which is phosphorylated into glucose-6-phosphate and then converted into fructose-6-phosphate, 2-deoxyglucose-6-phosphate cannot be converted to fructose-6-phosphate so its metabolism ceases (*152*). The result is an accumulation of trapped 2-deoxyglucose-6-phosphate in the cells that alter spin-locked relaxation rates through fast hydroxyl chemical exchange. The mechanism 2DG uses is very similar to that used in FDG PET imaging studies which has already been worked into RECIST 1.1 (*153*), but 2DG MRI is potentially a safer alternative since it uses no radioactive tracers. The ^{18}F-2-deoxy-2-fluoro-D-glucose used in FDG PET is a labeled radioactive tracer is also taken up an trapped in cells and emits two 511 keV photons that may be measured by a ring of detectors, but the radioactivity prevents it from being

reused in patients and the short lived isotopes require a coordinated effort between production, administration, and imaging to be successful (*154*). Other radioactive labeled versions of 2DG, such as that labeled with ^{13}C, have been used for similar purposes, but each method suffers from the same problems as FDG PET (*152*, *155*). Chemical Exchange Saturation Transfer (CEST) studies have already utilized 2DG to successfully monitor glucose uptake and even distinguish tumor types by measuring the attenuated water signal caused by the exchange with labile protons that have been saturated with off-resonance saturation pulses (*146*, *148*). There are conflicting reports about whether this can be done with regular D-glucose, since one study reported that blood glucose levels remain elevated 30 minutes after the glucose infusion ends while another study reports glucose levels drop immediately after terminating the infusion or after a bolus injection (*147*, *148*). Here, $R_{1\rho}$ dispersion methods are employed to assess the detection of 2DG in model systems and *in vivo*.

$R_{1\rho}$ dispersion methods have been shown to be capable of deriving image contrast that emphasizes exchanging metabolites of specific chemical exchange rates and chemical shifts. In order to compare $R_{1\rho}$ dispersion imaging methods with those of CEST for the exceedingly low concentrations expected *in vivo*, $R_{1\rho}$ contrast needs to be defined.

$$R_{1\rho}\ \text{contrast} = \frac{S(\text{high}) - S(\text{low})}{S_0} \tag{3.1}$$

In Eq. 3.1, S represents the signal intensity at either high or low locking amplitude and S_0 is the signal intensity when no locking amplitude is applied during the spin-lock pulse cluster. The signal intensity of the $R_{1\rho}$ contrast will be heavily influenced by chemical exchange effects and provides a more appropriate measure to compare to CEST than ERC at low concentrations.

Similarly, a CEST contrast may be defined by using $MTR_{asymmetry}$ analysis of a CEST z-spectrum acquired by measuring signal as a function of a saturation pulse frequency (*156*).

$$\text{CEST contrast} = \frac{S(\text{reference}) - S(\text{label})}{S_0} \qquad 3.2$$

In Eq. 3.2, S represents the image intensity at either the resonance-offset frequency of the 2DG peak or the frequency corresponding to the symmetric point on the opposite side of the water peak and S_0 represented the signal in the absence of a saturation pulse. These measures could be quantitatively evaluated to compare the available contrast from each technique.

Specific Aims

Aim 1

CEST has become very widely used within the MR community over the past decade for its spectral selectivity and ease of use. $R_{1\rho}$ dispersion methods potentially provide complementary information that could supplement or maybe replace the need for CEST acquisitions in certain cases. In order to assess the theoretical ability of each technique to detect 2DG, numerical simulations will be performed to compare the available $R_{1\rho}$ and CEST contrasts.

Aim 2

Quantifying glucose metabolism in live tissues would drastically improve magnetic resonance based cancer imaging methods. The current gold standard for measuring glucose uptake in vivo is by using FDG-PET, which relies on short-lived radioactive isotopes to directly measure trapped FDG. MR methods such as spin-locking and CEST have been proposed to detect the glucose analogue, 2DG, that would provide similar information as FDG-PET. Here the ability of $R_{1\rho}$ dispersion and CEST techniques will be evaluated for detecting 2-Deoxy-D-

Glucose in model systems and ex vivo tissue homogenates.

Aim 3

Simulations and model systems provide ideal ways to control the conditions and environments of the proposed experiment, but systems *in vivo* may present multiple factors that could potentially affect the experimental measurements. Here, the abilities of both $R_{1\rho}$ dispersion and CEST to assess glucose uptake in rat brains in vivo are evaluated at 7T by imaging the brain before and after a 2DG injection.

Methods

Numerical $R_{1\rho}$ and CEST Simulations

The effects of 2DG hydroxyl exchange on both $R_{1\rho}$ dispersion and CEST need to be theoretically confirmed. Realistic tissue simulations were implemented by employing slightly modified 3-pool Bloch McConnell equations described below in MATLAB with a bulk water pool (pool a), a solid component pool (pool b), and a 2DG solute pool (pool c) (*157*).

$$
\begin{aligned}
\frac{dM_x^a}{dt} &= -\left(\omega_{rf} - \Delta\omega_a\right)M_y^a - R_2^a M_x^a - k_{ac}M_x^a - k_{ab}M_x^a + k_{ca}M_x^c \\
\frac{dM_x^c}{dt} &= -\left(\omega_{rf} - \Delta\omega_c\right)M_y^c - R_2^c M_x^c - k_{ca}M_x^c + k_{ac}M_x^a \\
\frac{dM_y^a}{dt} &= \left(\omega_{rf} - \Delta\omega_a\right)M_x^a - R_2^a M_y^a + \omega_1 M_z^a - k_{ac}M_y^a - k_{ab}M_y^a + k_{ca}M_y^c \\
\frac{dM_y^c}{dt} &= \left(\omega_{rf} - \Delta\omega_c\right)M_x^c - R_2^c M_y^c + \omega_1 M_z^c - k_{ca}M_y^c + k_{ac}M_y^a \\
\frac{dM_z^a}{dt} &= -\omega_1 M_y^a - R_1^a\left(M_z^a - M_0^a\right) - k_{ac}M_z^a - k_{ab}M_z^a + k_{ca}M_z^c + k_{ba}M_z^b \\
\frac{dM_z^b}{dt} &= -R_1^b\left(M_z^b - M_0^b\right) - k_{ba}M_z^b + k_{ab}M_z^a - WM_z^b \\
\frac{dM_z^c}{dt} &= -\omega_1 M_y^c - R_1^c\left(M_z^c - M_0^c\right) - k_{ca}M_z^c + k_{ac}M_z^a
\end{aligned}
\qquad 3.3
$$

In Eq. 3.3, the components are the same as in previous chapters with ω_{rf} quantifies the off-resonance frequency of the saturation pulse and W in the z-component of the solid pool was the saturation rate of that pool, which is expressed below in Eq. 3.4 for specific relaxation times of the tissue (*158–160*).

$$W = \pi\omega_1^2 \int_0^{\pi/2} d\theta \sin(\theta) \sqrt{\frac{2}{\pi}} \frac{T_2^b}{\left|3\cos^2(\theta)-1\right|} e^{\left(-2\left[\frac{2\pi\omega_{rf}T_2^b}{3\cos^2(\theta)-1}\right]^2\right)} \quad 3.4$$

Chemical exchange was assumed to be present between the bulk water pool and 2DG, magnetization transfer (MT) was assumed to be present between bulk water and the solid component, and no chemical exchange occurred between the solid component and the 2DG pool. The 2DG solute pool relaxation times were $T_1^c = 1/R_1^c$ = 1.5 sec and $T_2^c = 1/R_1^c$ = 15 ms with a chemical shift of $\Delta\omega_c$ = 1 ppm, while the solid component relaxation times were $T_1^c = 1/R_1^c$ = 1.5 s and $T_2^c = 1/R_1^c$ = 15 μs with a chemical shift of $\Delta\omega_b$ = 1 ppm and an exchange rate of k_{ba} = 25 Hz. The $R_{1\rho}$ and CEST contrasts defined above were numerically evaluated for range of values for the exchange rate (k_{ca} = 1 – 5 kHz), 2DG pool fraction (p_c = 0.5 – 2.5%), water longitudinal relaxation time ($T_1^a = 1/R_1^a$ = 0.5 – 2.5 s), water transverse relaxation time ($T_2^a = 1/R_2^a$ = 20 – 100 ms), and solid component pool fraction (p_b = 3 – 15%). One parameter was varied at a time with the default parameters being k_{ca} = 2 kHz, p_c = 1%, T_1^a = 1.5 s, T_2^a = 60 ms, and p_b = 9%. $R_{1\rho}$ dispersions were simulated with 6 spin-lock times ranging from 1 – 100 ms for each of the 7 locking amplitudes logarithmically spaced from 10 – 10,000 Hz, and $R_{1\rho}$ contrast was calculated assuming the *S*(high) was the signal from the locking amplitude of 10,000 Hz and *S*(low) was the signal from the locking amplitude of 100 Hz at a locking time of 40 ms. $R_{1\rho}$ values were calculated by fitting the simulated decay curves to a simple monoexponential decay model.

CEST Z-spectra were calculated by sweeping through a frequency offset range of -5 – 5 ppm (-1,500 Hz – 1,500 Hz at 7T) in 61 increments of 0.167 ppm (50 Hz at 7T) with a 1 μT (42.6 Hz) saturation pulse power lasting 2 sec. CEST contrast was calculated using Eq. 3.2 by assuming *S*(reference) was the signal for the -1 ppm (-300 Hz at 7T) offset, *S*(label) was the signal from the 1 ppm (300 Hz at 7T) offset. The resulting $R_{1\rho}$ contrasts and CEST contrasts were plotted and analyzed to determine which method offered more contrast due to exchange with the 2DG pool.

$R_{1\rho}$ and CEST Measurements in Model Systems of 2DG

Experimental confirmation of the ability of $R_{1\rho}$ and CEST techniques to quantify exchange effects due to 2DG was needed for validation. In order to test and compare the imaging techniques, model systems of simple 2DG solutions in phosphate buffered saline (PBS) and rat brain tissue homogenates mixed with 2DG solution were prepared and imaged. The 2DG solutions were prepared at concentrations of 50 – 150 mM with 0.05 mM $MnCl_2$ to shorten T_1 and T_2, and titrated to a pH of 7.0. The homogenate samples were prepared by excising fresh brain tissue from Sprague-Dawley rats, washing the tissue with ice-cold PBS, and subsequently homogenized in various concentrations of buffered solutions of 2DG so the final concentrations ranged from 0 – 100 mM. $R_{1\rho}$ dispersions were measured in both model systems at 7T using a single shot echo-planar imaging (EPI) sequence with TR = 2 s, FOV = 30mm x 30mm (64x64 matrix), a bandwidth of 250 kHz, an echo time of 50 ms, and a slice thickness of 2 mm. The 2DG solutions were imaged with 5 locking times ranging from 1 – 100 ms for each of the 9 logarithmically spaced locking amplitudes ranging from 100 – 10,000 Hz before ROI analysis was performed and the signals were fit to a monoexponential decay curve to estimate $R_{1\rho}$ at each locking field. The homogenates were imaged using 6 logarithmically spaced locking times from 20 ms to 1 s for each of the 9 locking amplitudes from 100 – 10,000 Hz again. $R_{1\rho}$ contrast was

calculated as a function of 2DG concentration by using *S*(low) and *S*(high) to be the images at locking powers of 100 Hz and 3,160 Hz respectively, each with a locking time of 50 ms for all dispersion curves. CEST Z-spectra were acquired for the 2DG solutions with the same saturation powers as described in the simulations, and CEST contrast was calculated as a function of 2DG concentration. The resulting dispersions, Z-spectra, $R_{1\rho}$ contrasts, and CEST contrasts were all plotted and analyzed to determine which method provides superior contrast experimentally.

$R_{1\rho}$ and CEST Measurements in Rat Brains in vivo

The model systems examined possessed high concentrations that are unlikely in live tissues, so rat brains were imaged *in vivo* before and after being infused with 2DG. Five Sprague-Dawley rats were imaged at 7T, four healthy rats and one that had been inoculated with a 9L tumor. The rats were prepped by inserting a polyethylene catheter (PE50) into the tail vein, they were anesthetized with a 2%/98% isoflurane/oxygen mixture, and the temperature and respiration were monitored with an animal physiologic system. The internal temperature was measured by a rectal thermometer and held constant at 37 °C by a warm-air feedback system. The imaging of the rats began 20 minutes before the infusion with the same single shot EPI sequences and imaging parameters described above for the 2DG phantom experiments to measure $R_{1\rho}$ dispersions and CEST Z-spectra. Subsequently the rats were given a 3 mL bolus injection of 0.5 M 2DG solution followed by a slow infusion of 2 mL/hour for 90 minutes through the tail vein catheter. $R_{1\rho}$ dispersions and CEST Z-spectra were continually collected with the same imaging parameters for 90 minutes after the start of the infusion and $R_{1\rho}$ contrast and CEST contrast were calculated at each time point to generate a time course curve that should theoretically reflect the 2DG tissue concentration.

Results and Discussion

Numerical $R_{1\rho}$ and CEST Simulations

MR methods such as $R_{1\rho}$ dispersion and CEST allow indirect detection of the glucose analogue through their sensitivity to the chemical exchange mechanism. Both $R_{1\rho}$ and CEST methods have been successfully confirmed to be sensitive to changes in 2DG concentration through simulations that vary different exchange parameters shown below in Figure 37.

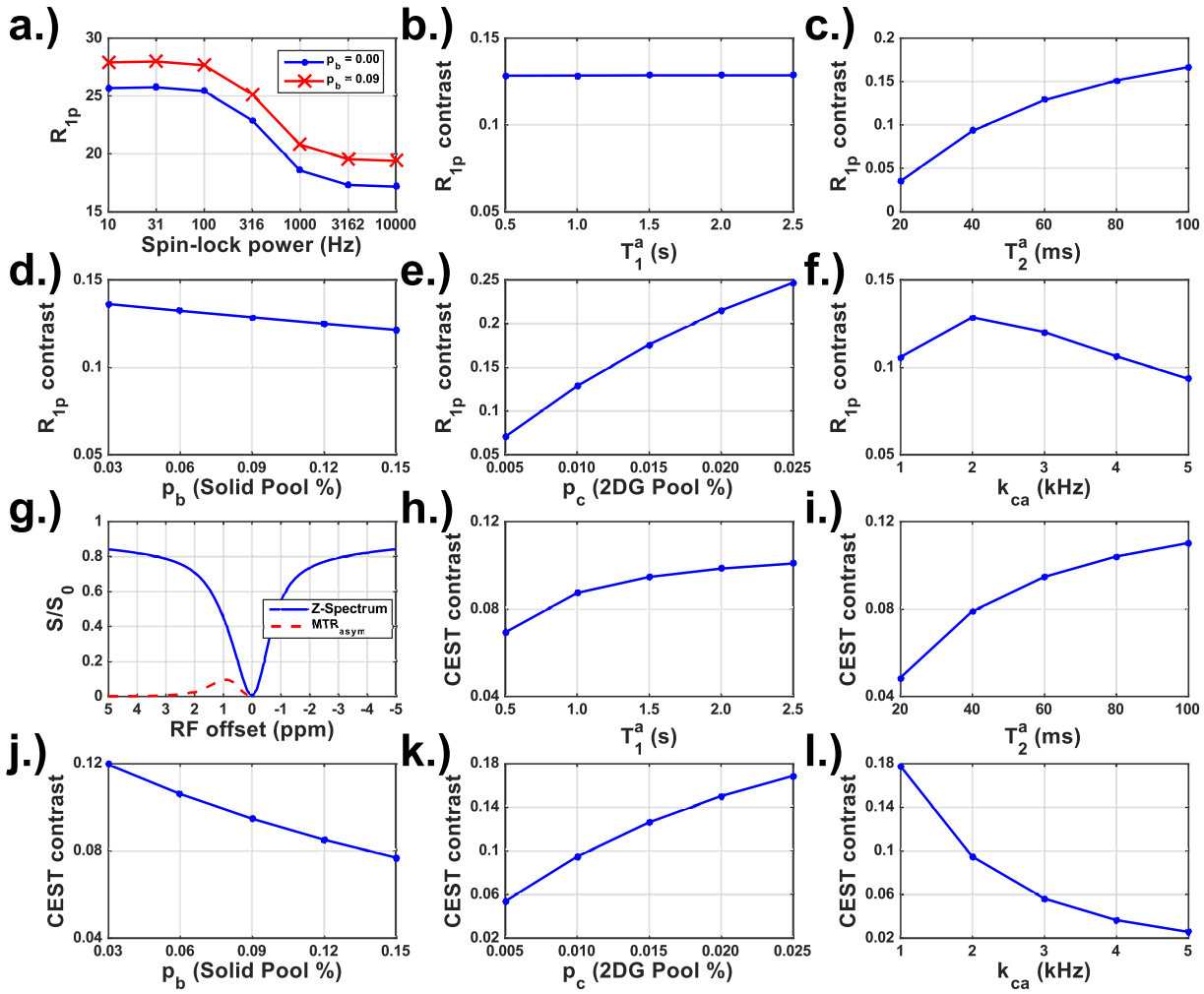

Figure 37: Simulated $R_{1\rho}$ dispersions and $R_{1\rho}$ contrasts plotted as functions of various exchange parameters (a-f). Z-spectra and CEST contrasts plotted as a function of the same exchange parameters for comparison (g-l).

The $R_{1\rho}$ contrast showed sensitivity to all the tested parameters except T_1^a, while CEST contrast was sensitive to all parameters tested. The $R_{1\rho}$ contrast curves generated higher contrast than the simulated CEST contrast curves in almost every point for each of the simulated parameters. $R_{1\rho}$ contrast displayed a greater positive change and magnitude than CEST contrast for T_2^a and p_c, and exhibited a smaller negative change in contrast and greater magnitude as a function of p_b. Though the greater contrasts were favorable, the fact that $R_{1\rho}$ exhibited greater changes to the T_2^a and p_c parameters may be argued as being a negative aspect of the technique since this shows the method may be changed by a number of factors that may influence experimental results. It should be pointed out that CEST contrast exhibited a greater change in contrast for all other simulated parameters though. The behavior of the contrast equations with respect to changing the exchange rate showed that CEST contrast does offer greater sensitivity at low exchange rates while $R_{1\rho}$ contrast quickly overcomes CEST and offers better contrast at fast exchange rates. This behavior and the manner in which the $R_{1\rho}$ contrast displays a maximum at a specific exchange rate before beginning to decrease at faster exchange rates were both predicted in chapter 2. Eq. 1.8 shows that the maximum $R_{1\rho}$ dispersion magnitude, and hence R_1 contrast, will be a function of the intrinsic chemical shift ($\Delta\omega_c$) and transverse relaxation rate (R_2^c). The ratio $\frac{k_{ca}}{\Delta\omega_c} \approx 6.7$, which put the exchange in the intermediate to fast regime and the corresponding Z-spectrum results in very close overlapping dips that produce a small MTR_{asym} curve. Experimentally there would be a risk of direct water saturation while attempting to saturate the solute pool, which could make estimating accurate exchange parameters more difficult. This did not negatively impact the $R_{1\rho}$ contrast since the method does not rely on distinguishing the solute pool on the chemical shift, but was rather shown to work very well in this exchange regime in

chapter 2. Since CEST was shown to be affected by more exchange parameters and generate lower CEST contrast than the competing $R_{1\rho}$ contrast for the majority of the simulations, the $R_{1\rho}$ dispersion method was shown to outperform the CEST for the theoretical case of 2DG chemical exchange. CEST contrast would most likely outperform $R_{1\rho}$ with slower exchanging exogenous agents, but 2DG exchange under physiologic conditions is better assessed with $R_{1\rho}$.

$R_{1\rho}$ and CEST Measurements in Model Systems of 2DG

Model systems of both liquid 2DG solutions and rat brain tissue homogenates were prepared with various concentrations of the glucose analogue to determine how it affected both $R_{1\rho}$ contrast experimentally, which is shown in Figure 38.

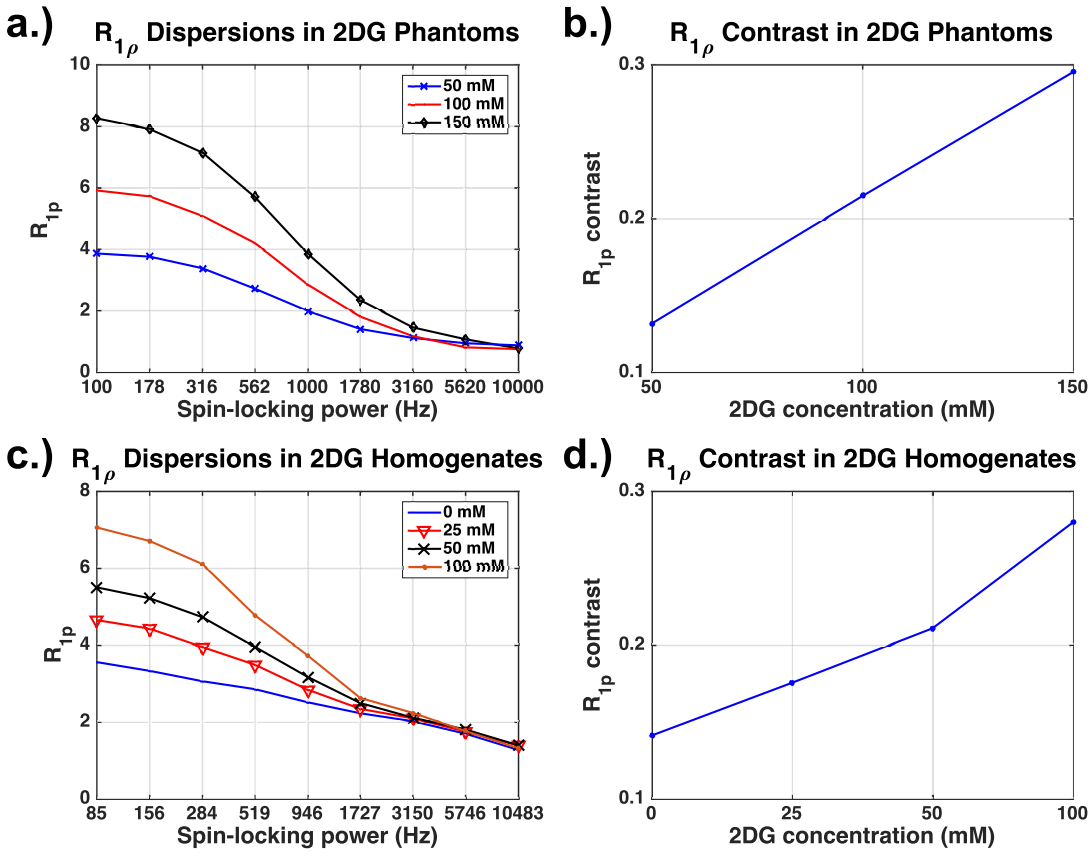

Figure 38: $R_{1\rho}$ dispersions for 2DG phantoms and homogenates at various concentrations (a,c). The corresponding $R_{1\rho}$ contrasts plotted as a function of 2DG concentration (b,d).

The phantom solutions of 2DG displayed roughly a linear increase in $R_{1\rho}$ contrast as a function of concentration, and the homogenates displayed a similar behavior at concentrations below 100 mM. The homogenate samples displayed an interesting behavior at high locking fields where they appear to form a double dispersion that remains constant with 2DG concentration. This may be due to other existing metabolites in the tissue, but this should not negatively affect the calculations since multiple pools were shown to produce linearly independent dispersions. The corresponding Z-spectra and CEST contrasts are shown below in Figure 39 for the 2DG phantoms.

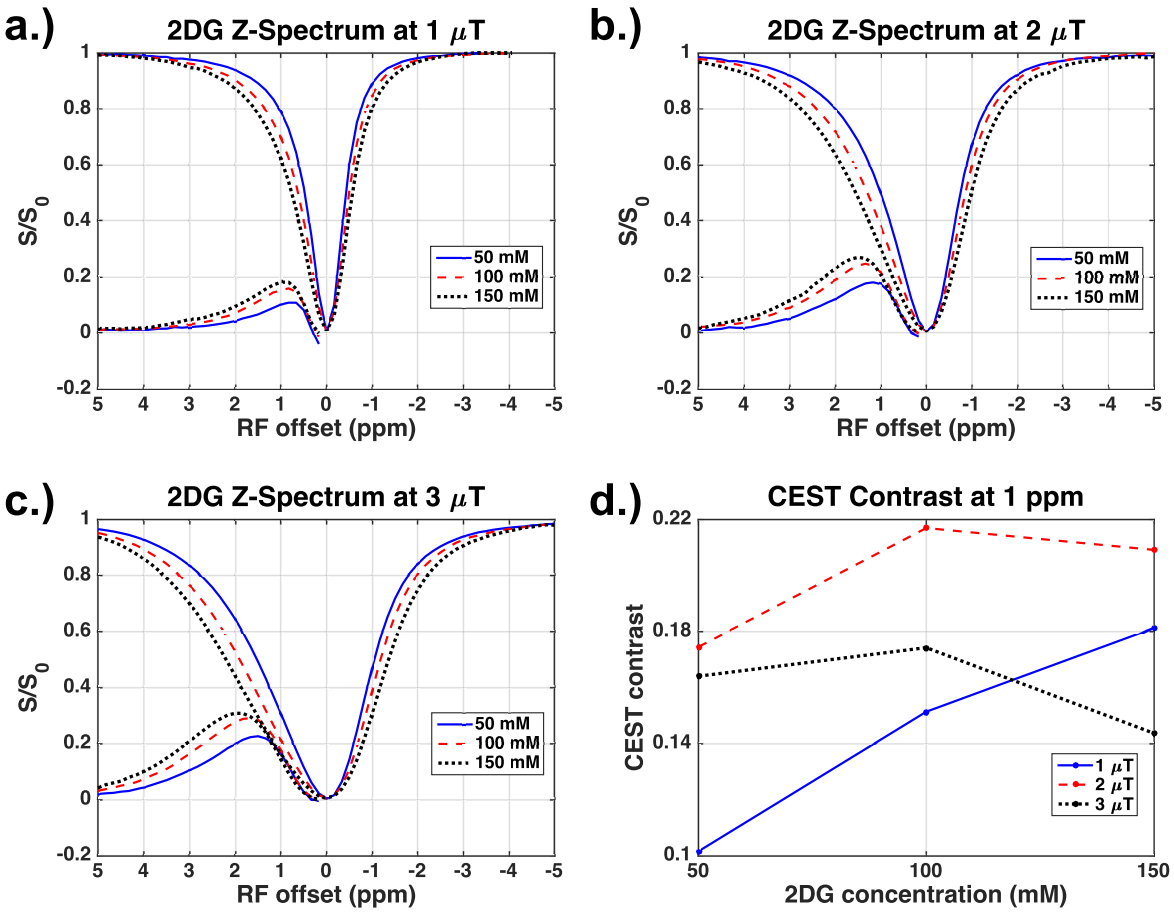

Figure 39: CEST Z-spectra with pulse powers of 1, 2, and 3 T for 2DG phantoms with concentrations of 50, 100, and 150 mM (a,b,c). The corresponding CEST contrasts are plotted as a function of 2DG concentration (d).

The CEST data are shown at the saturation pulse powers of 1, 2, and 3 μT for all three concentrations, and display a broadening dip in the Z-spectra at higher saturation powers. This broadening shifts the peaks of the MTR_{asym} curves due to greater direct water saturation and hence affects the CEST contrast calculations shown in Figure 39d. The CEST contrast calculations were done at an offset of 1 ppm and did not display the same linear behavior as the previously analyzed $R_{1\rho}$ contrast. The 1 μT saturation pulse produced a nearly linear CEST contrast dependence on 2DG concentration, but exhibited a smaller magnitude and slope than the $R_{1\rho}$ method since stronger irradiation pulses are required to efficiently saturate fast exchanging protons. This conflict between efficiently saturating the solute protons without directly saturating the water protons may be optimized to find the most advantageous power, but this will almost always produce less contrast compared to $R_{1\rho}$ contrast protons in the fast exchange regime. The higher power saturation pulses generate CEST contrast curves that appear to reach a maximum and begin to decrease due to the water saturation. This peak appears to occur at lower concentrations for higher powers due to the direct water saturation, which means CEST contrast works best while utilizing low irradiation powers for very low concentrations of 2DG. The $R_{1\rho}$ contrast did not display power dependence and worked well for the same range of concentrations, showing this method is more suitable for the fast hydroxyl exchange exhibited by the 2DG systems examined here.

$R_{1\rho}$ and CEST Measurements in Rat Brains in vivo

Imaging tissues in live animals presents new problems including physiologic motion that can result in image artifacts and low metabolite concentration that may make indirect detection with $R_{1\rho}$ or CEST methods difficult. For these reasons, maximizing contrast becomes paramount *in vivo* for any purpose. $R_{1\rho}$ and CEST methods were used to examine rat brains *in vivo* during a

constant slow infusion of 2DG through a tail vein injection. $R_{1\rho}$ dispersions, Z-spectra, and the time courses of $R_{1\rho}$ and CEST contrasts are plotted below in Figure 40.

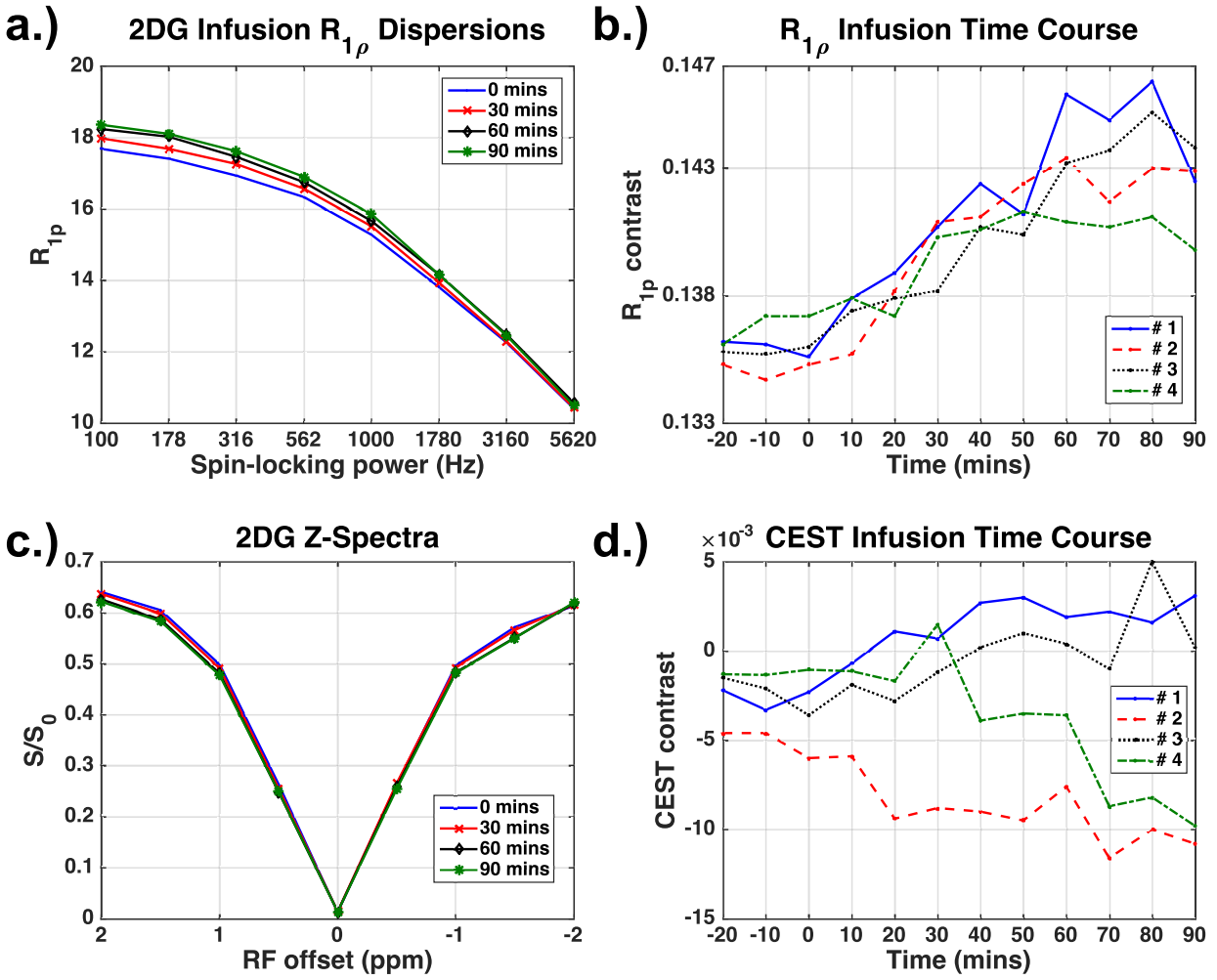

Figure 40: The $R_{1\rho}$ dispersions and Z-spectra are plotted for 4 time points for rat #1 (a,c). The corresponding $R_{1\rho}$ and CEST contrasts are plotted for all 4 healthy rats as a function of time (b.d).

The changes in both the $R_{1\rho}$ dispersion curves and Z-spectra were very small due to the low concentrations in the tissue at any given time. This is reflected in the very small changes in the $R_{1\rho}$ and CEST contrasts shown in Figure 40b and Figure 40d respectively. The CEST time courses displayed such minute changes, no conclusions could be confidently drawn and the

curves were not reliably repeatable. The $R_{1\rho}$ contrast time course curves were repeatable and displayed a constant increase in contrast for the first hour before leveling off. The contrast curves expressed much greater magnitudes than the CEST contrast curves and changed by an average of $7.5x10^{-3}$ over the first 60 minutes where they continually increase in concentration. A fifth rat with a 9L tumor was also imaged shown below in Figure 41.

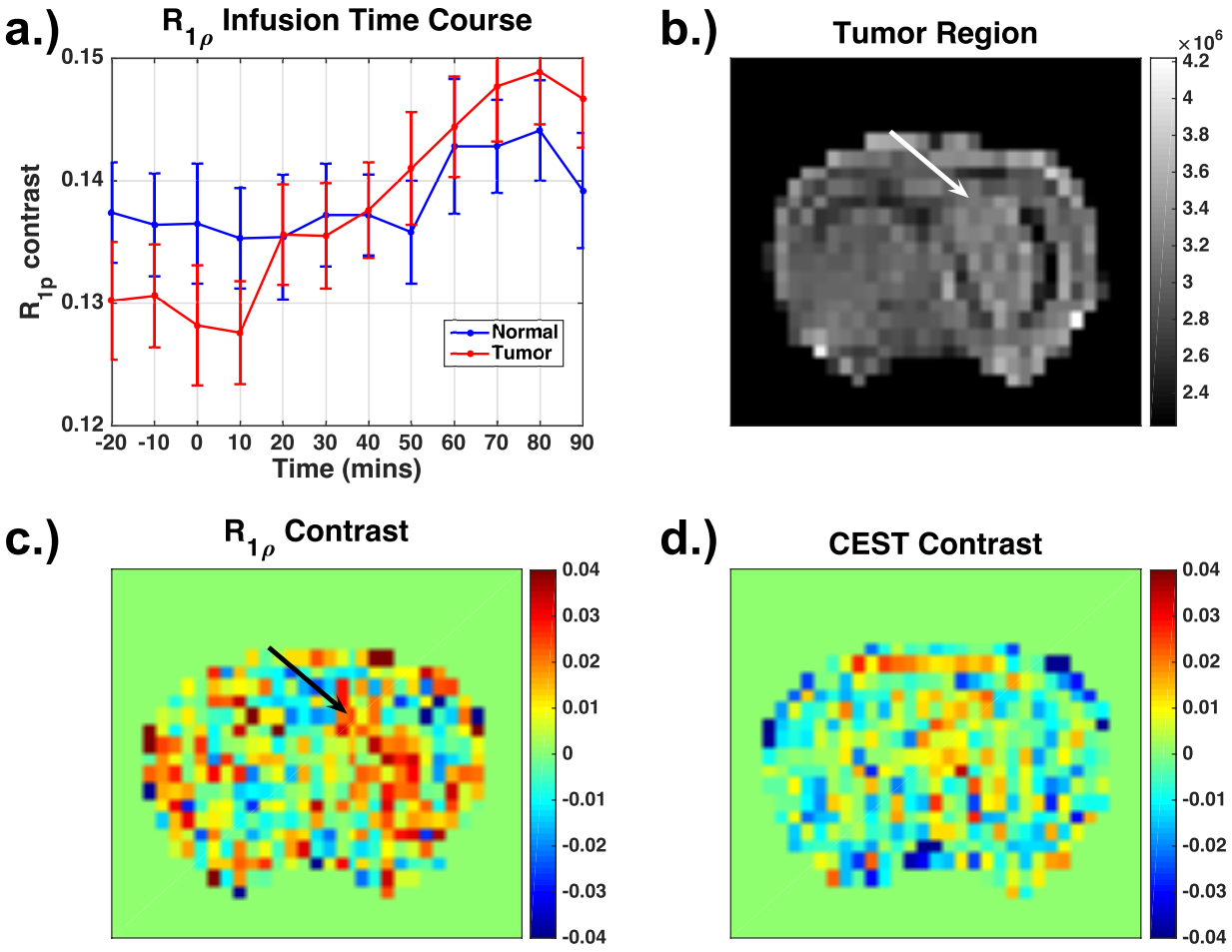

Figure 41: a.) $R_{1\rho}$ contrast time course in normal and tumor regions of the brain. b.) Anatomical image of the brain to illustrate the tumor region acquired prior to the infusion. c,d.) $R_{1\rho}$ contrast image depicting greater tumor differentiation reflecting elevated 2DG levels compared to the CEST contrast image. Both images represent the time point 70 minutes after the start of infusion.

ROI analysis was performed in the tumor and in a healthy region of the brain to plot the time course of $R_{1\rho}$ contrast in each region shown in Figure 41a. While the normal tissue displays a very small increase in $R_{1\rho}$ contrast, the tumor region exhibits a substantially larger increase over the same time span. This behavior was expected since the 2DG should become trapped in the cells and tumors have been shown to exhibit heightened glucose metabolism (*149*, *150*, *161*, *162*). The heightened glucose metabolism may also explain why the tumor tissue recorded a lower baseline $R_{1\rho}$ contrast than the normal tissue. The $R_{1\rho}$ and CEST contrast images are not extremely high resolution, but the $R_{1\rho}$ image clearly shows increased contrast in the tumor region compared to CEST. The $R_{1\rho}$ method has been shown to be the superior contrast method to probe 2DG exchange in rat brains *in vivo*.

Conclusions

Radioactive imaging methods using the labeled glucose analogue 2DG have the benefit of direct metabolite detection and FDG PET has already been an approved methodology that is beginning to be implemented in cancer treatments. Using glucose and analogues of glucose in MRI has become a topic of interest within the MR community over the past few years with more research emerging each year (*121*, *146–148*, *163*). The analysis above shows that in the case of 2DG, spin-locking measurements are more sensitive to the fast hydroxyl exchange and provide better chemical exchange dependent contrast than that available from CEST. CEST methods may be more proficient in quantifying chemical exchange in the slow exchange regime, but for fast exchange problems such as direct water saturation become significant and affect data. The concentrations used in this study were very high for the phantoms and homogenates were the effects were abundantly obvious, but were much lower *in vivo* since the amount of glucose was slowly infused and constantly regulated naturally by the rat. The concentrations *in vivo* could not

be increased to arbitrarily large values since 2DG may produce toxicity effects. Others have shown 2DG is relatively safe but can cause significant drops in blood pressure and decreases in respiratory frequency with large intravenous doses (*164*). Vijayaraghavan et. al. determined an oral LD_{50} > 8,000 mg/kg in mice and rats was considered safe and no deaths were exhibited with this dosage (*164*). Another potential advantage of 2DG MRI over FDG-PET is that FDG has demonstrated greater toxicity as a glycolytic inhibitor than 2DG (*165*). Though this overall toxicity has been shown to be relatively low for both compounds in rats and mice, some investigators have attempted to used 2DG as an anti-cancer drug by using it to impede tumor cell glycolysis or using it to supplement other chemotherapies (*166–168*). Further investigation of the use of 2DG may need to be performed to assess the optimal dosage or its potential with other spin-locking methods such as calculating parametric exchange rate contrast (ERC) images that emphasize regions of heightened glucose metabolism.

CHAPTER 5

Characterizing Heterogeneous Media by Analyzing the Spatial Scales of Susceptibility Variations With $R_{1\rho}$ Dispersion

Introduction

Previous chapters discussed how spin-locking induces precession about the effective field and overcomes the exchange effect of nuclei jumping between two sites with distinct chemical shifts when the frequency is on the order of the time scale of the exchange process. Analogously, water diffusion in the presence of inhomogeneities causing intrinsic susceptibility gradients also gives rise to dispersion in $R_{1\rho}$ due to the randomly fluctuating local field experienced by diffusing spins (*84*, *169*). Such variations arise in several contexts, notably within trabecular bone (*170*), in the presence of vasculature containing paramagnetic agents or deoxyhemoglobin (*171*), or in tissues that accumulate iron-bearing proteins (*172–174*). The intrinsic gradients cause dispersion to a degree that depends on the gradient strength at an inflection frequency that corresponds to the time scale of the local field fluctuations, which provides information about the mean spacing between inclusions. In general the local field variations experienced by nuclei are complex and usually random but may be described by a correlation function with a characteristic correlation time (τ_c). The corresponding effects on $R_{1\rho}$ have been considered much less often, and one study even reports seeing increases in $R_{1\rho}$ with locking field, contradictory to what is expected (*170*). The effect on $R_{1\rho}$ dispersion may not be frequently considered in the literature because a theoretical basis for how rapidly fluctuating fields modify $R_{1\rho}$ has not been established until recently. The overall purpose of the work reported here was to develop a novel imaging approach for characterizing inhomogeneous biological tissues distinguished by intrinsic spatial

variations of magnetic susceptibility.

Where susceptibility variations within a sample volume or image voxel are produced by discrete inhomogeneities or inclusions, such as the presence of paramagnetic particles, or deoxyhemoglobin within the microvasculature, the magnitude and spatial extent of the field perturbations depend on the nature and sizes of the inhomogeneities (*175*).

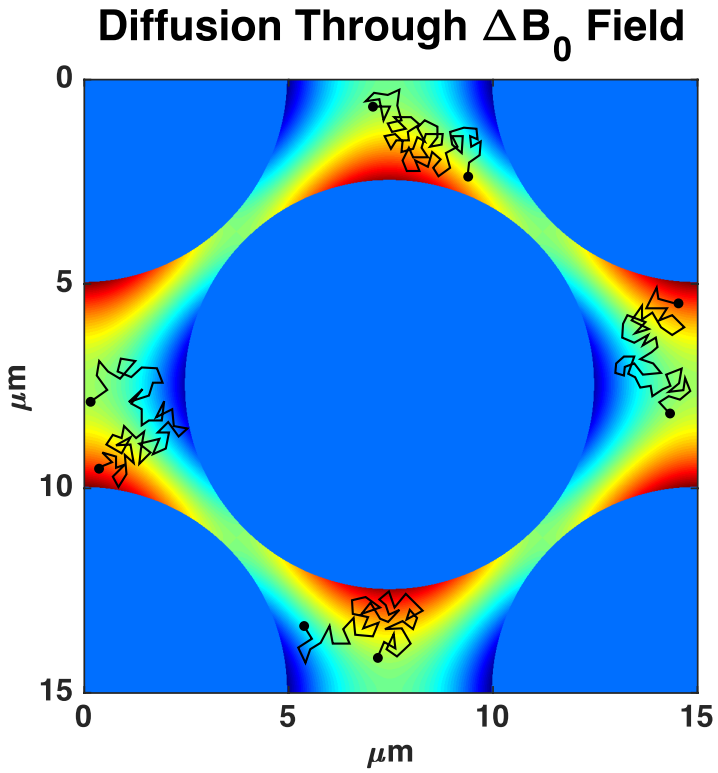

Figure 42: An example of four nuclei diffusing though a simulated gradient field induced by packed microspheres. Following the paths shows how the local field experienced by these nuclei fluctuates with time.

The influences of diffusion amongst such inhomogeneities, exemplified in Figure 42, on transverse relaxation rates R_2 and R_2^* have been previously extensively analyzed by theory and computer simulations, and studied experimentally in vitro and in vivo (*70–81*), and various

regimes have been defined for how diffusion affects relaxation in spin echo and gradient echo imaging. However, the corresponding effects on $R_{1\rho}$ have been much less considered previously. Lammentausta et al (*170*) reported measurements of $T_{1\rho}$ for water within trabecular bone but noted "to our knowledge there is currently no theoretical formalism considering $T_{1\rho}$ relaxation during diffusion in local field gradients." Moreover, they measured increases of $R_{1\rho}$ with respect to the locking field amplitude for water in bone, contradictory to what would be expected. They noted that "a more complete theoretical formalism… is required to better understand the behavior of $T_{1\rho}$ relaxation under these kinds of experimental conditions." Others, e.g. Kettunen et al (*171*), examined the effects of changes in intravascular susceptibility from the use of iron oxide contrast agents but saw little change in $R_{1\rho}$ at a single (relatively high) locking field. However, they did not measure the dispersion at other fields, though they did confirm that $R_{1\rho}$ decreases when blood is oxygenated because of changes in exchange-mediated relaxation by deoxyhemoglobin.

Here, a new simple analytic relationship is derived between the dispersion of $R_{1\rho}$ measureable by spin-locking methods and the rate of diffusion within spatially varying gradient fields. We subsequently use this theoretical result to predict how $R_{1\rho}$ may be used to quantify aspects of diffusive behaviors and intrinsic susceptibility variations in inhomogeneous media. The derivation hinges on the assumption that the gradient field oscillates sinusoidally to allow the math to work, and the model needs to be tested to confirm its utility in practical experiments. Given that real intrinsic gradients may not be well described with a single spatial frequency, it is of interest to explore whether this simple analysis may be used as an approximate description of more complex media, and used to extract useful characteristics such as the average spatial dimensions of the inhomogeneities in the media. Methods for quantifying these spatial scales of

intrinsic tissue variations may have far reaching applications for quantitative characterization of inhomogeneous material, and in biological applications, for the evaluation of pathologies. The effects of diffusion through simple geometries exhibiting intrinsic susceptibility gradients on transverse relaxation rates R_2 and R_2^* have been extensively investigated before through simulation, theory, and experiments (*73*, *78*, *176–178*). Simulations of diffusion within vascular networks have also been performed to evaluate geometry dependent effects on transverse relaxation (*81*, *179*). However, no previous simulation has quantified the effects of diffusion through susceptibility-induced gradients in the presence of spin-locking fields, which will be done here. Although the expression for the ideal case we analyze is only an approximation to realistic situations, we show how reasonable estimates may be obtained of novel material properties that can be used for quantitative tissue characterization.

Theory

Deriving the Influence of Diffusion on $R_{1\rho}$

In order to derive the expression for diffusion based $R_{1\rho}$, the approach of Deverell et al. (*45*) was adopted for analyzing the behavior of a system of spin-1/2 nuclei subject to a static magnetic field $B_0 = \frac{\omega_0}{\gamma}$ and an on-resonance rotating field of frequency ω_0 and amplitude $B_1 = \frac{\omega_1}{\gamma}$. They considered the effects of a time varying perturbation field $\delta\omega(t)$ that fluctuates with an average correlation time τ_c and which can induce relaxation of the magnetization aligned with B_1. If $\delta\omega\tau_c \ll 1$ and $\delta\omega \ll \omega_1 \ll \omega_0$, Deverell et al. show that the contribution to $R_{1\rho}$ from time-varying field perturbations depends on the spectral content of the autocorrelation of field variations experienced by the nuclei at the relevant locking frequency.

$$R_{1\rho} = \frac{1}{2}\int_{-\infty}^{\infty} \overline{\delta\omega(t)\delta\omega(t-\tau)}\cos(\omega_1\tau)d\tau \qquad 4.1$$

Eq. 4.1 describes the relaxation behavior of nuclei diffusing through a spatially varying field, $b(x)$, such that

$$\delta\omega(t) = \gamma b(x) = \gamma b\big(x(t)\big). \qquad 4.2$$

Here, the special case where the field varies sinusoidally in one dimension is considered. Cowan (*180*) has analyzed the correlation of displacements and fields experienced by spins diffusing in such a medium. In this case,

$$b(x) = A\sin(qx) \qquad 4.3$$

where q is the spatial frequency of the variation. Real fields in practice do not vary sinusoidally, but they do fluctuate about a mean value with some deviation that is determined by the gradient strength and the geometry. The spatial derivative of the field is then

$$\frac{\partial b(x)}{\partial x} = Aq\cos(qx). \qquad 4.4$$

The mean squared gradient, g, can be represented as

$$g^2 = \frac{A^2q^2}{2} \qquad 4.5$$

so that

$$b(x) = \sqrt{2}\,\frac{g}{q}\sin(qx) \qquad 4.6$$

where a linear gradient corresponds to the case $q=0$. Substituting for the correlation of the frequency variations,

$$\overline{\delta\omega(t)\delta\omega(t-\tau)}=\gamma^2\langle b(0)b(\tau)\rangle=2\left(\frac{\gamma g}{q}\right)^2\left\langle\sin\left(qx(0)\right)\sin\left(qx(t)\right)\right\rangle. \quad 4.7$$

The position $x(t)$ changes with time and the displacement may be written as

$$\Delta x(\tau)=x(\tau)-x(0) \quad 4.8$$

so that

$$\overline{\delta\omega(t)\delta\omega(t-\tau)}=2\left(\frac{\gamma g}{q}\right)^2\left\{\left\langle\sin^2\left(qx(0)\right)\cos\left(q\Delta x(\tau)\right)\right\rangle+\left\langle\sin\left(qx(0)\right)\sin\left(q\Delta x(\tau)\right)\cos\left(qx(0)\right)\right\rangle\right\}. \quad 4.9$$

Since the displacement and the starting position are not correlated for random diffusion, the second term on the right is zero, the average of the term $\sin^2\left(qx(0)\right)$ is ½, and

$$\overline{\delta\omega(t)\delta\omega(t-\tau)}=2\left(\frac{\gamma g}{q}\right)^2\left\langle\frac{1}{2}\cos\left(q\Delta x(\tau)\right)\right\rangle. \quad 4.10$$

For random Brownian motion, the probability distribution of $\Delta x(t)$ for unrestricted diffusion is Gaussian so that

$$P(\Delta x)=\frac{1}{\sqrt{2\pi\langle\Delta x^2\rangle}}e^{-\frac{\Delta x^2}{2\langle\Delta x^2\rangle}}. \quad 4.11$$

Then

$$\left\langle \frac{1}{2}\cos\left(q\Delta x(\tau)\right)\right\rangle = \int_{-\infty}^{\infty} \frac{1}{2}\cos\left(q\Delta x(\tau)\right)P\left(\Delta x(\tau)\right)d\Delta x = \frac{1}{2}e^{-\frac{q^2\left\langle \Delta x^2(\tau)\right\rangle}{2}} \quad 4.12$$

where

$$\left\langle \Delta x^2(\tau)\right\rangle = 2D\tau \quad 4.13$$

and D is the usual self-diffusion coefficient. Putting Eq.'s 4.10 - 4.13 together, we obtain

$$\overline{\delta\omega(t)\delta\omega(t-\tau)} = 2\left(\frac{\gamma g}{q}\right)^2 \frac{1}{2}e^{-q^2D\tau}. \quad 4.14$$

Many physical realistic correlation functions decay exponentially, and such functions are commonly adopted in relaxation theories such as that of the original analysis of Bloombergen, Purcell, and Pound (*33*). Substituting Eq. 4.14 into Eq. 4.1 leads to

$$R_{1\rho} = \frac{1}{2}\int_{-\infty}^{\infty}\left(\frac{\gamma g}{q}\right)^2 e^{-q^2D\tau}\cos\left(\omega_1\tau\right)d\tau \quad 4.15$$

or after evaluating the integral,

$$R_{1\rho} = \frac{\gamma^2 g^2 D}{\left(q^2D\right)^2 + \omega_1^2}. \quad 4.16$$

Eq. 4.16 states that the values of $R_{1\rho}$ will disperse for different locking fields and are strongly dependent on the gradient strength and the spatial frequency. Setting the second derivative of Eq. 4.16 with respect to ω_1 to zero, one can find the dispersion curve exhibits an inflection point that corresponds directly to the spatial distribution of the medium at $\omega_1^{\text{inflection}} = \frac{q^2D}{\sqrt{3}}$. A characteristic

locking field frequency ω_c may be defined for a specific spatial frequency q, $\omega_c = \frac{1}{\tau_c} = q^2 D$, so that

$$R_{1\rho} = \gamma^2 g^2 D \frac{\tau_c^2}{1+\omega_1^2 \tau_c^2}. \quad 4.17$$

This curve has an inflection (i.e. the steepest part of the curve where the second derivative $\frac{d^2 R_{1\rho}}{d\omega_1^2} = 0$) when $\omega_1^2 = \frac{1}{3\tau_c^2}$. The interval τ_c, or the correlation time, is an intrinsic characteristic of the medium that depends on the spatial scale of the inhomogeneities but not the magnitude of the susceptibility variations, which lies solely in the $g^2 D$ term. The correlation time is literally the time required for diffusing the spatial scale of inhomogeneity within the sample, or one period of the oscillating field.

Interpreting Diffusion Parameters

Equation 4.17 provides a useful starting point for the interpretation of $R_{1\rho}$ measurements of media with quasi-periodic distributions of non-uniform susceptibility at different locking fields. For example, spherical objects in a magnetic field produce an internal field that differs from the external field according to their susceptibility difference. Field gradients are generated external to the surfaces and decrease with distance (*48*, *181*). Both R_2^* and $R_{1\rho}$ will depend on the applied field (B_0), the magnetic susceptibility between the particle and the surrounding material ($\Delta\chi$), and the object radius (R) (*182*). For an array of small particles in relatively close proximity the field will vary across space and the characteristic spatial frequency will be of the order of $q = \frac{\pi}{R}$. $R_{1\rho}$ will then show an inflection in the dispersion when $\omega_1 = \frac{\pi^2 D}{\sqrt{3}R^2}$, i.e. when

the period of spin nutation about the locking field matches the time to diffuse the characteristic dimension of the inhomogeneity. For D = 2.5 x 10^{-5} cm^2/s, dispersion over the range of ≈ 23 - 363 Hz is expected for inhomogeneities of diameters 20 - 5 μm respectively.

The spatial frequency parameter q in the correlation time is what relates the spatial distribution to our relaxation rate, but the medium may not be adequately described by a single spatial frequency. In practice, the parameter will represent an averaged effective spatial frequency over the medium that will be referred to as q_{eff}. The precise meaning of q_{eff} will depend on the exact nature of the field distribution, but to assist in its interpretation the derived values of q_{eff} will be compared to a characteristic measure of an arbitrary field distribution, a measure of width of the spatial frequency distribution calculated from the second moment of the spatial frequency power spectrum of the ΔB_z field.

$$\langle q \rangle_{\text{theory}} = \sqrt{\frac{\iiint \left(k_x^2 + k_y^2 + k_z^2\right) \left|F_{\Delta B}\left(k_x, k_y, k_z\right)\right|^2 dk_x\, dk_y\, dk_z}{\iiint \left|F_{\Delta B}\left(k_x, k_y, k_z\right)\right|^2 dk_x\, dk_y\, dk_z}} \qquad 4.18$$

In Eq. 4.18, $k_{x,y,z}$ and $F_{\Delta B}\left(k_x, k_y, k_z\right)$ are the spatial frequencies and the Fourier transform of the ΔB_z field respectively. Eq. 4.18 is similar to the resolution index used by Van Vleck to calculate a mean squared RF absorption frequency (*183*) and later by Gore et al. to assess the resolution of ultrasound imaging systems with a corresponding transfer function (*184*), but here it is used to quantify the spatial changes in the local field diffusing protons experience. In the spatial domain,

$$\langle q \rangle_{\text{theory}} = \sqrt{\frac{\iiint \left(\nabla \Delta B_z\right)^2 dx\, dy\, dz}{\iiint \left(\Delta B_z\right)^2 dx\, dy\, dz}}. \qquad 4.19$$

Quantifying the correlation time experimentally is a primary goal of this work since this will allow the direct characterization of spatial distributions of inhomogeneities in tissues. Practically, collecting enough data to measure a dispersion curve may be very time consuming so being able to quantify the correlation time from a smaller set of images would be very advantageous. Using inspiration from the ERC method described earlier, another image combination technique will allow us to directly quantify the correlation time. Assuming the signal everywhere decays mono-exponentially with relaxation rate $R_{1\rho}$ under the influence of a locking pulse, the general image signal value can be written as

$$S = S_0 e^{-R_{1\rho} t}. \tag{4.20}$$

Acquiring images at 3 distinct locking strengths of $\omega_1 \approx 0$, ω_1, and $\omega_1 \sim \infty$, the correlation time can be directly calculated by combining these images according to Eq. 4.21.

$$\tau_c = \frac{1}{\omega_1}\sqrt{\frac{\log(I_\infty) - \log(I_0)}{\log(I_\infty) - \log(I_{\omega_1})} - 1} \tag{4.21}$$

Here in Eq. 4.21, I_0, I_{ω_1}, and I_∞ are the image intensities at $\omega_1 \approx 0$, ω_1= an intermediate value, and $\omega_1 \sim \infty$ respectively. The intermediate value of ω_1 must occur somewhere on the order of the inflection point and will ideally correspond to a value of $R_{1\rho}$ that is midway between the asymptotic values of $R_{1\rho}(0)$ and $R_{1\rho}(\infty)$. This method may require very high SNR acquisitions due to the logarithm of each image inside the square root, but this does allow for quick parameter estimation using only three images. The feasibility of using the theory and methods above will be assessed through simulations and experiments.

Specific Aims

Aim 1

The theory above derives the first theoretical expression relating diffusion of spins through susceptibility gradients to spin-lattice relaxation in the rotating frame. The theoretical magnitude of diffusion effects on $R_{1\rho}$ dispersion may be assessed by performing 3D finite difference simulations of water diffusing about unit cells of spheres that are packed in various manners as well as packed cylinders. The different geometries will be analyzed for their influence on the relaxation behavior and the estimated spatial frequency parameter described in Eq. 4.18. Different values of volume susceptibility will be examined to determine the sensitivity of rotating frame relaxation to susceptibility gradients.

Aim 2

With simulated confirmation of diffusion effects completed, experimental evidence needs to be gathered to validate diffusion effects in the presence of susceptibility gradients have significant influence on $R_{1\rho}$ dispersion at high field in model systems. Samples of packed polystyrene microspheres of various sphere sizes will be scanned at 7T. The estimated gradient parameters need to be examined for consistency and the correlation time mapping method described in Eq. 4.21 may be evaluated for feasibility and accuracy.

Methods

$R_{1\rho}$ Diffusion Simulations

In order to quantify the effects of diffusion on $R_{1\rho}$ relaxation, 3D finite difference Bloch simulations were performed in MATLAB by assigning specified unit cells and calculating ΔB_0 offsets through the principle of superposition in the spaces between the spheres and cylinders.

Three different unit cells were used shown in Figure 43, a spaced out Body-Centered Cubic (BCC) packing structure, a spaced out Face-Centered Cubic (FCC) packing structure, and a packed cylinder structure.

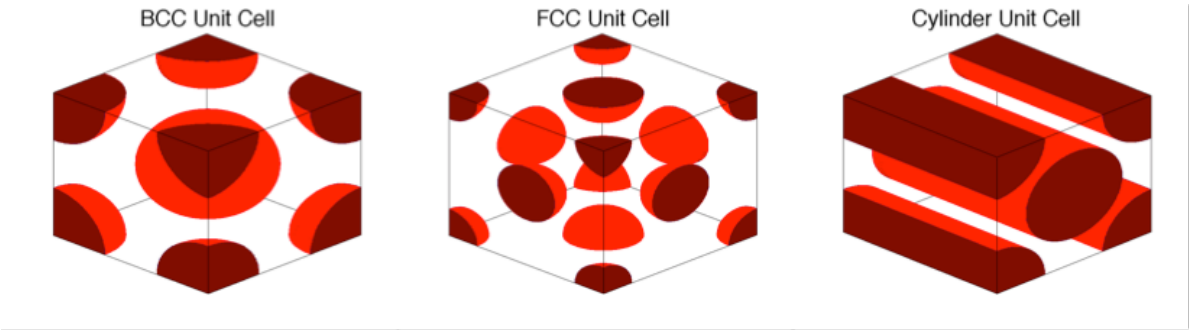

Figure 43: The 3 unit cells used for simulating diffusion through susceptibility variations. Each structure was assigned radii and spaced out to achieve specific volume fractions.

Two scenarios were simulated for each packing structure, constant volume fraction with various radii and constant radius with varying volume fraction. Changing the geometries in this manner should create different internal ΔB_z field patterns resulting in different $R_{1\rho}$ dispersion behaviors. The unit cells of impenetrable spheres and cylinders were generated in MATLAB using 64x64x64 matrices and the ΔB_z field was calculated using the principle of superposition with the following equations specifying the field shift for a single sphere or cylinder due to a susceptibility interface (*48*).

$$\Delta B_z^{sphere} = \frac{\Delta\chi}{3}\frac{a^3}{r^3}\left[3\cos^2(\theta)-1\right]B_0$$
$$\Delta B_z^{cylinder} = \frac{\Delta\chi}{2}\frac{a^2}{\rho^2}\cos(2\phi)B_0 \qquad 4.22$$

In Eq. 4.22, $\Delta\chi$ is the difference in susceptibility between the solid medium and the surrounding

water, a is the radius of the sphere, r is the distance from the sphere, θ is the azimuthal angle with respect to the z-axis, B_0 is the static field strength, ρ is the distance from the cylinder, and ϕ is the radial angle about the cylinder axis.

All simulations were conducted with the magnetization starting along the x-axis with time steps of 2 μsec and with the parameters R_1 = 0.385 Hz, R_2 = 0.833 Hz, with 60 different locking times ranging from 10 to 120 ms, and 12 locking fields ranging from 1 – 2,000 Hz. The low amplitude locking field was set at 5 Hz rather than 1 Hz to better capture the region of dispersion for small radii. A first set of fields was calculated with a constant volume fraction of 60% but with varying radii ranging from a = 5-15 μm. A second set of fields was calculated using a constant radius of a = 5 μm with varying volume fractions from 30 – 60%. The effects of spin diffusion were estimated by discrete sampling of the magnetization on a 64x64x64 grid, calculating the spin displacement probabilities prior to starting the simulation using D = 2.5 $\mu m^2/ms$, and redistributing the magnetization after every time step by multiplying the sparse transition matrix with the vector of magnetization at every position as described by Xu et al (*185*). Periodic boundary conditions were also implemented in the transition matrix to ensure edge effects at the boundaries of the unit cell did not contribute significant errors to the simulations. The simulations stepped through the Bloch equations describe in Eq. 4.23, with the ΔB_z offset absorbed into the chemical shift term ($\Delta\omega_0$) in every 3D voxel.

$$\begin{aligned}
\frac{dM_x(t)}{dt} &= \Delta\omega_0 M_y(t) - R_2 M_x(t) \\
\frac{dM_y(t)}{dt} &= -\Delta\omega_0 M_x(t) - R_2 M_y(t) + \omega_1 M_z(t) \\
\frac{dM_z(t)}{dt} &= -\omega_1 M_y(t) + R_1\left[M_0 - M_z(t)\right]
\end{aligned} \qquad 4.23$$

The field deviations, ΔB_z, were calculated in the space between the impenetrable spheres and cylinders by assuming the volume susceptibility was that of polystyrene, -8.21×10^{-6} (*186*, *187*). The x-axis signal values as a function of time were fit to a monoexponential decay model to estimate the relaxation rates for different locking fields and later used to fit to the expression below. More simulations were performed by changing the susceptibility difference ($\Delta\chi$ = 1 - 6 times polystyrene) to show that susceptibility will affect only the gradient strength and geometry estimates can still be made from the data. Also, one more set of simulations were executed by changing the grid sizes to achieve various voxel resolutions (0.171 μm – 0.314 μm) to show how significant pixelation effects can affect the simulated dispersions.

$R_{1\rho}$ Diffusion Experiments

Simulations are able to predict the behavior of very controlled systems, but real experimental systems of packed spheres will have random packing placements that may change the relaxation behavior. In order to demonstrate the feasibility of using this theory experimentally, a series of samples consisting of closely packed polystyrene microspheres (Polysciences Inc., PA, USA) in deionized (DI) water with diameters ranging from 1 – 90 μm were prepared. Spectroscopic measurements of $R_{1\rho}$ were performed at 7T using 10 logarithmically spaced spin-lock amplitudes ranging from $\frac{\omega_1}{2\pi} \approx 2 - 1{,}000$ Hz, each with 6 logarithmically spaced spin-lock times from 20 ms to 1 second. Temperature was monitored by the use of a thermocouple attached to an animal physiologic monitoring system (SA Instruments, Stony Brook, NY) and maintained at 20° C. Dispersions were obtained by calculating $R_{1\rho}$ values at each locking amplitude by a least squares fitting to a mono-exponential decay model, as described in previous chapters, and these values were fit to Eq. 4.16 to estimate g^2D and q^2D.

The correlation times were compared to those simulated with the BCC packing structure.

The packed samples with radii of 1 μm, 4.5 μm, 10 μm, and 20 μm were subsequently imaged at 7T with a 128x128 matrix and a 24mm x 24mm field of view (188 μm resolution) using a spin-lock prepped Fast Spin Echo acquisition with a fixed locking time (150 msec) and three different spin-lock amplitudes (0 Hz, 300 Hz, 1000 Hz) spanning an appropriate range that was derived by inspection of the measured dispersion curves. The spin-locking pre-pulse was the same as the spectroscopic sequence with the addition of a reverse adiabatic 90° pulse followed by a crusher gradient to spoil residual transverse magnetization before the Fast Spin Echo acquisition. The three images acquired with different values of the locking amplitude were then combined on a voxel by voxel basis as described in Eq. 4.21 to map the correlation times in each sample. Finally, the four samples were imaged twice more after being dispersed in larger volumes of water to increase the average spacing between spheres. Each of the original samples were packed in 20 μL of water, partially filling 0.6 mL tubes to start, and 100 μL of water was added to each bringing the total amount of water in each sample to 120 μL. The spheres were evenly dispersed in a BR-2000 vortexer (Bio Rad, Hercules, CA) so the average space between the spheres was $d \approx \sqrt[3]{\frac{V}{N}}$, where V and N are the total volume of water and number of spheres respectively. The samples of larger beads contained fewer spheres with larger spacing between them. During the time of measurement, only the spheres 45 μm diameter and larger showed small signs of settlement, and the others maintained reasonably uniform suspensions. The samples were imaged using the same method to depict how the correlation time changed with sphere spacing. This was repeated after adding another 100 μL of water to each of the samples bringing the total volume of water to 220 μL for the last images.

Results and Discussion

$R_{1\rho}$ Diffusion Simulations

A specific goal of these studies was to evaluate whether the analysis used previously for sinusoidal gradients of single spatial frequency could be usefully extended to more complex arrays of inhomogeneities. $R_{1\rho}$ measurements are shown to be very sensitive to diffusion effects in the presence of susceptibility gradients through simulations and experiments on packed microspheres. The calculated dispersion curves for the three types of structures are shown in Figure 44 for constant volume fractions with varying radii and for constant radii with varying volume fractions.

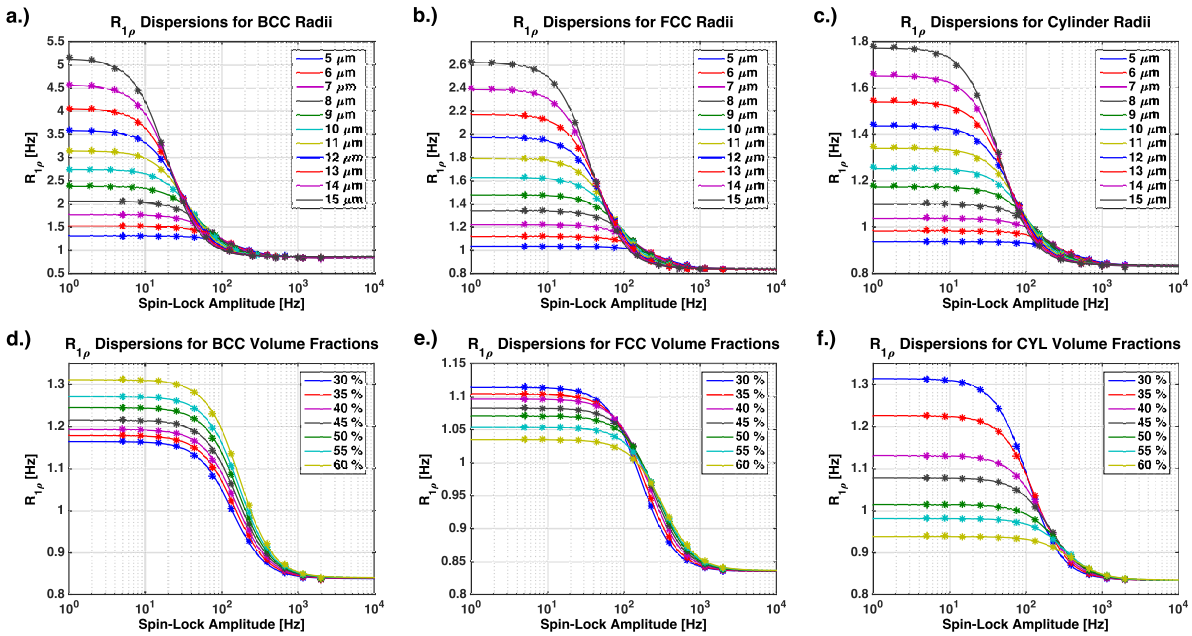

Figure 44: a-c.) $R_{1\rho}$ dispersions for various radii with 60% volume fractions packed in BCC, FCC, and Cylinder structures respectively. d-f.) $R_{1\rho}$ dispersions for various volume fractions of BCC, FCC, and Cylinder structures with 5 μm radii.

For constant volume fraction, in all samples the degree of dispersion increased near-linearly with

the radius of the perturbers. For these samples, the distance between inhomogeneities increases and the mean gradients decrease as the radius gets larger since the gradient is, by definition, the derivative of the field. The inflection points of the dispersions moved to lower locking field amplitudes with radius corresponding to the field variations having lower spatial frequencies so that the spins experience more slowly varying field fluctuations with longer correlation times. With increasing volume fraction but constant radius, the inflection points moved to higher locking fields, reflecting the increased spatial frequency of the average fields and a corresponding shorter correlation time. However, while the dispersion magnitudes for the FCC and cylinder structures decreased with volume fraction, the BCC structures displayed the opposite behavior. These differences reflect the manner in which the average field gradients behave for the different geometries as the number density of perturbers increases. Note that the inflection points were not influenced by the choice of $\Delta\chi$ and the resolution of the grid had only a small impact on the dispersion curves. For example, Figure 45 shows simulations for R = 5 μm, 60% volume fraction, BCC structures with various susceptibility differences and matrix sizes.

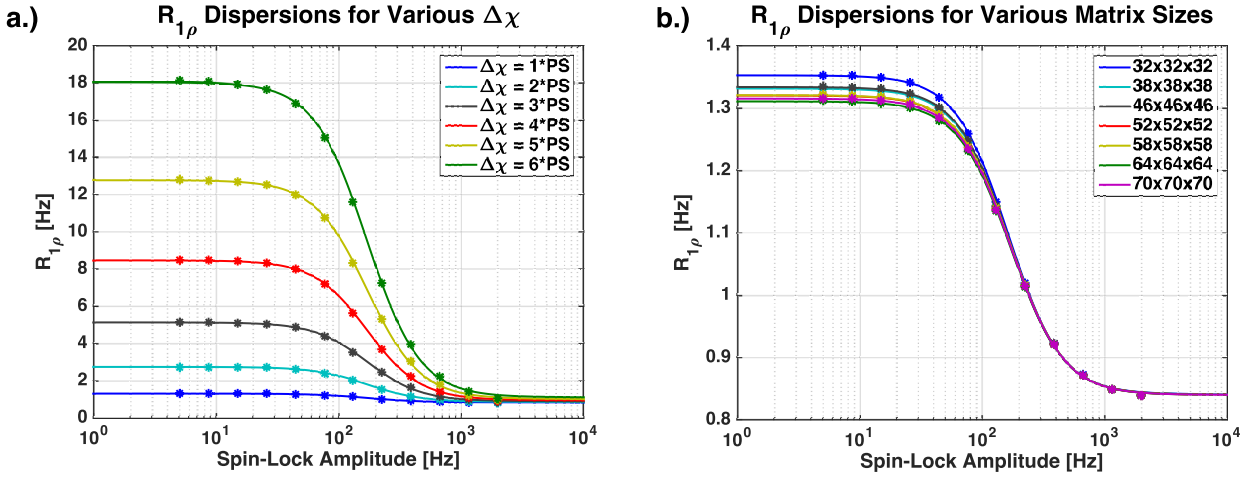

Figure 45: a.) $R_{1\rho}$ dispersions for R = 5 μm, 60% volume fraction BCC structures with susceptibilities 1 - 6 times that of polystyrene. b.) $R_{1\rho}$ dispersions of the same structure with varying matrix sizes to change the voxel resolutions.

The inflection points for each case do not change by more than 1.5% for the $\Delta\chi$ plots and no more than 4.5% for the matrix size plots indicating these parameters have little influence on the simulated dispersion when compared to the effects of changing the sphere radii or volume fraction of the spheres. The simulation results confirm that larger intrinsic gradients cause greater contributions to relaxation at low locking fields, and that more rapidly varying fields correspond to higher inflection point frequencies in the dispersions. Larger spheres (and cylinders) generate smaller gradients at their surfaces as evident by taking the derivative of Eq. 4.22, and so diffusion effects on $R_{1\rho}$ dispersion are smaller. On the other hand, larger structures (at constant volume fraction) are spaced further apart and generate more slowly varying fields (lower spatial frequency) so the correlation time of field fluctuations experienced by the spins is longer and the inflection point shifts to lower locking field. Our simulations differ from the traditional two-pool model, which designate free and bound water pools that exchange instantaneously, and incorporate a more continuous transition of the effective field the spins experience. Our model does not take into account the possibility of water adsorption or other interactions at the sphere surfaces. Regardless, the above results demonstrate that free diffusion through susceptibility gradients may produce similar dispersion behavior in $R_{1\rho}$ as chemical exchange mechanisms. The behavior in the simulations of the BCC structures with varying volume fraction in Figure 44d should be noted because the reason they behave differently from the FCC or cylinder structures is not intuitive. The low frequency asymptotic $R_{1\rho}$ values increased with volume fraction for the BCC structures because the correlation time decreased more slowly than the increase in the mean gradient magnitude, whereas the FCC and cylinder structures showed relatively slower increases in their gradient magnitudes reflecting differences in the geometrical properties of the systems. The correlation time, however, is independent of the relaxation rates

and the mean gradient strength. It reflects the spatial frequency content of the field variations and not their magnitudes.

The correlation time for every dispersion curve in Figure 44 is plotted as a function of radius or volume fraction in Figure 46.

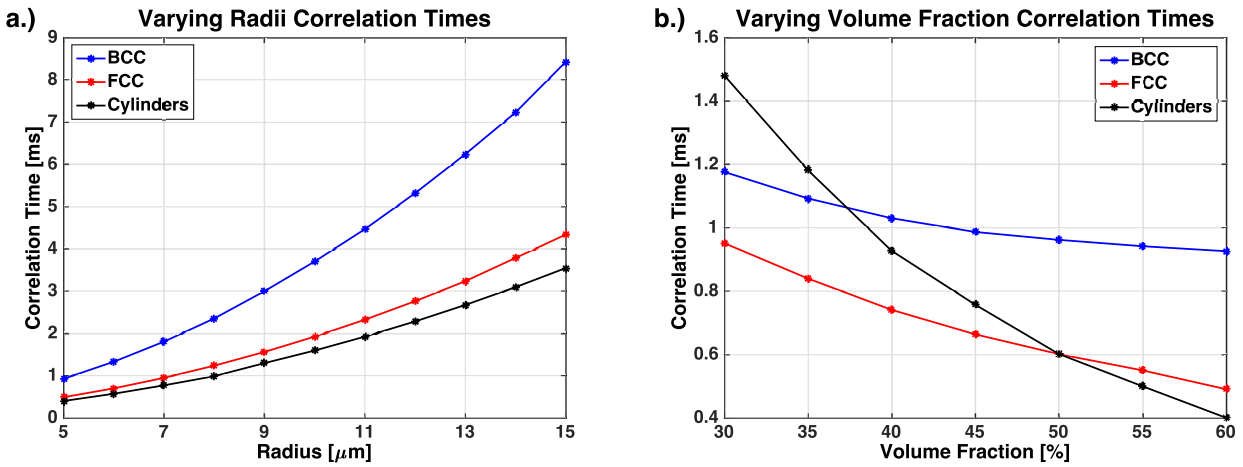

Figure 46: a.) Correlation times plotted against radius for each packing structure at 60 % volume fraction. b.) Correlation times plotted against volume fraction for each packing structure with 5 μm radii.

These are inversely related to the locking field at the inflection point of the dispersion curve, i.e. $\omega_1^{\text{inflection}} = \frac{1}{\sqrt{3}\tau_c}$, and increased with radius and decreased with volume fraction for all structures as expected. The correlation times will be compared with the experimental correlation times later. Assuming that the diffusion coefficient D = 2.5 μm^2/ms, using $\tau_c = \frac{1}{q_{\text{eff}}^2 D}$, values of the effective spatial frequency q_{eff} were derived and compared to the width of the spatial frequency spectrum calculated from Eq. 4.18 by plotting $\langle q \rangle_{\text{theory}}$ vs. q_{eff} as shown in Figure 47.

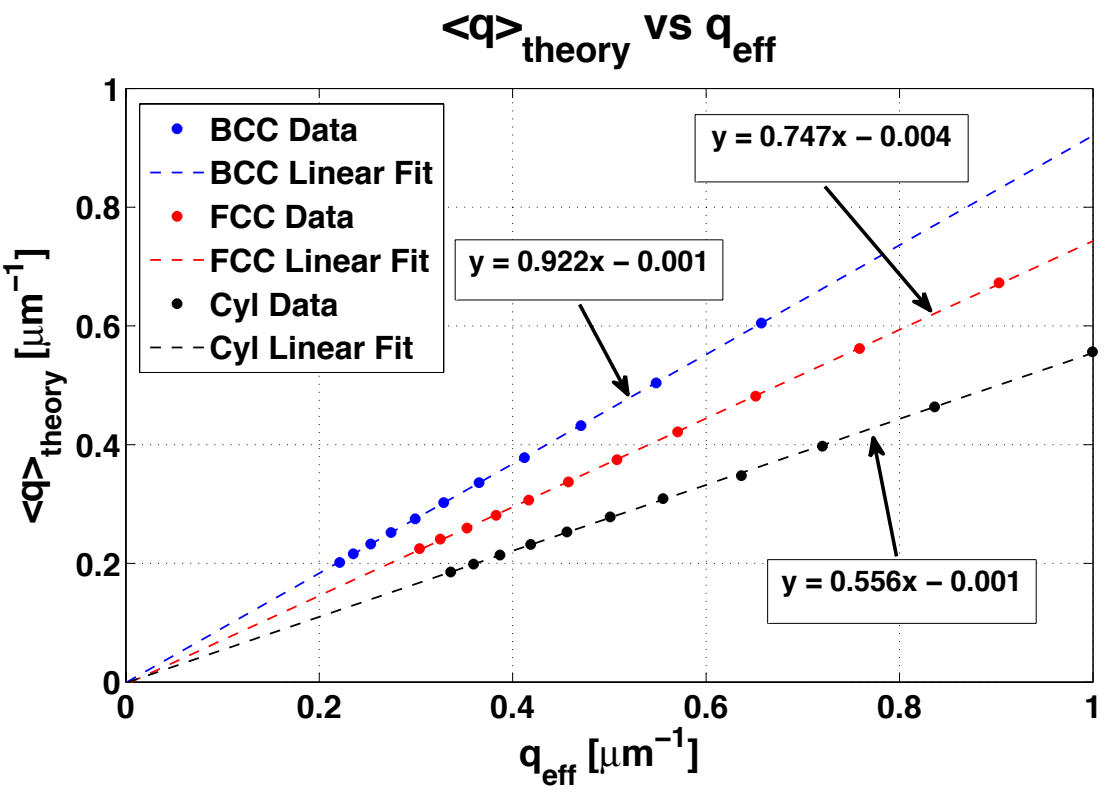

Figure 47: Theoretical spatial frequency plotted versus the fitted spatial frequency assuming D = 2.5 μm^2/ms for varying radii in each of the packing structures.

Remarkably, there was a strong linear correlation between these different measures of the field characteristics for all structures, suggesting that the derived parameter q_{eff} reliably captures essential features of the fields and that its absolute value may be interpreted as a direct measure of the average spatial scale of the intrinsic field variations. Real magnetic field variations from arbitrary arrays of inhomogeneities are likely to be complex and distributed over a range of values.

A common approach to capturing salient features of random fields is to compute higher moments of the field distribution, and the second moment or variance of the power spectrum is

one such metric. Thus, $\langle q \rangle_{\text{theory}}$ defined above is potentially a parameter for describing and differentiating arbitrary field distributions. The fact that it scales linearly with our derived spatial frequency parameter q_{eff} is remarkable and suggests that q_{eff} itself is a robust indicator of intrinsic properties of the sample with a distinct physical interpretation. Mapping q_{eff} via the correlation time in an imaging context may provide a means to characterize the spatial variations of fields produced by perturbing structures without being significantly influenced by gradient strengths. This was shown to be quick and feasible in polystyrene phantoms by combining just three images (*84*). In biological tissues mapping q_{eff} has potential, for example, for estimating mean microvascular densities and sizes in tumor regions with chaotic vasculature, or helping interpret the nature of fMRI activation maps by identifying the scale of vascular structures. Recently, Rane et al. showed that by adding a spin-lock prep pulse before a turbo spin-echo (TSE) sequence in human fMRI studies of the brain, smaller vasculature could be emphasized over larger venous structures to increase the spatial selectivity of the BOLD effect (*9*). The increase of oxygenated blood upon activation decreases extravascular gradients, but by judicious choice of the locking field the dephasing effects caused by larger structures can be suppressed. The TSE-fMRI applications will be described in further detail in chapter 7. This sensitivity to structural geometry in spin-locking methods is not readily available in other exchange sensitive techniques like CEST. There are also likely to be applications of this approach for the characterization of inhomogeneities in other media in which nuclear spins are able to diffuse.

$R_{1\rho}$ Diffusion Experiments

Diffusion effects have been shown through simulations to significantly influence $R_{1\rho}$ relaxation in a manner that only increases with static field strength, but relatively few studies have explicitly examined or demonstrated this experimentally. Lammentausta et al. (*170*)

reported diffusion effects of water in trabecular bone, but their results show a different behavior to this work and behave contrary to theoretical expectations. The cause of the discrepancy is unclear, but it may be noted that the gradients they studied may have been stronger and they studied mainly stronger locking fields and worked at lower main field. Others (*188*, *189*) have reported measurements of $R_{1\rho}$ but not the dispersion with locking field. Here, significant dispersion in $R_{1\rho}$ with locking field was apparent for all polystyrene microsphere samples shown in Figure 48.

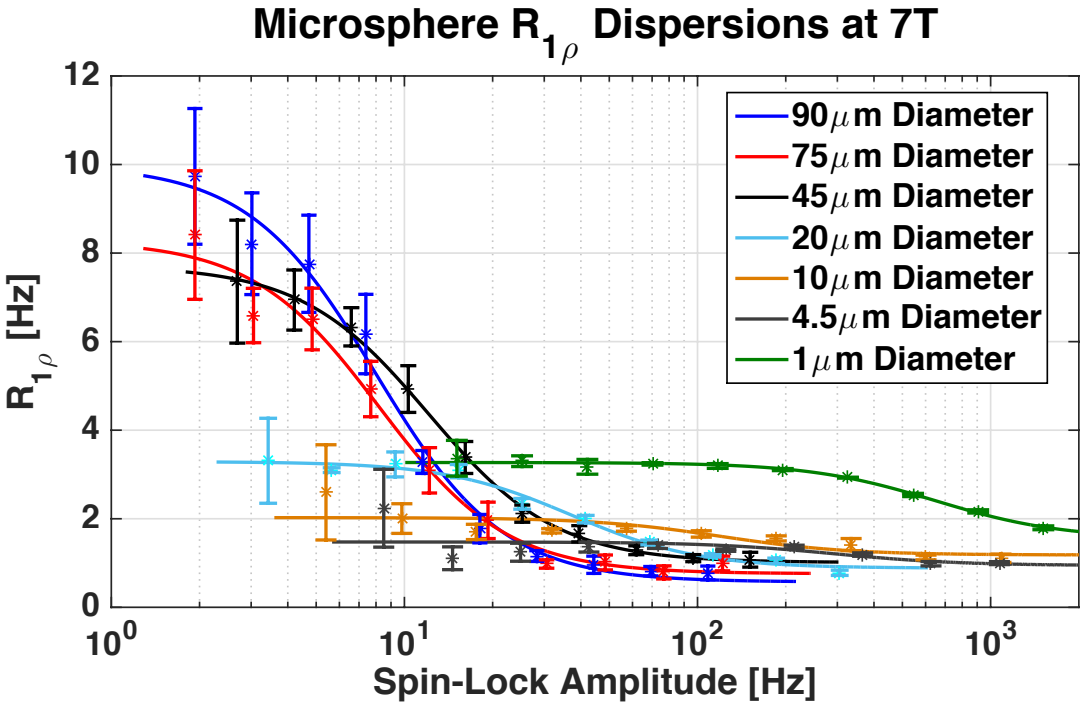

Figure 48: $R_{1\rho}$ dispersions of polystyrene microspheres ranging from 1 - 90 µm in diameter.

The behaviors of the dispersions are consistent with simulations in the sense that smaller packed beads generate $R_{1\rho}$ dispersions with higher inflection points (smaller correlation times) and smaller dispersion magnitudes. Even though all samples were polystyrene, the 1 µm diameter

micrsospheres were crosslinked with Divinylbenzene (DVB) during the manufacturing process, which may account for the faster relaxation rates shown by the green curve in Figure 48. Even with this deviation in the asymptotic relaxation limits, the 1 μm diameter sample still follows the trend of the inflection frequency. The gradient (g^2D) and inverse correlation time (q^2D) parameters were estimated in the fitting process to evaluate the intrinsic gradient strengths between spheres and a measure of the average spacing between spheres.

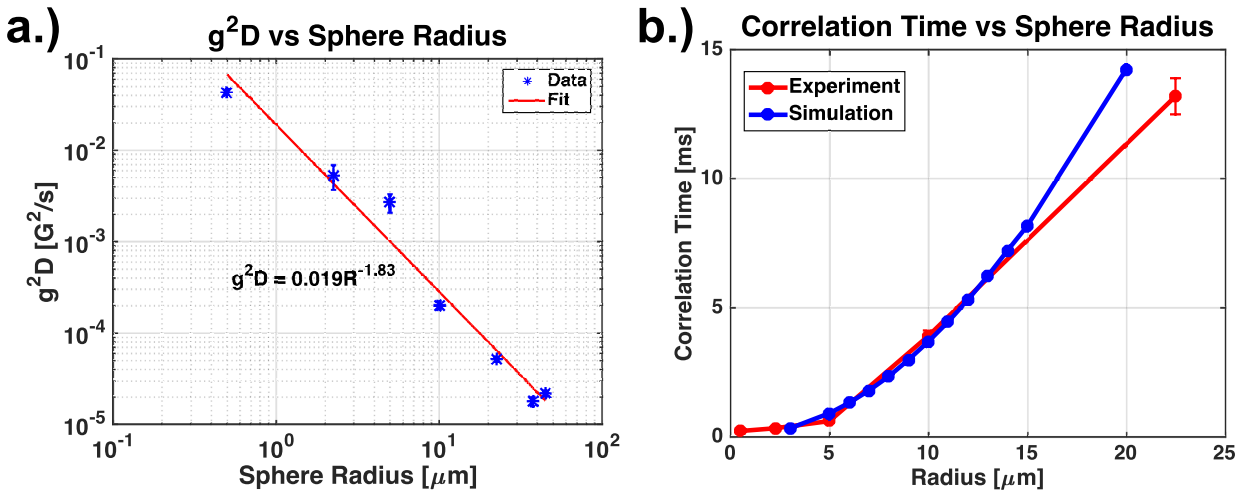

Figure 49: a.) g^2D plotted versus radius shows a gradient strength dependence of $r^{-0.915}$. b.) Experimental correlation times (red) are shown to match well with the simulated correlation times (blue) from the BCC structures.

Figure 49a shows how the gradient parameter decreases with sphere radius, as expected. Taking the derivative of $\Delta B_z^{\text{sphere}}$ in Eq. 4.22 reveals the gradient strength, g, at the surface ($r = a$) of the sphere should fall off as $\frac{1}{r}$, close to the fitted value of $r^{-0.915}$ exhibited here. Figure 49b shows the correlation times, τ_c, for the microspheres agree well with the BCC simulations described earlier, but begin to diverge for larger radii. This effect was thought to be due to the tighter

packing of the larger beads since they settled much faster, which would explain lower correlation times than the simulations that were exactly a volume fraction of 60%. It should be noted the simulated results did not include radii below 3 μm due to the computation time necessary to carry out the simulations with these spatial resolutions. Also, whereas double dispersion curves are observed when there are 2 exchanging species, they not expected for diffusion amongst mixtures of different sized inhomogeneities. The double dispersion for mixtures of compounds with different chemical shifts reflects the discrete possibilities of frequencies of the exchanging species. By contrast, dephasing by diffusion corresponds to motion through a continuously varying field, and the addition of different sized inhomogeneities merely changes the scales and magnitudes of gradient values to still form a smoothly varying field distribution that will be averaged in the experimental signal acquisition.

The microsphere samples were also imaged to derive correlation time maps using Eq. 4.21 and to test this method for different sphere volume fractions. Figure 50a shows the correlation time map for the samples with sphere diameters of 1 μm, 4.5 μm, 10 μm, and 20 μm.

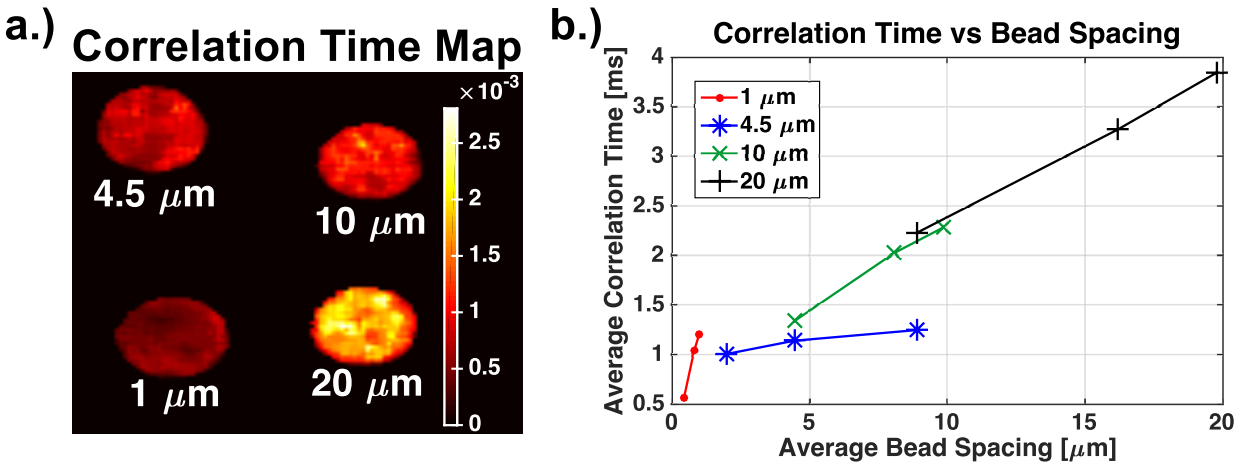

Figure 50: a.) Correlation time map (seconds) for microsphere samples ranging from 1 - 20 μm in diameter. b.) Correlation times for each sample with different sphere spacings achieved by diluting.

Mapping the correlation times clearly provides image contrast that reflects the size of the spheres. This method looks to have potential in mapping cell sizes or vessel sizes in relatively homogeneous tissues since Figure 50a generated ~4x the image intensity that corresponds to a size difference of 9.5 μm in radius. The average correlation times from the imaging method were plotted versus the average spacing between the spheres shown in Figure 50b. The points for each sample correspond to the spheres being dispersed in 20 μL, 120 μL, and 220 μL of water respectively. The correlation time increased almost linearly with bead spacing since this corresponded to lower sphere volume fractions. This provides a reasonably fast procedure for estimating the correlation times without collecting entire dispersion curves, though it should be noted that the choice in locking amplitude of the intermediate image should be chosen based on the position of the inflection points to maximize the accuracy of the method. Thus, knowing the dispersion behaviors may still be important, even if the correlation times are the only parameters of interest.

Conclusions

Random Brownian motion of water in the presence of intrinsic susceptibility gradients has been shown to induce significant rotating frame relaxation at low locking fields. Measuring the dispersion in $R_{1\rho}$ for systems containing magnetic inhomogeneities can provide information about the spatial extent or the geometry of the perturbers. The simulations show the spatial frequency parameter, q, directly reflects the characteristic frequency of the spatially fluctuating field experienced by diffusing protons and is independent of the gradient strength. This spatial frequency of the field cannot be measured directly, but the above simulations show derived values of q parameter may act as adequate surrogate measures of intrinsic structure. One

limitation of the simulation study was that some of the results were affected by the discrete pixelation of the structures, which may have affected the estimation of spatial frequencies, especially in the volume fraction simulations. Changing the radius with constant volume fraction was the equivalent to keeping the same structure and simply increasing the assigned voxel spacings, but changing the volume fraction meant calculating entirely new structures. The digital resolution of the structures and relative resolution of the ΔB_z fields tended to decrease with smaller volume fractions, and edge effects may cause voxels immediately surrounding the spheres or cylinders to be weighted more as simulated spins spend more time on average in these positions. Lower spatial resolution of stronger gradients may result in a more smoothed gradient field that changes the spatial frequency spectra. However, the simulations with varying matrix sizes in figure 3b show that the resolution had a small effect on the R_2 limit and did not significantly change the calculated inflection frequency. The effect should be evaluated but does not change any of the trends of the simulations presented here. The data above clearly show this method may be used to infer average spatial distributions on the sub-voxel level.

Spin-echo and gradient-echo measurements have previously been shown to characterize susceptibility variations within tissues, and appropriate comparisons between these have been used to infer spatial scales e.g. vessel size imaging (*77*, *190–193*). Here, an alternative approach is shown using a spin-locking imaging method to derive parametric images characterizing the dimensions of inhomogeneities that, at high field, cause dephasing via diffusion. Note that for scales of practical interest, these dispersion effects occur at much lower frequencies than the range in which chemical exchange effects between labile protons and water cause dispersion in $R_{1\rho}$ with locking field, which should allow for separate analysis of each relaxation mechanism (*91*). Further imaging studies examining the behavior of different media and the influence of

microvasculature will be of particular interest. Tissue microvasculature may be considered as producing susceptibility inhomogeneities within tissues with a characteristic scale and separation. However, the simple theory outlined here, while providing a useful pragmatic guide to the interaction of rotating frame relaxation and diffusion in inhomogeneous materials, may need to be refined for accurate practical applications in more complex media. For example, more complex and realistic correlation functions may be required to properly describe vasculature in which multiple scale parameters and modified assumptions must be incorporated, as have previously been considered for transverse relaxation effects (*78–81*). For the more general case, as long as the correlation function decays exponentially, the same type of $R_{1\rho}$ dependence is predicted but with a more realistic and appropriate interpretation of the effective spatial frequency q_{eff}. Other specific cases have been investigated by others for other relaxation processes (*78*, *176*, *179*, *194*). One other caveat to using this method is the correlation time will have a direct dependence on temperature due to its relation to the diffusion coefficient, *D*. This may complicate certain experiments, but as long as the temperature remains constant throughout the duration of an experiment, this dependence may be largely ignored. This theory does provide a basis for using spin-locking pulse sequences to quantify tissue parameters based on either gradient strength or spatial geometry. Other applications of interest for this technique that will be explored later include analyzing systems with both diffusion and chemical exchange (such as blood) or emphasizing specific vessel sizes in fMRI activation experiments.

CHAPTER 6

Analyzing Systems With Both Chemical Exchange and Diffusion in the Presence of Susceptibility Gradients With $R_{1\rho}$ Dispersion

Introduction and Theory

Few prior reports of spin-lock imaging have emphasized its ability to quantify dynamic processes such as chemical exchange or diffusion at high fields. Both exchange and diffusion in the presence of susceptibility gradients create dispersion in $R_{1\rho}$ by inducing rapidly changing local fields that experienced by the protons of interest. Each of these effects has been shown in previous chapters to contribute to rotating frame relaxation in a manner that may be analyzed to indicate the time scale of the changing local fields experienced by the spins. In realistic tissue systems, both effects are often present and may be simultaneously significant. The processes are believed to be independent of each other and therefore each will contribute a single $R_{1\rho}$ dispersion, resulting in a double dispersion similar to the case of three-pool exchange explained earlier. Relevant systems such as blood, liver, regions tissues with dense microvasculature, or any tissues that accumulate iron-bearing proteins are complex and may exhibit both effects simultaneously. Blood, for example, may contain low concentrations of multiple exchanging metabolites like glucose and creatine in the plasma, while simultaneously consisting of a significant amount of red blood cells (RBC's) that can hold either oxygenated or deoxygenated hemoglobin that will cause diffusion effects due to their drastically different susceptibility (*195*, *196*). This means there could be a significant exchange and/or diffusion effects contributing to the overall $R_{1\rho}$ dispersion in different locking regimes. Most of the exchange processes naturally occurring in blood are all close in exchange rates and add to produce an overall coalesced

dispersion that is difficult to resolve, similar to the example in Figure 32a,b. Differentiating the contributions from individual metabolites cannot be achieved in this case, but a general exchange based dispersion that encompasses all the metabolites may be defined. A pictorial example of simultaneous diffusion and chemical exchange is shown in Figure 51.

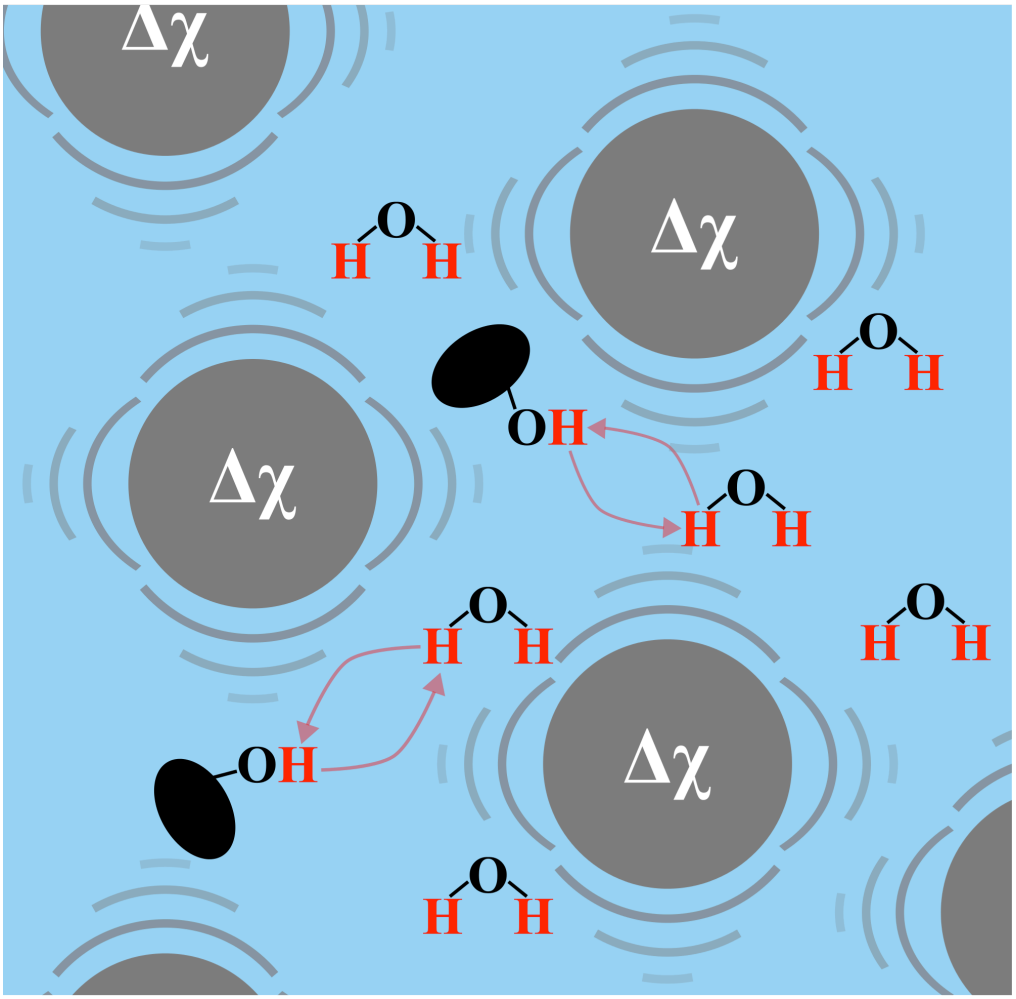

Figure 51: Illustration of chemical exchange occurring in the presence of susceptibility gradients.

Dispersion resulting from proton diffusion through susceptibility gradients will typically occur at much lower locking amplitudes than the exchange based dispersion since the time scale of the

interactions dictates the inflection point frequencies. The representation in Figure 51 is not drawn to scale, but the magnetic perturbers are orders of magnitude larger than the molecules undergoing exchange so diffusion about these will be relatively slow. The local field experienced by a proton in hydroxyl exchange fluctuates much faster than a proton diffusing around inclusions on the order of 1-100 μm in diameter, which means all the diffusion effects will contribute to a general diffusion based dispersion at lower locking fields than the dispersion arising from exchange based contributions.

The overarching theory to how a system with both diffusion and exchange would affect $R_{1\rho}$ dispersion has already been explained in chapters 2, 3, and 5 since these processes should act similar with or without the other, so this theory is a special case extension of those. The 3-pool simulations and experiments described in chapter 3 demonstrated simultaneous chemical exchange between different metabolites with unique exchange parameters gave rise to linearly independent $R_{1\rho}$ dispersions. For this reason and the lack of evidence suggesting local field variations may affect exchange rates, exchange and diffusion are also expected to be independent processes that contribute unique $R_{1\rho}$ dispersions. This may be represented explicitly by Eq. 5.1.

$$R_{1\rho} = R_{1\rho}^{\text{Exch.}} + R_{1\rho}^{\text{Diff.}} = \left[\frac{R_2 + \frac{R_{1\rho}^{\infty}\omega_1^2}{S_\rho^2}}{1 + \frac{\omega_1^2}{S_\rho^2}} \right] + \left[\frac{\gamma^2 g^2 D}{\left(q^2 D\right)^2 + \omega_1^2} \right] \qquad 5.1$$

This expression may be used to describe a system containing a dominant exchanging pool and with significant intrinsic gradients that affect water diffusion and to fit for R_2, $R_{1\rho}^{\infty}$, S_ρ^2, g^2D, and q^2D. Similar to the case of *n*-pool exchange where only two solute pools could be accounted for in the analysis due to practical limitations in the fitting procedure, only one exchange based

dispersion and one diffusion based dispersion can practically be accounted for with Eq. 5.1. More than two dispersions in the experimentally accessible spin-lock amplitude range would result in excessive overlap, generating high uncertainty in the estimation of all parameters. When multiple exchange pools contribute to very similar overlapping dispersions, the resulting estimated parameters will reflect the weighted average of solute pools. This is a fundamental limitation to spin-locking but the theory may still be useful when the diffusion and exchange dispersions can be resolved.

Specific Aims

Aim 1

Previous studies have not demonstrated exchange and diffusion effects are independent in their contributions to spin-locking experiments, or have tried resolving these effects using $R_{1\rho}$ dispersion analysis. The first goal of this chapter is to test the feasibility of analyzing systems with both chemical exchange and diffusion present by adding chemical exchange to the 3D finite difference simulations in chapter 5. These results will be compared to simulated cases of pure exchange and diffusion with the same simulated parameters by themselves to demonstrate their independent nature.

Aim 2

Realistic biological media present new challenges in terms of having different susceptibility variations, random geometries, and multiple exchanging metabolites present. This theory will be used to confirm these effects can be analyzed simultaneously in the physiologically relevant system of whole bovine blood *ex vivo*. Blood exemplifies a system with multiple exchanging metabolites with similar exchange parameters, which will test the ability of

this method to produce average exchange parameter estimates in the presence of diffusion.

Aim 3

Other solid biological tissues will not be as homogeneous as blood since there will be blood present with vasculature and other tissue interfaces. Measuring $R_{1\rho}$ dispersions in livers with and without a susceptibility contrast agent will confirm the feasibility of this technique to assess cell sizes in relatively homogeneous regions of solid tissues.

Methods

Simulations with Exchange and Diffusion

Both chemical exchange and diffusion have been shown through simulations and experiments to significantly contribute to $R_{1\rho}$ dispersions measured with spin-locking pulse sequences separately. Both effects were simulated simultaneously using spatially resolves Bloch McConnell equations with the same finite difference method described in chapter 5.

$$\begin{aligned}
\frac{dM_x^a(t)}{dt} &= \Delta\omega_a M_y^a(t) - R_2^a M_x^a(t) - k_{ab} M_x^a(t) + k_{ba} M_x^b(t) \\
\frac{dM_x^b(t)}{dt} &= \Delta\omega_b M_y^b(t) - R_2^b M_x^b(t) - k_{ba} M_x^b(t) + k_{ab} M_x^a(t) \\
\\
\frac{dM_y^a(t)}{dt} &= -\Delta\omega_a M_x^a(t) - R_2^a M_y^a(t) + \omega_1 M_z^a(t) - k_{ab} M_y^a(t) + k_{ba} M_y^b(t) \\
\frac{dM_y^b(t)}{dt} &= -\Delta\omega_b M_x^b(t) - R_2^b M_y^b(t) + \omega_1 M_z^b(t) - k_{ba} M_y^b(t) + k_{ab} M_y^a(t) \\
\\
\frac{dM_z^a(t)}{dt} &= -\omega_1 M_y^a(t) - R_1^a \left[M_z^a(t) - M_0^a \right] - k_{ab} M_z^a(t) + k_{ba} M_z^b(t) \\
\frac{dM_z^b(t)}{dt} &= -\omega_1 M_y^b(t) - R_1^b \left[M_z^b(t) - M_0^b \right] - k_{ba} M_z^b(t) + k_{ab} M_z^a(t)
\end{aligned} \qquad 5.2$$

These are simply the 2-pool Bloch McConnell equations, but now the chemical shift terms ($\Delta\omega_a$, $\Delta\omega_b$) are 3D matrices describing the spatially resolved local field offset due to the susceptibility variations and the spatially independent chemical shift of the respective pool. This method assumed the concentration of both pools was constant everywhere (well mixed), the exchanging system is in equilibrium, and that diffusion has no effect on the exchange rate. Simulations were performed using the same BCC structures described in chapter 5 with 12 locking fields varying from B_1 = 10 - 5,000 Hz, k_b = 6,000 Hz, a solute chemical shift of $\Delta\omega_b$ = 3 ppm, and a time step dt = 400 ns to ensure $k_b dt << 1$ in order to keep the simulation stable. The structures were kept at a constant volume fraction of 60% while the radii were varied from 5 – 12 μm. When exchange was added, small but significant oscillations were observed in the signal decay with low locking fields caused by off-resonance effects so, rather than fitting to a monoexponential decay model, the approach of Yaun et al. was adopted to account for these oscillations with a $T_{2\rho}$ term in the following equation (*197*).

$$\text{Signal} = S_0\left[\cos(\alpha)\cos^2(\theta)e^{-\text{SLT}/T_{2\rho}} + \sin^2(\theta)e^{-\text{SLT}/T_{1\rho}}\right] \qquad 5.3$$

In Eq. 5.3, $\alpha = \frac{\text{SLT}}{2}\sqrt{\omega_1^2 + \Delta\omega_0^2}$, $\theta = \tan^{-1}\left(\omega_1 / \Delta\omega_0\right)$, and SLT was the spin-locking time. With low locking field, $\theta \to 0$ and the oscillatory $T_{2\rho}$ term becomes significant, but goes to zero as ω_1 >> $\Delta\omega_0$. The $R_{1\rho}$ values estimated using this model were plotted and fit to the model described in Eq. 5.1. The estimated diffusion and exchange parameters from the system with both effects were compared to the parameters from systems with diffusion and exchange alone for accuracy and consistency. The individual simulations were performed on the same structures with either $\Delta\chi$ = 0 (no diffusion effects) or p_b = 0 (no exchange effects).

Measuring $R_{1\rho}$ Dispersions in Blood

Measuring double dispersions in biological media presents more potential complications than are encountered in simulations such as noisy signal acquisitions, physiological motion, or very low concentrations of exchanging metabolites. In order to demonstrate that diffusion and chemical exchange effects are independent experimentally, the simple system of bovine blood with varying levels of oxygen saturation was chosen for analysis. The *ex vivo* system of whole blood made it possible to prevent any physiologic motion and boast relatively high metabolite concentrations in the plasma. Fresh whole bovine blood with Na-Citrate anticoagulant (Lampire Biological Laboratories) was acquired and the blood was bubbled with pure O_2 to achieve oxygen saturations of 70, 73, 77, 85, 89, and 94%, as measured by a blood gas analyzer. Changing the blood oxygenation will alter the amount of paramagnetic deoxyhemoglobin in the RBC's compared to diamagnetic oxygenated hemoglobin. More deoxyhemoglobin will result in stronger internal susceptibility gradients within the blood and greater low frequency dispersion magnitudes. The blood was constantly rocked to hinder the precipitation of RBC's, and though hematocrit (Hct) was not directly measured, nothing was done to alter the physiologic level which should be ~40% based on previous studies. The blood was then immediately placed in 5 mm NMR tubes and imaged at 7 T with a $T_{1\rho}$-weighted Fast Spin-Echo sequence using a repetition time of TR = 2 sec, echo train length of 4, 64x64 voxel matrix, and six logarithmically spaced spin-lock times from 10-100 ms, each measured at 10 logarithmically spaced spin-lock amplitudes ranging from 50-6,000 Hz. ROI analysis was performed on each sample to evaluate the average signal intensity of each sample for every locking time and amplitude. There was no evidence of oscillations in the acquired signal decays so the decay points were fit to a simple monoexponential decay function to estimate $R_{1\rho}$. The resulting double dispersions were fit to the

model in Eq. 5.1 to estimate exchange and diffusion parameters simultaneously for each oxygen saturation level. The two components of the fitted double dispersion were separated compared for each oxygen saturation to identify and quantify the trends in the low frequency diffusion based dispersion, since only the diffusion effects should be altered by the oxygen saturation.

Measuring $R_{1\rho}$ Dispersions in Rat Liver

Pools of whole blood constituted a very simplistic biological system, but in solid tissues more interfaces will be present and the medium may be much more complex. Rat livers were examined due to their large (~5% body weight), relatively homogenous nature with respect to other organs that have very similar vasculature to human livers (*198*). Liver cells, vessels, and metabolites like glycogen will all contribute to the overall $R_{1\rho}$ dispersion. Four healthy Sprague-Dawley Rats were sacrificed and the livers were immediately removed, placed in a plastic tube, and imaged at 7T using a spin-lock prepped fast spin-echo pulse sequence with TR = 5 sec., an echo train length of 4, 15 locking amplitudes from 1 – 2,000 Hz, each with 6 locking times from 10 – 80 ms. The 90 images for each liver were acquired with 64x64 matrix and a 16 mm field of view (250 μm resolution), and ROI analysis was performed to estimate the average signal intensity at every locking time and amplitude. The signal was again fit to a monoexponential decay model to estimate $R_{1\rho}$, and the double dispersion was fit to Eq. 5.1 to quantify the diffusion and exchange parameters. Four additional rats were sedated with isoflurane, given a tail vein injection of 0.5 mmol/kg Gd-DTPA, and kept alive for 10 minutes post injection to allow for the agent to circulate and accumulate in the extravascular extracellular space in the liver naturally before being sacrificed to remove the livers. The gadolinium was expected to pool in the extracellular space of the liver and not the vessels, so the dispersions with Gd-DTPA should emphasize the effects on magnetic inhomogeneity of the liver cells over the vessels.

Results and Discussion

Simulations with Exchange and Diffusion

Simulating chemical exchange in the presence of diffusion effects was expected to produce linearly independent $R_{1\rho}$ dispersions similar to the manner 3-pool exchange gave rise to independent double dispersions. The linear independence assumption in the situation of exchange and diffusion should be more accurate since the pool fraction ratios do not change as they did when a third pool was added in the exchange simulation in chapter 3. Analyzing the $R_{1\rho}$ simulations showed both exchange and diffusion are independent of each other and can be analyzed simultaneously when the inflection points of the two resulting dispersions are separated by a reasonable frequency difference. Figure 52a shows the simulated double dispersions resulting from the BCC unit cells with radii from 5 – 12 μm. The exchange and diffusion time scales are different enough for the double dispersions to be distinctive in most of the simulated cases, but they begin to coalesce as the radius decreases.

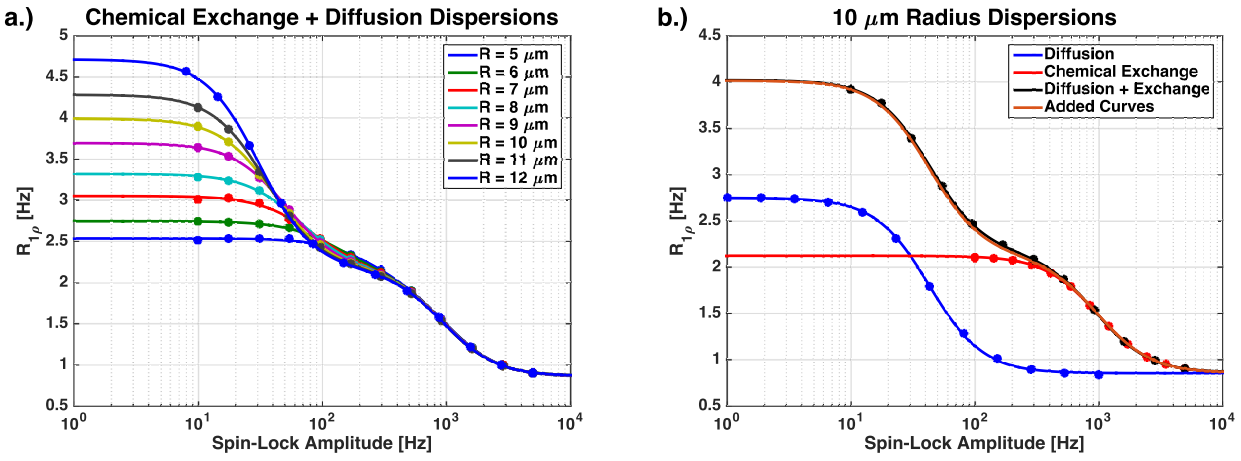

Figure 52: a.) Simulated $R_{1\rho}$ dispersions for the case of chemical exchange and diffusion for the BCC structures. b.) The R = 10 μm double dispersion compared to individual effects shows the effects are independent of one another.

Changing the structural dimensions alters the behavior of the low frequency diffusion based dispersion but has no bearing on the higher frequency exchange based dispersion, as expected. The dispersion magnitudes increased and the inflection points of the diffusion based dispersion decreased in the same manner as the pure diffusion simulations in chapter 5. The effects were shown to be independent of one another in Figure 52b. Adding the pure diffusion (blue) and pure exchange (red) curves results in the orange curve that coincides very well with the simulated black double dispersion. The estimated exchange parameters from the double dispersions were compared to the theoretical values and the diffusion parameters were compared to those from the individual dispersions in Figure 53.

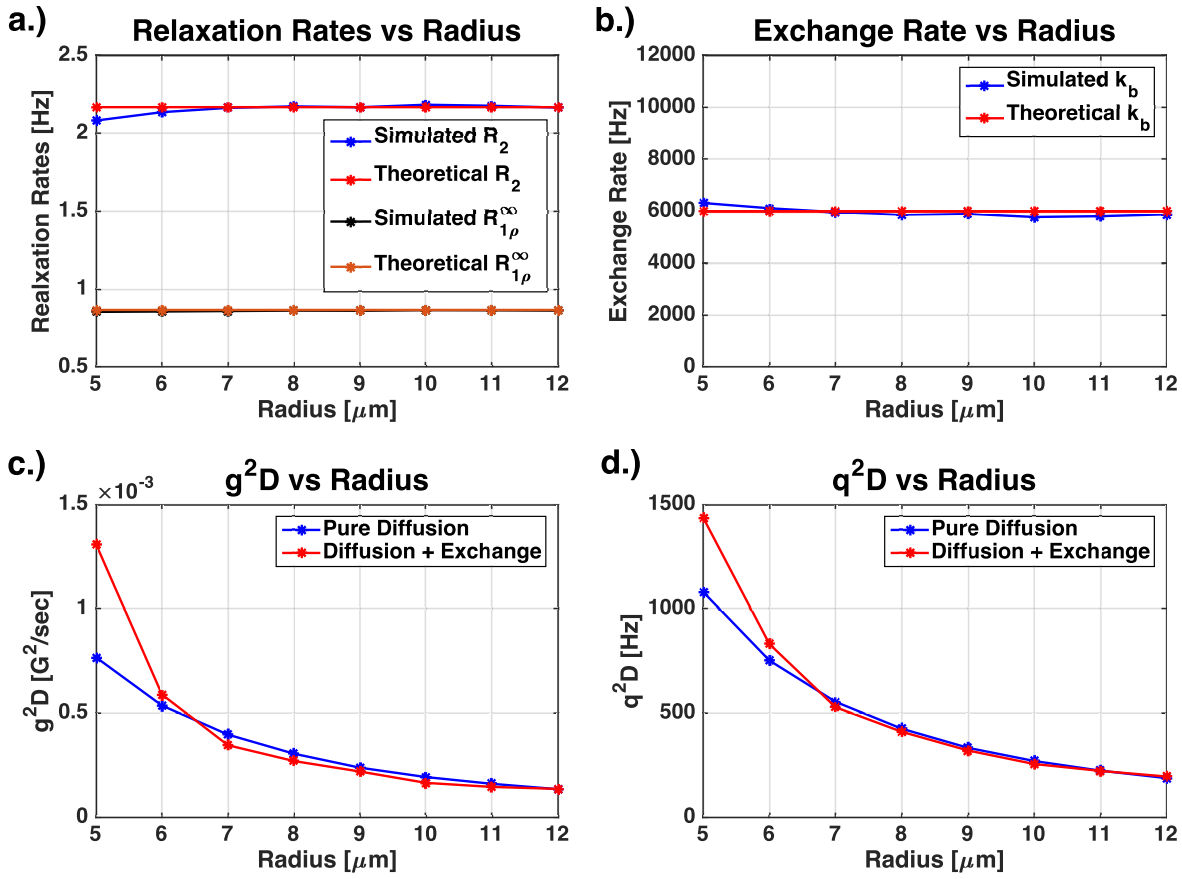

Figure 53: Estimated exchange parameters compared to the theoretical values (a,b). The estimated diffusion parameters were compared to the individual diffusion parameters from chapter 5 (c,d).

The exchange parameters were very consistent and accurately estimated compared to the theoretical values shown in Figure 53a,b. The exchange parameters R_2, $R_{1\rho}^{\infty}$, and k_{ba} varied by less than 4%, 1.5%, and 5.1% respectively for all simulated radii sizes. The general trend for all the parameters was the larger radii structures gave rise to more accurate estimates. This was because the dispersions from the smaller radii structures coalesced and increased the uncertainty in the estimates. The diffusion parameters in Figure 53c,d were not able to be compared to theoretical values, but were instead compared to the estimates from the pure diffusion simulations in chapter 5. The g^2D and q^2D parameters have drastic differences of 52.3% and 28.3% for R = 5 μm respectively, but the estimates are much more accurate for R ≥ 7 μm with percent differences less than 12.5% and 4.8% respectively.

The simulated signal decay curves were notably no longer monoexponential when both effects were present, but could be accounted for by Eq. 5.3. Figure 54 illustrates the difference in the decay curves when both effects are present compared to when only diffusion contributes to the relaxation.

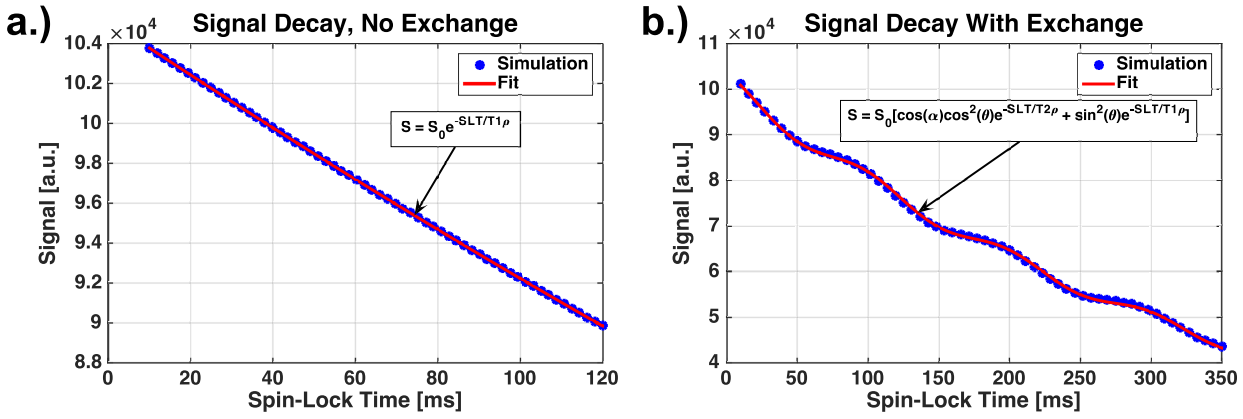

Figure 54: Simulated spin-locked signal decay in the presence of only diffusion (a) and in the presence of both diffusion and exchange (b) may be accounted for with different decay models.

The solid red curves depict the least squares best fit for each scenario and demonstrates the oscillations in the decay curves may be adequately accounted for when present. The $T_{2\rho}$ component in the model needed to be accounted for since the oscillations were present but was ignored for when analyzing the dispersions since only $R_{1\rho}$ was being analyzed. The off-resonance effects were significant enough to produce signal oscillations but were small enough to be accurately accounted for with the model described by Yaun et al. When the off-resonance terms in the Bloch equations become too large, the oscillations may become substantial enough that they cannot be accounted for with Eq. 5.3 and a new model may be needed.

Measuring $R_{1\rho}$ Dispersions in Blood

$R_{1\rho}$ dispersion in whole blood should be affected by both diffusion about susceptibility gradients due to the presence of deoxyhemoglobin in RBC's, and chemical exchange from metabolites in the surrounding plasma. $R_{1\rho}$ maps were calculated for each of the 10 locking amplitudes, and the map corresponding to the amplitude of 50 Hz is shown in Figure 55a.

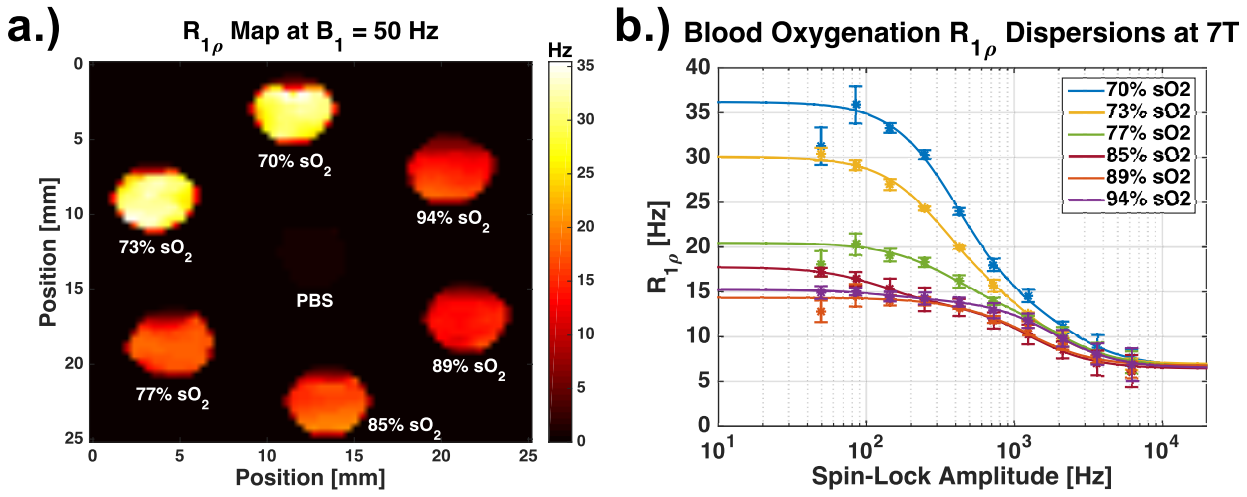

Figure 55: a.) $R_{1\rho}$ map calculated in whole bovine blood at the locking field of 50 Hz for all oxygenation levels. b.) The corresponding $R_{1\rho}$ double dispersions.

Note the manner in which the relaxation rates tend to increase at the bottom of each sample, which is thought to be due to the settling of the blood cells throughout the scan. This behavior was unavoidable since rocking the blood during the scan would be very difficult and cause considerable artifacts. Keeping this in mind, the dispersion points were calculated using ROI analysis over the bottom half of each sample to ensure the high RBC concentrations were captured and the diffusion effects would be significant. The blood double dispersions calculated from $R_{1\rho}$ maps using Eq. 5.1 are shown in Figure 55b confirm higher relaxation rates were measureable in the lower oxygen saturation samples due to the presence of more paramagnetic deoxyhemoglobin in the RBC's. The double dispersion phenomenon is apparent in these curves and the individual fitted contributions of diffusion and chemical exchange from Eq. 5.1 are plotted in Figure 56a.

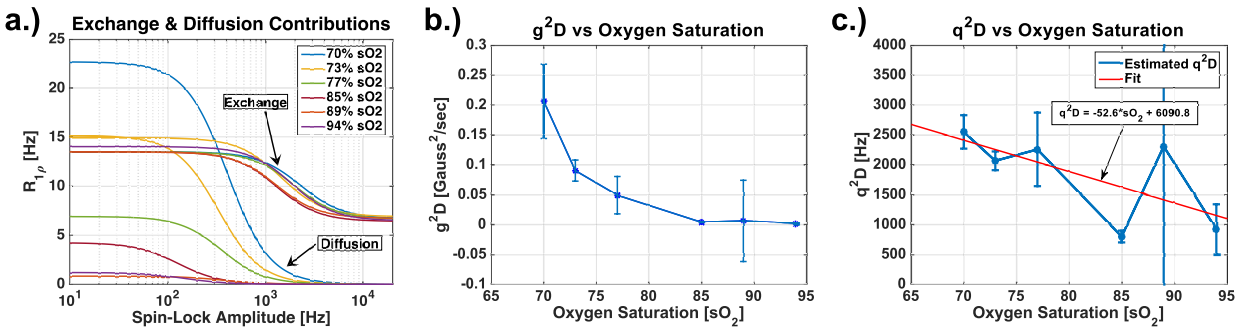

Figure 56: a.) The exchange and diffusion portions of Eq. 6.1 are plotted individually to show the manner in which the diffusion dispersion decreases with oxygen saturation. b.) The gradient strength parameter decreases as expected with sO_2. c.) The spatial frequency parameter decreases with sO_2 indicating a smaller concentration of cells containing deoxyhemoglobin.

Note how the chemical exchange based curves stayed relatively consistent while the diffusion based curves were greatly affected by oxygen saturation and diminish as the deoxyhemoglobin constituent in the blood decreases. The g^2D parameter used in the fitting procedure represents the

mean field offset magnitude for that dispersion, and is shown to decrease in the expected manner in Figure 56b. The more paramagnetic present in the cells in any given blood sample should correspond to a greater the average internal gradient strength. The spatial frequency parameter, q^2D, displayed a tendency to decrease with a rate of ~53 Hz/% sO_2 corresponding to more space between cells on average with higher saturation levels. This was an unexpected finding since the average cell spacing should remain constant. The average correlation time for all the blood samples was $\tau_c \approx 0.55$ ms, and in order to elucidate the meaning of this calculated parameter, the simulations performed in chapter need to be reexamined. The BCC simulations with varying radii coincided very well with the experimental system of packed polystyrene microspheres, so fitting an exponential curve to the correlation times provides an approximate function that relates τ_c to the radius of the packed spheres.

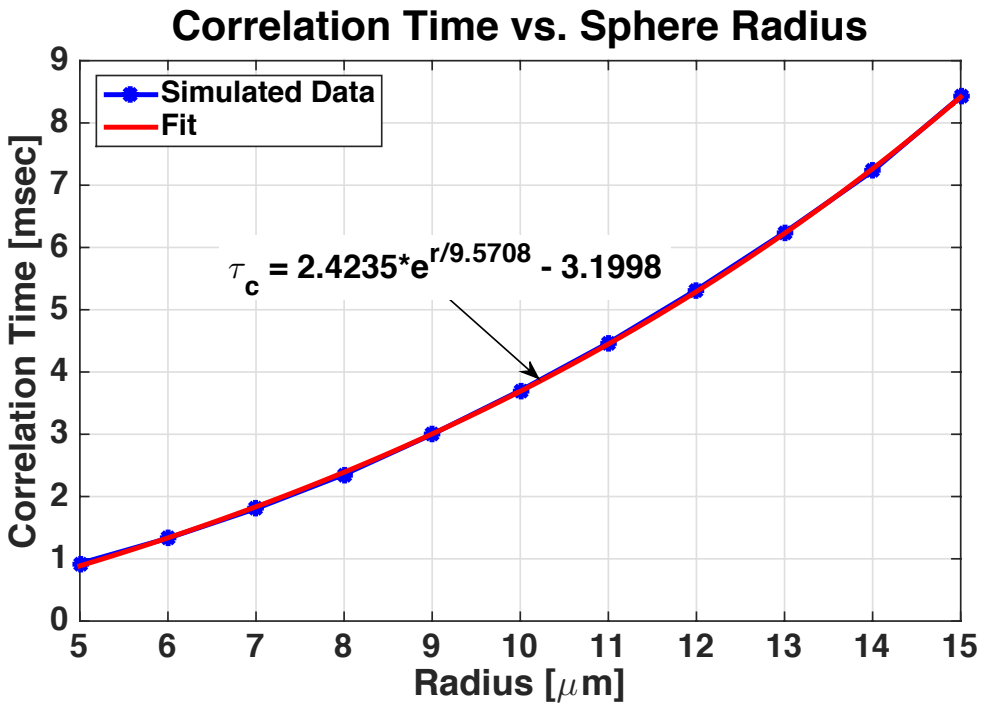

Figure 57: The simulated correlation times from the BCC structures were related to radius by fitting to an exponential model.

This function shown in Figure 57 relates $\tau_c \approx 0.55$ ms to a radius of R ≈ 4.18 μm, within the previously reported range of 3.75 – 4.35 μm (*199*). Given this is not a direct measure of radius and the fact that multiple factors like packing fraction, temperature, or shape of the perturbers may influence the estimated correlation times, this estimate is remarkably accurate compared to the expected range for RBC's.

It is noteworthy that Silvennoinen et. al. performed more elaborate whole bovine blood $R_{1\rho}$ dispersion experiments at 4.7T examining multiple oxygen saturation levels as well as multiple hematocrit levels and a lysate sample (*200*). These experiments revealed similar increases in the low locking field limit, but the locking fields used only went down to 0.2 G (≈ 850 Hz), which is significantly higher than the lower limit of 50 Hz reached in the experiment described above. The higher frequencies are unable to accurately detect the double dispersion phenomenon described in this thesis. Their study concluded that exchange and diffusion effects both influence the dispersion, but also stated that the difference in mobility of hemoglobin in cells and free solution may play a critical role. This may be the case, but for situations when only the oxygen saturation changes, as described above, the high frequency dispersion stays constant and the low frequency dispersion is clearly governed by the oxygenation level and intrinsic susceptibility. Clearly this approach can be used to estimate characteristic dimensions of tissue microstructure related to cell sizes or vascular spacings, depending on what dominates the variation of intrinsic susceptibility.

Measuring $R_{1\rho}$ Dispersions in Rat Liver

Rat livers present more complex tissue structures since there will be blood, vasculature, and multiple types of cells all simultaneously contributing to $R_{1\rho}$ relaxation. Eight fresh rat livers from Sprague-Dawley rats were imaged, 4 with Gd-DTPA injection and 4 controls, with the

resulting $R_{1\rho}$ double dispersions shown below in Figure 58.

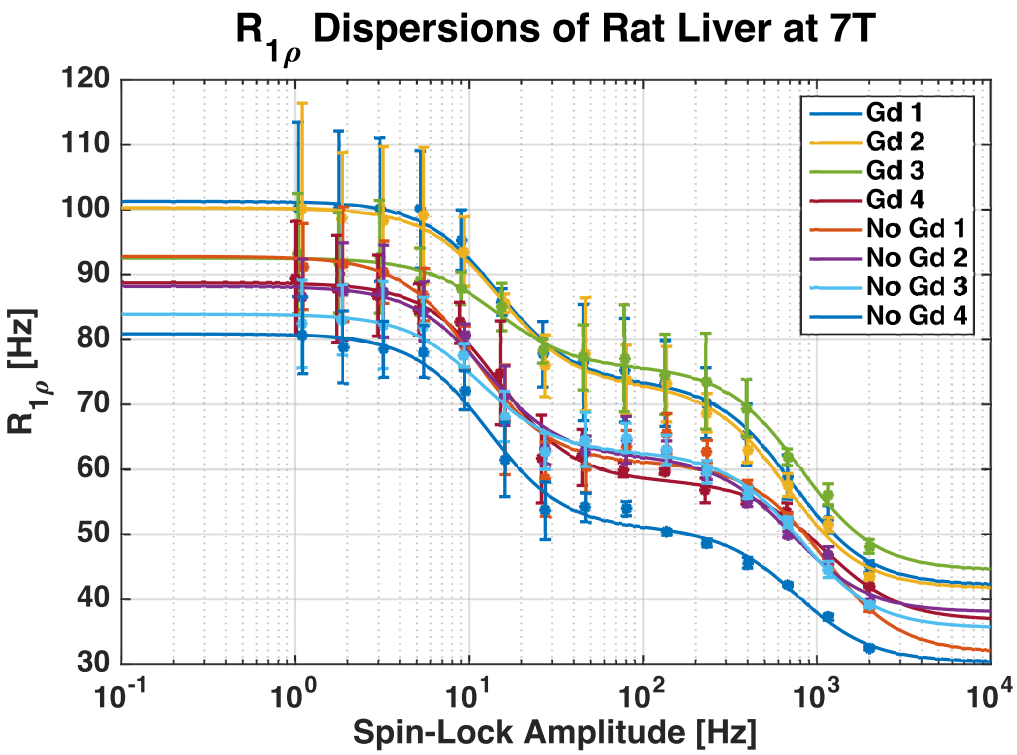

Figure 58: $R_{1\rho}$ dispersions in 8 separate rat livers at 7T, 4 after a tail vein injection of Gd-DTPA and 4 controls without Gd-DTPA.

The relaxation rates are noticeably faster than any of the simulations or phantom studies presented in previous chapters since there are many avenues for relaxation to occur in real tissues. The double dispersion is prominent in every liver, with and without gadolinium, and no noticeable shift in either inflection point due to gadolinium injection can be plainly seen visually from the dispersions. The low frequency dispersions display a very large magnitude and occur at much lower frequencies than detectable exchange based dispersions are expected to arise so the dispersion is most likely due to significant susceptibility effects arising from both the cells and vessels present. Examining the fitted parameters reveals there was no significant difference

between proton exchange rates before and after the Gd-DTPA injection, which exchanged relatively fast with an average estimated exchange rate of k_{ba} = 5,266 Hz. Though this rate may be fast, it is still within reason for the hydroxyl exchange in glycogen at under physiological conditions. Figure 59a shows a statistically significant ($p << 0.05$) decrease in average T_1 before and after injection, which indicated the gadolinium did in fact enter the liver.

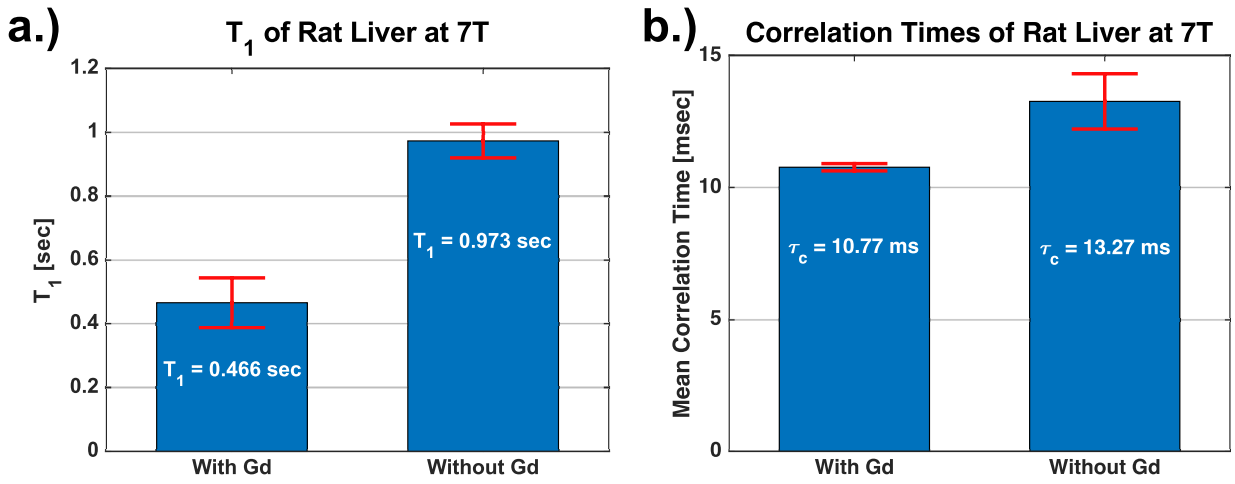

Figure 59: Average values of rat liver T_1 (a) and the correlation times, τ_c (b), before and after a tail vein injection of Gd-DTPA. Both parameters revealed statistically significant changes.

The concentration of Gd-DTPA can be estimated by examining the change in T_1 before and after injection, and can be quantified in Eq. 5.4 shown below (*201*).

$$[\text{Gd-DTPA}] = R\left(\frac{1}{T_1} - \frac{1}{T_{1,\text{Baseline}}}\right) \qquad 5.4$$

Using this formula, the livers were infused with an average concentration of [Gd-DTPA] ≈ 0.25 mM, which is small but significant due to the intrinsic susceptibility of the gadolinium. The statistically significant drop in correlation time from τ_c = 13.27 ms for the controls to τ_c = 10.77

ms with Gd-DTPA ($\Delta\tau_c$ = -2.5 ms) shown in Figure 59b indicated smaller structures were being emphasized in the relaxation process. This provides evidence that the liver cells became more dominant than the vasculature in promoting relaxation, though both probably continued to contribute. The susceptibility of Gd-DTPA is ~3x that of blood, so the cells should indeed dominate any vessels containing blood theoretically (*202–205*). Gd-DTPA should have practically no presence within the vasculature since it was allowed to circulate and pool in the liver naturally for 10 minutes prior to the removal of the liver.

Since the cells should be packed relatively homogeneously, the equation relating correlation time to radius shown in Figure 57 may be used to estimate cell sizes. The model estimates a cells radius of R = 16.8 μm when the Gd-DTPA is present, larger than previously reported values but still reasonable in magnitude (*206*). The overestimated value could be due to multiple factors including the cells being non-spherical, the cells having an unknown structure and packing fraction, and other contributions like intracellular water. The small shift in correlation time, coupled with the fact it was statistically significant, means the cells and the vasculature would give rise to very similar diffusion based dispersions by themselves. It is noteworthy that this scenario differs from the microsphere experiments in chapter 5 and even the blood experiments described above since rather than changing the susceptibility of the perturbers (like in the case of the blood cells), here the susceptibility of the surrounding medium where the diffusion occurs changes with the introduction of extracellular Gd-DTPA. Though the physical situation is reversed, the principle of the gradients resulting from the difference in susceptibilities between the intra- and extracellular spaces remains the same. The intrinsic pool relaxation rates may be slightly altered, but the simulations in chapter 2 showed this to have relatively small effects on the overall exchange based dispersion behavior, and only the low frequency diffusion

based dispersion should change significantly. This method has shown both exchange and diffusion effects may be exploited using $R_{1\rho}$ dispersion methods to infer quantitative information about exchange rates and tissue structures of realistic biological media.

Conclusions

Diffusion is typically a slower process than chemical exchange and can therefore be analyzed simultaneously using $R_{1\rho}$ methods in realistic tissue. The sensitivity of spin-locking pulse sequences to gradient geometry has been exploited to estimate mean spatial frequencies of small inhomogeneities to overall dephasing. Simulations have verified the manner in which free diffusion in the presence of susceptibility-induced gradients promotes dispersion in measurements of $R_{1\rho}$, how chemical exchange acts independently of diffusion and typically occurs on a faster time scale, and that the characteristic inflection point in a dispersion plot reflects a measure of the spatial frequency spectral content of the field distribution for complex three dimensional fields. The point of inflection for diffusion or exchange-based dispersions elucidates the time scale of the respective interactions. This was evident in the double dispersion chemical exchange simulations in chapter 3 where the slower exchange process produces an inflection at a much lower frequency than the faster exchange process. This was also the case in the hybrid systems described above with both diffusion through internal gradients and chemical exchange occurring. The process of water molecules diffusing through a medium typically occurs with $D = 2.5\ \mu m^2/ms$, so gradients that repeat every 10 μm translate to a correlation time of ~1 msec which is much longer than the fast exchange times seen with hydroxyls. Diffusive effects were shown to be detectable in biological tissues and measures of $R_{1\rho}$ dispersion could be used to derive a structural measure of interest. The methods described above very accurately estimated the average size of red blood cells by comparing the dispersions to simulations, and

also predicted the average liver cell size within reason. Further simulations may be needed to examine the effects of non-spherical magnetic perturbers on $R_{1\rho}$ dispersion and the effects of both cells and cylindrical vessels simultaneously promoting $R_{1\rho}$ relaxation. Other experiments examining the increased correlation times in blood with sO_2 and the effects of changing the intravascular space in tissues like the brain should be performed to evaluate if and why the correlation time unexpectedly exhibits a shift. Overall, spin-locking has proven to be a powerful technique with the ability to probe both chemical exchange and diffusion to characterize tissues in a ways previously unavailable.

CHAPTER 7

Spin-Locking Preparation Pulses in Functional MRI

Introduction

The previous chapters have shown how $R_{1\rho}$ measurements may be valuable in a variety of different settings to assess the underlying processes of chemical exchange and diffusion. There are other applications in which $R_{1\rho}$ methods may be useful including functional MRI (fMRI). These experiments are able to detect subtle hemodynamic changes that may result from evoked or resting-state neuronal activity through a mechanism known as the Blood Oxygen Level Dependent (BOLD) effect (*207–209*). The BOLD effect was discovered in 1992 and originates from a change in blood flow and/or volume accompanied with a change in the concentration of RBC's with paramagnetic deoxyhemoglobin (*210*, *211*). This principle has already been shown to be effective in promoting $R_{1\rho}$ relaxation in the previous chapter by imaging whole blood with different oxygen saturation levels. Evoked neuronal activity may result in a hemodynamic rush of oxygenated blood to an activated region that will decrease the local field gradients and result in a slight signal intensity increase. The characteristics of the susceptibility induced gradients have been shown to originate mostly from the influence of deoxyhemoglobin and significantly affect proton transverse relaxation (*71*, *212–215*). Figure 60 illustrates the manner in which deoxyhemoglobin in RBC's generate local field gradients in the intravascular space. Most fMRI studies utilize transverse relaxation described by R_2^* through gradient echo planar imaging (EPI) methods due to their rapid acquisitions and sensitivity to minute changes in local field gradients. Though this technique may be indirectly sensitive to neuronal activity through the BOLD effect, many other factors may affect the acquired signal such as static field strength, echo time (TE), or

changes in blood volume and flow.

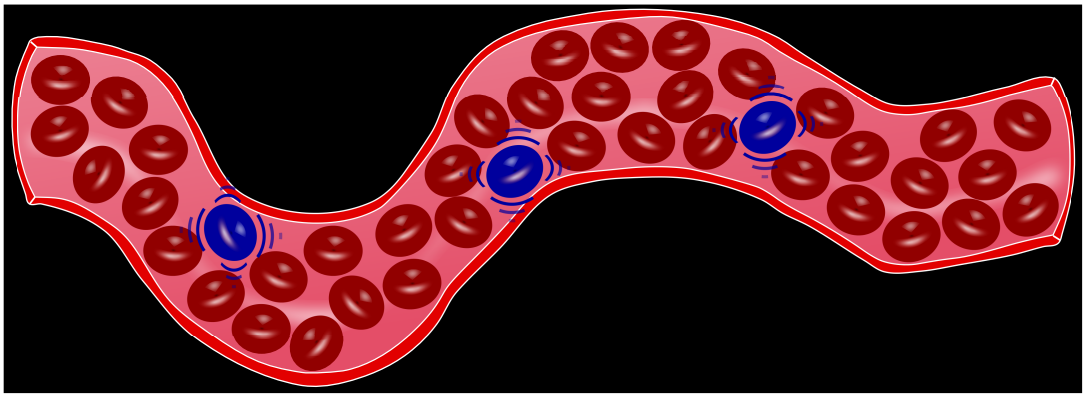

Figure 60: Red blood cells containing paramagnetic deoxyhemoglobin (blue) generate relatively large local field gradients that can induce transverse dephasing.

Signal may also originate from different tissue compartments like the intra- and extravascular space, but the former tend to decrease at high fields resulting in the bulk of the signal originating from the extravascular protons in the tissue, similar to the diffusion simulations performed for cylindrical inhomogeneities described in chapter 5. Spin-echo acquisitions have been used to reduce static dephasing resulting from intrinsic gradients generated by large vessels, but water diffusion through the field gradients in the extravascular space remains significant since it cannot be refocused (*216–219*). These diffusion effects have been shown in previous chapters and by others to be dependent on the magnitude and spatial characteristics of the field gradients, as well as the static field and echo time, which means both gradient-echo and spin-echo sequences will be influenced by greater microvascular effects at high fields (*175*, *220*, *221*).

Spin-locking techniques have been shown in chapters 5 and 6 to be sensitive to the spatial scales of field variations in magnetically inhomogeneous media. Acquiring $R_{1\rho}$ dispersion curves allows the average correlation times to be determined that reflect the average spacing between inclusions, but acquiring the entire dispersion curves is very time consuming in practice and

impractical for fMRI experiments. Though dispersion analysis may be impractical, $R_{1\rho}$ weighted images have been shown previously to be advantageous in fMRI by generating contrast that differs from standard gradient echo acquisitions (*6*, *8*). Most previous studies of $R_{1\rho}$ weighted fMRI have been acquired with relatively high locking amplitudes, typically strengths of $\omega_1 \geq 400$ Hz, and have attributed the relaxation effects to changes in blood volume and chemical exchange (*7*, *222*, *223*). While this may be the case, the contrast in $R_{1\rho}$ weighted images will depend on the spacing between inhomogeneities, which will be a function of the average size and packing fraction as described by the diffusion theory in chapter 5. The rate of relaxation due to diffusion can be quantified by Eq. 6.1.

$$R_{1\rho} = \frac{\gamma^2 g^2 D}{\left(q^2 D\right)^2 + \omega_1^2} \qquad 6.1$$

Here, g is the gradient strength, q is the spatial frequency of the ΔB_z field, and D is the self-diffusion coefficient. The correlation time, $\tau_c = \frac{1}{q^2 D}$, is an important parameter that represents the time needed for a spin to diffuse the characteristic length of the gradient field on average. The relaxation rate will then depend on the relative magnitudes of the correlation time and the locking field, ω_1, so stronger locking amplitudes will tend to suppress relaxation due to structures with higher correlation times. This shows that low locking field $R_{1\rho}$ relaxation will be dominated by large structures with small q values since the rate has a dependence of q^{-4}, and smaller structures will begin to dominate as the locking field becomes larger. Thus, spin-locking enables the ability to selectively emphasize certain ranges of vessel sizes that cannot be effectively done with standard gradient-echo or spin-echo techniques. Without the application of a locking field, the relaxation rate will approach standard diffusion based transverse relaxation,

R_2^{diff}, and possess contrast similar to traditional fMRI experiments that is dominated by large-scale structures like draining veins. Utilizing a lower locking field than previous experiments such as 80 Hz, will prompt $R_{1\rho}$ to exhibit the largest change in contrast to structures with a radius ≈ 8 μm ($q \approx 0.393\ \mu m^{-1}$). For perspective, $R_{1\rho}$ contributions at this locking field from an object with a radius of 1 cm should decrease by a factor of ~10^8 when compared with $R_{1\rho}$ at $\omega_1 = 0$, while an object with radius 0.1 cm will only be decreased by a factor of ~10^4. Effects due to even smaller objects on the order of 1 μm will not be significantly attenuated and will dominate relaxation. Thus, by judiciously selecting an appropriate locking amplitude, the relaxation should emphasize the contributions from smaller structures with significant susceptibility variations that may be of importance like microvasculature. This work attempts to use the selectivity afforded through $R_{1\rho}$ weighted fMRI to compare the contrasts at different locking amplitudes.

Specific Aims

Aim 1

$R_{1\rho}$ methods have rarely been used to measure hemodynamic responses in animal or human brains, and the studies that have used spin-lock prep pulses use only high locking amplitudes. Here, the sensitivity of spin-locking to vessel sizes is used to selectively emphasize vessels of specific dimensions in functional MRI with the hopes of eventually improving the detection of brain activation. $R_{1\rho}$ fMRI will be investigated with low and high locking amplitudes of ω_1 = 80 Hz and 400 Hz respectively to determine their effect on activation maps.

Methods

Eight (5 male, 3 female) live, healthy, adult patient volunteers aged 26 - 32 were imaged at 3T using a $R_{1\rho}$ weighted fMRI protocol approved by the Institutional Review Board. Each

volunteer was subjected to visual checkerboard stimulation that flickered at 8 Hz with equal duration blank display before and after for 7 functional runs consisting of 5 blocks of 36 seconds. Each patient was imaged using a single slice turbo spin echo (TSE) with slices passing through the visual cortex with a matrix size of 96 x 96 and 3 x 3 x 4 mm^3 spatial resolution. Six functional runs using the $R_{1\rho}$ prep pulse described by Witschey et. al. were acquired for ω_1 = 80 Hz and 400 Hz using locking times of 20, 50, and 80 ms with a minimal echo time of TE = 5.3 ms to minimize R_2^* contributions and a repetition time of 2.2 s (*62*). These locking times were chosen based on the previously reported grey matter value of $T_{1\rho} \approx 99$ ms at ω_1 = 500 Hz (*7*). In order to minimize conditioning or other systematic effects, the order of the ω_1 = 80 Hz and 400 Hz acquisitions were randomized. T_2 weighted fMRI images were collected with the same sequence and parameters, but here the locking time was 50 ms and ω_1 = 0 Hz to attain T_2 contrast. Finally, conventional gradient echo EPI fMRI images were collected with matrix size = 96 x 96 with of 3.5 mm isotropic spatial resolution, a repetition time of 2 s, and an echo time of 30 ms. In an effort to reduce the acquisition time, only 3 blocks of the visual checkerboard stimulus was used.

The data were analyzed by combining the ω_1 = 80 Hz and 400 Hz into one time series, leaving out the first and last two time points of the blank screen interval to minimize transition effects. The slices were motion corrected using previously described methods with the Analysis of Functional NeuroImages (AFNI) software package (*224*, *225*). $R_{1\rho}$ maps were calculated at each locking amplitude on a voxel by voxel basis using a linear log fit to each locking time point. Average $R_{1\rho}$ values were calculated in cortical grey and white matter using ROI analysis along with baseline $R_{1\rho}$ values during the blank screen intervals. The fMRI Expert Analysis Tool (FEAT) in the FSL software library was used to fit each series to a general linear model (*226*,

227). The voxels in the visual cortex were corrected for multiple comparisons and only those with an activation threshold $z > 4$ with the standard threshold of $P < 0.05$ were considered for further analysis. Percent signal changes were calculated in the selected voxels for the T_2-weighted sequence and in the voxels for both the $\omega_1 = 80$ Hz and 400 Hz of the $R_{1\rho}$ sequence to calculate the time course of the hemodynamic response. A rate of change in fMRI signal was also calculated for the 11 second transition period (5 points) after the start of the flashing checkerboard by using a linear fit to compare the measured responses from each of the BOLD, T_2-weighted, and both $R_{1\rho}$ methods at $\omega_1 = 80$ Hz and 400 Hz with 50 ms. Statistical significance testing was performed in MATLAB using a paired non-parametric test to report p-values.

Results and Discussion

In the absence of any visual stimuli, there was no statistically significant difference in the $R_{1\rho}$ of white matter or grey matter at $\omega_1 = 80$ Hz and $\omega_1 = 400$ Hz. The white matter displayed values of $R_{1\rho} = 74 \pm 14$ ms and 77 ± 18 ms ($p = 0.89$) at $\omega_1 = 80$ Hz and $\omega_1 = 400$ Hz respectively, while grey matter displayed values of $R_{1\rho} = 91 \pm 17$ ms and 93 ± 16 ms ($p = 0.18$) respectively. This lack of change was important to report since it shows no significant dispersion in either tissue with locking field at 3T. Previous experiments have shown dispersion in tissues may be quite large under certain conditions, but the locking fields used here are lower than those used for chemical exchange experiments and the static field is significantly lower than all experiments described in previous chapters ($\geq$ 4.7T). Even if chemical exchange contributed, the locking fields used were not strong enough to overcome their contribution to relaxation, making them inconsequential. This shows that there is no statistically significant change in tissue relaxation rate due to changes in the concentration of deoxyhemoglobin while at rest.

The checkerboard visual stimulus did elicit statistically significant changes throughout the visual cortex. Figure 61 shows the activation maps with the corresponding Z-scores for one volunteer using each of the gradient–echo BOLD, T_2 prepared BOLD, 80 Hz $T_{1\rho}$ prepped, and 400 Hz $T_{1\rho}$ prepped pulse sequences.

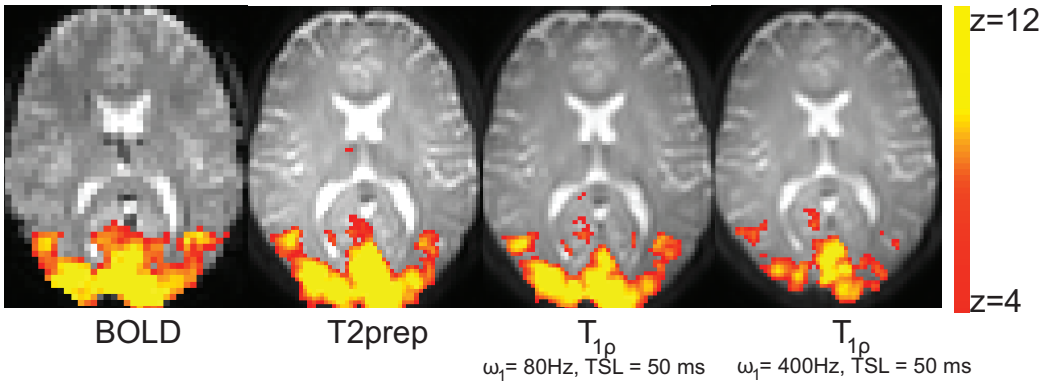

Figure 61: Activation maps for one volunteer using each sequence. The number of significant pixels decreases from left to right due to the sequences becoming more selective.

Comparing the activation map derived from the $R_{1\rho}$ weighted images with the standard activation maps shows this method is more selective in their detection. The number of significant voxels for each sequence decreased from left to right since each of the sequences became more selective by either refocusing magnetization or increasing the locking amplitude of the preparation pulses. The $T_{1\rho}$-weighted image corresponding to $\omega_1 = 400$ Hz exhibited a drastic decrease in significant voxels ($p < 0.01$) when compared to the other three images, which can be interpreted to be due to the strength of the locking pulse overcoming the majority of the susceptibility induced dephasing from the deoxyhemoglobin in large vessels. Though the low resolution inhibits finer differentiation of vasculature contributions, the interpretation follows from the results of the diffusion experiments in previous chapters. For completeness, the voxels in the frontal cortex were analyzed as a control region and showed no statistically significant change in signal with

the application of the visual stimulus. Figure 62 shows the time course of both the frontal cortex and visual cortex to illustrate the effect in both regions.

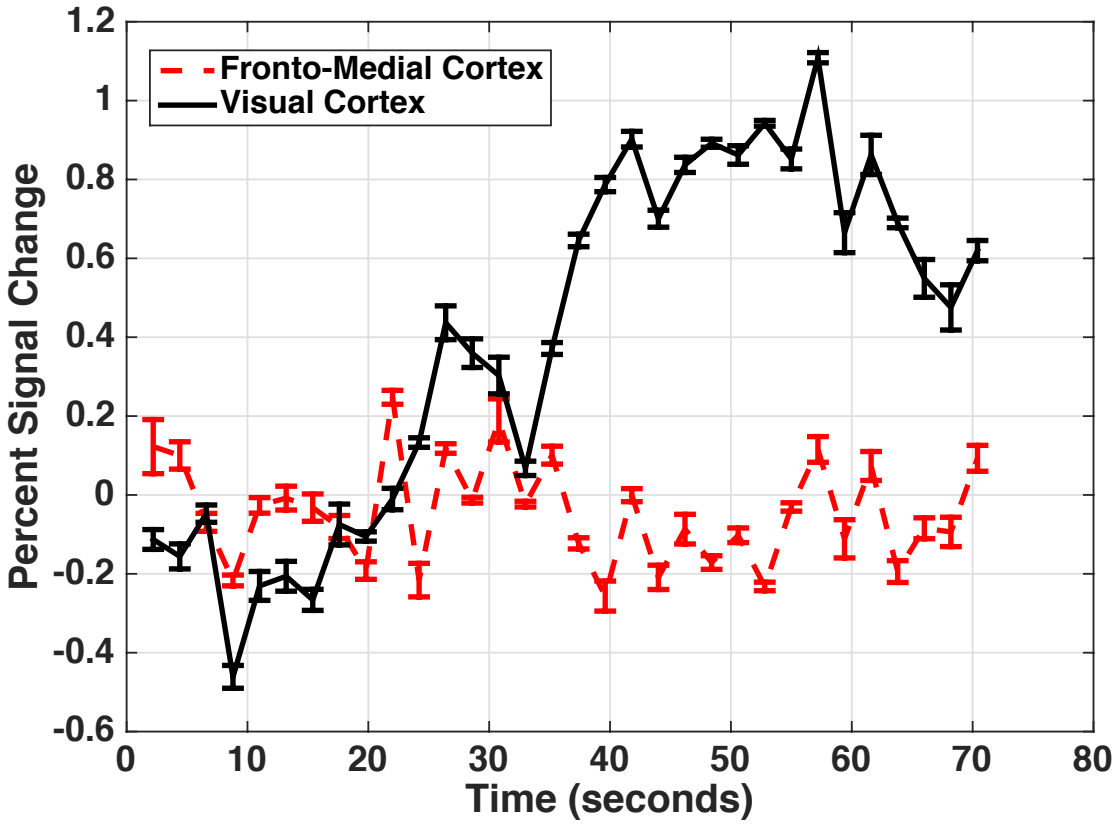

Figure 62: Time course of the frontal cortex and the visual cortex shows only significant changes due to the stimulus occurred in the visual cortex.

The time courses indicated that no significant changes in relaxation occurred due to the application of a stimulus outside of the visual cortex. This provided further evidence the change in signal was due to the BOLD effect, which also then implied the spin-locked sequences with fewer voxels showing significant signal change were more selective than the traditional gradient-echo BOLD or spin-echo BOLD sequences.

The average percent signal change for all sequences after the application of the checkerboard stimulus is shown in Figure 63a. All the acquisitions displayed statistically significant ($p < 0.01$) changes in signal except the 80 Hz spin-lock and T_2 prep pulses.

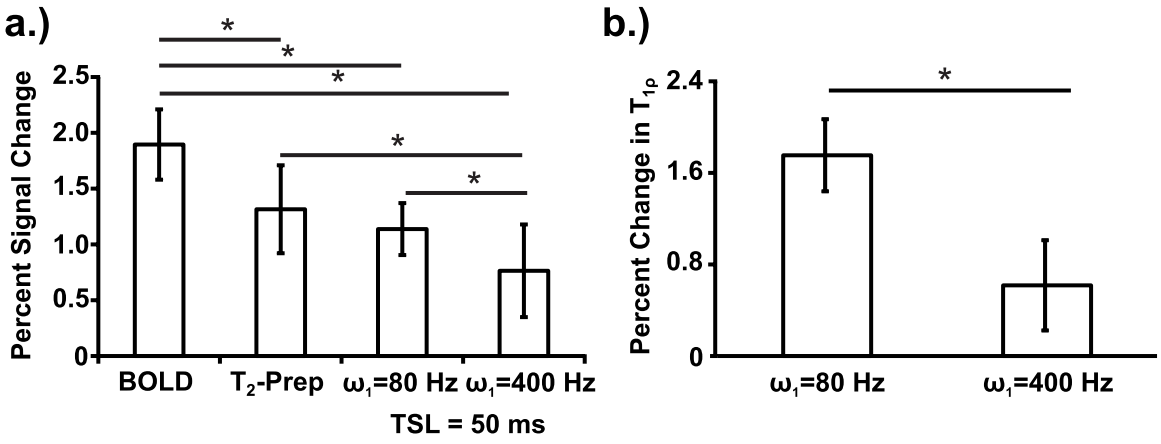

Figure 63: a.) Percent signal change plotted for all sequences, with statistical significance indicated by *. b.) The change in $T_{1\rho}$ compared at both locking fields was shown to be statistically significant.

The percent signal changes were BOLD = 1.9 ± 0.3%, T_2 prep = 1.3 ± 0.4%, $T_{1\rho}$ prep (ω_1 = 80 Hz) = 1.1 ± 0.4%, and $T_{1\rho}$ prep (ω_1 = 400 Hz) = 0.7 ± 0.2%. Figure 63b indicates the average changes in $T_{1\rho}$ at ω_1 = 80 Hz and 400 Hz were significantly different, indicating more relaxation contributions were suppressed at the higher locking amplitude. Figure 64 below shows the average signal changes at each locking time for each of the spin-lock pulses at 80 Hz and 400 Hz. These data indicated greater changes in signal occurred at longer locking times and that significant changes in signal between the two locking powers only occurred at longer times indicated by ** ($p < 0.05$) and * ($p < 0.01$). This behavior was simply due to the fact that there was not enough time for the signal to adequately dephase to measure large differences since the rates of relaxation were so similar between locking amplitudes.

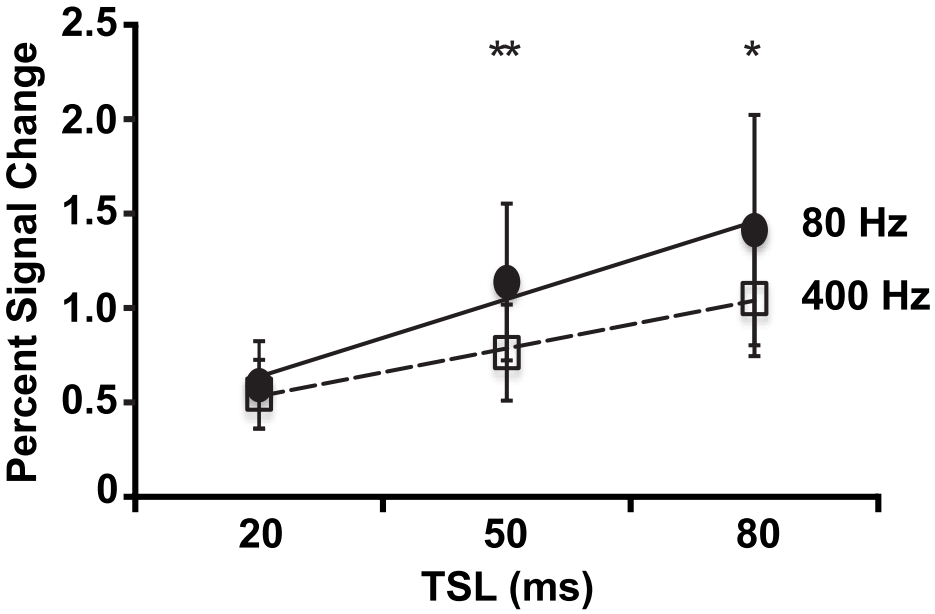

Figure 64: Percent signal change in the visual cortex resulting from the spin-lock sequence at each amplitude. Statistical significance with $p < 0.05$ represented by ** while * represented $p < 0.01$.

The locking time of 80 ms produced a larger *p*-value than at the time of 50 ms due to a substantial drop in SNR, which caused more variability and increased the uncertainty in the measurements. These effects were similar to the signal changes reported in BOLD acquisitions with changes in echo-time, assuming $TE \leq T_2^*$ for $\omega_1 = 400$ Hz (*6*).

The time courses in the visual cortex are shown for all 4 sequences collapsed across all subjects and acquisitions in Figure 65. The data shown here are in accord with Figure 61 and Figure 63 in that the percent signal change decreases from BOLD to T_2-weighted, and on down to the locking field of 400 Hz. The BOLD acquisition displayed significantly higher ($p < 0.05$) signal changes than all other sequences, and showed the greatest rate of change in signal (0.25 ± 0.05 %/s) upon the onset of the stimulus. The derivative of the averaged BOLD signal time course peaked at ~2.0 s, while the T_2 and $T_{1\rho}$ prepped sequences peaked at ~4.4 s.

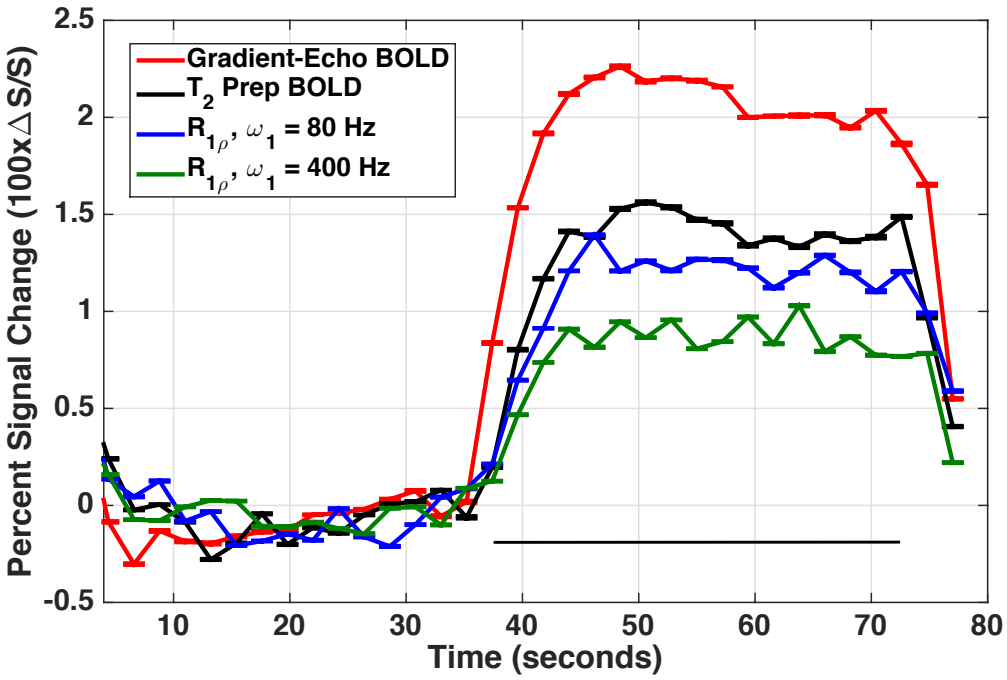

Figure 65: Signal change time course for all 4 pulse sequences collapsed across all subjects and acquisitions. The solid horizontal bar indicates the application of the visual stimulus.

This is in contrast to previous reports that showed $R_{1\rho}$ weighted signals increased faster than BOLD signals (*8*), which must be explained by a non-vascular contribution to the relaxation. The above data agree with other previous reports of gradient-echo BOLD acquisitions display signals that increase more rapidly than spin-echo BOLD due to the gradient-echo sequences being sensitive to both static dephasing as well as contributions from larger vessels. The T_2-weighted acquisitions are more sensitive to smaller vessels since they refocus some of the larger vessel contributions, but they are not as flexible as the $T_{1\rho}$-weighted sequences since they have the ability to tune the locking field to desired amplitudes. The fact that the signal change in the 80 Hz locking pulse was smaller than the T_2-weighted signal, and the 400 Hz experiment showed a larger decrease, again suggested these sequences were more selective in emphasizing only smaller vessel contributions.

Conclusions

The diffusion $R_{1\rho}$ theory presented in chapter 5 was successfully applied to the application of detecting the BOLD effect in fMRI to increase the specificity of the acquired activation maps. This represents the first work of directly comparing the effects of multiple locking fields on BOLD signal changes. Traditional spin-echo BOLD has been shown to be sensitive to smaller vessel contributions than gradient-echo BOLD, but still lacks the specificity and flexibility of spin-lock prepped sequences since they do not apply tunable locking fields. Other studies that applied $T_{1\rho}$ sequences to fMRI applications in the past only used one relatively high locking field of $\omega_1 \geq 400$ Hz. One study in particular by Jin et. al. (*8*) did perform measurements at a range of locking fields from 500 – 2,000 Hz and largely attributed signal changes to chemical exchange effects, in agreement with everything presented in previous chapters. This study, and all other studies, did not explain the effect that spin-locking may suppress signal from vessels that create gradient fields that fluctuate slowly compared to the applied locking field. This conclusion makes this work novel and proves that spin-lock fMRI methods provide a more specific alternative to traditional fMRI methods.

CHAPTER 8

Conclusions and Future Directions

Chemical Exchange $R_{1\rho}$ Dispersion Methods

Three separate models of $R_{1\rho}$ were discussed in the first two chapters, the dipolar contributions were described by BPP theory, and chemical exchange effects were quantified by the Trott and Chopra theories. The exchange theories were revealed to produce very similar results numerically, but the Chopra model was determined to be superior since it was derived on more realistic assumptions and performed moderately better in simulations and fitting to experimental data. Deuterium substitution of protons in glucose at 4.7T and 7T demonstrated the manner in which dipolar effects decreased and exchange effects increased with static field strength. This notion had been expressed previously, but no systematic experiment previously demonstrated the effects in the manner presented here. Realizing the tremendous importance of exchange on spin-locked relaxation, the effects of temperature and pH were examined to establish their influence on $R_{1\rho}$ dispersion and verify the feasibility of calculating exchange parameters in such systems for realistic applications. For example, the significant monotonic increase of exchange rate over physiologically relevant pH ranges implies chemical exchange based imaging may provide the capacity to estimate acidic pH changes in regions of solid tumors. This method was shown to have significant potential since the inflection point of $R_{1\rho}$ dispersions was shown to increase roughly linearly with exchange rate for metabolites like glucose that exhibit hydroxyl exchange in the fast exchange regime. Other specialized methods using $R_{1\rho}$ dispersion analysis including Exchange Rate Contrast (ERC) and Exchange Weighted Image Contrast (EWIC) were analyzed and compared. Though they provide similar information,

the ERC method was verified to be more robust due to the strong dependence on the specified locking time shown by the EWIC method. ERC and EWIC images provide new ways to emphasize protons of specific exchange rates and regions of altered exchange due, for example, to pH changes.

The first two chapters discussed idealized examples of biological tissue that may not be applicable to all cases. The Chopra model was extended to *n*-pools, though it was shown that more than 3 pools introduced too many variables to be experimentally useful. In the case of 2 solute pools (3 total pools), a double dispersion was produced that almost identically reflected the linear addition of the two individual dispersions. The slight disparity at low locking fields may be attributed to slight pool fraction differences in the simulations as well as very minor coupling of the solute pools through the exchange terms in the Bloch-McConnell equations. This effect was shown to be small for realistic pool fractions and not affect the corresponding inflection points, assuring the method was practical for estimating exchange parameters. The simulations established minor exchange had the potential to affect $R_{1\rho}$ dispersion, but was deemed insignificant for practical biological scenarios since pool fractions would be very low and the exchange would have to be extremely fast. This double dispersion analysis was shown to predict exchange parameters well when the individual inflections were distinctly separated by large frequency differences, but failed when the inflections overlapped closely. When the dispersions were distinguishable, simulations and experiments demonstrated the ERC method could also be extended to 3-pools to generate image contrast that directly reflected solute concentrations. This method was proven feasible to separate glucose and uracil in mixtures, though the technique does possess limitations since the concentrations used were larger than most metabolites in live tissues. Further studies are required to assess the method *in vivo* using a

fast exchanging exogenous contrast agent with known concentration and known exchange parameters to quantify the natural concentrations of a slower exchanging metabolite such as acidic glucose or creatine.

$R_{1\rho}$ Dispersion vs. CEST

$R_{1\rho}$ and Chemical Exchange Saturation Transfer (CEST) methods were directly compared in chapter 4 in the application of detecting increased glucose uptake in tumor tissue. The difficulties of working were realized in this section since the tissue concentration of injected 2-Deoxy-D-glucose (2DG) was so dilute. For this reason, $R_{1\rho}$ contrast was introduced and used to compare against CEST methods. $R_{1\rho}$ dispersions and CEST Z-spectra were simulated with parameters similar to those expected in a system of 2DG, and the effects of varying single parameters were evaluated. CEST was shown to be sensitive to more parameters than $R_{1\rho}$ contrast, making it less specific and more difficult to analyze in realistic systems. The CEST simulations were also negatively affected by direct water saturation, which was of no concern in the spin-locking acquisitions. $R_{1\rho}$ contrast was shown to be superior experimentally by exhibiting greater contrast magnitudes and a near linear dependence with 2DG concentration in solutions and tissue homogenates, which was not the case for the Z-spectra in the same model solutions that were complicated from direct water saturation effects. Similar results were discovered when the methods were compared using *in vivo* injections of 2DG in live rats. The $R_{1\rho}$ contrast showed a monotonically increasing trend in contrast with the 2DG infusion with greater magnitudes than the seemingly random changes in CEST contrast in the same rats. The $R_{1\rho}$ contrast curve in malignant tissue exhibited significant increases upon 2DG infusion that were not present in the surrounding healthy tissue, indicating this method may be used to estimate glucose uptake *in vivo* in means similar to established FDG-PET methods. The experiment focused on the specific

glucose analogue 2DG, which displayed exchange behavior that made spin-locking methods more advantageous. It should be noted CEST still provides complementary information to $R_{1\rho}$ dispersion and is more suited for slower exchanging metabolites. The 2DG experiment simply highlights the utility of $R_{1\rho}$ dispersion methods in situations when CEST is not optimal.

$R_{1\rho}$ Diffusion Methods

Proton diffusion through a medium with intrinsic susceptibility gradients was proven to contribute significantly to spin-locked relaxation rates in chapter 5. Though these effects have been mentioned in the literature to influence spin-lattice relaxation in the rotating frame, few have directly investigated them and no quantitative model of these effects had been presented prior to this work. This $R_{1\rho}$-diffusion model, though hinged on an oversimplified notion of a sinusoidally oscillating local field, was proven to be useful in estimating the sizes of packed inhomogeneities through simulations and microsphere experiments. The derived correlation time directly relates the average spatial frequency of the immensely complicated fluctuating local field to a characteristic distance through the rate of diffusion, which was assumed to be 2.5 $\mu m^2/ms$ throughout this work. The simulations revealed the resulting $R_{1\rho}$ dispersion magnitudes were related to the gradient strength while the inflection points, and hence the correlation times, were related to the spacing between the packed spheres and cylinders. This was confirmed in the microsphere experiments through dispersion analysis and through the mapping of the correlation time with different sphere packing fractions. The novel equation used in mapping the correlation times provides the means to potentially map vessel densities or cell sizes in dense tissues, but it should be noted this method requires very high SNR acquisitions since noisy voxels and artifacts may prominently propagate through the equation. The effects of diffusion were shown to be completely independent of chemical exchange effects through simulations since the two effects

resulted in a double dispersion that was the uncoupled linear superposition of single dispersions. Similar problems to those encountered in the 3-pool exchange simulations arose when the inflection points overlapped and the dispersions coalesced. The parameters could not be accurately estimated in this situation, so this is an inherent limitation of examining multiple processes in general using $R_{1\rho}$ dispersion methods. This theory allows the use of spin-locking methods to elucidate novel information about sub-voxel geometric structures experimentally.

Combined Effects and Applications

Quantifying $R_{1\rho}$ diffusion effects in biological tissues was shown to provide viable experimental metrics in various applications. The simplest of these systems was whole bovine blood, where both chemical exchange and diffusion were present in the plasma surrounding the Red Blood Cells (RBC's). These effects were again demonstrated to be independent by only measuring distinct changes in the low frequency diffusion-based dispersion when varying the blood oxygen saturation. The diffusion performed well since the gradients decreased roughly exponentially with oxygen saturation and were independent of the spatial frequency. Average RBC sizes were estimated to be ~4.18 μm by comparing the parameter to the values attained through simulations, which was remarkably close to previously reported values and demonstrated the accuracy and usefulness of the method. Rat livers were analyzed *ex vivo* since they represented more complex solid tissues that should exhibit simultaneous exchange and diffusion effects. The liver experiments measured statistically significant decreases in correlation times with the presence of gadolinium, indicating smaller cells were being emphasized over larger vessels. This demonstrated the ability to measure changes in real tissues with realistic concentrations of contrast agents. Finally, the $R_{1\rho}$ diffusion theory was applied to the application of fMRI with the hopes of increasing the specificity of derived activation maps. This was the

first study to directly link the effects of using different locking fields in a preparation pulse to detect BOLD effects due to vasculature of different scales. These data indicated spin-locked fMRI generated significantly different contrast that more selectively emphasized smaller vasculature than traditional gradient-echo and spin-echo BOLD sequences. This method offered more flexibility by allowing the locking field to be tuned to different amplitudes to reflect different sizes of vessels. Further research needs to be conducted to establish $R_{1\rho}$ fMRI as a viable alternative method and to apply the $R_{1\rho}$ diffusion theory to different biological models for more thorough tissue characterization.

Overall Evaluations of $R_{1\rho}$ Methods

$R_{1\rho}$ dispersion methods have proven to be very powerful in the context of elucidating characteristics of chemical exchange and proton diffusion through intrinsic susceptibility gradients at high static fields. Many studies of $R_{1\rho}$ exist at low fields that are more similar to traditional T_1 or T_2 sequences due to their sensitivity to traditional dipolar or cross-relaxation effects. This work has provided a wealth of evidence that spin-locking methods may provide novel contrasts at high field that can more quantitatively characterize and differentiate tissues across multiple pathologies. A potentially important and recurring conclusion from studies of the dispersion of tissues is that no single locking field is adequate to emphasize or quantify the presence of exchanging species. The low locking field values of $T_{1\rho}$ may reflect multiple contributions, whereas the chemical exchange contributions are substantially reduced at appropriate higher locking fields. Thus it is essentially the difference in rates between low and higher locking fields that indicates the presence and magnitude of exchanging species, not the values at either one condition. This should be borne in mind when using spin locking sequences to quantify, for example, the presence of a dominant exchangeable species such as proteoglycans

in knee cartilage due to degeneration (*228*). Two important limitations of $R_{1\rho}$ dispersion methods are the long acquisition times to collect entire dispersions and the necessary RF power to capture rapid chemical exchange effects. Both of these hurt the potential of using rotating frame relaxation clinically since acquisition times need to be minimized and human scanners cannot reach the same high power B_1 levels as the animal research scanners used here. This calls for more research in parametric imaging techniques like the correlation time mapping or ERC methods that require fewer images than entire $R_{1\rho}$ dispersions.

Another recurring conclusion from every chapter in this thesis is that the inflection point of the dispersion in $R_{1\rho}$ provides quantitative information on the time scale of the interactions responsible for the dispersion. The first 4 chapters focused on the chemical exchange contributions while the 3 subsequent chapters discussed the implications of diffusion on $R_{1\rho}$ dispersion. In all of these chapters, including the scenarios that analyzed double dispersions, the inflection points of the dispersions were the most important parameter for quantifying the rates of any process. $R_{1\rho}$ dispersion provides an accessible method to calculate exchange rates or correlation times that could aid in quantifying parameters reflecting various physico-chemical processes. There were limitations in quantifying these parameters in the cases when multiple dispersions overlap, or in the case of significant chemical exchange between solute pools in mixtures. The methods described above cannot completely overcome these effects so they need to be recognized when they occur in practice. These limitations should not discourage the use of spin-locking experiments since they may still be applied to many applications. Exchange between multiple solute pools is expected to be negligible in most biological tissues though due to realistic metabolite concentrations though, so this effect needs to be considered only in special cases. Also, even though individual pool parameters cannot be derived when exchange-based

dispersions overlap, an overall baseline dispersion may be defined that can be useful in detecting changes due to exogenous contrast agents or other diffusion-based effects. Collectively, these studies suggest spin-locking methods can be a powerful adjunct to the range of MRI methods available for studies of tissue and for the detection of pathological or physiological changes, especially at higher magnetic field strengths.

References

1. U. Duvvuri *et al.*, Quantitative T1rho magnetic resonance imaging of RIF-1 tumors in vivo: detection of early response to cyclophosphamide therapy. *Cancer Res.* **61**, 7747–7753 (2001).
2. Gröhn OHJ *et al.*, Early detection of irreversible cerebral ischemia in the rat using dispersion of the magnetic resonance imaging relaxation time, T1rho. *J. Cereb. Blood Flow Metab.* **20**, 1457–66 (2000).
3. J. M. Hakumäki *et al.*, Early gene therapy-induced apoptotic response in BT4C gliomas by magnetic resonance relaxation contrast T1 in the rotating frame. *Cancer Gene Ther.* **9**, 338–45 (2002).
4. a Sierra *et al.*, Water spin dynamics during apoptotic cell death in glioma gene therapy probed by T1rho and T2rho. *Magn. Reson. Med.* **59**, 1311–1319 (2008).
5. T. Jin, P. Wang, X. Zong, S.-G. Kim, Magnetic resonance imaging of the Amine-Proton EXchange (APEX) dependent contrast. *Neuroimage*. **59**, 1218–27 (2012).
6. J. Hulvershorn *et al.*, T1rho contrast in functional magnetic resonance imaging. *Magn. Reson. Med.* **54**, 1155–1162 (2005).
7. A. Borthakur *et al.*, In vivo measurement of T1rho dispersion in the human brain at 1.5 tesla. *J. Magn. Reson. Imaging*. **19**, 403–9 (2004).
8. T. Jin, S.-G. Kim, Characterization of non-hemodynamic functional signal measured by spin-lock fMRI. *Neuroimage*. **78C**, 385–395 (2013).
9. S. Rane, J. T. Spear, Z. Zu, M. J. Donahue, J. C. Gore, Functional MRI using spin lock editing preparation pulses. *Magn. Reson. Imaging*. **32**, 813–818 (2014).
10. A. Borthakur, M. Sochor, C. Davatzikos, J. Q. Trojanowski, C. M. Clark, T1rho MRI of Alzheimer's disease. *Neuroimage*. **41**, 1199–205 (2008).
11. M. Haris *et al.*, Early marker for Alzheimer's disease: hippocampus T1rho estimation. *J. Magn. Reson. Imaging*. **29**, 1008–12 (2009).
12. M. Haris *et al.*, T(1ρ) MRI in Alzheimer's disease: detection of pathological changes in medial temporal lobe. *J. Neuroimaging*. **21**, e86–90 (2011).
13. A. Borthakur *et al.*, In vivo measurement of plaque burden in a mouse model of Alzheimer's disease. *J. Magn. Reson. Imaging*. **24**, 1011–1017 (2006).
14. L. M. Jazrawi, M. J. Alaia, G. Chang, E. F. Fitzgerald, M. P. Recht, Advances in magnetic resonance imaging of articular cartilage. *J. Am. Acad. Orthop. Surg.* **19**, 420–9 (2011).
15. W. R. T. Witschey *et al.*, T1rho MRI quantification of arthroscopically confirmed cartilage degeneration. *Magn. Reson. Med.* **63**, 1376–82 (2010).
16. U. Duvvuri *et al.*, T1rho-relaxation in articular cartilage: effects of enzymatic degradation. *Magn. Reson. Med.* **38**, 863–7 (1997).
17. J. G. Cobb, J. H. Kan, J. C. Gore, T1ρ mapping of pediatric epiphyseal and articular

cartilage in the knee. *J. Magn. Reson. Imaging*. **38**, 299–305 (2013).

18. U. Duvvuri *et al.*, Water magnetic relaxation dispersion in biological systems: the contribution of proton exchange and implications for the noninvasive detection of cartilage degradation. *Proc. Natl. Acad. Sci. U. S. A.* **98**, 12479–84 (2001).

19. S. K. Koskinen, P. T. Niemi, S. a Kajander, M. E. S. Komu, T1rho Dispersion profile of rat tissues in vitro at very low locking fields. *Magn. Reson. Imaging*. **24**, 295–9 (2006).

20. A. Redfield, Nuclear Magnetic Resonance Saturation and Rotary Saturation in Solids. *Phys. Rev.* **98**, 1787–1809 (1955).

21. A. Abragam, *Principles of Nuclear Magnetism* (Clarendon Press, Oxford, 1961).

22. D. G. Davis, M. E. Perlman, R. E. London, Direct Measurements of the Dissociation-Rate Constant for Inhibitor-Enzyme Complexes via the T1ρ and T2 (CPMG) Methods. *J. Magn. Reson. Ser. B*. **104**, 266–275 (1994).

23. D. M. Korzhnev, M. Billeter, A. S. Arseniev, V. Y. Orekhov, NMR studies of Brownian tumbling and internal motions in proteins. *Prog. Nucl. Magn. Reson. Spectrosc.* **38**, 197–266 (2001).

24. P. C. Lauterbur, Image Formation by Induced Local Interactions: Examples Employing Nuclear Magnetic Resonance. *Nature*. **242**, 190–191 (1973).

25. W. Gerlach, O. Stern, Der experimentelle Nachweis der Richtungsquantelung im Magnetfeld. *Zeitschrift für Phys.* **9**, 349–352 (1922).

26. J. S. Townsend, *A Modern Approach to Quantum Mechanics* (University Science Books, Sausalito, CA, 2000).

27. J. M. B. Kellogg, I. I. Rabi, N. F. Ramsey, J. R. Zacharias, The Magnetic Moments of the Proton and the Deuteron. The Radiofrequency Spectrum of H2 in Various Magnetic Fields. *Phys. Rev.* **56**, 728–743 (1939).

28. E. D. Becker, A Brief History of Nuclear Magnetic Resonance. **65**, 295–302 (1993).

29. C. J. Gorter, L. J. F. Broer, Negative result of an attempt to observe nuclear magnetic resonance in solids. *Physica*. **9**, 591–596 (1942).

30. E. M. Purcell, H. C. Torrey, R. V. Pound, Resonance Absorption by Nuclear Magnetic Moments in a Solid. *Phys. Rev.* **69**, 37–38 (1946).

31. F. Bloch, W. W. Hansen, M. Packard, Nuclear Induction. *Phys. Rev.* **69**, 127 (1946).

32. F. Bloch, Nuclear induction. *Phys. Rev.* **70**, 460–474 (1946).

33. N. Bloembergen, E. Purcell, R. Pound, Relaxation Effects in Nuclear Magnetic Resonance Absorption. *Phys. Rev.* **73**, 679–712 (1948).

34. E. Hahn, Spin Echoes. *Phys. Rev.* **80**, 580–594 (1950).

35. H. Carr, E. Purcell, Effects of Diffusion on Free Precession in Nuclear Magnetic Resonance Experiments. *Phys. Rev.* **94**, 630–638 (1954).

36. W. Knight, Nuclear Magnetic Resonance Shift in Metals. *Phys. Rev.* **76**, 1259–1260

(1949).

37. W. Proctor, F. Yu, The Dependence of a Nuclear Magnetic Resonance Frequency upon Chemical Compound. *Phys. Rev.* **77**, 717 (1950).

38. W. Dickinson, Dependence of the F19 Nuclear Resonance Position on Chemical Compound. *Phys. Rev.* **77**, 736–737 (1950).

39. J. T. Arnold, S. S. Dharmatti, M. E. Packard, Chemical Effects on Nuclear Induction Signals from Organic Compounds. *J. Chem. Phys.* **19**, 507 (1951).

40. H. S. Gutowsky, D. W. McCall, C. P. Slichter, Nuclear Magnetic Resonance Multiplets in Liquids. *J. Chem. Phys.* **21**, 279 (1953).

41. A. W. Overhauser, Polarization of Nuclei in Metals. *Phys. Rev.* **92**, 411–415 (1953).

42. I. Solomon, Relaxation Processes in a System of Two Spins. *Phys. Rev.* **99**, 559–565 (1955).

43. A. G. Redfield, On the Theory of Relaxation Processes. *IBM J. Res. Dev.* **1**, 19–31 (1957).

44. H. M. McConnell, Reaction Rates by Nuclear Magnetic Resonance. *J. Chem. Phys.* **28**, 430–431 (1958).

45. C. Deverell, R. E. Morgan, J. H. Strange, Studies of chemical exchange by nuclear magnetic relaxation in the rotating frame. *Mol. Phys.* **18**, 553–559 (1970).

46. P. Mansfield, P. K. Grannell, NMR "diffraction" in solids? *J. Phys. C Solid State Phys.* **6**, L422–L426 (1973).

47. R. Damadian, Tumor detection by Nuclear Magnetic Resonance. *Science (80-.).* **171**, 1151–1153 (1971).

48. E. M. Haacke, R. Brown, M. Thompson, R. Venkatesan, *Magnetic Resonance Imaging: Physical Principles and Sequence Design* (John Wiley & Sons, Hoboken, ed. 1, 1999).

49. D. Griffiths, *Introduction to Electrodynamics* (Prentice-Hall, Inc., Upper Saddle River, NJ, 3rd ed., 1999).

50. M. H. Levitt, *Spin Dynamics: Basics of Nuclear Magnetic Resonance* (John Wiley & Sons Ltd, West Sussex, England, ed. 2nd, 2008).

51. J. S. Rigden, Quantum states and precession: The two discoveries of NMR. *Rev. Mod. Phys.* **58**, 433–448 (1986).

52. F. Bovey, L. Jelinski, P. Mirau, *Nuclear Magnetic Resonance Spectroscopy* (Academic Press, Inc., San Diego, California, 1988).

53. J. D. Jackson, *Classical Electrodynamics* (John Wiley & Sons, Inc., Hoboken, NJ, ed. 3rd, 1999).

54. R. K. Harris, *Nuclear Magnetic Resonance Spectroscopy: A Physicochemical View* (Longman Scientific & Technical, Essex, England, 1983).

55. B. Blumich, *NMR Imaging of Materials* (Oxford University Press, New York, NY, 2000).

56. H. I. Mäkelä *et al.*, B0 dependence of the on-resonance longitudinal relaxation time in the rotating frame (T1rho) in protein phantoms and rat brain in vivo. *Magn. Reson. Med.* **51**, 4–8 (2004).

57. P. S. Belton, B. P. Hills, G. A. Webb, Eds., *Advances in Magnetic Resonance in Food Science* (The Royal Society of Chemistry, Cambridge, 1999).

58. A. Virta, M. Komu, M. Kormano, T1ρ of protein solutions at very low fields: Dependence on molecular weight, concentration, and structure. *Magn. Reson. Med.* **37**, 53–57 (1997).

59. A. D. Bain, Chemical exchange in NMR. *Prog. Nucl. Magn. Reson. Spectrosc.* **43**, 63–103 (2003).

60. S. Michaeli, D. J. Sorce, D. Idiyatullin, K. Ugurbil, M. Garwood, Transverse relaxation in the rotating frame induced by chemical exchange. *J. Magn. Reson.* **169**, 293–299 (2004).

61. S. Michaeli, D. J. Sorce, C. S. Springer, K. Ugurbil, M. Garwood, T1rho MRI contrast in the human brain: modulation of the longitudinal rotating frame relaxation shutter-speed during an adiabatic RF pulse. *J. Magn. Reson.* **181**, 135–147 (2006).

62. W. R. T. Witschey *et al.*, Artifacts in T1 rho-weighted imaging: compensation for B(1) and B(0) field imperfections. *J. Magn. Reson.* **186**, 75–85 (2007).

63. P. T. Callaghan, *Principles of Nuclear Magnetic Resonance Microscopy* (Oxford University Press, New York, 1991).

64. W. R. T. Witschey *et al.*, Compensation for spin-lock artifacts using an off-resonance rotary echo inT1ρoff-weighted imaging. *Magn. Reson. Med.* **57**, 2–7 (2007).

65. S. Taheri, R. Sood, Spin-lock MRI with amplitude- and phase-modulated adiabatic waveforms: an MR simulation study. *Magn. Reson. Imaging*. **24**, 51–9 (2006).

66. S. Mangia, T. Liimatainen, M. Garwood, S. Michaeli, Rotating frame relaxation during adiabatic pulses vs. conventional spin lock: simulations and experimental results at 4 T. *Magn. Reson. Imaging*. **27**, 1074–87 (2009).

67. S. Mangia, N. J. Traaseth, G. Veglia, M. Garwood, S. Michaeli, Probing slow protein dynamics by adiabatic R(1rho) and R(2rho) NMR experiments. *J. Am. Chem. Soc.* **132**, 9979–9981 (2010).

68. J. G. Cobb, J. Xie, K. Li, D. F. Gochberg, J. C. Gore, Exchange-mediated contrast agents for spin-lock imaging. *Magn. Reson. Med.* **67**, 1427–1433 (2012).

69. J. H. Zhong, J. C. Gore, I. M. Armitage, Relative contributions of chemical exchange and other relaxation mechanisms in protein solutions and tissues. *Magn. Reson. Med.* **11**, 295–308 (1989).

70. J. L. Boxerman, L. M. Hamberg, B. R. Rosen, R. M. Weisskoff, MR contrast due to intravascular magnetic susceptibility perturbations. *Magn. Reson. Med.* **34**, 555–66 (1995).

71. R. P. Kennan, J. Zhong, J. C. Gore, Intravascular susceptibility contrast mechanisms in tissues. *Magn. Reson. Med.* **31**, 9–21 (1994).

72. F. Q. Ye, P. S. Allen, Relaxation enhancement of the transverse magnetization of water protons in paramagnetic suspensions of red blood cells. *Magn. Reson. Med.* **34**, 713–20 (1995).

73. R. M. Weisskoff, C. S. Zuo, J. L. Boxerman, B. R. Rosen, Microscopic susceptibility variation and transverse relaxation: theory and experiment. *Magn. Reson. Med.* **31**, 601–610 (1994).

74. S. Majumdar, S. Zoghbi, C. F. Pope, J. C. Gore, A quantitative study of relaxation rate enhancement produced by iron oxide particles in polyacrylamide gels and tissue. *Magn. Reson. Med.* **9**, 185–202 (1989).

75. J. Zhong, R. P. Kennan, J. C. Gore, Effects of susceptibility variations on NMR measurements of diffusion. *J. Magn. Reson.* **95**, 267–280 (1991).

76. R. P. Kennan, J. Zhong, J. C. Gore, On the relative importance of paramagnetic relaxation and diffusion-mediated susceptibility losses in tissues. *Magn. Reson. Med.* **22**, 197–203 (1991).

77. V. G. Kiselev, S. Posse, Analytical model of susceptibility-induced MR signal dephasing: effect of diffusion in a microvascular network. *Magn. Reson. Med.* **41**, 499–509 (1999).

78. J. H. Jensen, R. Chandra, NMR relaxation in tissues with weak magnetic inhomogeneities. *Magn. Reson. Med.* **44**, 144–56 (2000).

79. A. L. Sukstanskii, D. a. Yablonskiy, Gaussian approximation in the theory of MR signal formation in the presence of structure-specific magnetic field inhomogeneities. *J. Magn. Reson.* **163**, 236–247 (2003).

80. A. L. Sukstanskii, D. a Yablonskiy, Gaussian approximation in the theory of MR signal formation in the presence of structure-specific magnetic field inhomogeneities. Effects of impermeable susceptibility inclusions. *J. Magn. Reson.* **167**, 56–67 (2004).

81. a F. Frøhlich, L. Østergaard, V. G. Kiselev, Theory of susceptibility-induced transverse relaxation in the capillary network in the diffusion narrowing regime. *Magn. Reson. Med.* **53**, 564–73 (2005).

82. B. P. Hills, K. M. Wright, P. S. Belton, Proton N.M.R. studies of chemical and diffusive exchange in carbohydrate systems. *Mol. Phys.* **67**, 1309–1326 (1989).

83. B. P. Hills, S. L. Duce, The influence of chemical and diffusive exchange on water proton transverse relaxation in plant tissues. *Magn. Reson. Imaging*. **8**, 321–31 (1990).

84. J. T. Spear, Z. Zu, J. C. Gore, Dispersion of relaxation rates in the rotating frame under the action of spin-locking pulses and diffusion in inhomogeneous magnetic fields. *Magn. Reson. Med.* **71**, 1906–1911 (2014).

85. J. T. Spear, J. C. Gore, Effects of diffusion in magnetically inhomogeneous media on rotating frame spin–lattice relaxation. *J. Magn. Reson.* **249**, 80–87 (2014).

86. M. I. Kettunen, O. H. Gröhn, M. Penttonen, R. a Kauppinen, Cerebral T1rho relaxation time increases immediately upon global ischemia in the rat independently of blood glucose and anoxic depolarization. *Magn. Reson. Med.* **46**, 565–572 (2001).

87. G. Jones, Spin-Lattice Relaxation in the Rotating Frame: Weak-Collision Case. *Phys. Rev.* **148**, 332–335 (1966).

88. S. R. Charagundla, T1rho-Weighted Magnetic Resonance Imaging: Principles and Diagnostic Application. *Appl. Radiol.* **33**, 32–43 (2004).

89. H. Poptani *et al.*, T1rho imaging of murine brain tumors at 4 T. *Acad. Radiol.* **8**, 42–7 (2001).

90. P. C. M. van Zijl, N. N. Yadav, Chemical exchange saturation transfer (CEST): what is in a name and what isn't? *Magn. Reson. Med.* **65**, 927–48 (2011).

91. J. G. Cobb, J. Xie, J. C. Gore, Contributions of chemical exchange to T1ρ dispersion in a tissue model. *Magn. Reson. Med.* **66**, 1563–1571 (2011).

92. M. Zaiss, P. Bachert, Exchange-dependent relaxation in the rotating frame for slow and intermediate exchange - modeling off-resonant spin-lock and chemical exchange saturation transfer. *NMR Biomed.* **26**, 507–518 (2013).

93. S. Chopra, R. E. . McClung, R. B. Jordan, Rotating-frame relaxation rates of solvent molecules in solutions of paramagnetic ions undergoing solvent exchange. *J. Magn. Reson.* **59**, 361–372 (1984).

94. O. Trott, A. G. Palmer, R1rho relaxation outside of the fast-exchange limit. *J. Magn. Reson.* **154**, 157–160 (2002).

95. T. Jin, J. Autio, T. Obata, S.-G. Kim, Spin-locking versus chemical exchange saturation transfer MRI for investigating chemical exchange process between water and labile metabolite protons. *Magn. Reson. Med.* **65**, 1448–60 (2011).

96. C. MacLean, E. Mackor, Transverse Relaxation in Systems of Two Nonidentical Spins. *J. Chem. Phys.* **44**, 2708 (1966).

97. B. P. Hills, Multinuclear NMR studies of water in solutions of simple carbohydrates. *Mol. Phys.* **72**, 1099–1121 (1991).

98. J. G. Cobb, K. Li, J. Xie, D. F. Gochberg, J. C. Gore, Exchange-mediated contrast in CEST and spin-lock imaging. *Magn. Reson. Imaging*. **32**, 28–40 (2013).

99. B. P. Hills, The proton exchange cross-relaxation model of water relaxation in biopolymer systems II. The sol and gel states of gelatine. *Mol. Phys.* **76**, 509–523 (1992).

100. M. G. Irving, I. M. Brereton, J. Field, D. M. Doddrell, In vivo determination of body iron stores by natural-abundance deuterium magnetic resonance spectroscopy. *Magn. Reson. Med.* **4**, 88–92 (1987).

101. M. Cotten, R. Fu, T. a Cross, Solid-state NMR and hydrogen-deuterium exchange in a bilayer-solubilized peptide: structural and mechanistic implications. *Biophys. J.* **76**, 1179–89 (1999).

102. M. W. F. Fischer, A. Majumdar, E. R. P. Zuiderweg, Protein NMR relaxation: theory, applications and outlook. *Prog. Nucl. Magn. Reson. Spectrosc.* **33**, 207–272 (1998).

103. E.-L. Chen, R. J. Kim, Magnetic resonance water proton relaxation in protein solutions

and tissue: T1rho dispersion characterization. *PLoS One*. **5**, e8565 (2010).

104. A. L. Hansen, P. Lundström, A. Velyvis, L. E. Kay, Quantifying millisecond exchange dynamics in proteins by CPMG relaxation dispersion NMR using side-chain 1H probes. *J. Am. Chem. Soc.* **134**, 3178–89 (2012).

105. M. D. Finucane, O. Jardetzky, The pH dependence of hydrogen-deuterium exchange in trp repressor: the exchange rate of amide protons in proteins reflects tertiary interactions, not only secondary structure. *Protein Sci.* **5**, 653–62 (1996).

106. A. G. Doukas *et al.*, On the mechanism of hydrogen-deuterium exchange in bacteriorhodopsin. *Biophys. J.* **33**, 275–279 (1981).

107. S. H. Koenig, W. E. Schillinger, Nuclear Magnetic Relaxation Dispersion in Protein Solutions. *J. Biol. Chem.* **244**, 3283–3289 (1969).

108. S. Campbell, M. T. Rodgers, E. M. Marzluff, J. L. Beauchamp, Deuterium Exchange Reactions as a Probe of Biomolecule Structure. Fundamental Studies of Gas Phase H/D Exchange Reactions of Protonated Glycine Oligomers with D2O, CD3OD, CD3CO2D, and ND3. *J. Am. Chem. Soc.* **117**, 12840–12854 (1995).

109. V. Tugarinov, Indirect use of deuterium in solution NMR studies of protein structure and hydrogen bonding. *Prog. Nucl. Magn. Reson. Spectrosc.* **77**, 49–68 (2014).

110. W. D. Morgan, A. Kragt, J. Feeney, Expression of deuterium-isotope-labelled protein in the yeast pichia pastoris for NMR studies. *J Biomol NMR*. **17**, 337–347 (2000).

111. W. R. Arnold, A. Roberts, The Magnetic Moments of the Neutron and the Deuteron. *Phys. Rev.* **71**, 878–886 (1947).

112. D. B. Northrop, Steady-state analysis of kinetic isotope effects in enzymic reactions. *Biochemistry*. **14**, 2644–2651 (1975).

113. W. D. Phillips, J. C. Rowell, L. R. Melby, Quadrupole Splittings in the Deuterium Magnetic Resonance Spectra of Liquid Crystals. *J. Chem. Phys.* **41**, 2551 (1964).

114. M. Silberberg, *Principles of General Chemistry* (McGraw-Hill Companies, Inc., New York, ed. 1st, 2007).

115. A. Allerhand, H. S. Gutowsky, J. Jonas, R. A. Meinzer, Nuclear magnetic resonance methods for determining chemical-exchange rates. *J. Am. Chem. Soc.* **88**, 3185–93 (1966).

116. S. D. Wolff, R. S. Balaban, NMR imaging of labile proton exchange. *J. Magn. Reson.* **86**, 164–169 (1990).

117. E. Liepinsh, G. Otting, Proton exchange rates from amino acid side chains--implications for image contrast. *Magn. Reson. Med.* **35**, 30–42 (1996).

118. K. M. Ward, a H. Aletras, R. S. Balaban, A new class of contrast agents for MRI based on proton chemical exchange dependent saturation transfer (CEST). *J. Magn. Reson.* **143**, 79–87 (2000).

119. M. Zaiss, P. Kunz, S. Goerke, A. Radbruch, P. Bachert, MR imaging of protein folding in vitro employing Nuclear-Overhauser-mediated saturation transfer. *NMR Biomed.* **26**,

1815–22 (2013).

120. A. G. Palmer, Chemical exchange in biomacromolecules: past, present, and future. *J. Magn. Reson.* **241**, 3–17 (2014).

121. T. Jin, H. Mehrens, K. S. Hendrich, S.-G. Kim, Mapping brain glucose uptake with chemical exchange-sensitive spin-lock magnetic resonance imaging. *J. Cereb. Blood Flow Metab.* **34**, 1402–1410 (2014).

122. J. Yuan, J. Zhou, A. T. Ahuja, Y.-X. J. Wang, MR chemical exchange imaging with spin-lock technique (CESL): a theoretical analysis of the Z-spectrum using a two-pool R(1ρ) relaxation model beyond the fast-exchange limit. *Phys. Med. Biol.* **57**, 8185–8200 (2012).

123. J. G. Cobb, J. Xie, J. C. Gore, Contributions of chemical and diffusive exchange to T(1ρ) dispersion. *Magn. Reson. Med.* **69**, 1357–1366 (2013).

124. I. F. Tannock, D. Rotin, Acid pH in tumors and its potential for therapeutic exploitation. *Cancer Res.* **49**, 4373–4384 (1989).

125. R. J. Gillies *et al.*, Applications of magnetic resonance in model systems: tumor biology and physiology. *Neoplasia*. **2**, 139–51 (2000).

126. W. Anderson, J. Arnold, Proton Relaxation Times in H2O—D2O Mixtures. *Phys. Rev.* **101**, 511–512 (1956).

127. D. E. Woessner, S. Zhang, M. E. Merritt, a D. Sherry, Numerical solution of the Bloch equations provides insights into the optimum design of PARACEST agents for MRI. *Magn. Reson. Med.* **53**, 790–9 (2005).

128. O. Trott, A. G. Palmer, Theoretical study of R(1rho) rotating-frame and R2 free-precession relaxation in the presence of n-site chemical exchange. *J. Magn. Reson.* **170**, 104–112 (2004).

129. P. C. M. van Zijl, C. K. Jones, J. Ren, C. R. Malloy, a D. Sherry, MRI detection of glycogen in vivo by using chemical exchange saturation transfer imaging (glycoCEST). *Proc. Natl. Acad. Sci. U. S. A.* **104**, 4359–64 (2007).

130. M. Haris *et al.*, Exchange rates of creatine kinase metabolites: feasibility of imaging creatine by chemical exchange saturation transfer MRI. *NMR Biomed.* **25**, 1305–9 (2012).

131. P. Thureau, B. Ancian, S. Viel, A. Thévand, Determining chemical exchange rates of the uracil labile protons by NMR diffusion experiments. *Chem. Commun. (Camb).*, 200–2 (2006).

132. R. E. Hurd, B. R. Reid, NMR spectroscopy of the ring nitrogen protons of uracil and substituted uracils; relevance to A psi base pairing in the solution structure of transfer RNA. *Nucleic Acids Res.* **4**, 2747–55 (1977).

133. R. R. Rizi *et al.*, Proton T1ρ-dispersion imaging of rodent brain at 1.9 T. *J. Magn. Reson. Imaging*. **8**, 1090–1096 (1998).

134. R. Sood, Off-resonance binomial preparatory pulse technique for high sensitivity MRI of H2O17. *Magn. Reson. Imaging*. **22**, 181–195 (2004).

135. K. S. McCommis *et al.*, Cardiac 17O MRI: toward direct quantification of myocardial oxygen consumption. *Magn. Reson. Med.* **63**, 1442–1447 (2010).

136. B. Mimic *et al.*, Comparison of high glucose concentration blood and crystalloid cardioplegia in paediatric cardiac surgery: a randomized clinical trial. *Interact Cardiovasc Thorac Surg*, 1–8 (2016).

137. American Diabetes Association, Screening for Type 2 Diabetes. *Diabetes Care*. **27**, S11–S14 (2004).

138. R. Gruetter, K. Ugurbil, E. R. Seaquist, Steady-state cerebral glucose concentrations and transport in the human brain. *J. Neurochem.* **70**, 397–408 (1998).

139. I.-Y. Choi, H. Lei, R. Gruetter, Effect of deep pentobarbital anesthesia on neurotransmitter metabolism in vivo: on the correlation of total glucose consumption with glutamatergic action. *J. Cereb. Bloood Flow Metab.* **22**, 1343–1351 (2002).

140. K. C. C. Van De Ven, M. Van Der Graaf, C. J. Tack, A. Heerschap, B. E. De Galan, Steady-state brain glucose concentrations during hypoglycemia in healthy humans and patients with type 1 diabetes. *Diabetes*. **61**, 1974–1977 (2012).

141. C. K. Jones *et al.*, Nuclear Overhauser enhancement (NOE) imaging in the human brain at 7T. *Neuroimage*. **77**, 114–24 (2013).

142. T. Jin, P. Wang, X. Zong, S.-G. Kim, MR imaging of the amide-proton transfer effect and the pH-insensitive nuclear overhauser effect at 9.4 T. *Magn. Reson. Med.* **69**, 760–70 (2013).

143. S. Walker-Samuel, P. Johnson, B. Pedley, M. Lythgoe, X. Golay, in *Proceedings of the 19th Annual Meeting of ISMRM* (Montreal, Canada, 2011), p. 962.

144. K. Chan *et al.*, in *Proceedings of the 19th Annual Meeting of ISMRM* (Montreal, Canada, 2011), p. 551.

145. S. Walker-Samuel *et al.*, in *Proceedings of the 20th Annual Meeting of ISMRM* (Melbourne, Australia, 2012), p. 182.

146. S. Walker-Samuel *et al.*, In vivo imaging of glucose uptake and metabolism in tumors. *Nat. Med.* **19**, 1067–1072 (2013).

147. K. W. Y. Chan *et al.*, Natural D-glucose as a biodegradable MRI contrast agent for detecting cancer. *Magn. Reson. Med.* **68**, 1764–73 (2012).

148. F. a Nasrallah, G. Pagès, P. W. Kuchel, X. Golay, K.-H. Chuang, Imaging brain deoxyglucose uptake and metabolism by glucoCEST MRI. *J. Cereb. Blood Flow Metab.* **33**, 1270–8 (2013).

149. M. G. Vander Heiden, L. C. Cantley, C. B. Thompson, Understanding the Warburg effect: the metabolic requirements of cell proliferation. *Science (80-.).* **324**, 1029–33 (2009).

150. B. M. Madhok, S. Yeluri, S. L. Perry, T. a Hughes, D. G. Jayne, Targeting glucose metabolism: an emerging concept for anticancer therapy. *Am. J. Clin. Oncol.* **34**, 628–35 (2011).

151. Z. Zu, J. Spear, H. Li, J. Xu, J. C. Gore, Measurement of regional cerebral glucose uptake by magnetic resonance spin-lock imaging. *Magn. Reson. Imaging*. **32**, 1078–1084 (2014).

152. L. Sokoloff *et al.*, The [14C]deoxyglucose method for the measurement of local cerebral glucose utilization: theory, procedure, and normal values in the conscious and anesthetized albino rat. *J. Neurochem.* **28**, 897–916 (1977).

153. E. a Eisenhauer *et al.*, New response evaluation criteria in solid tumours: revised RECIST guideline (version 1.1). *Eur. J. Cancer*. **45**, 228–47 (2009).

154. M. Reivich *et al.*, The [18F]fluorodeoxyglucose method for the measurement of local cerebral glucose utilization in man. *Circ. Res.* **44**, 127–37 (1979).

155. D. M. Cohen *et al.*, A method for measuring cerebral glucose metabolism in vivo by 13C-NMR spectroscopy. *Magn. Reson. Med.* **48**, 1063–1067 (2002).

156. J. Zhou, P. Zijl, Chemical exchange saturation transfer imaging and spectroscopy. *Prog. Nucl. Magn. Reson. Spectrosc.* **48**, 109–136 (2006).

157. J. G. Sled, G. B. Pike, Quantitative interpretation of magnetization transfer in spoiled gradient echo MRI sequences. *J Magn Reson*. **145**, 24–36 (2000).

158. D. Tozer *et al.*, Quantitative magnetization transfer mapping of bound protons in multiple sclerosis. *Magn. Reson. Med.* **50**, 83–91 (2003).

159. C. Morrison, G. Stanisz, R. M. Henkelman, Modeling Magnetization Transfer for Biological-like Systems Using a Semi-solid Pool with a Super-Lorentzian Lineshape and Dipolar Reservoir. *J. Magn. Reson. Ser. B*. **108**, 103–113 (1995).

160. C. Morrison, R. M. Henkelman, A model for magnetization transfer in tissues. *Magn. Reson. Med.* **33**, 475–482 (1995).

161. O. Warburg, K. Posener, E. Negelein, Uber den Stoffwechsel der Carcinomzelle. *Biochem. Z.* **152**, 309 – 344 (1924).

162. O. Warburg, On the Origin of Cancer Cells. *Science (80-.).* **123**, 309–314 (1956).

163. R. Gruetter, M. Garwood, K. Uğurbil, E. R. Seaquist, Observation of resolved glucose signals in 1H NMR spectra of the human brain at 4 Tesla. *Magn. Reson. Med.* **36**, 1–6 (1996).

164. R. Vijayaraghavan *et al.*, Acute toxicity and cardio-respiratory effects of 2-deoxy-D-glucose: a promising radio sensitiser. *Biomed. Environ. Sci.* **19**, 96–103 (2006).

165. M. Kurtoglu, J. C. Maher, T. J. Lampidis, Differential toxic mechanisms of 2-deoxy-D-glucose versus 2-fluorodeoxy-D-glucose in hypoxic and normoxic tumor cells. *Antioxid. Redox Signal.* **9**, 1383–1390 (2007).

166. P. Muley, A. Olinger, H. Tummala, 2-Deoxyglucose induces cell cycle arrest and apoptosisin colorectal cancer cells independent of its glycolysis inhibition. *Nutr. Cancer*. **67**, 514–522 (2015).

167. B. Dwarakanath, V. Jain, Targeting glucose metabolism with 2-deoxy-D-glucose for improving cancer therapy. *Futur. Oncol.* **5**, 581–585 (2009).

168. O. Zagorodna *et al.*, 2-Deoxyglucose-induced toxicity is regulated by Bcl-2 family members and is enhanced by antagonizing Bcl-2 in lymphoma cell lines. *Oncogene*. **31**, 2738–2749 (2012).

169. P. Martirosian, E. Rommel, F. Schick, M. Deimling, Control of susceptibility-related image contrast by spin-lock techniques. *Magn. Reson. Imaging*. **26**, 1381–1387 (2008).

170. E. Lammentausta *et al.*, T2, Carr-Purcell T2 and T1rho of fat and water as surrogate markers of trabecular bone structure. *Phys. Med. Biol.* **53**, 543–555 (2008).

171. M. I. Kettunen, O. H. J. Gröhn, M. J. Silvennoinen, M. Penttonen, R. a Kauppinen, Effects of intracellular pH, blood, and tissue oxygen tension on T1rho relaxation in rat brain. *Magn. Reson. Med.* **48**, 470–477 (2002).

172. E. M. Haacke *et al.*, Imaging iron stores in the brain using magnetic resonance imaging. *Magn. Reson. Imaging*. **23**, 1–25 (2005).

173. R. a. Iles, a. N. Stevens, J. R. Griffiths, NMR Studies of metabolites in living tissue. *Prog. Nucl. Magn. Reson. Spectrosc.* **15**, 49–200 (1982).

174. C. V Bowen, X. Zhang, G. Saab, P. J. Gareau, B. K. Rutt, Application of the static dephasing regime theory to superparamagnetic iron-oxide loaded cells. *Magn. Reson. Med.* **48**, 52–61 (2002).

175. L. Li, J. S. Leigh, Quantifying arbitrary magnetic susceptibility distributions with MR. *Magn. Reson. Med.* **51**, 1077–82 (2004).

176. S. Majumdar, J. . Gore, Studies of diffusion in random fields produced by variations in susceptibility. *J. Magn. Reson.* **78**, 41–55 (1988).

177. K.-T. Yung, Empirical models of transverse relaxation for spherical magnetic perturbers. *Magn. Reson. Imaging*. **21**, 451–63 (2003).

178. F. T. Kurz *et al.*, Theoretical model of the single spin-echo relaxation time for spherical magnetic perturbers. *Magn. Reson. Med.* **71**, 1888–1895 (2014).

179. V. G. Kiselev, Effect of magnetic field gradients induced by microvasculature on NMR measurements of molecular self-diffusion in biological tissues. *J. Magn. Reson.* **170**, 228–35 (2004).

180. B. Cowan, *Nuclear Magnetic Resonance and Relaxation* (Cambridge University Press, Cambridge, 1997).

181. J. A. Glasel, K. H. Lee, Interpretation of water nuclear magnetic resonance relaxation times in heterogeneous systems. *J. Am. Chem. Soc.* **96**, 970–978 (1974).

182. L. A. Stables, R. P. Kennan, J. C. Gore, Asymmetric spin-echo imaging of magnetically inhomogeneous systems: theory, experiment, and numerical studies. *Magn. Reson. Med.* **40**, 432–42 (1998).

183. J. Van Vleck, The Dipolar Broadening of Magnetic Resonance Lines in Crystals. *Phys. Rev.* **74**, 1168–1183 (1948).

184. J. C. Gore, S. Leeman, Transfer functions for describing ultrasound system performance.

Phys. Med. Biol. **24**, 146–156 (1979).

185. J. Xu, M. D. Does, J. C. Gore, Numerical study of water diffusion in biological tissues using an improved finite difference method. *Phys. Med. Biol.* **52**, N111–N126 (2007).

186. H. Watarai, M. Namba, Magnetophoretic behavior of single polystyrene particles in aqueous manganese(II) chloride. *Anal. Sci.* **17**, 1233–6 (2001).

187. H. Zhang *et al.*, Establishment and implications of a characterization method for magnetic nanoparticle using cell tracking velocimetry and magnetic susceptibility modified solutions. *Analyst*. **130**, 514–27 (2005).

188. O. H. Gröhn *et al.*, Quantitative magnetic resonance imaging assessment of cerebral ischemia in rat using on-resonance T(1) in the rotating frame. *Magn. Reson. Med.* **42**, 268–276 (1999).

189. N. M. Menezes, M. L. Gray, J. R. Hartke, D. Burstein, T2 and T1rho MRI in articular cartilage systems. *Magn. Reson. Med.* **51**, 503–509 (2004).

190. J. Dennie *et al.*, NMR imaging of changes in vascular morphology due to tumor angiogenesis. *Magn. Reson. Med.* **40**, 793–9 (1998).

191. K. . Packer, The effects of diffusion through locally inhomogeneous magnetic fields on transverse nuclear spin relaxation in heterogeneous systems. Proton transverse relaxation in striated muscle tissue. *J. Magn. Reson.* **9**, 438–443 (1973).

192. I. Troprès *et al.*, In vivo assessment of tumoral angiogenesis. *Magn. Reson. Med.* **51**, 533–41 (2004).

193. I. Troprès *et al.*, Vessel size imaging. *Magn. Reson. Med.* **45**, 397–408 (2001).

194. B. Audoly, P. N. Sen, S. Ryu, Y.-Q. Song, Correlation functions for inhomogeneous magnetic field in random media with application to a dense random pack of spheres. *J. Magn. Reson.* **164**, 154–159 (2003).

195. V. Jain, O. Abdulmalik, K. J. Propert, F. W. Wehrli, Investigating the magnetic susceptibility properties of fresh human blood for noninvasive oxygen saturation quantification. *Magn. Reson. Med.* **68**, 863–867 (2012).

196. W. M. W. Spees, D. A. Da Yablonskiy, M. C. Oswood, J. J. H. Ackerman, Water proton MR properties of human blood at 1.5 Tesla: Magnetic susceptibility, T1, T2, T2*, and non Lorentzian signal behavior. *Magn. Reson. ….* **45**, 533–542 (2001).

197. J. Yuan *et al.*, Quantification of T(1ρ) relaxation by using rotary echo spin-lock pulses in the presence of B(0) inhomogeneity. *Phys. Med. Biol.* **57**, 5003–16 (2012).

198. P. N. A. Martins, P. Neuhaus, Surgical anatomy of the liver, hepatic vasculature and bile ducts in the rat. *Liver Int.* **27**, 384–392 (2007).

199. M. Diez-Silva, M. Dao, J. Han, C.-T. Lim, S. Suresh, Shape and Biomechanical Characteristics of Human Red Blood Cells in Health and Disease. *MRS Bull.* **35**, 382–388 (2010).

200. M. Johanna Silvennoinen, M. I. Kettunen, C. S. Clingman, R. a Kauppinen, Blood NMR

relaxation in the rotating frame: mechanistic implications. *Arch. Biochem. Biophys.* **405**, 78–86 (2002).

201. P. J. Haar *et al.*, Gd-DTPA T1 relaxivity in brain tissue obtained by convection-enhanced delivery, magnetic resonance imaging and emission spectroscopy. *Phys. Med. Biol.* **55**, 3451–65 (2010).

202. R. E. Hendrick, E. M. Haacke, Basic physics of MR contrast agents and maximization of image contrast. *J. Magn. Reson. Imaging*. **3**, 137–48 (1993).

203. N. M. Hijnen *et al.*, The magnetic susceptibility effect of gadolinium-based contrast agents on PRFS-based MR thermometry during thermal interventions. *J. Ther. ultrasound*. **1**, 8 (2013).

204. J. F. Schenck, The role of magnetic susceptibility in magnetic resonance imaging: MRI magnetic compatibility of the first and second kinds. *Med. Phys.* **23**, 815 (1996).

205. R. M. Weisskoff, S. Kiihne, MRI susceptometry: image-based measurement of absolute susceptibility of MR contrast agents and human blood. *Magn. Reson. Med.* **24**, 375–383 (1992).

206. R. P. Evarts, E. Marsden, P. Hanna, P. J. Wirth, S. S. Thorgeirsson, Isolation of preneoplastic rat liver cells by centrifugal elutriation and binding to asialofetuin. *Cancer Res.* **44**, 5718–5724 (1984).

207. M. D. Greicius, B. Krasnow, A. L. Reiss, V. Menon, Functional connectivity in the resting brain: A network analysis of the default mode hypothesis. *Proc. Natl. Acad. Sci.* **100**, 253–258 (2003).

208. P. Fransson, Spontaneous low-frequency BOLD signal fluctuations: An fMRI investigation of the resting-state default mode of brain function hypothesis. *Hum. Brain Mapp.* **26**, 15–29 (2005).

209. M. De Luca, C. F. Beckmann, N. De Stefano, P. M. Matthews, S. M. Smith, fMRI resting state networks define distinct modes of long-distance interactions in the human brain. *Neuroimage*. **29**, 1359–1367 (2006).

210. S. Ogawa *et al.*, Intrinsic signal changes accompanying sensory stimulation: functional brain mapping with magnetic resonance imaging. *Proc. Natl. Acad. Sci.* **89**, 5951–5 (1992).

211. N. K. Logothetis, The underpinnings of the BOLD functional magnetic resonance imaging signal. *J. Neurosci.* **23**, 3963–3971 (2003).

212. J. L. Boxerman *et al.*, The intervascular contributions to fMRI signal change: Monte Carlo modeling and diffusion-weighted studies in vivo. *Magn. Reson. Med.* **34**, 4–10 (1995).

213. V. Toronov *et al.*, The roles of changes in deoxyhemoglobin concentration and regional cerebral blood volume in the fMRI BOLD signal. *Neuroimage*. **19**, 1521–1531 (2003).

214. E. Yacoub, P. F. Van De Moortele, A. Shmuel, K. U??urbil, Signal and noise characteristics of Hahn SE and GE BOLD fMRI at 7 T in humans. *Neuroimage*. **24**, 738–

750 (2005).

215. J. Zhong, R. P. Kennan, R. K. Fulbright, J. C. Gore, Quantification of intravascular and extravascular contributions to BOLD effects induced by alteration in oxygenation or intravascular contrast agents. *Magn. Reson. Med.* **40**, 526–536 (1998).

216. T. Q. Duong *et al.*, Microvascular BOLD contribution at 4 and 7 T in the human brain: Gradient-echo and spin-echo fMRI with suppression of blood effects. *Magn. Reson. Med.* **49**, 1019–1027 (2003).

217. J. Hulvershorn, L. Bloy, E. E. Gualtieri, J. S. Leigh, M. A. Elliott, Spatial sensitivity and temporal response of spin echo and gradient echo bold contrast at 3 T using peak hemodynamic activation time. *Neuroimage*. **24**, 216–223 (2005).

218. K. M. Johnson, J. Z. Tao, R. P. Kennan, J. C. Gore, Intravascular susceptibility agent effects on tissue transverse relaxation rates in vivo. *Magn. Reson. Med.* **44**, 909–14 (2000).

219. L. M. Parkes *et al.*, Quantifying the spatial resolution of the gradient echo and spin echo BOLD response at 3 Tesla. *Magn. Reson. Med.* **54**, 1465–1472 (2005).

220. S. Ogawa *et al.*, Functional brain mapping by blood oxygenation level-dependent contrast magnetic resonance imaging. A comparison of signal characteristics with a biophysical model. *Biophys. J.* **64**, 803–812 (1993).

221. M. J. Silvennoinen, C. S. Clingman, X. Golay, R. A. Kauppinen, P. C. M. Van Zijl, Comparison of the dependence of blood R2 and R2* on oxygen saturation at 1.5 and 4.7 Tesla. *Magn. Reson. Med.* **49**, 47–60 (2003).

222. A. Borthakur *et al.*, A pulse sequence for rapid in vivo spin-locked MRI. *J. Magn. Reson. Imaging*. **23**, 591–596 (2006).

223. V. A. Magnotta *et al.*, Detecting activity-evoked pH changes in human brain. *Proc. Natl. Acad. Sci. U. S. A.* **109**, 8270–8273 (2012).

224. R. W. Cox, J. S. Hyde, Software tools for analysis and visualization of fMRI data. *NMR Biomed.* **10**, 171–178 (1997).

225. W. P. Road, AFNI : Software for Analysis and Visualization of Functional Magnetic Resonance Neuroimages. **173**, 162–173 (1996).

226. S. M. Smith *et al.*, Advances in functional and structural MR image analysis and implementation as FSL. *Neuroimage*. **23**, 208–219 (2004).

227. M. W. Woolrich *et al.*, Bayesian analysis of neuroimaging data in FSL. *Neuroimage*. **45**, 173–186 (2009).

228. P. Wang, J. Block, J. C. Gore, Chemical exchange in knee cartilage assessed by R1rho (1/T1rho) dispersion at 3T. *Magn. Reson. Imaging*. **33**, 38–42 (2015).